Phase-Advanced Attitude Sensing and Control for Fixed-Wing Micro Aerial Vehicles in Turbulence

A thesis submitted in fulfilment of the requirements for the degree of Doctor of Philosophy

Abdulghani H. Mohamed

B.Eng (Hons)

School of Aerospace Mechanical and Manufacturing Engineering

College of Science Engineering and Health

RMIT University

February 2015

Declaration

I certify that except where due acknowledgement has been made, the work is that of the author alone; the work has not been submitted previously, in whole or in part, to qualify for any other academic award; the content of the thesis/project is the result of work which has been carried out since the official commencement date of the approved research program; any editorial work, paid or unpaid, carried out by a third party is acknowledged; and, ethics procedures and guidelines have been followed.

Abdulghani H. Mohamed

25 June 2015

Acknowledgements

The research could not have been successfully completed without the support of a number of people. The author will be forever grateful for the friendship, advice and empathy of those people

I wish to express my sincere appreciation and gratitude to my supervisors, Prof. Simon Watkins and Dr. Reece Clothier for their continuous support, advice, and friendship in the duration of the program. Prof. Watkins' unique mentoring skills to elevate one's knowledge, skills, comprehension, understanding, and problem solving is superlative. His ability to see the "bigger picture" and foresee and rapidly overcome the never ending "research speed bumps" have inevitably saved the research from drowning into termination. His humor always brought upon a refreshing outlook on engineering practice. Dr. Clothier has also been an exceptionally thorough and comprehensive mentor who has developed my attention to detail. His ability to organize, categorise, and structure any problem at hand for producing an optimal solution has been a fundamental part of the research. His critical eye has always saved the research from mishaps. The patience, motivation, and enthusiasm of this exceptional and extraordinary supervisory team is deeply appreciated. Their passed knowledge, experience and teachings have elevated me, and will always be remembered and applied throughout my career.

Further, thanks are extended to Dr. Kevin Massey who acted as the primary supervisor in the first stage of the research before leaving RMIT. His experience, knowledge, and patience have proven to be invaluable. Dr Massey has shown a unique ability to steer the research in the right direction with his fundamental questions. His guidance and perspective will never be forgotten.

The author also wishes to express his sincere appreciation to Dr. Mujahid Abdulrahim for his extensive support. He has heavily supported the research by sharing his technical knowledge and expertise. The author wishes to express his gratitude to Dr. Mujahid for having the patience to deal with the finite ignorance of the author.

The support provided by Mr. Phred Petersen for obtaining flow visualization images is greatly appreciated. The author is also indebted to RMIT technical staff, in particular Mr. Gil Atkins who has assisted with the manufacturing of the specialised experimental apparatus in addition to supporting the experimental setups.

Sincerest thanks are extended to colleagues and friends Dr. Alex Fisher, Dr. Matthew Marino and Mr. Mohamed Elbenhawi for their technical support and critical review of experimental results. Their enthusiasm, dedication, and encouragement will always be remembered and appreciated.

The author is also grateful for the funding provided by the Australian Government through the APA scholarship.

Last but not least, the author wishes to thank his parents for their extensive support and patience, without which this work could not have been completed.

Executive Summary

The scale of fixed-wing Micro Aerial Vehicles (MAVs) lend them to many unique applications. These applications often require low speed flights close to the ground, in the vicinity of large obstacles and in the wake of buildings. A particular challenge for MAVs is attitude control in the presence of high turbulence.

Such flights pose a challenging operational environment for MAVs, and in particular, ensuring sufficient attitude control in the presence of significant turbulence. Low-level flight in the atmospheric boundary layer without sufficient attitude control is hazardous, mainly due to the high levels of turbulence intensity close to the ground. MAV accidents have occurred due to the lack of a reliable attitude control system in turbulent conditions as reported in the literature (McCarley and Wickens, 2004; Williams and Harris, 2002).

Challenges associated with flight control of fixed-wing MAVs operating in complex environments are significantly different to any larger scale vehicle. The scale of MAVs makes them particularly sensitive to atmospheric disturbances thus limiting their operation. A review of the literature revealed that rolling inputs from turbulence were the most challenging whereby conventional inertial-based attitude control systems lack the responsiveness for roll control in high turbulence environments.

The solution might lie with flying animals, which have adapted to flight within turbulence. The literature survey identified bio-inspired phase-advanced sensors as a promising sensory solution for complementing current reactive attitude sensors. The development of a novel bio-inspired phase-advanced sensor and associated control system, which can sense the flow disturbances before an attitude perturbation, is the focus of this research.

The development of such a system required an in-depth understanding of the features of the disturbing phenomena; turbulence. Correlation studies were conducted between the oncoming turbulence and wing-surface pressure variations. It was found that the highest correlation exists between upstream flow pitch angle variation and the wing-surface pressure fluctuations. The leading edge of the wing was found to attain the highest correlation with relatively constant correlation in the span-wise direction. Then the correlation evident between the upstream flow pitch angle and the vehicle's roll perturbation was determined via the development of a specialised roll-axis rig. It was found that high correlation also exists in the vicinity of the leading edge. The correlation peaked in the region producing most of the lift along the span. However, due to the insufficient time-forward advantage, surface pressure sensing was not used for attitude control.

A second sensing approach was explored to cater for the control system's time-lags. Multi-hole pressure probes were embedded in the wings of the MAV to sense flow pitch angle and magnitude variation upstream of the wing. The sensors provide an estimate of the disturbing turbulence. The probes extend from the leading edge of the wings into the oncoming flow. This approach caters for the time-lags of the system providing sufficient time to counteract the gust before it results in an inertial response. Using the knowledge acquired from previous experiments, the probes were optimally placed along the wingspan. The measured signal was used as a dynamic control input for

perturbation mitigation. Statistical analysis was used to assess the disturbance rejection performance of the phase-advanced sensory system, which was benchmarked against a conventional inertial-based sensory system in a range of turbulence conditions. Unconstrained but controlled test flights were conducted inside the turbulence environment of two wind-tunnels, in addition to outdoor flight testing in the atmosphere. These three different turbulence conditions enabled testing of a wide range of turbulence spectra believed to be most detrimental to the MAV. A significant improvement in disturbance rejection performance was observed in relation to conventional inertial-based sensory systems. Secondary beneficial effects have been observed when using the phase-advanced sensory system such as reduced adverse yaw, drag, and the ability to estimate the turbulence to an acceptable degree of accuracy. It can be concluded that sensory systems providing time-forward estimates of turbulence can complement conventional inertial-based sensors to improve the attitude stability performance.

Contents

List of Figures

List of Tables

Nomenclature

a	Power law exponent
b	Wingspan (m)
c	Average chord length (m)
C	Magnitude squared coherence
C_p	Average pressure coefficient
$C_{p'}$	Instantaneous pressure coefficient
C_{lp}	Roll damping derivative in roll
G	*C*ross-spectral density
σ	Standard deviation
L	turbulence length scale (m)
L_{xx}	Longitudinal turbulence length scale (m)
L_p	Roll damping
P_∞	Free-stream static pressure (Pa)
ρ	Normalized cross-correlation
Re	Reynold's number
S	Wing area (m^2)
s	Semi-span (m)
Ti	Turbulence intensity (%)
t	Time (s)
t_p	Aerodynamic advection time-lag of the turbulent properties over the wing (s)
t_d	Time-lag associated with the detection of the disturbance (i.e. sensor time-lag) (s)
t_m	Time-lag associated with communication between the sensor and the controller(s)
t_c	Microcontroller's processing time-lag (s)
t_s	Servo/Actuator response time-lag (s)
t_a	Pressure distribution lag following deflection of an aerodynamic surface (s)
t_i	Inertial response time-lag following aerodynamic variation caused by actuation (s)

t_v	Displacement lag of the wing through a fluid, rather than a vacuum (s)
t_{CR}	Total time-lag associated with a controlled response (s)
τ	Time-lag (s)
U'	Fluctuating component of longitudinal velocity (m/s)
$\bar{U}$	Mean longitudinal velocity (m/s)
$\bar{u}_z$	wind speed at height z (m/s)
$\bar{u}_g$	wind speed at gradient height(m/s)
z_g	gradient height (depends upon terrain) (m)
N	Number of cycles travelled by carrier
ϕ	Phase angle (°)
λ	Wavelength (m)
ϑ	Inclination angle (°)
σ_r	Range error
σ_ϑ	Inclination angle error

Acronyms

ABL	Atmospheric Boundary Layer
AoA	Angle of Attack
DPMS	Digital Pressure Measurement System
DoF	Degrees of Freedom
GNSS	Global Navigation Satellite System
GAD	GNSS Attitude Determination
MAV	Micro Air Vehicle
NAV	Nano Air Vehicle
UAV	Unmanned Air Vehicle
CL1	Control Level 1
CL2	Control Level 2
CMD	Command
ISR	Intelligence Surveillance and Reconnaissance
PSD	Power Spectral Density
Tx	Transmitter
RF	Radio Frequency
RQ	Research Question
SWaP	Size Weight and Power
SPA	Sense Plan and Act

Chapter 1

The Attitude Control of MAVs in Challenging Levels of Turbulence

Summary

In this chapter, the attitude control problem of fixed-wing MAVs is outlined and relevant literature is reviewed and summarised. The chapter builds an understanding of the atmospheric conditions experienced by a MAV and how it adversely affects attitude stability. Other factors limiting the disturbance rejection performance of attitude control systems are explored. The sensing component of the attitude control system is identified as a major limiting factor. A review of conventional attitude sensors is conducted revealing various limitations degrading disturbance rejection performance. The need to investigate the use of sensors capable of sensing the turbulence before the MAV undergoes an inertial response to the turbulence is briefly discussed. Finally, the scope of the research is defined.

1.1 Introduction to MAVs

Micro Air Vehicles are small portable unmanned air vehicles typically used for close-range surveillance, detection, and communications missions. Other operational requirements are summarised in Figure 1. The original impetus of Micro Air Vehicles (MAVs) was the development of an aircraft that weighed less than 90g with maximum dimension of ~0.15m (Mueller, 2007). However due to various technological limitations, the size definition of MAVs became loose in today's definition of the vehicle. Although not all of the original requirements materialized yet and seemed optimistic for the 1990's, they are still pursued today.

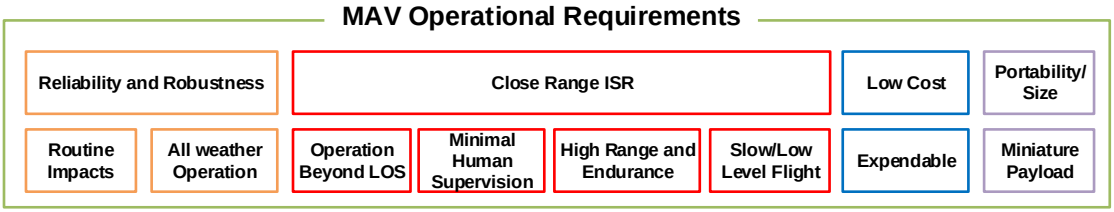

Figure 1: MAV Operational Requirements

The MAV's unique mission requirements (close-range ISR) which involves operation in cluttered environments (in some cases in close proximity to obstacles) imposes significant challenges in navigation and control (Galiński and Żbikowski, 2007; Langelaan and Roy, 2009). MAVs need agility to navigate around obstacles, and stability to counteract flow disturbances caused by the wake of obstacles (Cybyk et al., 2009; White et al., 2012). The MAV's relative size with respect to flow disturbances (i.e. turbulence), can have detrimental effects on its attitude stability (Watkins et al., 2006).

MAVs did benefit from the introduction of Micro-Electro-Mechanical Systems (MEMS) technology, which enabled miniaturization of its avionics, however MAVs require ever smaller and faster avionics with the lowest power consumption. The significantly limited payload capacity (Palmer, 2009) prevents the utility of complex avionics systems, due to the stringent Size Weight and Power (SWaP) constraints. MAV development has advanced ever since its proposal, by overcoming various difficulties in aerodynamics, avionics and communications. However, operation in turbulent cluttered environments has not been fully realized yet.

1.2 MAV Configurations

Operation in turbulent cluttered environments imposes various requirements on MAVs, leading to the design of different configurations which exhibit different characteristics (Galiński and Żbikowski, 2007). MAV configurations can be broadly grouped into three possible types; conventional fixed wing with rotating propeller(s), rotary wing (either single or multiple rotor) and flapping. Each have their own merits in terms of endurance, propulsion, and controllability. In nature flapping flight is the norm since true rotation only exists at bacterial scale and the discovery of the wheel by any other species than man is

considered to be unattainable (Anon, 1946). Man's early attempts at heavier-than-air aviation resulted from adopting ideas from the natural flying world. This often involved flapping bird-like wings and jumping from an elevated platform. The earliest documented attempt appears to be in 875 AD (White, 1961). Flapping wings have once again become a focal research topic but this time for the recently introduced MAVs (De Wagter et al., 2013; Fisher, 2013; Ratti and Vachtsevanos, 2012; Nakata et al., 2011; Ratti and Vachtsevanos, 2010; Shyy et al., 2010; Abate et al., 2008). Flying animals' unique ability to effortlessly and gracefully navigate through atmospheric turbulence, have inspired flapping wing MAVs. Many designs and prototypes have been built, some with novel design features inspired from birds and insects (Wootton, 2000) such as the DelFly (Croon et al., 2012) and SmartBird (Mackenzie, 2012). However, progress in flapping wing MAVs has been less than expected, since little to no commercial flapping MAV products exist. Current technology limits replication of flapping wing flight and constrains this configuration to laboratory environments.

Rotary wing designs are extensively used for civil and military applications as evident by the large number of small single and multi-rotor craft (Murphy et al., 2008; Young et al., 2002; Chopra, 2007). There appears to be little scientific evaluation of their stability in turbulence given that the majority of the relevant research studies are performed in smooth flow conditions as explained by Marino (2013). The most relevant research to date was conducted by Watkins et al. (2010b) which compared the stability performance of rotary and fixed wing MAVs in turbulence. Rotary-wings were demonstrated to have shown promise for a more stable configuration in turbulence in contrast to fixed-wing MAVs. However, the range and endurance of such platforms can limit their use for applications requiring operation beyond Line-Of-Sight (LOS). Currently, conventional fixed-wing MAVs have superior efficiency, endurance and range compared to rotary and flapping wing designs (Galiński and Żbikowski, 2007; Hall, 1998; Hall and Hall, 2001). If MAVs can attain sufficient stability in the presence of flow disturbances, fixed-wing MAVs may be the preferred configuration for a wide range of applications where endurance is important (Galiński and Żbikowski, 2007).

The scale of fixed-wing MAVs lend them to many unique applications. Many existing and potential applications require flights close to the ground, near large obstacles and in the wake of buildings (see Figure 2). Such flights pose a challenging operational environment for MAVs (Watkins et al., 2006). One particular challenge is ensuring sufficient attitude control in the presence of significant turbulence (i.e. series of gusts) (Abdulrahim et al., 2010). Attitude perturbations induced by turbulence are detrimental to a MAV's stability (Galinski, 2006; Galiński and Żbikowski, 2007; Lissaman, 2009; Shyy et al., 2010; Ol et al., 2008). Hence, on-board automatic attitude control systems are required to ensure the safe and controlled operation of MAVs in very turbulent environments.

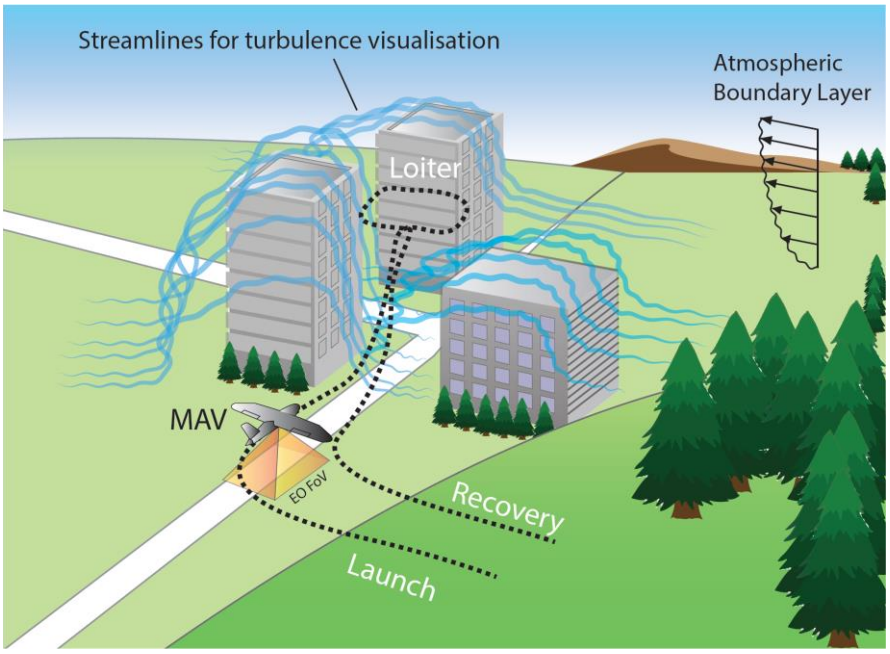

Figure 2: MAV operation in turbulent environments.

1.3 Turbulence and its impact on MAV Attitude Control

Deviation from a set flight trajectory can easily occur as a consequence of turbulence induced attitude perturbations. Severe turbulence is evident in built up areas where fixed-wing MAVs are most likely to conduct Intelligence Surveillance and Reconnaissance (ISR) missions (Watkins et al., 2010a). The operation of optical payload sensors also requires a high degree of stability for focusing on ground targets, where aircraft motion due to turbulence can blur a video stream, or even move targets outside the camera's field of view. Attitude control is thus important and needs to be considered for flights in the turbulent atmospheric boundary layer. Human pilots can find difficulty in stabilizing MAVs on a windy day. Jenkins et al. (2001) found that a human's control input flying an MAV, ranges from 1-10Hz, whereby the control input rate was found to be proportional to the rapid correction control movements required to maintain stability. A lower human control input (0-2Hz) was found by Chen et al. (2014) whereby the workload of 38 volunteers to control a MAV in turbulence was studied. Wang et al. (2011) asserted that the attitude data update rate of a MAV needs to be greater than 25Hz. Such rates are not achievable by humans thus implying the need for an automatic attitude control system when flying in severe turbulence.

A range of methods have been developed to mitigate the disrupting effects of turbulence on aircraft stability. These methods can be classified as being active or passive. Passive methods involve design considerations that ensure the aircraft has an inherent resilience to perturbations. Examples include; adding wing dihedral for lateral stability, or the use of flexible membrane wings that can alleviate the wing loads and minimise transfer of perturbations to the MAV's Centre of Gravity (CG) (Lucas et al., 2009; Baldelli et al., 1993; Fujii et al., 1990; Heimbaugh, 1987).

Active approaches involve a system that can sense and compensate for the attitude perturbations or their secondary effects on the MAV. Active approaches can be designed to either warn the operator or actively suppress the induced motion. Turbulence warning systems are suited for human-in-the-loop operations (for example, windshear warning systems used in large passenger aircraft). Systems that actively attempt to counter perturbations caused by turbulence use automatic feedback control to mitigate perturbations. This can be as simple as deflecting an aerodynamic surface(s) to counteract the response (Roman et al., 2006). More complex approaches utilise aeroelasticity for turbulence mitigation (Joseba et al., 2012)

1.3.1 Passive Turbulence Mitigation Techniques

Vulnerability to turbulence-induced perturbations varies with the physical design and scale of the aircraft. There are a number of sizing considerations and design features, which can enhance the stability of MAVs in the presence of disturbances. Abdulrahim et al. (2010) conducted experiments exploring the dynamic sensitivity of a model aircraft to atmospheric turbulence by varying a range of parametric factors. The factors included: mass, Centre of Gravity (CG), moment of inertia, wing-loading, and wing-span. It was generally deduced that turbulence-induced perturbations are attenuated with increasing aircraft mass, inertia, and wingspan. However, increasing the vehicle's inertia reduces the control input response. Increasing wingspan reduces the yaw stability influence of the wing, in addition to reduced pitch and roll damping authority (Abdulrahim et al., 2010).

The effectiveness of passive stabilisation reduces as the weight and scale of an aircraft reduces (McMichael and Francis, 1997). Thus, alternate passive stabilization techniques, such as the concept of gust resistant wings and segmented trailing edges have been explored (Singh et al., 2006). Researchers have also investigated the use of flexible and morphing wing mechanics as passive techniques to dampen the perturbations (Abdulrahim et al., 2005; Abdulrahim, 2004; Abdulrahim et al., 2003; Garcia et al., 2003; Abate et al., 2008; Ol et al., 2008). A highly stable vehicle can be achieved using these passive techniques. However, stability is inversely proportional to control authority. Subsequently an excessively stable MAV is not agile and will lack the manoeuvrability required for navigation. Passive attitude control is permanent whereby it cannot be disabled to enable agile manoeuvres when required.

1.3.2 Active Attitude Control

Abdulrahim et al. (2010) found that passive techniques can only attenuate limited frequencies of perturbations in addition to reducing the MAV's manoeuvrability and directional control. Active attitude control can offer the stability and controllability required to operate in turbulent and complex environments. MAVs require control input rates higher than 25Hz (Wang et al., 2011), which is beyond the bandwidth of human operators. Employment of an active attitude control system is therefore vital. A micro-controller employed by the attitude control system can provide higher input rates to match the

MAV's attitude perturbations. The high input rates imply the need for an attitude sensor, of sufficient bandwidth, to detect the high perturbation rates.

An active control system goes through a Sense, Plan, and Act (SPA) cycle (Murphy, 2000), see Figure 3. An attitude sensor detects attitude perturbations and sends its output for processing by a micro-controller, which then computes the required deflection of the aerodynamic control surfaces. Effective attitude control requires the SPA cycle to loop at fast rates equivalent to the perturbation rates. Ensuring minimal time-lag from the instance a perturbation occurs until a counteracting aerodynamic response is completed is therefore critical. Computing technology has matured and the time-lag associated with computational processing (i.e. planning stage of the SPA cycle) is insignificantly small relative to other components of the SPA cycle (Kuroda et al., 1998; Intel, 2014). The sense and act components of the cycle will contribute most to the attitude control system's time-lag, thus limiting a fast control response.

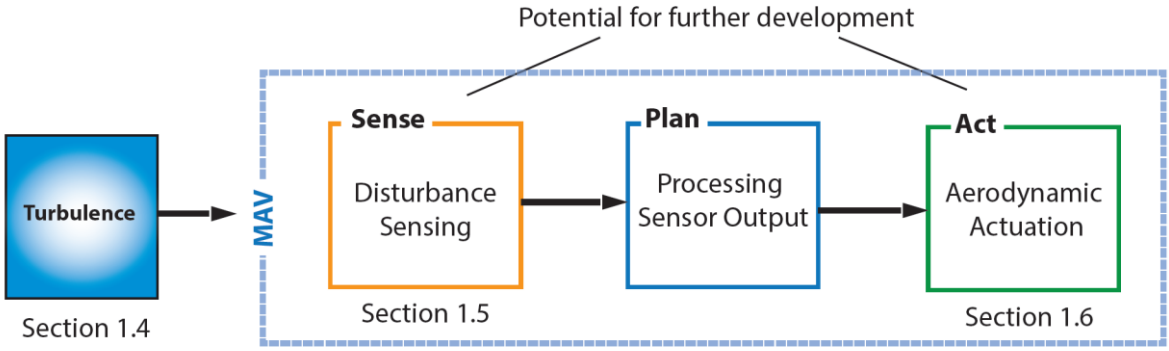

Figure 3: Control system's process for controlling attitude.

Based on Figure 3, the remainder of this chapter will explore the areas outlined below.

1. **Turbulence:** Section 1.4 explores the disturbing phenomena in more detail.
2. **Sensors:** Section 1.5 reviews state of the art attitude sensors.
3. **Actuation:** Section 1.6 reviews state of the art MAV actuators.

1.4 The Challenging Environment of MAVs

Large passenger aircraft are designed to operate in relatively smooth flow at higher Reynold's numbers. Their large mass and inertia attenuates the effects of the higher turbulence frequencies, thus reducing the control bandwidth. The physical design and operational requirements of MAVs significantly vary from larger aircraft. MAVs require unique agility/manoeuvrability to operate at low altitudes in complex terrain. This can be challenging, whereby high levels of turbulence are abundant in at low altitudes in obstacle rich environments. The MAV's miniature size relative to turbulence also brings greater control challenges compared to larger aircraft.

1.4.1 The Turbulent Atmospheric Boundary Layer

MAVs operate exclusively within the lower domain of the Atmospheric Boundary Layer (ABL). The height of the ABL varies, but generally extends up to 5 km from ground level depending on surface heating, climatic conditions, and terrain (Garratt, 1994). MAVs need to operate within that altitude range, which is significantly lower than the conventional flight altitudes of larger counterparts, see Figure 4. There is a significant flight challenge posed by the ABL where the turbulence intensity (Ti) increases rapidly at lower altitudes due to the mechanical mixing induced by ground roughness (Davenport, 1961).

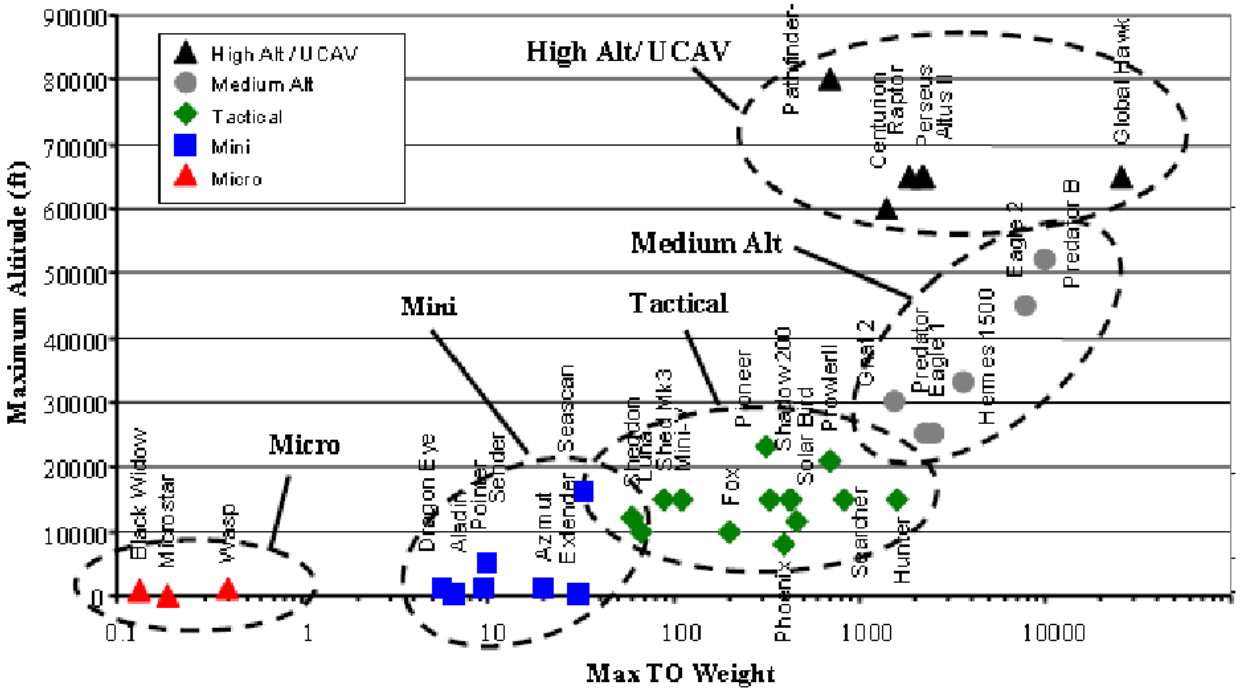

Figure 4: Altitude to maximum take-off weight distribution of various UAV categories (Weibel, 2005).

The atmospheric boundary layer has been documented by a number of researchers and meteorological agencies, which have compilations of mean wind speeds throughout the year (Watkins et al., 2010a). Walshe (1972) has categorised the variation of velocity profiles over different types of terrain as shown in Figure 5. These profiles follow the power law given in Equation 1 (Davenport, 1961).

$$\bar{u}_z = \bar{u}_g \left[\frac{z}{z_g}\right]^a \quad (1)$$

Where,

$\bar{u}_z$ is the speed at height z

$\bar{u}_g$ is the speed at gradient height (wind is no longer affected by frictional forces)

z_g is the gradient height (depends upon terrain)

a is the power law exponent (depends upon terrain)

The intensity of turbulence (Ti) is defined in Equation 2. Walshe (1972) categorised the variation of Ti with height and terrain as depicted in Figure 5. From Figure 5 it is evident that city environments have the highest intensities of up to 50%. Figure 6, shows a 32 meter, world-record bubble, which provides a visual illustration of the turbulent flow structure and the associated length scales (L) present at low altitudes. The turbulence length scale in the longitudinal direction (L_{xx}) is characterised by average dimensions of the eddies or gusts within the flow. The soap film's surface tension will smear the small flow structures (i.e. smaller L), but medium to large scale structures are still visible. MAVs are expected to fly through such structures while attaining sufficient attitude stability.

$$Ti = \frac{(\sigma_U)_z}{\bar{U}_z} \quad (2)$$

Where,

z is the height

z_{10} is the standard reference height (10meters) at which wind is measured.

σ is the standard deviation

U is the fluctuating component of velocity

$\bar{U}$ is the mean velocity component

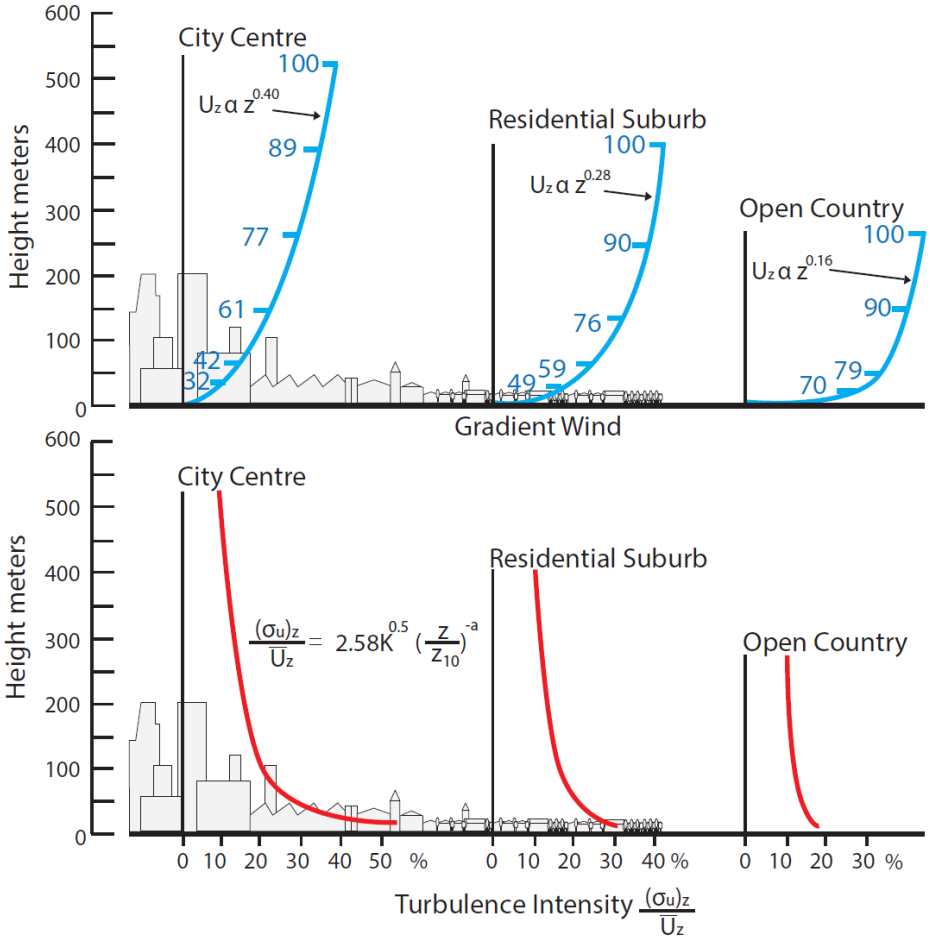

Figure 5: Mean wind and Ti profiles for different terrain. Adapted from (Walshe, 1972).

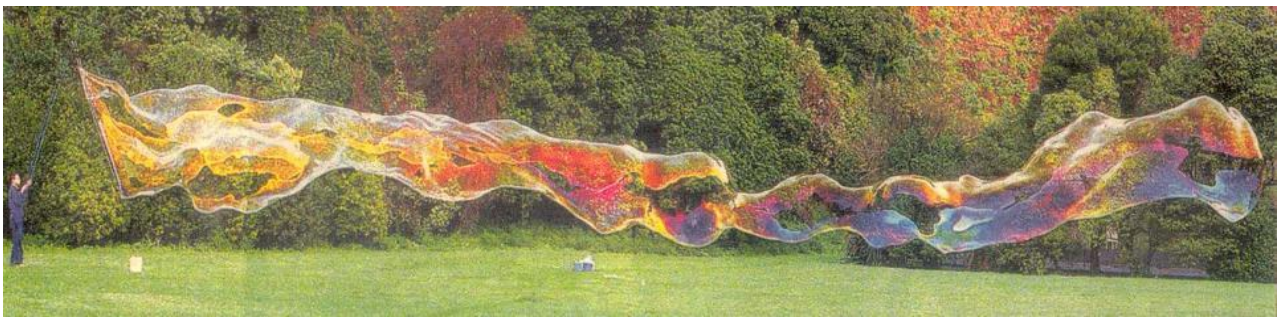

Figure 6: The longest bubble in the worlds (courtesy Alan McKay, copyright Garry Norman)

1.4.2 Flying through Turbulence

The ABL is well documented and properly understood through stationary measurements for various purposes, such as buildings and wind engineering studies (Baklanov et al., 2011; Garratt, 1994; Vermeir et al., 2012; Thompson, 2013). Flying through the turbulence changes the relative Ti levels. The denominator in Equation 2 therefore becomes the aircraft flight speed relative to the air (i.e. airspeed). The combination of miniature size, low flight altitude, and relatively high turbulent winds (relative to the MAV flight speeds) represents a unique and challenging environment. Watkins et al. (2006) made one of the first attempts in statistically recording some of the flows, which can be experienced by MAVs. This study illustrated data relating turbulence with relative vehicle speed (represented as Indicated Airspeed (IAS)). The data were

generated using four multi-hole pressure probes laterally separated on a mast above a moving vehicle. The data collected by Watkins et al. (2006) provide an understanding of the flow characteristics potentially experienced or encountered by a MAV. The results are shown in Figure 7 to Figure 9. Figure 7 shows the relative Ti, and how it reduces with increasing flight speeds. Figure 8 illustrate pitch variation and fluctuations; Figure 8a shows the pitch angle recorded by the four probes during a two second sampling time showing large fluctuations in the order of ±10^o. At first, it might seem that there is correlation between the four probes, however closer examination (Figure 8b) reveals that there are differences, where at some instances the variation is ~15^o. Figure 9a shows the pitch angle standard deviation at various lateral spacings. Figure 9b shows the pitch angle coherence at various L for different lateral spacings. The displayed results show that pitch angle coherence reduces with reducing turbulence scale. The increase of lateral spacing also results in reduced coherence.

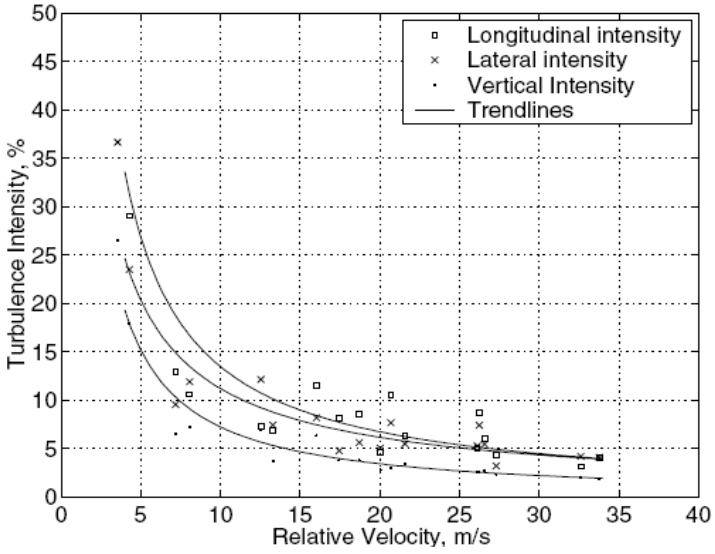

Figure 7: The relationship between turbulence and velocity (Watkins et al., 2006)

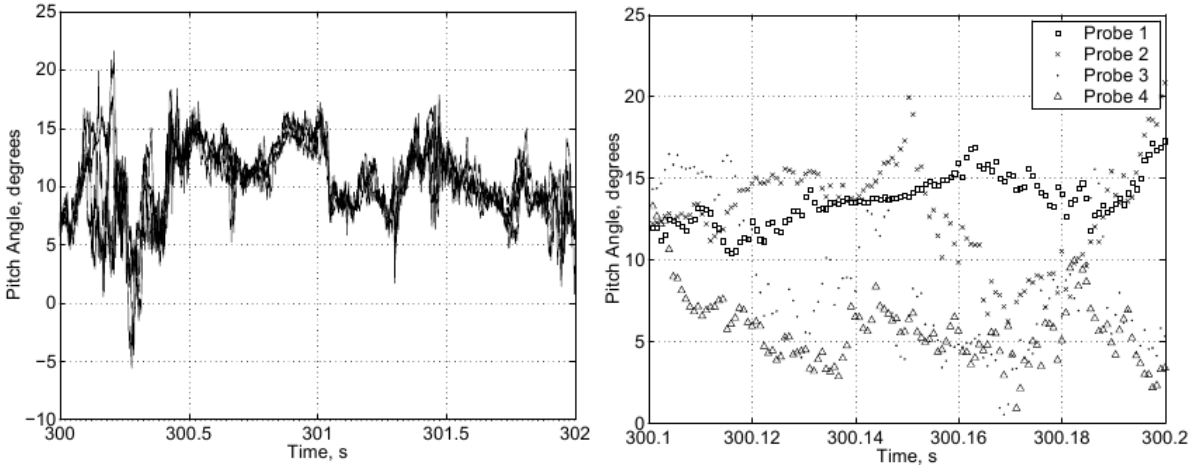

(a) (b)

Figure 8: Pitch angle variation: (a) 2 second sample (b) 0.2 second sample (Watkins et al., 2006)

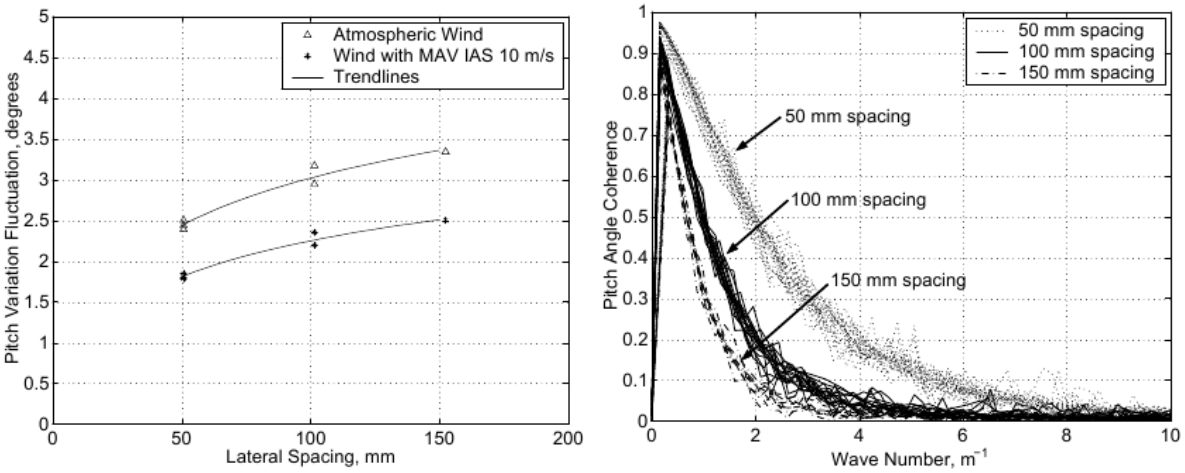

(a) (b)

Figure 9: (a) Pitch variation fluctuation versus measurement spacing (b) Pitch angle coherence (Watkins et al., 2006).

1.4.3 MAV Gust Response

A gust disturbance can be described as a series of varying velocity vectors consisting of direction and magnitude changes. Turbulence therefore consists of a series of gusts (see Figure 10). The Ti is illustrated in Figure 11 by the fluctuating component of the velocity vectors. The disturbance can perturb any of the six Degrees of Freedom (DoF) of the aircraft. The work by Thompson et al. (2011b), has revealed that the roll axis is the most sensitive axis to turbulence. The local variation in flow pitch angle along a section of the MAV's wingspan will lead to a change in sectional lift. This induces an uneven lift distribution relative to the MAVs wingspan, thus in turn causes a rolling motion. For atmospheric turbulence it has been shown that variations in pitch angle are more significant than velocity magnitude variation which occupy a lesser role in inducing rolling perturbations (Thompson et al., 2011b).

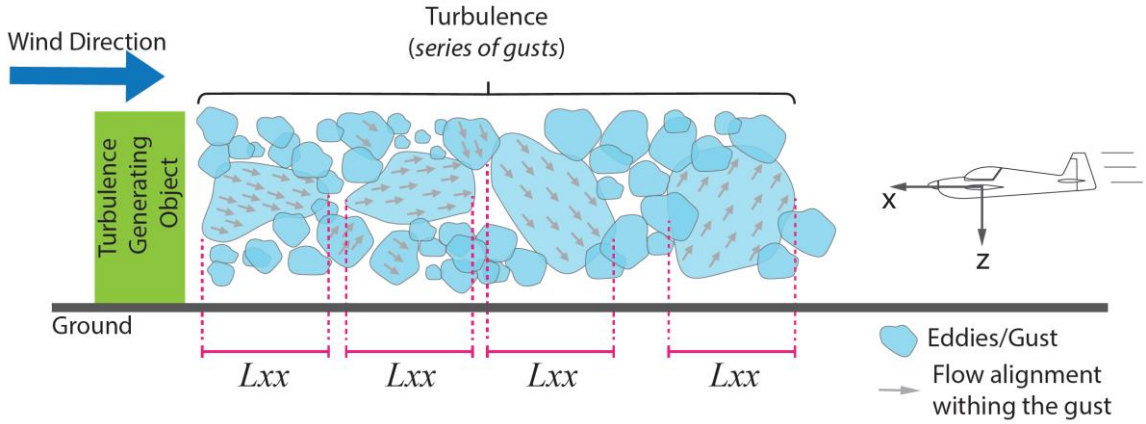

Figure 10: Turbulence consisting of a series of gusts.

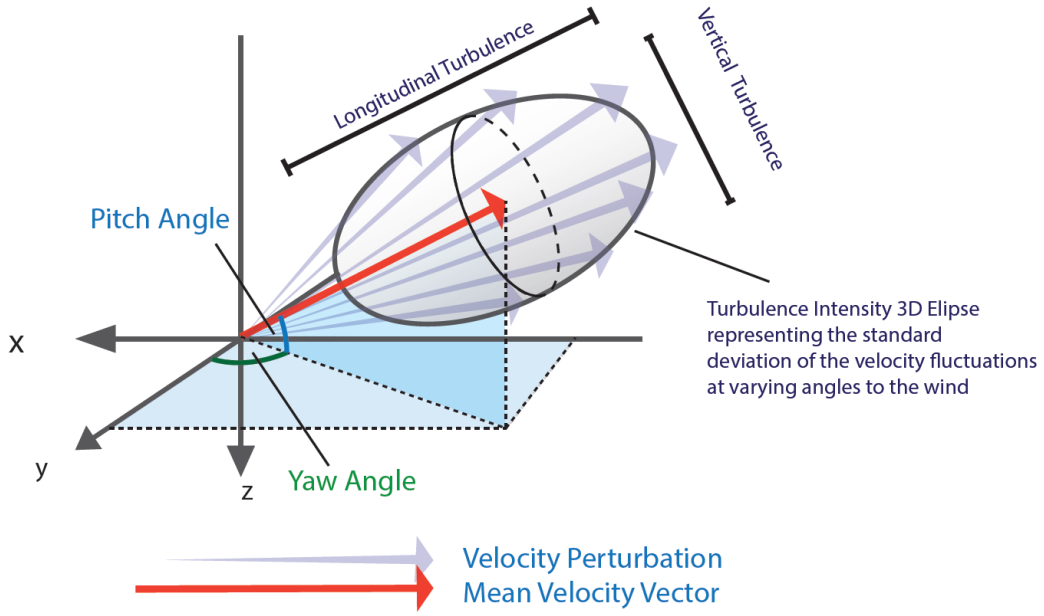

Figure 11: The fluctuating velocity vectors within a gust.

An aircraft's response to gust inputs also depends on its stability in a particular axis. MAVs tend to attain higher sensitivity to gust inputs in the rolling and pitching axes in contrast to the yawing axis (see Figure 12 for axes convention). This is traced back to the physical design of the vehicle, where it is directionally stable in the presence of a larger moment arm between an aerodynamic surface, associated with controlling a particular axis, and the CG (Watkins et al., 2006). As a gust imparts on the leading edge of a wing, the flow angle and velocity is altered inducing variations in the wing load distribution, see Figure 13a. If the gust length were larger than the wingspan (i.e. both wings travel through the same gust), then this would result in a pitching motion. Gusts smaller than the wingspan will lead to uneven lift distribution over the wings, inducing a rolling motion (Figure 13a). However, since turbulence structures are highly three dimensional in nature instability to rolling motion forms the most significant disturbing factor for MAVs (Watkins et al., 2006).

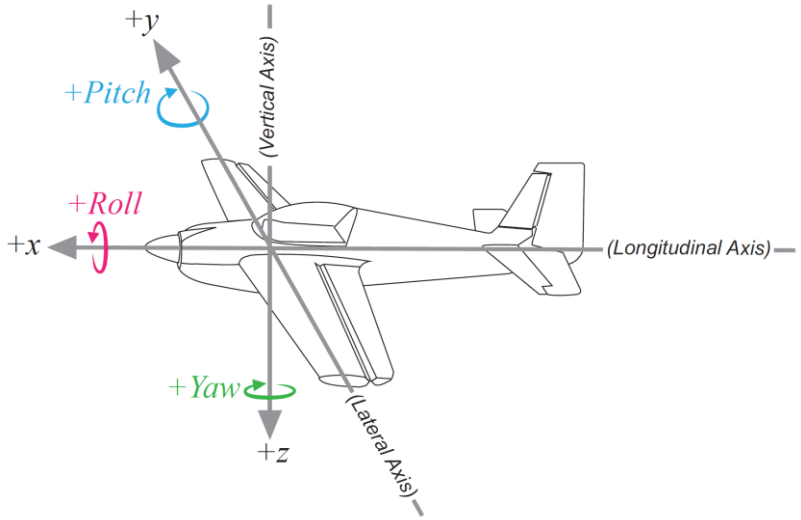

Figure 12: Axes convention.

Large turbulence structures (significantly larger than MAVs) can be considered quasi-static, and relatively easily compensated for, when compared with eddy structures of similar size to the MAV (Watkins et al., 2006). Thompson and Watkins (2010) confirm that instability to rolling motion forms the most significant disturbing factor for fixed-wing MAVs flying outdoors. Lissaman (2009) demonstrated that a sinusoidal load distribution with a period slightly larger than the span of the aircraft will result in the maximum roll moment, see Figure 13b. Based on the latter it can be argued that L equivalent to or smaller than the MAV wingspan are the most destructive. Van der Hoven (1957) presented the Power Spectral Density (PSD) plot of the wind velocity fluctuations evident within the ABL (Figure 14). In this plot, MAV destabilizing gusts, correspond to lower frequency energy gusts (micro-meteorological range), while higher frequency flows are considered quasi-static.

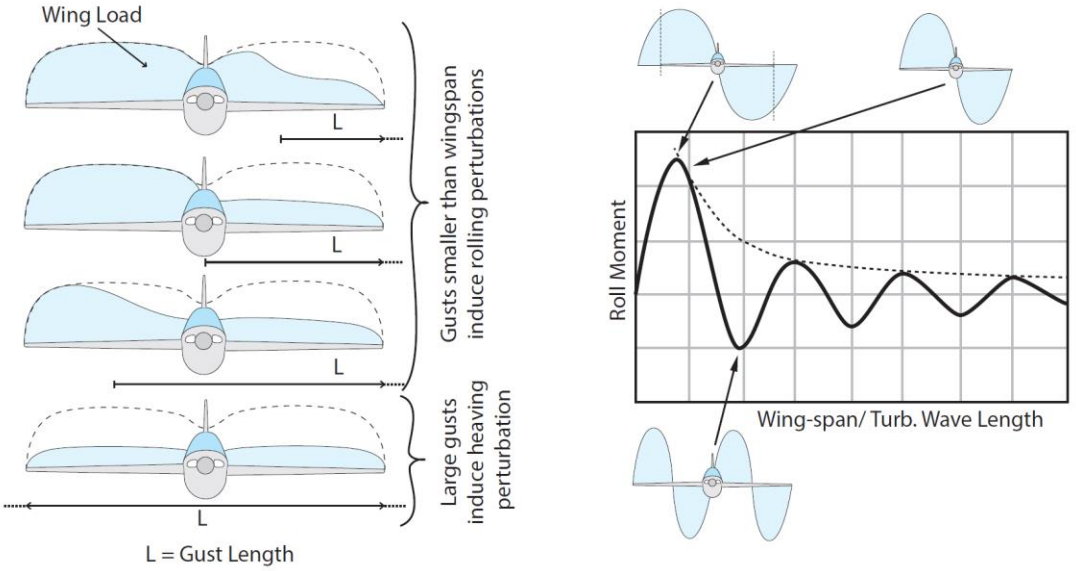

Figure 13: (a) Effect of length scale on wing loading. (b) Maximum roll moment possible from sinusoidal span-wise velocity distributions. Adapted from Lissaman (2009).

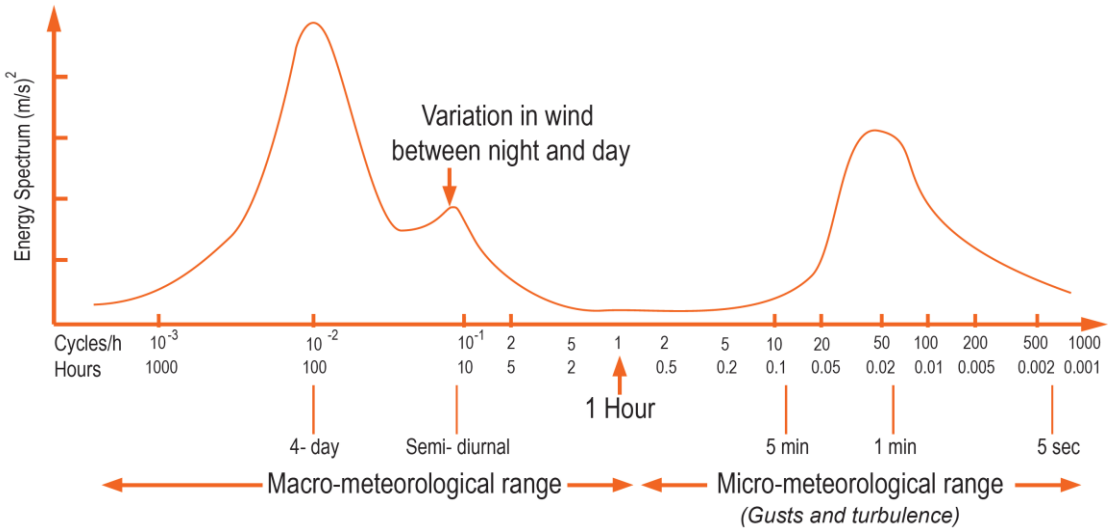

Figure 14: Power spectral density plot of velocity fluctuations within the atmosphere. Adapted from Van der Hoven (1957).

1.4.4 Effect of MAV Size on Stability

The reduced wingspan of MAVs and low inertia of the vehicle has many operational benefits, however as discussed in the previous section, these properties also contribute to degrading the attitude control performance compared to larger aircraft. An illustrative example is that provided by Bogos and Stroe (2012). The study explored the handling characteristics of a 2m wingspan model, which was a 1/10 scale model of an actual aircraft. As shown in Figure 15 the time to half a roll perturbation is reduced from the full-scale value of 0.22s to 0.07s for the 1/10 scale aircraft. What is even more important to consider is the roll response to a single gust disturbance as shown in Figure 16. It is seen that the amplitude of the scale model's roll rate (Ps) is increased by about three times compared to the full aircraft's roll rate (PF). The frequency of the response for the scale model is also increased by about three times. The study by Bogos and Stroe (2012) clearly illustrates the challenges associated with MAVs with respect to roll response.

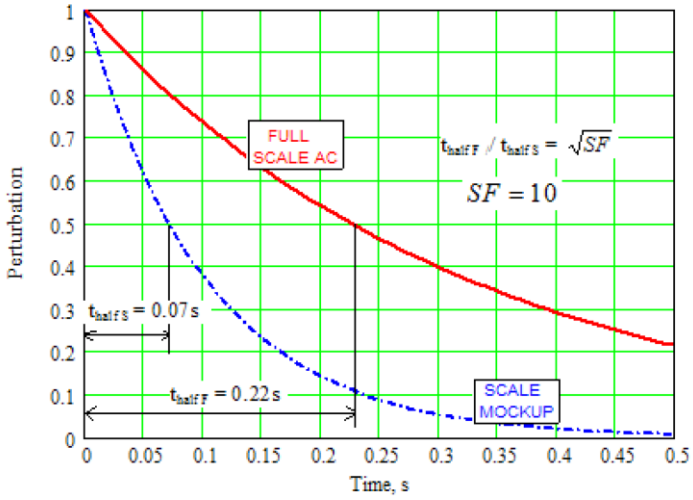

Figure 15: Characteristic transient roll mode Bogos and Stroe (2012).

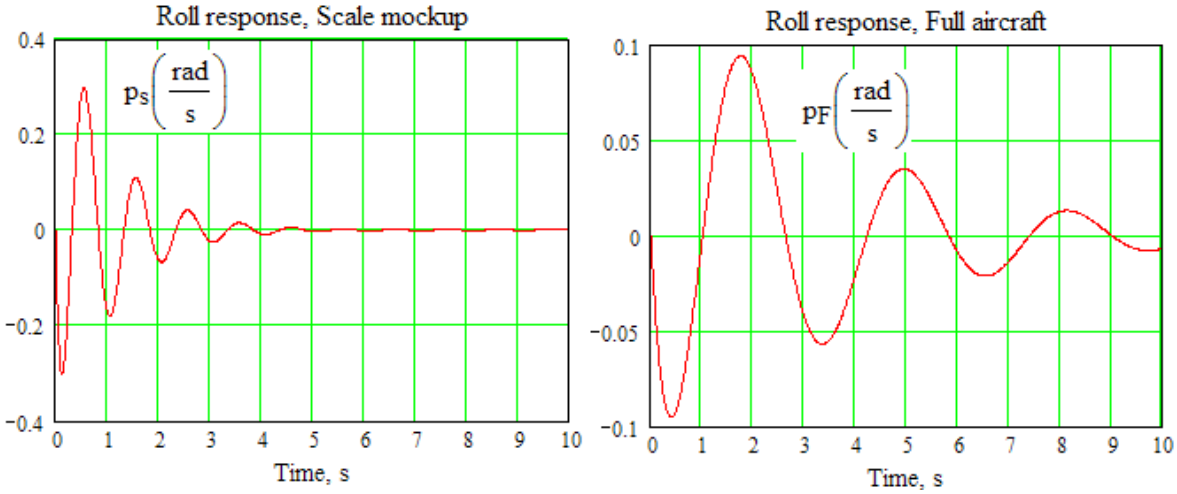

Figure 16: Roll response at a lateral gust for: (left) Scale mockup (right) Full aircraft (Bogos and Stroe, 2012)

1.5 Conventional Attitude Sensors

As identified in Section 1.3.2, the sense component of the SPA cycle contributes to the time-lags of the MAV's attitude control system. Therefore, in this section conventional attitude sensors are reviewed with respect to their utility for MAVs operating in turbulence. Conventional sensors which measure the attitude perturbations on the MAV consist of: accelerometers, gyroscopes, Global Navigation Satellite systems (GNSS), and electro-optical sensors. Combinations of these sensors which have been utilised are also explored.

1.5.1 MEMS Accelerometers

Accelerometers can be used to estimate an MAV's attitude with reference to the local gravity vector by measuring accelerations in multiple axes. A Micro-Electro-Mechanical Systems (MEMS) accelerometer is a suspension system employing a proof mass (McNamara and Gianchandani, 2011). Accelerations are detected by measuring the displacement or oscillations of the proof mass. The smaller the size of the proof mass, the greater the acceleration-induced noise. However, there are methods to increase the size of the proof mass such as exploitation of the entire substrate (Yazdi et al., 1998). The use of closed-loop accelerometers can considerably improve performance (Liu et al., 2013). A closed-loop accelerometer uses a feedback loop to regulate the motion of the proof mass. Acceleration is derived from the feedback forces applied. The performance is mostly determined by electrostatic force generated by high stability voltage (Dong et al., 2011). Since the proof mass is nearly stationary, sensitivity and bias to manufacturing tolerances can be considerably reduced, in addition to an improved dynamic range and linearity (Kulah et al., 2006).

There are various physical mechanisms, which can be used to measure acceleration, including capacitive, piezoresistive, optical, and tunnelling-current. The most common types of MEMS accelerometers are capacitive, piezoresistive or tunnelling-current (see Figure 17 and Figure 18) (McNamara and Gianchandani, 2011). Piezoresistive accelerometers indirectly measure the strain of the spring holding the proof mass (Roylance and Angell, 1979; Suminto, 1991). Piezoelectric accelerometers inherently possess a low output signal and high output impedance requiring the use of built-in electronics to amplify the output signal. Capacitive accelerometers detect the capacitance between the inertial mass and the substrate to measure displacement (Chae et al., 2005; Xiao et al., 2008). Closed-loop capacitive sensors counterbalance the proof mass by inducing an electrostatic force controlled by a force-feedback system. Capacitive sensing interfaces are suitable for closed-loop operation allowing high output signal, improved linearity, and low thermal sensitivity (Lewis et al., 1996; Ji and Wang, 2005). MEMS capacitive closed loop accelerometers are currently attracting more research interest due to their superior performance (Liu et al., 2013). It is predicted that this accelerometer type will dominate over other types with respect to performance over the next decade (Perlmutter and Robin, 2012). Tunnelling-current accelerometers exhibit the highest

sensitivity of the MEMS-based devices (Dong et al., 2005; Hartwell et al., 1998; Liu et al., 1998a; Liu and Kenny, 2001; Miao et al., 2007; Yazdi et al., 1998). Tunnelling current accelerometers use a conductive tip, referred to as a "tunnelling tip", to bring two conductors within close proximity of one another with an applied bias. The amount of electrons crossing the gap between the tip and the surrounding conductor is proportional to the size of the gap, which is proportional to the applied acceleration. The tunnelling tip improves measurement sensitivity and resolution. Fabrication imperfections can lead to large-gap designs (i.e. the distance between the two conductors) degrading performance (McNamara and Gianchandani, 2011). There are significant drift, repeatability, reliability robustness and noise problems compared with the piezoresistive and capacitive accelerometer types (McNamara and Gianchandani, 2011). Tunnelling-current accelerometers cost more to fabricate and require more sophisticated control circuitry.

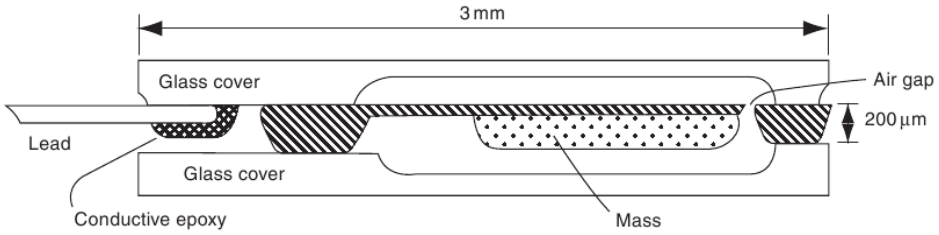

Figure 17: Piezoresistive accelerometer's main three components: Substrate (Cover), inertial mass, and restoring spring (McNamara and Gianchandani, 2011).

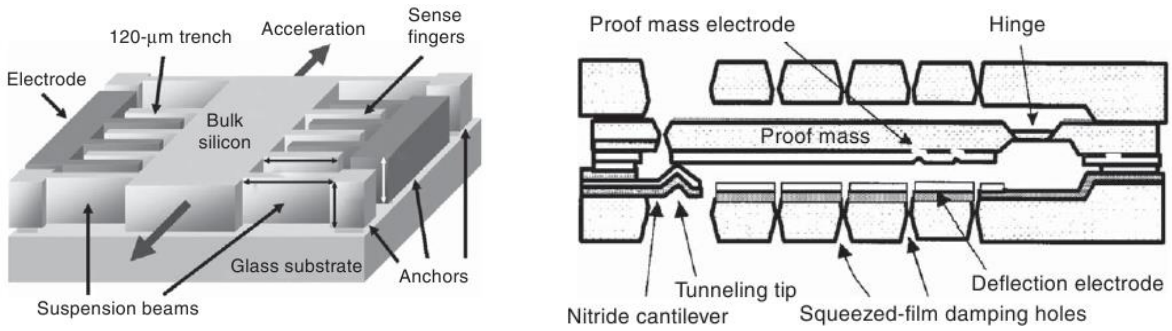

Figure 18: (a) Capacitive accelerometer schematic (b) Tunnel-current accelerometer anatomy (McNamara and Gianchandani, 2011).

1.5.1.1 Deficiencies of MEMS Accelerometers

Accelerometers can be classified based on their performance as Rate grade, Tactical grade, and Inertial (or navigation) grade. Rate grade accelerometers have the lowest performance, while Navigation grade attains the highest performance. The limitations unique to MAVs limit the choice of accelerometers to MEMS type, which struggled to reach Tactical grade (Dong et al., 2011) and more recently Navigation grade (Keller, 2013). MEMS accelerometer's vulnerability to vibration and temperature variation has led to lower performance and reliability issues (Li et al., 2005; Sarihan et al., 2008). Packaging stresses due to temperature variation, humidity, and vibration can affect performance and increase the potential for sensor failures (Jian et al., 2011). Failures can be caused by fatigue, fracture, interfacial delamination or stiction (i.e. sticking of the sensing elements) (Spengen et al., 2003). Consequently, performance

degradation from the harsh operating conditions of MAVs can be significant. Accelerometers are unable to differentiate between the different components of acceleration (specifically gravity and platform motion). In this case, the sensor measures all forces acting on the MAV, which can lead to significant noise at higher frequencies, with a stable output signal at lower frequencies. However, it is the higher frequencies, which are relevant for attitude control of MAVs and are critical in the presence of atmospheric turbulence. As a consequence of miniaturisation, MEMS accelerometers have linearity issues in addition to limited dynamic range, cross-axis sensitivity and are more vulnerable to signal noise (McNamara and Gianchandani, 2011).

1.5.2 MEMS Gyroscopes

Gyroscopes measure the angular rate (i.e. speed of rotation). MEMS type gyroscopes are small and light compared to other types (McNamara and Gianchandani, 2011) thus are most suited for MAV utility. Vibratory gyroscopes were inspired from an insect's halters, which serve a similar purpose in insect flight stability (Anon, 1946). Vibratory gyroscopes take advantage of the Coriolis Effect to determine motion perturbations. The sensor converts the momentum of a vibrating mass into a force proportionate to the angular rate in the plane of vibration (Madni et al., 2003). Conventional implementations utilise single DOF drive-and-sense-modes (Weinberg and Kourepenis, 2006; Yazdi et al., 1998).

There are several design variations of MEMS vibrating gyroscopes. The most widely used are tuning fork gyroscopes and ring gyroscopes (McNamara and Gianchandani, 2011), see Figure 19 . Tuning fork gyroscopes use a pair of masses, which oscillate in opposite directions but at the same amplitude. When the masses undergo rotation, a force perpendicular to the plane of rotation is created by the Coriolis force, which is sensed during rotation. Ring gyroscopes employ a highly symmetrical structure, which is excited by electrostatic forces. Ring gyroscopes benefit from reduced cross-axis interference. One design difficulty of vibratory gyroscopes is the requirement of the sensing element to move and to be controlled in two DOF. One DOF is for the driven mode while the other is for the sense mode. The drive direction represents the resonator while the sense direction represents an accelerometer. It is desirable to maximise the frequency and amplitude of the drive mode, but it is also necessary to keep both constant since minute variations can affect the Coriolis acceleration (Kraft, 2000). An auto gain control loop and phased locked loop is used for amplitude and frequency control, respectively.

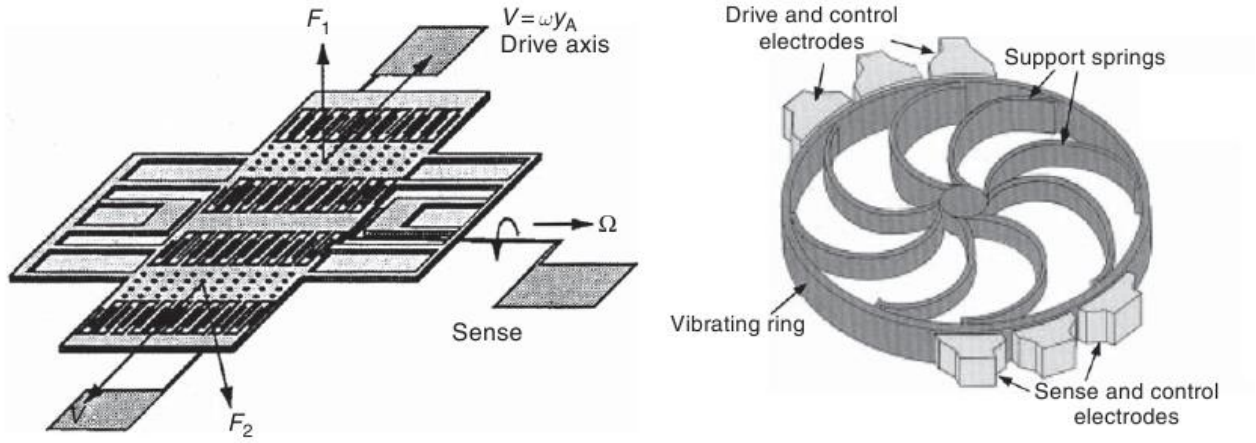

(a) (b)

Figure 19: (a) Tuning fork gyroscope. (b) A ring gyroscope (McNamara and Gianchandani, 2011).

1.5.2.1 Deficiencies of MEMS Gyroscopes

Gyroscopes can be classified based on their performance in a similar manner to accelerometers. Perlmutter and Robin (2012) predict that MEMS Gyroscopes will dominate the tactical grade performance range (100 – 0.1 °/h). However, the miniaturisation of MEMS gyroscopes comes at the price of resolution, bandwidth, and gain, where the magnetic actuation and detection can be problematic at smaller scales (Kraft, 2000; Trusov et al., 2009). There is also an additional trade-off between the sensitivity and bandwidth of the sensor. Performance is highly sensitive to manufacturing tolerances (Trusov et al., 2009), in addition to packaging stresses (Joo and Choa, 2007; Rogers et al., 2005). The stresses are influenced by variations in the temperature, leading to significant drift in the sensor output, changes to the sensitivity, and potentially failures. Drift can be reduced by adjusting the resonant frequencies electrostatically, where an electronic circuit can be devised to continually perform electrostatic tuning. However, this comes at the penalty of additional weight and computation (McNamara and Gianchandani, 2011). There are numerous gyroscopes that utilise a closed-loop feedback controller to match the resonant frequencies and account for temperature variations (Gallacher et al., 2006; Oboe et al., 2005; Park and Horowitz, 2003; Saukoski et al., 2007; Sung et al., 2008; Sung et al., 2007). Quadrature error, which occurs from the misalignment of the drive mode from its optimum direction, can be problematic (Kraft, 2000). This error introduces a signal in the sense mode that needs to be filtered by additional computation.

Drift is a major concern for attitude control of MAVs, which will result in significant accumulated error over time (McNamara and Gianchandani, 2011). The output signal is stable in the short term (i.e. higher frequencies perturbations) however is unstable in the long term (i.e. lower frequencies perturbations). The stability in the higher frequencies is beneficial for highly turbulent conditions, subsequently gyroscopes are usually combined with accelerometers to provide a more stable signal (see section 1.5.5.3). However, in their current form MEMS gyroscopes cannot operate individually for attitude estimation of MAVs.

1.5.3 Electro Optical Sensors

An alternative and well-established attitude measurement technique involves image processing. On-board cameras record successive images for feature detection and matching; and/or velocity measurement of detected features. Input to the control system are the spatial derivatives obtained from the sequence of images. The following subsections will individually explore the main image processing techniques.

1.5.3.1 Optical Flow

Optical flow is a biologically inspired image processing approach for visual guidance and first published by Gibson (1950). Optical flow can be described as the apparent visual motion in a scene as seen by a moving observer. It is perceived as a vector field representing angular speed, at which a contrasting object in the scene is moving past the observer (Aubépart and Franceschini, 2007). Optic flow is heavily used by insects where large portions of the neurons of the brain contribute to visual information processing. Flies such as *Musca* and *Calliphora* use two-thirds of their brain for processing visual information (Strausfeld, 1976). Neurons responsible for measuring the angular speed of the vectors are known as Elementary Motion Detectors (EMD). Flies are equipped with an array of EMDs for assessing optical flow, which makes this species well suited for optical flow studies (Franceschini, 1985). Insects have generally mastered this sensory system for controlling their altitude and speed, landing, and attitude control (Taylor and Krapp, 2007). The idea of using visual cues for the attitude control is therefore an attractive option for robotics motivating a diversity of investigations.

MAV attitude control can be achieved through the use of optical flow. The approach requires algorithms to extract, identify and treat visual information from an on-board camera for attitude estimation of a MAV (Wang et al., 2011). This approach is advantageous for applications requiring high positional accuracy in reference to objects during close-range (low proximity) flights. Optical flow can also be adapted for navigation and collision avoidance (Green et al., 2003). These advantages have made optical flow a research focus, where it is seen as the key for automatic guidance of aerial vehicles (Ruffier and Franceschini, 2005). It is also considered fundamental for MAV employment, which requires some degree of decision-making autonomy (Aubépart and Franceschini, 2007). Kendoul et al. (2009) also assert the importance of optical flow for small aerial vehicle's control and guidance, however, further research into the practical problems associated with the implementation of the approach on software and hardware is needed (Liu et al., 1998b).

Advancements in the performance of Charge-Coupled Devices (CCD) cameras and digital signal processors have aided advancements in the implementation of optical flow (Kim and Brambley, 2007). This has facilitated the utilisation of optical flow in MAVs where an embedded computer processing chip is dedicated entirely to the determination of displacement measurements through optical flow (Zufferey and Floreano, 2006). There are also recent attempts for utilising multiple sensors for performance improvement

of optical flow (Kim and Brambley, 2007; Chahl et al., 2011). A major limitation to optical flow and all other electro-optical based approaches, is that their performance is highly dependent on the visual scene. Poor lighting, lack of discernible or distinct features, and weather conditions (such as rain or fog) can deteriorate performance (Dusha et al., 2007). This limits the MAV's utility in certain conditions reducing its operational spectrum.

Despite major advances in computer processing hardware, optic flow approaches are computationally intensive, which will introduce undesirable time-lag. The additional computational hardware required to process optic flow-based approaches means that they have a higher relative power consumption than conventional sensing options. Optical flow can also be constrained by the bandwidth of the input visual data (Ollero and Merino, 2004). Liu et al. (1998b) studied the trade-offs between accuracy and efficiency in optical flow algorithms. The study found that the design of optical flow algorithms has focussed exclusively on improving accuracy to the detriment of algorithm efficiency, and vice versa. Thus, current solutions lack either accuracy or efficiency. All the aforementioned challenges associated with optical flow techniques, limit its applicability for MAV attitude control and until researchers resolve its associated issues, this approach is not well suited for MAV attitude control in elevated turbulence.

1.5.3.2 Horizon Tracking

Most flying insects use an auxiliary visual system known as the ocelli, which are three eyes located on the head in a triangular arrangement for horizon detection (Chahl et al., 2011). Owing to the simplicity of this system, the ocelli sensing system work faster than compound eyes, thus covering a higher dynamic range of light intensity variation (Taylor and Krapp, 2007). The ocelli are anatomically adapted to mainly serve as a fast horizon detector, where the triangular arrangement allows detection in two axes (Chahl et al., 2011). Figure 20 shows the anatomical structure of a dragonfly's head, clearly outlining the ocelli. Dragonflies are generally considered sophisticated flyers due to their impressive manoeuvring flight performance. The dragonfly will balance its lateral visual field intensities for levelling in reference to the horizon as shown in Figure 21. It is believed that the ocelli serve as the primary input to the insect's control system (Chahl et al., 2011).

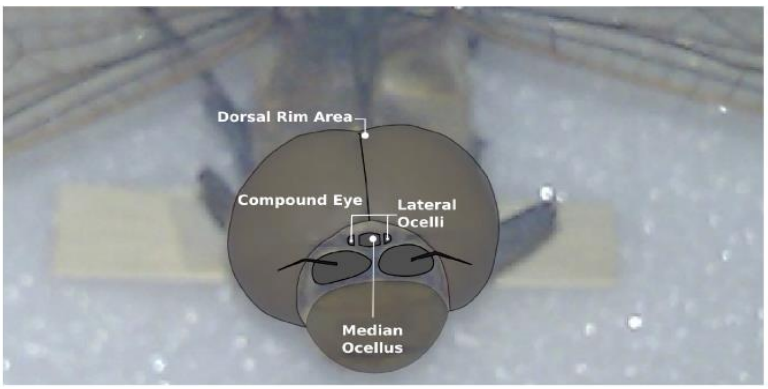

Figure 20: Visual systems of the dragonfly, *Hemianax Papuensis* (Chahl et al., 2011).

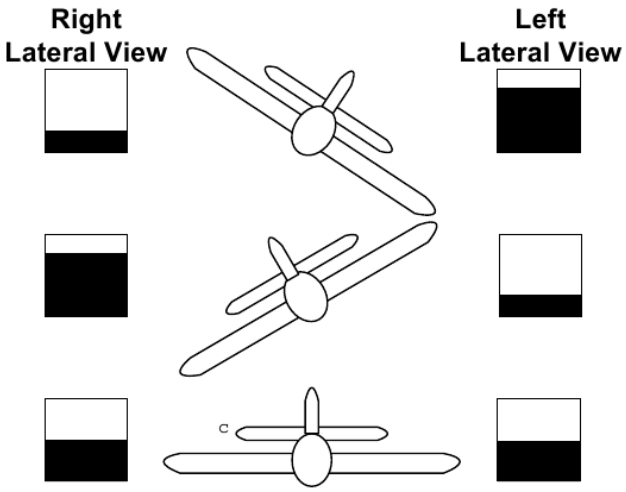

Figure 21: Opposed sensors detecting imbalance in light levels for attitude control (Chahl et al., 2011).

The earliest attempt to replicate ocelli horizon sensors can be traced back to 1971, where The Royal Aircraft Establishment in the United Kingdom (U.K.) demonstrated successful operation of albedo horizon sensors (Brookman, 1971). Later attempts used MEMS thermopiles, which detect temperature variations in the infrared band (Jalink et al., 1972; Gwozdecki, 2001; Taylor et al., 2003; Herrmann et al., 2005). Horizon infrared sensors use Planck's Blackbody Radiation Law and Wien's Displacement Law to detect the horizon. Detection is possible because of the temperature difference existent between the ground and atmosphere. Through the use of multiple pairs of MEMS thermopiles arranged 180^{o} apart and oriented along the aircraft's x,y,z axes, temperature differencing between the sky and ground surface is possible. Implementation comprises of two or three sets of sensor pairs, so that during a rolling or pitching motion differential temperature readings are induced outputting a signal corresponding to the vehicle's orientation with respect to the horizon. The sensor requires a clear unobstructed view of the horizon, otherwise erroneous readings will results. Taylor et al. (2003) extended and installed the thermopiles to the wingtips to overcome this problem as shown in Figure 22.

Figure 22: Wingtip thermopiles sensing rolling motion in reference to the horizon (Taylor et al., 2003).

Another similar implementation uses image-processing techniques for optical detection of the horizon(Todorovic et al., 2003). The approach uses an on-board forward-looking camera where the regions of the image are identified either sky or ground. Processing of the images can be performed on-board the

MAV (Cornall et al., 2006) or off-board through an on-ground computer (Todorovic et al., 2003) depending on the processing requirements, which then transmits its output back to aircraft. Dusha et al. (2007) present a horizon detection technique that also used optical flow in order to reduce false horizon detections and improve robustness in the presence of noise, poor video link or variable lighting conditions. However, there were cases where their algorithm failed to correctly identify the horizon from a number of possible horizon candidates or identified the incorrect candidate (typically due to straight-line features present in most manmade structures). Image-based horizon sensing techniques are more computationally intensive than simpler thermopile-based approaches. Horizon sensing is limited to those operations where an unobstructed view of the horizon can be maintained. Thus, it is not suitable for MAVs operating at low altitudes around buildings or in valleys. Weather conditions can also limit the performance of horizon sensors, although the aforementioned studies attempt to improve the robustness of the system.

1.5.3.3 Scene Structure Tracking

Scene structure tracking is an alternative image processing technique for low flying vehicles where the horizon is invisible. A number of studies attempt to reconstruct an invisible horizon by analysing vanishing points (Antone and Teller, 2000; Demonceaux et al., 2007; Bazin et al., 2008). Alternatively, Hwangbo and Kanade (2011) proposed the concept of exploiting the strong regularities of structure in man-made environments for visual cues on the gravitational direction. A drift-less attitude estimator technique was presented, that extracted image line segments from the observed image of man-made structures (i.e. buildings) to measure the absolute attitude (Hwangbo and Kanade, 2011). The technique is largely based on the regularity of the surrounding environment, assuming that the extracted line segments are either parallel or orthogonal to the gravitational direction. The visual measurements are then used for correcting the accumulated errors of inertial sensors. This technique is challenged by distant images when the extracted line segments become sparse, short, and noisy, thus increasing error. Additionally, the sampling rate of the optical sensor can be a limiting factor if the perturbations occur at an equivalent or higher rate. Hwangbo and Kanade (2011) achieved a measurement output rate of 5Hz using a 1GHz pico-ITX on-board computer, see Figure 23 and Figure 24. Apart from the higher computational requirement, typical of most vision-based sensing approaches, the achievable output rate by Hwangbo and Kanade (2011) is not sufficient for sensing of atmospheric turbulence which happen at rates greater than 5Hz. This method is also heavily reliant on object identification and tracking between images. Erroneous identification due to scene irregularities (i.e. false alarms) can occur. This method works best in built up areas, where MAVs are expected to operate regularly. However, MAV operations using a scene structuring system in environments of low or repetitive features (*e.g.*, deserts, farms, ocean), would be limited. The performance of this approach is coupled to the sensor's Field of View (FoV), where the tracking may fail in certain situations (*i.e.*, fog, clouds, rain *etc.*)

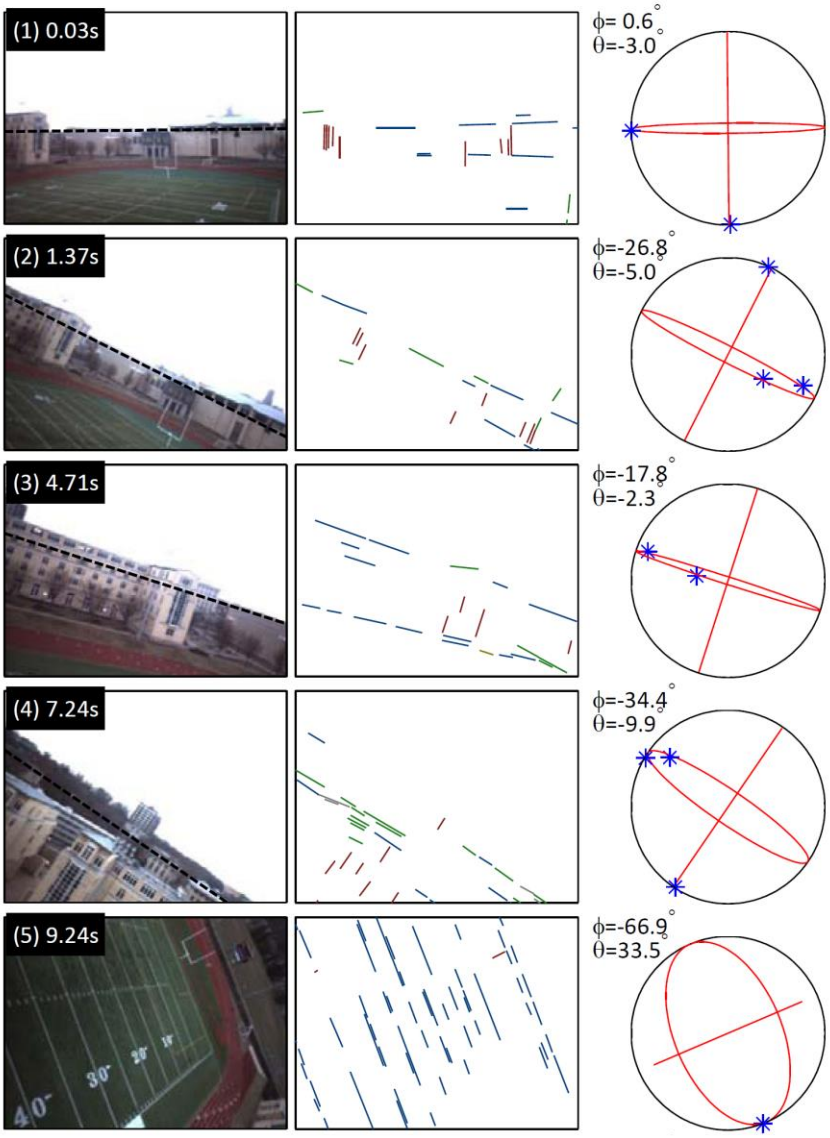

Figure 23: (Left column) images taken during flight. (Middle column) Line segments extracted from images (Right column) Attitude estimate the pole axis and the great circle indicate the current attitude estimate. Adapted from Hwangbo and Kanade (2011).

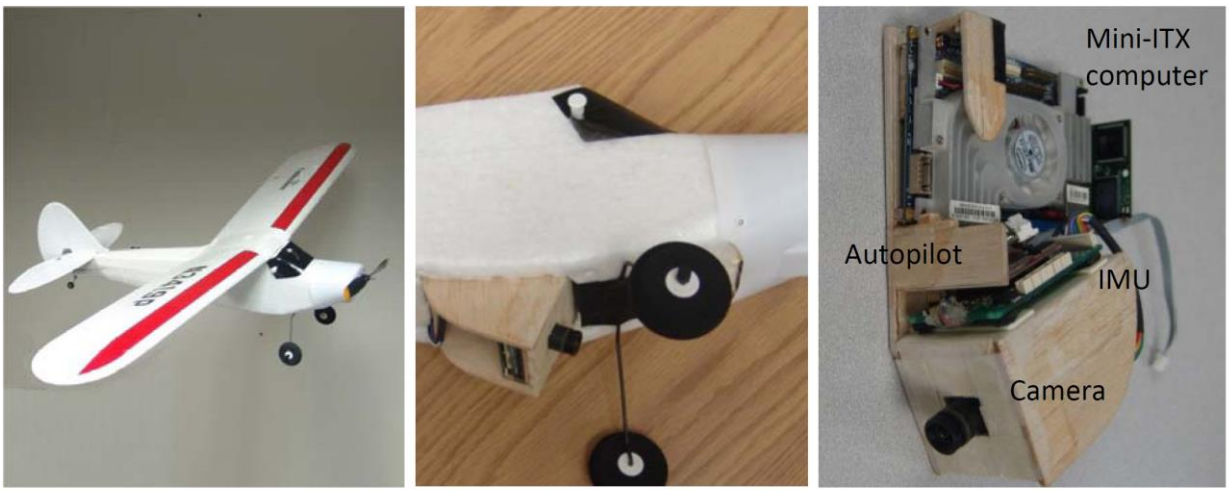

Figure 24: RC model used by (Hwangbo and Kanade, 2011) for scene structure tracking. Model was equipped with Inertial attitude sensors, CCD camera and onboard computer (Hwangbo and Kanade, 2011).

1.5.3.4 Deficiencies of Image Processing Techniques

Image processing techniques rely primarily on the quality of the recorded images. Image quality can be easily degraded with aggressive manoeuvres or excessive vibrations, which are common in turbulent environments, due to low frame rate. Additionally, significant image distortion by optics or severe image noise can induce false computations (Sabatini et al., 2012a) possibly leading to failure as demonstrated in Figure 25. Phenomenal interference such as varying-light conditions, snow/rain, or canyons can confuse the system, reducing its coverage and availability, see Figure 26. The hardware required for image processing can easily exceed the payload capacity and available power on-board MAVs as demonstrated in Figure 24. Subsequently, depending on the available computational power and algorithms used, the response time of such systems can be significantly large.

Figure 25: Poor image quality or video link potentially altering horizon perception (Dusha et al., 2007).

True False False

Figure 26: Horizon detection requires robust algorithms to avoid false detections (Dusha et al., 2007).

1.5.4 Global Navigation Satellite Systems

GNSS can be used for attitude measurements using antenna line-up technology or phase-interference principles. This sensing approach allows the heading and altitude of an MAV to be realised. In the fundamental concept of interferometric GNSS Attitude Determination (GAD), the measurement of the phase of the GNSS signal carrier enables determination of the relative displacement of the antennae in the body reference frame (see Figure 27). This information is directly related to the attitude of the vehicle. The displacement of the antenna baseline length (b) with respect to the Line of Sight (LOS) of the GNSS signal is given by Equation 3. The relative position of the antennae on the vehicle is known a priori, thus reducing the number of satellites required for GAD.

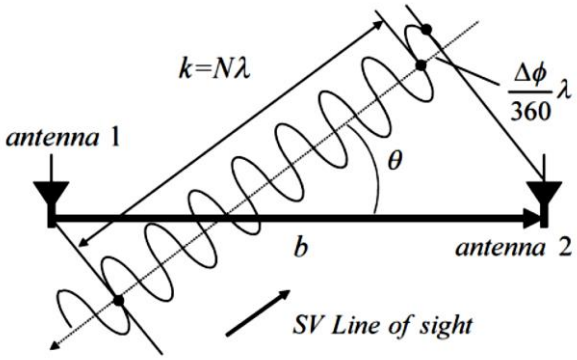

Figure 27: GNSS attitude determination principle (Sabatini et al., 2012b)

The error in attitude calculation, σ_ϑ, can be unacceptably large with baselines in the order of MAV wingspans. The σ_ϑ can be determined using the relation given in Equation 4, where Attitude Dilution of Precision (ADOP) is a parameter used to indicate the accuracy of the attitude solution, generally assumed to be ≤ 1 (see equation 5). Based on the analysis of different sources of error outlined by Sabatini et al. (2012b), the range error, σ_r can be estimated to be 0.5m. This simplifies σ_ϑ to the expression presented in Equation 6. Using this relation, the error present at small baselines (in the order of MAV wingspans) is shown in Figure 28. The accuracy is inversely proportional to the size of the antenna baseline used. Thus, the small size of MAVs limits the accuracy achievable through multi-antenna attitude sensing. Accuracy can be improved by adding antennas but this is constrained by the MAV's size and weight limitations.

$$\theta = cos^{-1}\left[\frac{k+\frac{\Delta\phi}{360}}{b}.\lambda\right] \tag{3}$$

$$\sigma_\theta = ADOP\ \frac{\sigma_r}{b} \tag{4}$$

$$\sigma_\theta = \frac{\sigma_r}{b} \tag{5}$$

$$\sigma_\theta = \frac{0.5}{b} \tag{6}$$

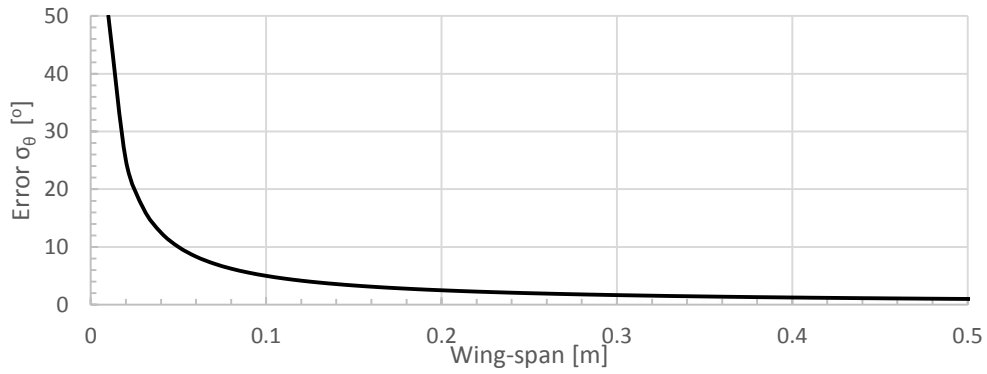

Figure 28: GAD attitude calculation error at micro-scale wingspans

Apart from accuracy, other issues can challenge the use of GAD for MAVs. Communication dropouts with satellites present a major problem, possibly leading to failure of the system, requiring a redundant system on-board. Low altitude operation can also challenge GAD, where Electromagnetic Interference (EMI) from a range of Radio Frequency (RF) transmitters can be problematic (Srini, 2006). Masking and multipath issues may also arise due to manoeuvres and when operating near the ground (Sabatini, 2013b). In urban environments, masking and multipath are also likely to occur around large obstacles. GAD has poor dynamic performance (i.e. not suited for high update rates) challenging its use in MAV attitude sensing. It is therefore concluded that GAD in its current technological form is unsuitable for employment in MAV attitude control.

1.5.5 Sensor Arrangements

Arrangements of common sensors have been used to reduce detection time-delays and extract further performance gains. These are considered in the following subsections

1.5.5.1 Dual Gyroscope Arrangement

Self-contained MEMS gyroscopes can only take measurements within their own reference frame (McNamara and Gianchandani, 2011), however extra performance can be achieved through implementing multiple MEMS gyroscopes. The utility of two gyroscopes outboard on the wings, can improve the detection time-delay. The further apart the sensors can be implemented, the higher the sensitivity. This arrangement will also benefit from the aero-elasticity inherent in all real wings (Durmaz and Kaya, 2013), since the deflection of the wings (implying a translation/rotation of the sensors) may help improve the SNR.

1.5.5.2 Accelerometer Arrays

The concept of utilising accelerometers for rigid body motion detection was first demonstrated by DiNapoli (1965). The concept was further improved by various researchers (Schuler, 1967; Mital and King, 1979; A.J.Padgaonkar et al., 1975; Chen et al., 1994; Zappa et al., 2001; Wang et al., 2003; Tan and Park, 2005; Akeila et al., 2008; Kao and Chen, 2008). Recent work has explored optimal arrangements of accelerometers for highest resolution and lowest noise for compact size applications. For example, Latt et al. (2011) showed how novel arrangements of accelerometers can enhance sensitivity of motion detection and reduce noise by between 17-72%. Although the study was aimed at medical hand-held instruments, the concept could be adapted to MAV application, where novel arrangements of accelerometers embedded along the wing can increase sensitivity and reduce noise. Additionally, since all real MAV wings are flexible, the accelerations measured from the wing flexing will be detected before the effect is measured in the body of a MAV. Apart from the improvement in update rate, the angular accelerations can be detected directly without the need for noisy differencing of angular rate measurements. However, there is a computational penalty in addition to the alignment problem associated with employment of multiple

accelerometers due to the fact that the micro-controller now synthesises a response from multiple discrete accelerometers (McNamara and Gianchandani, 2011).

1.5.5.3 The Inertial Measurement Unit

Gyroscopes and accelerometers are commonly integrated to create an Inertial Measurement Unit (IMU), which can have significantly less noise and drift (however, their individual problems still persist). IMUs are the most commonly used sensory system in MAVs (Beard et al., 2005; Kingston and Beard, 2004; Andersen and Taylor, 2007). The fusion of the signals from the different sensors is achieved through a range of filters, the most common of which are the Kalman or complementary filters. The filters provide a "hybrid" or "combined" signal, which improves on the performance of any one sensor (Zhang et al., 2005).

A filter can be tuned to allow the control system to depend more on the output of the gyroscopes, which are more stable in the short term (*i.e.*, high frequency), and on accelerometers in the longer term (*i.e.*, lower frequency). The result is a signal with reduced accelerometer noise and gyroscopic drift. To further improve performance, the IMU is usually fused with the outputs from a GNSS receiver (Vörsmann et al., 2012). The IMU can also be fused with a barometric system for altitude correction, a magnetic compass for heading correction, and a speed sensor for velocity correction.

Although the sensory system's output error can be improved through the use of sensor fusion, there are practical implications. Employing multiple sensors requires more space, power, and processing resources. These can potentially challenge the Size Weight and Power (SWAP) constraints of a MAV. The more complicated the applied signal processing techniques become, the larger the time-lag becomes to output a reading. Current MAVs rely primarily on IMUs fused with correction sensors (mainly GNSS) for guidance, navigation, and attitude control (Ratti et al., 2011; Vörsmann et al., 2012). With the advancements of MEMS-based IMUs to navigation grade (Keller, 2013), this sensory system is still preferred over all others.

1.5.6 Inspiration from Biological Sensory Systems

Although turbulence is challenging for MAVs, birds and insects can hold relatively straight and level flight even under high turbulence conditions. Flying animals have evolved to cope with high turbulence levels during flight. Birds such as Kestrels can withstand elevated levels of turbulence while hovering and maintaining a spatial "head-lock" with a high degree of accuracy for spotting moving prey below (Videler and Groenewold, 1991). These birds may provide an inspiration and benchmark for MAVs. It is thus wise to consult nature's flyers for technological cues, to enhance attitude control of MAVs.

Animal flight in turbulence has been studied since the 1900's (Hankin, 1913). Animals employ a combination of integrated sensory systems linked directly to their central nervous system (Taylor and Krapp, 2007). Researchers have studied a variety of biological sensors for replication such as insect's halters to develop vibratory gyroscopes (Anon, 1946). Biologically inspired vision-based attitude estimation has

also been explored (Brookman, 1971; Hankin, 1913; Srinivasan et al., 1999; Chahl et al., 2011). Among the relatively unexplored sensory systems hypothesised to contribute to the motor control of flying animals is aerodynamic sensing for feedback to the brain. Strong evidence suggests that the hairs and feathers of flying animals can be used to sense flow parameters such as separation, airspeed, or flow angle (Sterbing-D'Angelo et al., 2011; Taylor and Krapp, 2007; Carruthers et al., 2007; Hörster, 1990a; b; Necker, 1985a; b; Brown and Fedde, 1993). Despite the growing evidence identifying the significant role of flow sensing in the feedback control of birds, little research explores the advantages (from a time-lag perspective) of replicating this sensing strategy for MAVs.

1.6 Actuation

As identified in the SPA cycle of Figure 3, actuation contributes to the time-lags of the MAV's attitude control system. In the most turbulent cases, aerodynamic actuation may be too slow to counteract the perturbations induced by gusts. Attaining sufficient flight control actuation that fulfils the requirements of MAVs (SWaP, reliability, bandwidth, and load rating) is challenging (Osgar et al., 2012). Traditionally MAVs use conventional servomotors (also known as servos) as actuators for deflecting aerodynamic control surfaces. These servos occupy significant volume and may be less reliable than desired (Osgar et al., 2012; Sarson-Lawrence et al., 2014). Novel actuation techniques, which have significantly high bandwidth and occupy less volume, have been identified in the literature. The following subsections therefore explore conventional and unconventional actuators.

1.6.1 Servo Motors

The miniaturization of DC motors has enabled the fabrication of micro-scale servos. As their size is reduced, servos' response characteristics become important. Miniaturization of servos enabled micro flight, however their actuation speed is insufficient for rapid actuation of aerodynamic surfaces (Osgar et al., 2012). The response times of servos are largely determined by the inertial requirements needed to accelerate the sub-components up to the required speed. The higher the torque required to accelerate the subcomponents, the slower the response will be and vice-versa. This is substantially alleviated in smaller sized servos, which require less torque to accelerate smaller components, implying faster responses.

A range of small commercially available digital servos (<30grams) which are suited for MAVs were surveyed and their "no-load" performance plotted in Figure 29. The illustrated data were obtained from manufacturer datasheets. The performance degrades in the presence of loads. Degradation will depend on flight speed, gust amplitude, and aerodynamic surface area. It is evident that the highest actuation rate (25Hz) is evident at the smallest mass (1.9g). Although these actuation rates are sufficient for smooth flight, they are still insufficient to match the higher rates of perturbations (Wang et al., 2003).

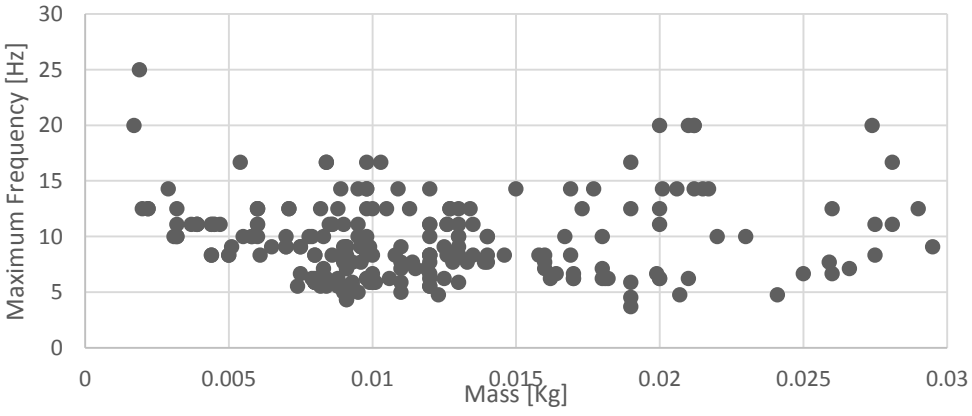

Figure 29: Max frequency for a range of commercially available servos

1.6.2 Novel Actuators

There are a number of novel actuation mechanisms applicable to MAVs, which are expected to outperform conventional servomotors through technological advancements. This section focuses on five maturing technologies applicable to MAVs; electrostatic (Tang et al., 1989), piezoelectric (Wang and Cross, 1998), thermal (Prasanna and Spearing, 2007), shape memory (Krulevitch et al., 1996), and dielectric elastomer (Kornbluh et al., 2002). Karpelson et al. (2008) reviewed these technologies with respect to employment for MAVs as shown in Table 1. The evaluation of the technologies was based on simplified first order models where many assumptions where made, such as linear elastic behaviour.

Table 1: Review of different actuator technologies (Karpelson et al., 2008).

Actuator category	Operating principle	Representative geometries	Maximum deflection	Maximum force	Speed of actuation	Efficiency range (%)	Notes
Electrostatic	Electrostatic force	Comb drive, parallel plate	Low	Low	Very fast	> 90	Requires MEMS manufacturing processes, high operating voltage.
Thermal	Thermal expansion	Expansion, bimaterial bending cantilever	Medium	Very high	Slow	< 5	Versatile geometries, largest materials selection.
Piezoelectric cantilever	Converse piezoelectric effect	Bimorph, unimorph bending cantilevers	High	Medium	Fast	10-30	Simple planar structure, high operating voltage.
Shape memory alloy	Thermally induced phase change	Wire, bimaterial bending cantilever	High	Very high	Slow	< 5	Very high energy density.
Dielectric elastomer	Maxwell stress causing viscoelastic deformation	Linear extender	Highest	Medium	Medium	60-90	Capable of over 300% strain, very high operating voltage.

From the results presented in Table 1, piezoelectric actuators are ideally suited for MAV applications due to their high actuation rates and large deflections. Piezoelectric actuators have the potential to replace conventional servomotors. Piezoelectric actuators have no moving parts, which can wear or get contaminated, thus improving reliability (Osgar et al., 2012). These actuators can be imbedded within the skin of the wing improving aerodynamics (no extruding linkages or grooves in wing) and reducing required volume. The associated electronics can be placed independently of the actuators allowing more freedom of internal layout.

Osgar et al. (2012) embedded piezoelectric elements within flexible wing skin to form a conformal smart material actuator, known as piezoelectric Macro Fibre Composites (MFC). Through the concept of bimorphing, the MFC can convert axial strain of the piezo element into a bending motion. The performance of MFC was compared to that of conventional servomotors. It was found that MFCs show significant improvements in reliability and aerodynamic performance. The bandwidth of MFC was an order of magnitude more than conventional servos. The disadvantages to this actuation technology is that they are specific to certain designs (i.e. not interchangeable with any MAV). Furthermore, a failed actuator will result in replacement of the entire aerodynamic surface in which the actuator is embedded in. The system's mass is also slightly heavier than an equivalent system of servomotors. A further disadvantage to MFC is the high voltage required. This problem was solved by Osgar et al. (2012) through additional circuitry.

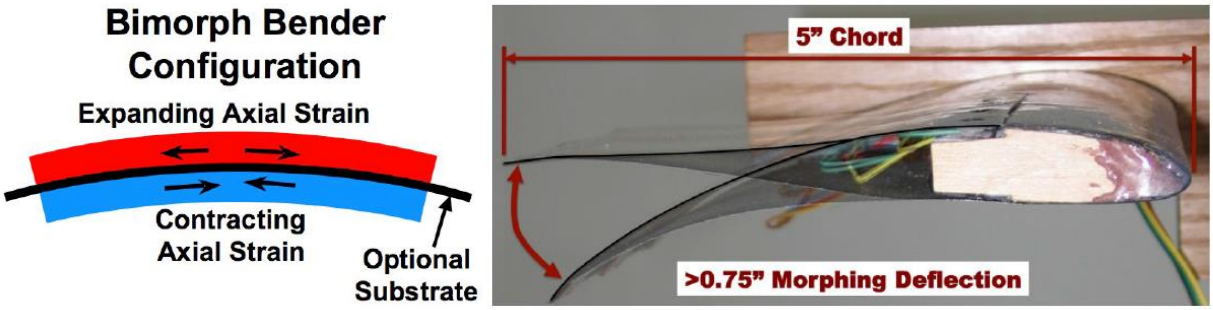

Figure 30: Piezoelectric Actuation: (a) Biomorph configuration. (b) Prototype of MPC MAV wing. (Osgar et al., 2012)

Piezoelectric-based actuation is ideally suited for MAV application from a reliability, and aerodynamic perspective. The high bandwidth (up to 10^4Hz) of piezoelectric actuators (Karpelson et al., 2008) relative to other types will provide the fast actuation required for MAVs operating in high turbulence.

1.7 Literature Review Discussion

Research opportunities to enhance the attitude control of MAVs operating in high turbulence were identified. Most opportunities were found to be in the sensing and actuation components of the SPA cycle. Through the use of novel actuation technology, limited bandwidth is no longer a limitation. Piezoelectric actuators will replace conventional servo motors allowing rapid actuation. Research in the sensing component of the SPA seems to have settled upon inertial and vision based sensors with little research exploring alternative sensing approaches. The published literature focuses on improvements of conventional inertial and optical based sensors for extracting further performance gains. The apparent objective of existing studies is the extraction of further performance through advancements in signal processing, measurement techniques, and fabrication. From the literature, it is evident that conventional attitude sensors are well suited for attitude control, thus there is little motivation to explore other approaches. Although this notion is somewhat true for larger UAs and commercial aircraft, it is not the only possible turbulence mitigation technique applicable for MAVs. Despite strong evidence suggesting that flying animals use feedback flow sensing systems researchers have not yet investigated the utility of flow sensing and whether it can reduce the time-lag of the attitude control system. There seems to be promise in the exploration of biologically inspired sensors, which may replace or complement inertial based sensors to enhance the attitude control of MAVs.

1.8 Proposed Research

1.8.1 Justification

Various MAV accidents have occurred due to the lack of a reliable attitude control system in turbulent flow conditions (McCarley and Wickens, 2004; Williams and Harris, 2002). Increasing the operational spectrum of MAVs in turbulent condition is important, allowing them to reach their full operational status. Advancements in attitude control of fixed-wing MAVs will improve their utility in complex terrain and adverse weather conditions. Achieving higher attitude stability will also reduce on-board sensory noise thus improving quality of acquired data. Improved attitude control will make MAVs a more attractive option for specialist missions. The sensing and actuation component of the attitude control system were identified as the main sources degrading attitude stability in turbulence. Research into high bandwidth actuation technology exists, however a research gap was identified in studying sensors capable of detecting the high rates of the disturbing phenomenon (i.e. flow disturbances) before inducing a perturbation.

1.8.2 Research Scope

The scope of this research includes both theoretical and experimental work. Only fixed-wing vehicles are considered. The literature survey identified roll perturbations as the most significant destabilising motion, and hence only roll stability will be considered. This research will focus on enhancing the sensing component of the control system and actuation is considered beyond the scope. Although the literature survey identified piezoelectric actuators as ideal for MAV application, they are not readily available, and require custom development. Consequently, high-speed servo motors are used in this research for a conservative approach.

1.8.3 Research Questions

After consideration of the results of the literature review, the following Research Questions (RQ) were specified to be answered in this thesis:

1. How can the attitude control performance of MAVs operating in turbulent conditions be improved?
    1.1. How do velocity variations of the oncoming turbulence correlate with wing surface-pressure distribution?
    1.2. How do velocity variations in oncoming turbulence correlate with perturbations in roll?
    1.3. How can we use sensed velocity variations to improve the performance of the attitude control system?

1.9 Thesis Layout

The individual sections in this thesis are outlined below:

Chapter 1 Contains relevant literature providing background understanding of the research problem.

Chapter 2 Contains the theoretical contribution associated with identifying time-delays and outlining relevant biologically inspired flow disturbance sensors. Further literature is reviewed where relevant.

Chapter 3 Contains the rationale and description of apparatus used throughout the experimental research including details of the selected MAV airframe.

Chapter 4 Contains an investigation of the relationship between wing surface-pressure fluctuations and its correlation to upstream turbulence.

Chapter 5 Contains an investigation of phase-advanced attitude control through the aid of a specially developed roll-axis rig.

Chapter 6 Contains the flight test results of the developed phase-advanced attitude control system inside wind-tunnels and outdoors.

Chapter 7 Outlines the key conclusions from this work with discussion on its contribution within the MAV field of research.

Chapter 2

The Gust Perturbation Process and Phase-advanced Sensors

Summary

In this chapter, the time-lags within an attitude control system are explored. Improvements in the sensing component of the control system are identified as key to enhancing attitude control in turbulence. This chapter includes the author's theoretical contribution to the field, which involves the introduction of new terminology, namely the gust perturbation process. Conventional attitude sensors are shown to have a time-lagged output relative to perturbations. An exploration of sensors capable of sensing the flow disturbances before a perturbation occurs are identified. These sensors are reviewed and an ideal sensor is selected for experimental testing in the subsequent chapters.

2.1 The Gust Perturbation Process and Time Delays

In order to develop a more effective attitude control system it is first necessary to explore the physics underlying the disturbance input. The flow chart in Figure 31 represents the stick-fixed response in roll and illustrates the sequence of events induced by an oncoming gust, defined here as the *gust perturbation process*. A perturbation in roll was chosen since it was previously identified as the most problematic for MAVs. Between each event, there is a finite time-lag and sensors associated with each event are categorised according to their measured parameter. Theoretically, some of the events presented can occur at the same instance, such as roll acceleration and roll rate, while there is a delay between others such as variation in Angle of Attack (AoA) and structural stress. Hence, the sequence illustrated is flow-influenced as well as sensor-influenced. The latter statement can be further clarified by the plots of Figure 32, which illustrate an example of a roll with constantly increasing roll rate, comparing responses of typical sensors. From Figure 32 it can be seen that accelerometers can capture infinitesimal perturbations while other sensors are detecting no change.

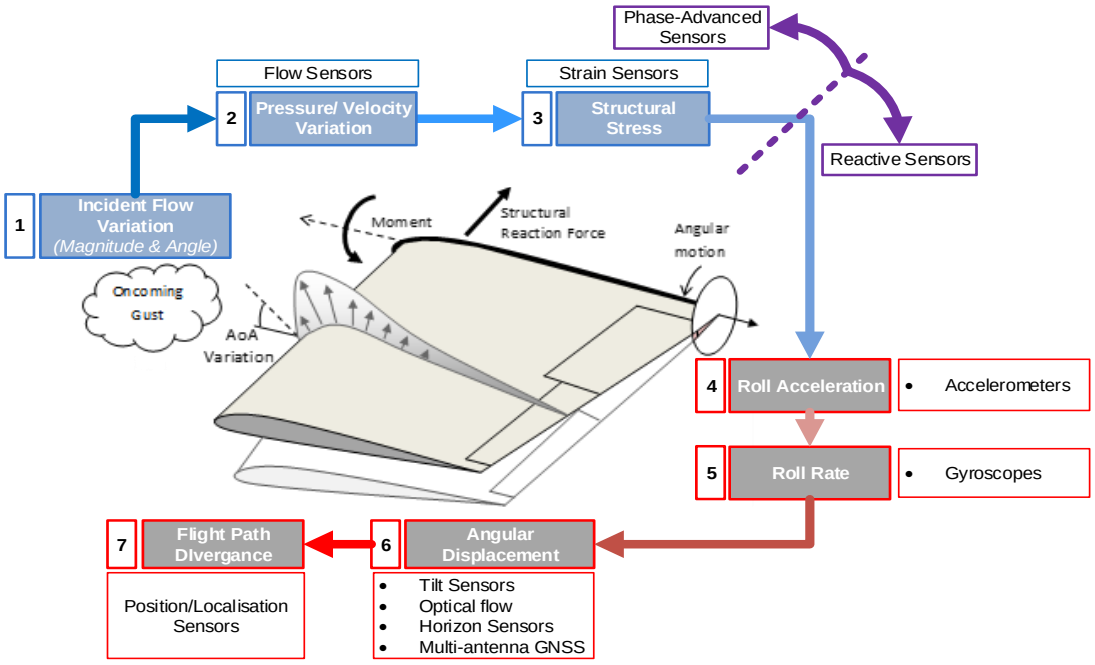

Figure 31: The sequence of events induced after encountering a gust.

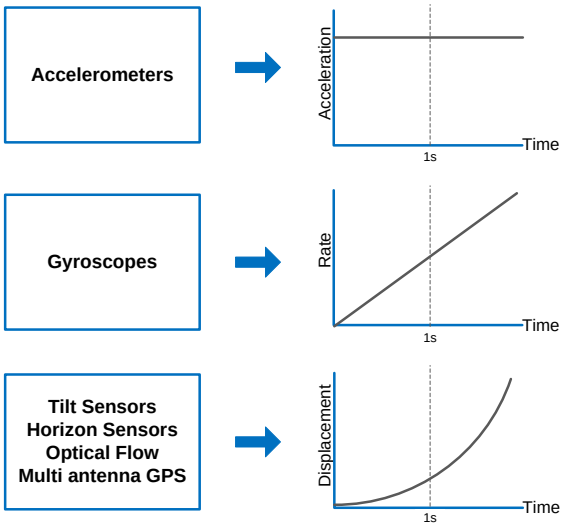

Figure 32: Comparison of various sensor responses to a roll with constantly increasing roll rate

There are various time-lags underlying the controlled response of a MAV counteracting a perturbation. The time-lags can be the result of physical phenomena or technological limitation. Minimising these time-lags is useful in improving the disturbance rejection performance of the attitude control system. However, to characterise and quantify the latencies it is crucial to track and understand the process underlying the source of the disturbance (i.e. gusts advection over the wing). The nature of the event-related parameter measured by sensors, and its sequencing in the aforementioned process, will influence time-delays. The conventional sensors presented in Figure 32 require the MAV to respond inertially before a perturbation is detected. Sensors which detect disturbances (i.e. gusts) before the vehicle starts to respond inertially will permit more effective attitude control.

An equation and process describing the time response is developed. The gust perturbation process' relationship to the other responses in a roll event, including control surface deflection is illustrated in Figure 33. The contributions of the physical phenomena and aircraft subcomponents to a delayed response are shown. The presented terms can be approximated to determine a nominal $t_{CR,}$ as presented in Equation 7. In this work, the time required to communicate and compute data, t_m and t_c, by a microcontroller is considered negligible. Furthermore, the work presented by Abdulrahim et al. (2010), aids the estimation of t_a, t_i, *and* t_v combined. From the flight measurement results presented by Abdulrahim et al. (2010), the response time following actuation is ~ 2Hz (0.5s) for a 1m wingspan MAV flying at 10ms^{-1}. Considering the fastest and lightest surveyed commercially available servo actuators (see Section 1.6), a loaded servo will attain a response of ~ 0.015s. These estimates lead to the simplification presented in Equation 8. It can therefore be seen that within current technological constraints, the MAV used by Abdulrahim et al. (2010) will attain a control response

duration of > 0.52s. Based on these assumptions, it would be impractical to reject adverse roll frequencies above 2Hz assuming that t_p and t_d were infinitesimally small. If one assumed that the gust perturbation process was of the same order as the response time, then the control response would be on the order of 1s, and thus MAVs would be unable to compensate for high intensity turbulence at frequencies above 1 Hz. Inertial based detection is assumed in the previous analysis, which requires a response (roll) of the MAV before any corrective action can be taken. If a sensing or detection system can be developed that could provide a means to sense a disturbance before an inertial response was initiated, then the possibility may exist to shorten the overall response time of the control system and expand the operational envelope of the MAV.

$$Control\ Response_{\ t_{CR}} = Gust\ Perturbation\ Process_{\ t_P} + Detection_{\ t_d} + Multiplexing_{\ t_m} + Computation_{\ t_c} + Actuation_{\ t_s} + Aerodynamic_{\ t_a} + Inertial_{\ t_i} + Virtual\ Mass_{\ t_v}{}^{1} \quad (7)$$

$$t_{CR} = t_P + t_d + 0.515 \quad (8)$$

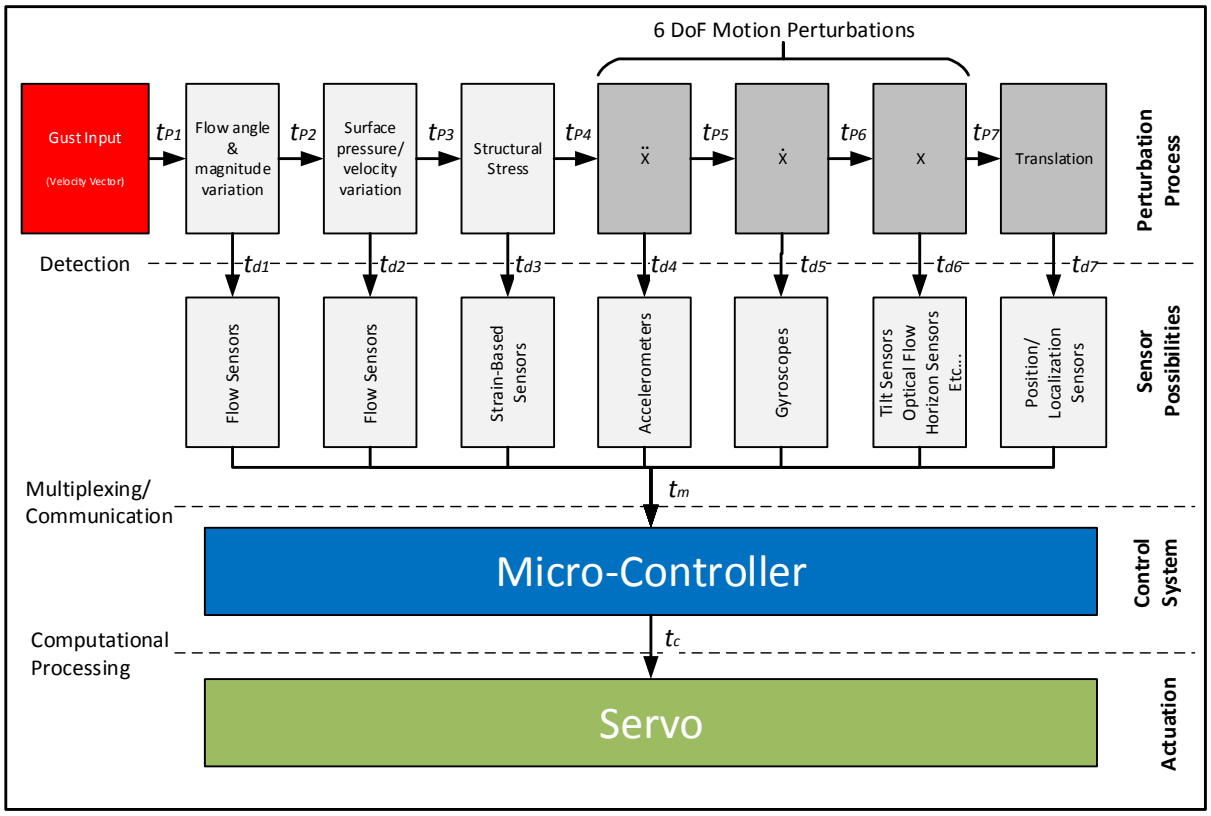

Figure 33: Block diagram illustrating attitude control with respect to gust physics

[1] Caused by moving the volume of the surrounding fluid as it the body moves through it thus decelerating the motion

Sensor time-lags stated by manufacturers in the specification datasheets only involve the t_d and t_m terms of Equation 7. This detection time-lag is a result of the measurement mechanism adopted by the sensor. The entire lag t_{CR} is only fully realized once put in context with its application. The block diagram of Figure 33 attempts to view sensors as sub-components of a larger system by graphically representing Equation 7 up to the 5th term. This diagram relates MAV attitude sensors with their control architecture and response dynamics. Sensors can be put into context and categorized according to their measured parameter. Early perturbation sensing or phase-advanced sensing led to investigations into novel sensory approaches that exploit the first four events illustrated in Figure 31. The following section therefore attempts to explore phase-advanced sensors.

2.2 Bio-Inspired Phase-Advanced Attitude Sensors

Sensors capable of detecting a phenomenon early in the gust perturbation process are referred to as *phase-advanced* sensors. The previous chapter showed that reactive attitude sensors are not well suited for sufficient attitude control of MAVs in the presence of turbulence. Alternative sensors that can detect the first three events of the gust perturbation process (see Figure 31) are considered in this section. Although phase-advanced sensors do not measure attitude directly, they sense the disturbance itself, which is potentially advantageous in providing phase-advanced information to the control system for early motion mitigation.

As identified and proposed in Chapter 1, it is useful to explore biological sensory systems to determine whether artificial replication of such systems can enhance attitude control systems of MAVs. There are a number of unexplored sensory receptors used by flying animals that could be replicated and adapted to MAVs. Biological receptors sense different parameters such as scent, flexure, or light intensity. Inputs from these receptors are often combined and fed through nerves to the brain. Receptors relevant to attitude control include photoreceptors and mechanoreceptors. Photoreceptors have been extensively studied in the context of flight control (Srinivasan et al., 1999; Chahl et al., 2011), however exploitation of mechanoreceptors for MAV flight control is not well established.

The function of mechanoreceptors in detecting flow qualities can be replicated in a variety of ways. Bio-mimicry (i.e. exact copy) is usually ineffective where biological structures often serve multiple purposes (Michelson, 2010). In contrast, bio-inspiration presents a practical approach whereby only the fundamentals are exploited for an implementation that suits the application. In-terms of mechanoreceptor replication this means that sensing flow parameters should be done through individual specialised sensors. For example, feathers can mechanically respond to a number of inputs depending on their position and condition, such as pressure difference, velocity, or variations

in AoA. Such parameters can be sensed individually through currently available sensors such as: thermal, strain or capacitance-based flow sensors. Their use in phase-advanced sensing is discussed later. There are many types of flow sensors. Flow sensors can be laboratory-based such as: Particle Image Velocimetry (PIV), Laser Doppler Anemometry (LDA), Light Detection and Ranging (LiDAR) and Radio Detection and Ranging (RADAR). However, such sensors are generally too large to currently be incorporated into MAVs. The following subsections only consider bio-inspired sensors that can be installed on-board a MAV. Published attempts of using such sensors for attitude control are reviewed.

2.2.1 Feathers and Hairs

Feathers and hairs serve multiple purposes including temperature regulation, water protection, and in combination with other parts of the sensory system, a detection method of local flow. Hence, strain-based flow sensors could be considered analogous to a feather and its receptor. The sensing element of such sensors is fundamentally similar to the feather, which deforms with changes in incident flow. The sensing element's vibration and/or deflection are typically measured with a physical mechanism such as electric resistance or capacitance, which is conceptually similar in function to Herbst corpuscles[2]. The following subsections explore various attempts in replicating flow sensors.

2.2.1.1 MEMS Flow Sensors

MEMS flow sensors are ideal for MAV employment due to their miniature size. They also have the benefits of low power dissipation and fast response time, which is essential for measuring turbulent flow (McNamara and Gianchandani, 2011). The miniature size of these sensors allows for their utilisation in small spaces without significantly interfering with the flow and consequently altering its behaviour. These miniature flow sensors are widely used for fluid measurements in various disciplines. The two most common flow sensing mechanisms, thermal and mechanical, are described in Table 2.

Basic implementations of miniature flow sensors measure localised flow velocity (Chen et al., 2007), while more complicated implementations can output a magnitude and direction of velocity (Fan et al., 2002) (see Figure 34). Often an array of sensors is used, similar to the multitude of sensors used by insects and birds, to overcome the limited information available from a single velocity vector. Multi sensor implementations require a study into the optimum sensor placement and their corresponding density in a given area. This implementation can be challenging in MAVs because of the SWaP constraints.

[2] Nerve endings found in feather follicles which sense vibration

Flow sensors can be used for detecting the surface velocity distribution over critical locations of the wing, such as the points of flow transition, reversal, or separation. Locating sensors thus requires a comprehensive understanding of the aerodynamics of the wing. Out-of-plane mechanical flow sensing (Kim et al., 2000; Svedin et al., 2003b) is another approach that can provide utility in measuring the fluctuations in the lift force over the wing (see Figure 35 and Figure 36). Other unexplored implementations of mechanical flow sensors could potentially measure variation of AoA, where a high density array can be embedded in the leading edge of the wings to detect the incoming flow's pitch angle.

Table 2: Flow sensor types

Sensor Type	Description
Mechanical	Uses various techniques in the implementation of the sensing elements to measure airflow through deformation induced strain variation. Drag sensors have been developed which employ a cantilevered structure that deforms due to viscous drag as shown in Figure 35 (Gass et al., 1993; Radhakrishnan and Lal, 2003; 2005). Another interesting approach is the lift force sensor which employs a miniature flat plate airfoil that deflects due to fluid flow as shown in Figure 36 (Svedin et al., 1998a; 1998b; 2003a; 2003b). The deflection or pitch is measured through strain and is correlated with a lifting force.
Thermal	Based on the transport of heat into the moving fluid (Buder et al., 2005; Buder et al., 2007), there are various implementations to measure the flow rate. Examples include measuring resistance of a heating element, or the current required to maintain element temperature. There have also been early attempts at integrating separate heating and temperature sensing as shown in Figure 37 (Stemme, 1986; Lofdahl et al., 1989). Another form of this approach uses multiple temperature sensors arranged symmetrically around the heating element which provides additional directional information (Kim et al., 2003; Kim et al., 2004; Ohnstein et al., 1990; Park et al., 2003; Tan et al., 2007). This approach can be used for two-dimensional in-plane measurement of flow. Out-of-plane sensing has also been studied which offers improved response times, lower power requirements, and improved flow coupling (Ebefors et al., 1998; Chen et al., 2002). However, thermal based flow sensors can be sensitive to the ambient temperature fluctuations thus influencing performance.

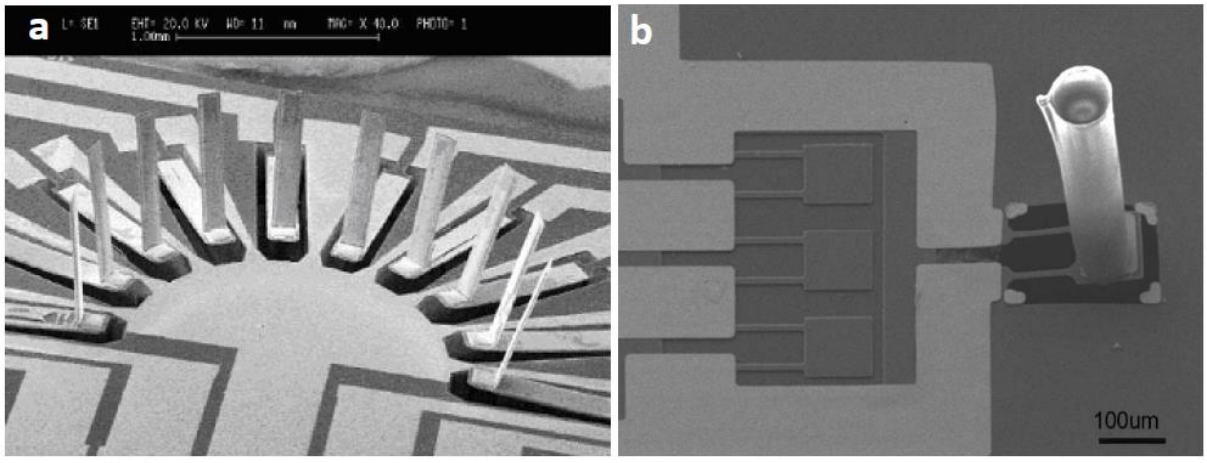

(a) (b)

Figure 34: Mechanical flow sensor arrangements with different outputs: (a) velocity vector (Fan et al., 2002) (b) velocity magnitude (Chen et al., 2007).

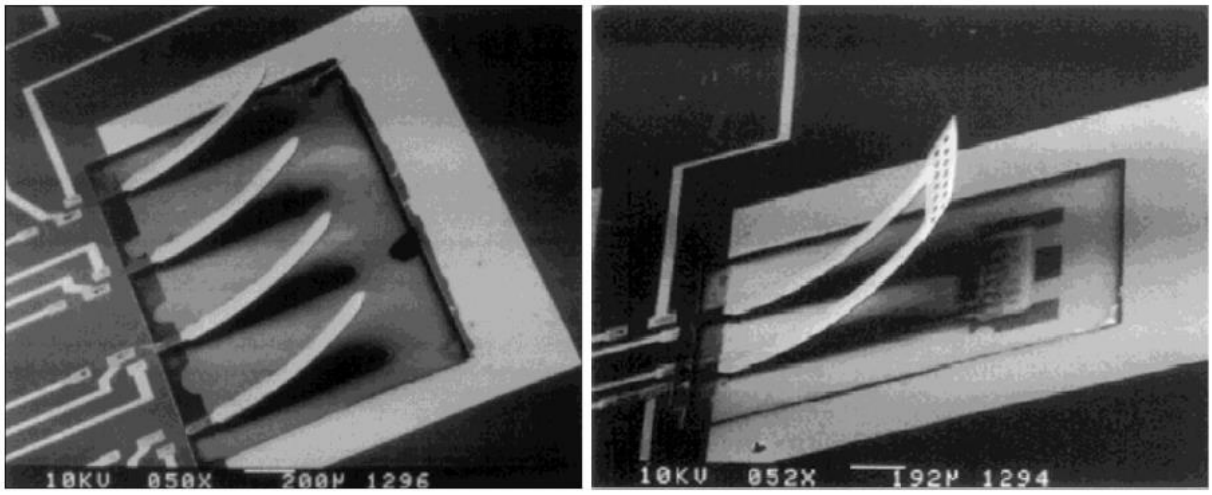

Figure 35: Cantilevered MEMS flow sensor (Kim et al., 2000).

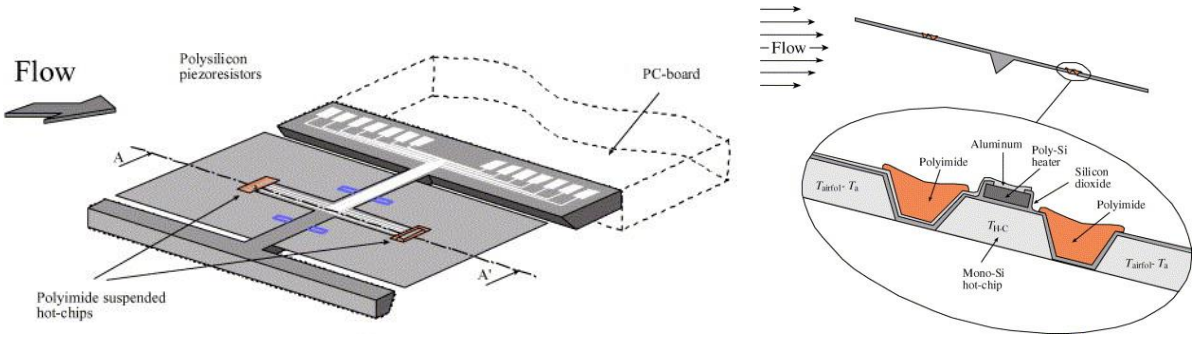

(a) (b)

Figure 36: (a) Lift force flow sensor (b) Schematic of the flat plate sensing element (Svedin et al., 2003b)

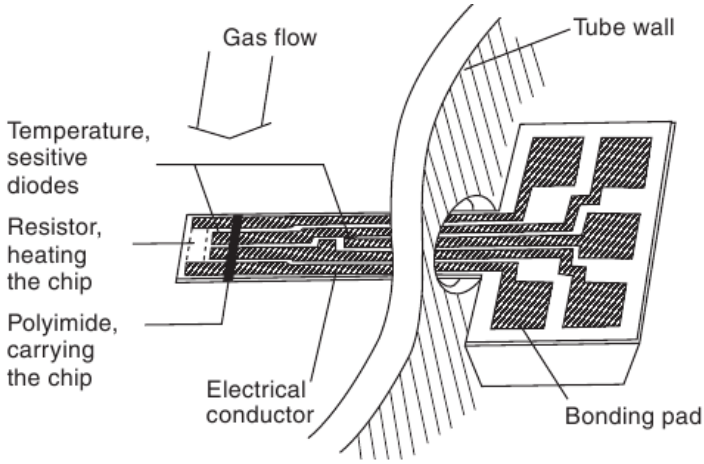

Figure 37: MEMS thermal based flow sensor showing separate heater and temperature sensors (Stemme, 1986) reproduced by (McNamara and Gianchandani, 2011).

The natural environment is expected to cause detrimental effects on performance of flow sensors. The designer/engineer must address several design considerations. For example, operating in high temperatures can introduce error in thermal-based flow sensors. Mechanical flow sensors may also be challenged by rain, elevated humidity or fine airborne particles, which can all cause stiction of the cantilever sensing element. Vibration or high impact forces commonly experienced during the take-off and landing phases of MAVs can also degrade performance or cause sensor failure.

Multiplexing of the array and synthesizing a response by the control system can potentially introduce computational complexities, especially with dense arrangements. Finally, these sensors are platform specific where they require an in-depth understanding of the airfoil properties in the given flight domain, and require calibration to those conditions, unlike inertial sensors for example which can be easily adopted by any design, in a "plug and play" fashion.

2.2.1.1.1 Artificial Hairs

Strain-based flow sensors can be modified to mimic the function of biological hair. Mimicking insect hairs for adaption to robotics and other applications is receiving considerable interest by researchers (Dijkstra et al., 2005; Krijnen et al., 2007; Bruinink et al., 2009; Casas et al., 2010; Dagamseh, 2011). The sensory system of the cricket provided the inspiration to develop an artificial capacitive hair-like flow sensor array for flow pattern measurements (see Figure 38). The fundamental concept of these artificial hairs is to resolve mechanical responses induced by viscous drag-torque as a function of space and time. Fabricated using MEMS technology, these artificial hair sensors can be made in different lengths (100-900µm) and widths (25-80µm) with reduced spacing between the hairs thus allowing dense clustering (see Figure 39). The hairs are constructed from rows and columns of conductive electrodes, which are separated by dielectrics. The induced torque tilts the base membrane, consequently varying capacitance. The variance in capacitance is proportional to the velocity of the artificial hair through the fluid. The sensors were shown to attain high sensitivity to airflow down to a few mm/s (Dagamseh, 2011). The stiffness of the sensory hairs can differ for each axis of deflection to provide information on the direction of the velocity vector. It is reported that these physical parameters of the hairs influence their sensitivity and bandwidth (Dagamseh, 2011). A delicate design balance is hence required to achieve high sensitivity while maintaining sensor bandwidth.

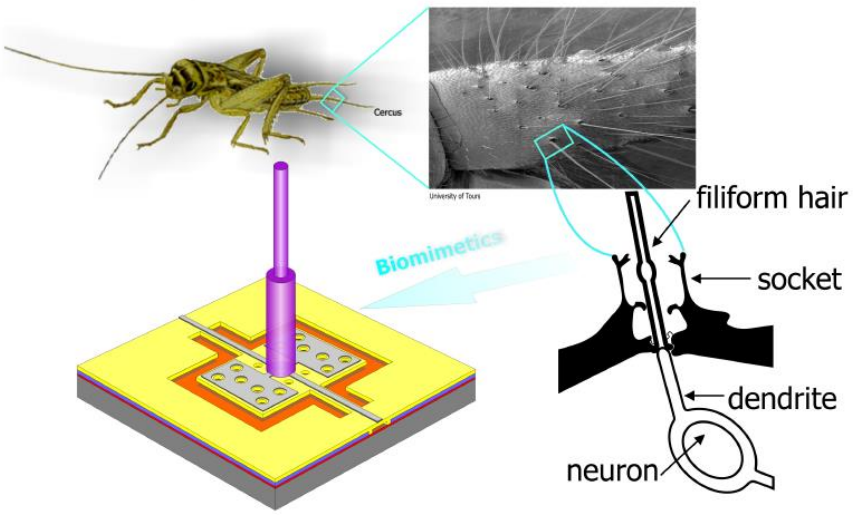

Figure 38: Hair-like sensor geometry and its biological source of inspiration (Dagamseh, 2011)

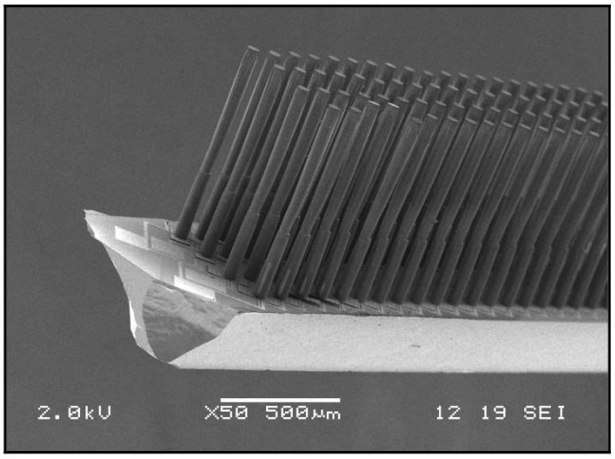

Figure 39: Scanning Electron Microscope (SEM) image of hair-like sensor array (Krijnen et al., 2007)

Dagamseh (2011) states that there are considerable challenges in the design and use of an array of artificial hair sensors. Various issues with electronic interfacing can limit overall performance of the sensory array. To achieve spatio-temporal flow measurements, hairs are interrogated solitarily, where each hair in an array uses a separate acquisition channel to communicate with a central processor. The larger the array, the more spatial resolution can be achieved. Typically the size of the array is constrained by the available processing resources (e.g., clock speed and memory), and the hardware (e.g., number and speed of the analogue to digital processors) available. Field Programmable Gate Array (FPGA) and other microprocessors capable of parallel processing could address some of these computational and timing issues associated with large sensor arrays.

Issues concerning the size, weight, complexity, and cost must still be addressed before large artificial hair arrays become a feasible sensing technology for MAVs. Finally (Dagamseh, 2011) states that further improvements are required to match the performance of the cricket's hair.

2.2.1.1.2 Artificial Feathers

Another biologically inspired variant of flow sensors comes in the form of covert feather-like wing panels. Blower and Wickenheiser (2010) replicate avian covert feathers and explore their use for gust alleviation. The feather-like panels were installed on the upper and lower wing surface as illustrated in Figure 40. The panels act as sensors, actuators, and load bearing members. The underlying concept is to integrate sensors with aerodynamic surfaces to detect gusts, and alleviate them.

The work by Blower and Wickenheiser (2010) focuses on the use of the panels for flow control rather than their use for flow sensing. For flow sensing, the feather-like panels need to be free to rotate in and out of the boundary layer to allow gusts to pass through the skeletal structure with minimal impedance. Using piezoelectric panel actuation, the panels are claimed to achieve enhanced

manoeuvrability for gust mitigation. Blower and Wickenheiser (2010) suggest that the concept of aero-braking will permit stable flight in elevated turbulence. Additionally, trajectory deviation is also expected to reduce considerably. The research is still in its early stages. Blower and Wickenheiser (2011) have explored the aerodynamic characteristics of the panels using numerical methods. Later papers by Blower et al. (2011); (2012) present results on the development of a dynamic model of the system.

This approach has yet to be validated by flight trials and seems to be better suited to larger unmanned aircraft due to the size constraints of MAVs. Furthermore, this sensing approach takes up valuable usable volume in the wings, which can be critical for storing energy (i.e. batteries or fuel). There are additional disadvantages associated with the complexity of the approach, its operation, control and robustness. Failure of one or more panels disrupting the lift distribution could lead to failure of the MAV. Finally, multiplexing, powering and commanding a panel array would be limited by the available processing and power resources on-board a MAV.

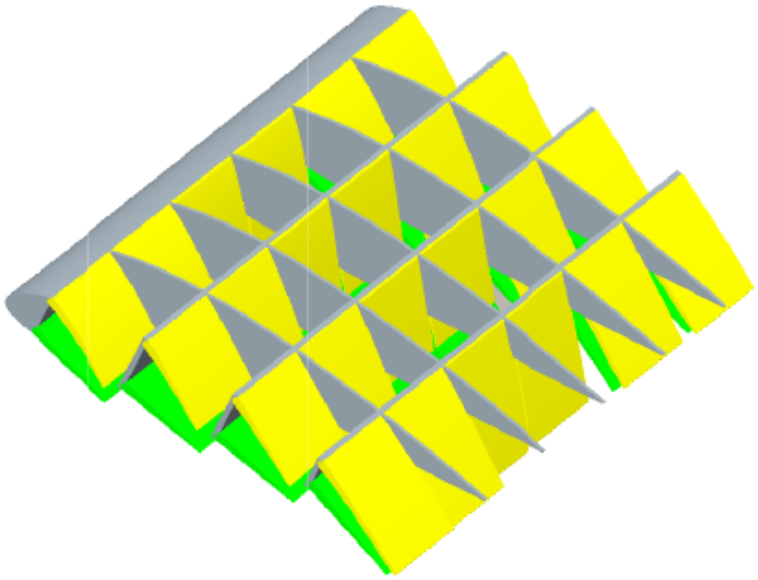

Figure 40: Gust alleviation system mimicking avian covert feathers (Blower and Wickenheiser, 2011)

A robust replication of the sensing function of a feather may be to implement surface-mounted pressure taps over the wing to sense the flow disturbances. The deformation of the sensor's membrane with variation in local pressure could be considered similar to the sensing by a feather, which deforms with flow instabilities. A pressure sensor could therefore be considered analogous to a feather and its receptor, see Figure 41. The membrane's vibration/deflection is typically measured by a change in capacitance or strain, which is conceptually similar to Herbst corpuscles. A description of the most common physical mechanisms employed by pressure transducers is outlined in Table 3.

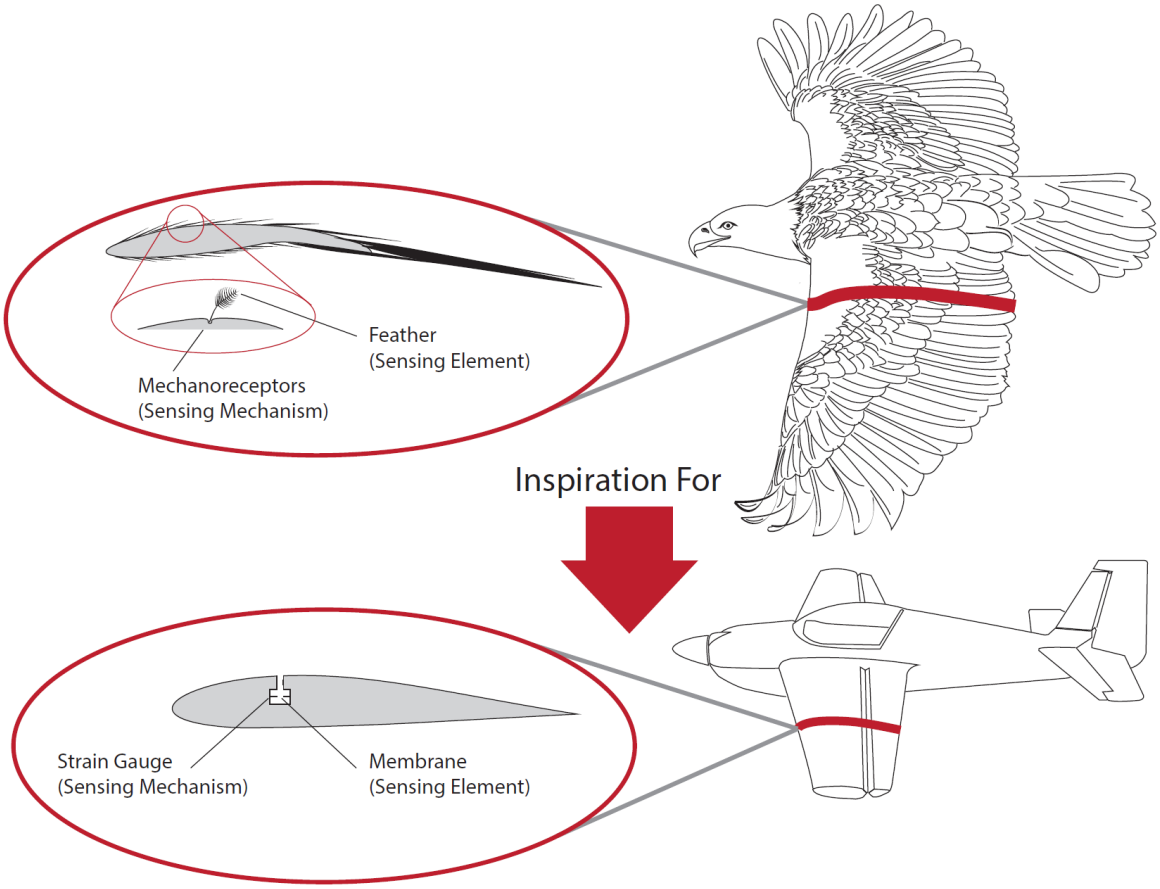

Figure 41: Bio-inspired pressure sensing for MAV attitude control

Table 3: Summary of pressure sensor types

Sensor Type	Description
Piezoresistive	Widely used due to simple fabrication. It takes advantage of the piezoelectric effect to measure the deformation of its piezo-membrane caused by pressure. This allows for dynamic detection of pressure fluctuations. Its resistors are usually configured in a Wheatstone bridge configuration for improved voltage output (McNamara and Gianchandani, 2011). These sensors generally suffer from reduced sensitivity and high temperature drift. Krause (2011) states that this sensor type is rarely feasible for measuring turbulent flow, although attempts have been made (Kälvesten, 1996).
Capacitive	The applied pressure is measured by detecting the strain, which is outputted as a capacitance between the membrane and an electrode underlying it. This type of sensor is greatly researched since it has improved temperature sensitivity, and dynamic range compared to its piezoresistive counterpart (Cho et al., 1990; Farooqui and Evans, 1987; Kung and Lee, 1992; Hin-Leung and Wise, 1988). The performance depends on various features of design. There are several design variants of the capacitive pressure sensor permitting improved sensitivity and dynamic range (Park and Gianchandani, 2003; Park and Gianchandani, 2000; Ming-Shuang et al., 2007; Akar et al., 2001; Yamamoto et al., 2002; Daigle et al., 2007). However, capacitive sensors inherently suffer from non-linearity along with high impedance (McNamara and Gianchandani, 2011; Krause, 2011) in addition to the external power required for operation. Packaging effects, and humidity are considered prime causes of performance reduction or even failures over lifetime (de Groot et al., 2011).
Optical	Typically, utilises an optical fiber, which uses a Fabry-Perot interferometer to detect deformations of a silicon membrane attached to its end. This typical approach has several advantages including reduced temperature sensitivity, high linearity, immunity to electromagnetic interference and capability of multiplexing. This sensor type is more suited for array implementations. The setback is the high cost and the use of complicated technologies, although an attempt of using simpler technology is published (Lia et al., 2010). There are also other variants studied (Abeysinghe et al., 2001; Chih-Wei et al., 2012; Reck et al., 2011).
Tunnelling	Implementations are either based on resonant tunnelling diodes (RTDs) which are sensitive to pressure (Mutamba et al., 1999; Fobelets et al., 1994), or the use of sharp tips near deformable membranes (Chingwen and Najafi, 1994). The latter requires a closed-loop system controlling the tip placement where the force required is the output.
Resonant	Operates by measuring the stress or the damping coefficient induced by a change in resonant frequency, which is caused by pressure (Greenwood, 1984; Petersen et al., 1991; Andrews et al., 1993; Welham et al., 1999; Burns et al., 1995; Melvas et al., 2001). For improved performance, the vibrating element is sealed in a vacuum to prevent gas damping. Although potentially this sensor has superior precision, it suffers from fabrication complexities, and consequently increased cost. Stiction can also be problematic.

Pressure sensors are largely employed by MAVs as velocity and/or barometric sensors along with an IMU for navigation. Recently Watkins and Melbourne (2003), drawing inspiration from the function of avian feathers, proposed the use of readily available pressure sensors as an input for MAV attitude control. The concept has been further explored by a number of researchers. Patel et al. (2007); (2009) explored the time response of pressure sensors for predicting leading edge flow separation, in order to trigger a plasma flow actuator. Cox et al. (2010) also used pressure-based sensing to approximate sectional lift to provide a feedback signal for automated flap control. (Barnwell, 2003; Lion, 2007) studied the effectiveness of a morphing wing type control strategy based on pressure feedback. Pressure-based feedback has also been utilised for guiding a small fixed wing UAV through a hover transition manoeuvre (Yeo et al., 2012). Other attempts involved

detecting leading edge flow separation, or predicting AoA using specially fabricated pressure or shear sensors, which were imbedded in the wing of a UAV (Xu et al., 2003; Callegari et al., 2006; Fei et al., 2007). More relevantly the feasibility of using the pressure signal from a few well-positioned pressure taps as a control input for MAVs was demonstrated numerically using simulations (Shen and Xu, 2013) and statistically using correlation studies (Marino et al., 2012). Finally, Guerreiro and Hubbard Jr (2008) explored the use of pressure information from a few selected positions on a model aircraft for lift distribution control.

This promising concept seems practical whereby it takes advantage of the miniature commercially available pressure transducers, which represents a mature sensing technology for measuring flow parameters. This reduces the costs and complexities significantly building on the available technology.

However, pressure sensing suffers from a few setbacks challenging its application in MAVs. Tubing may be necessary for wing embedment. The dynamic response of tubing is sometimes an issue and whilst dynamic calibration and correction (see Bergh and Tijdeman (1965)) is becoming increasingly commonplace, calibration of different lengths of tubing can introduce errors in the measurements. Since differential pressure transducers are usually used (as opposed to absolute, which are less sensitive) maintaining a reference pressure is problematic due to environmental drift, induced by temperature variation. Although surface embedment of MEMS pressure sensors can eliminate some of the setbacks associated with tubing, it comes at the cost of fabrication complexities. Embedding sensors into the wing is limited by the thickness of the MAVs airfoil.

2.2.1.2 Load Sensors

Load sensors can be used to measure the destabilising effects of flow disturbances on the flight vehicle. These sensors can be replicated using commercially available strain sensors such as strain gauges or piezo film. Such sensors can be utilised in wing load estimation of MAVs to potentially predict the vehicle's attitude. Apart from the numerical simulation conducted by Thompson et al. (2010) to identify the feasibility of the approach, the author is unaware of any experimental work conducted attempting to test this sensory approach for attitude control. The time-forward advantage of load sensing is less than flow sensing in accordance with the gust perturbation process. Load sensing can still complement a control system potentially improving attitude estimation; however it is not considered any further in this thesis.

2.3 Concluding Remarks

It has been shown that the time-lags in the gust perturbation process leads to ineffective disturbance rejection performance. Phase-advanced sensing offers a control system with the time advantage to cater for the time-lags, potentially eliminating perturbations completely. Bio-inspired phase-advanced sensing methods have been investigated where they often are complex, requiring custom development. Amongst the most feasible sensors for MAV attitude control are pressure sensors, which are readily available and may be easily adapted to replicate the sensing function of feathers. These sensors may offer enough time-forward advantage when placed on the leading edge of a MAV's wing. Research opportunities exist to test and identify the suitability of using pressure sensors as phase-advanced sensors for enhancing the attitude control performance of MAVs. Consequently, pressure sensors are selected for further experimentation in the remainder of this thesis to validate their adaption as bio-inspired phase-advanced sensors.

Chapter 3

Experimental Design, Setup, and Instrumentation

Summary

This chapter outlines the common experimental setup and instrumentation. Specific experimental setups used for the individual studies are detailed in the results chapters (4-7). The methodology for turbulence replication and testing used is outlined in this chapter. The measurement instrumentation experimental rigs used in experimentation are also detailed. This is followed by the MAV selection process along with details on its characteristics. Finally, data analysis methodologies are presented.

3.1 Experimental Overview

As detailed in the following chapters, experiments relating to the testing, and placement of a flow sensor used for the attitude control of MAVs are explored. The experiments are designed to answer the research questions identified in Chapter 1 as outlined in Table 1. Common experimental instrumentation and setups are outlined in this Chapter. Specific instruments and setups are further detailed in the respective experimental Chapters.

Table 4: Experimental plan

#	EXPERIMENT DETAILS	RESEARCH QUESTIONS	CHAPTER
1	Quantifying the correlation between velocity variations of the oncoming turbulence with wing surface pressure distribution	RQ 1.1	4
2	Quantifying the correlation between wing surface pressure distribution with perturbations in roll.	RQ 1.2	5
3	Quantifying the level of correlation between velocity variations of the oncoming turbulence with perturbations in roll	RQ 1.2 & RQ 1.3	5
4	Testing the performance of sensed velocity variations to improve the performance of the attitude control system through flight testing	RQ 1.3	5 & 6

3.2 MAV Selection

The presented research requires an airframe, which represents a typical fixed-wing MAV of conventional configuration (i.e. standard empennage). This section explores the characteristic parameters of MAVs, in an effort to aid the selection of a commercially available airframe to be used as a test-bed. The selected airframe and its subcomponents are discussed and specifications are outlined.

Mass and wingspan are defining parameters for MAVs. These parameters affect their transportability for which their reduction is a key quality, allowing rapid field deployment. Mueller (2007) categorised MAVs according to their wingspan and mass as shown in Figure 42. Conventional fixed-wing MAVs cannot hover nor flap, thus they are also bound by a minimum flight speed, which varies with wing loading, see Figure 43. According to Equation 9, which describes the relationship of wing loading and velocity, a reduction in wingspan and/or chord length translates to higher flight speeds. Lower mass leads to reduced velocities.

$$Velocity \propto \sqrt{\frac{Weight}{Wingspan \times Chord}} \tag{9}$$

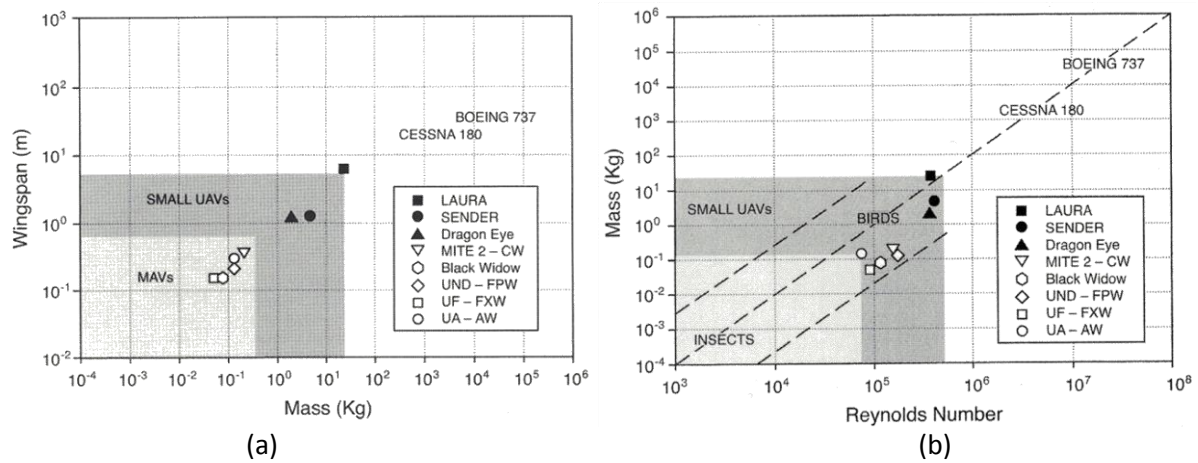

(a) (b)

Figure 42: (a) Wingspan versus mass for selected aerial vehicles (b) Reynolds number versus mass for selected aerial vehicles (Mueller, 2007).

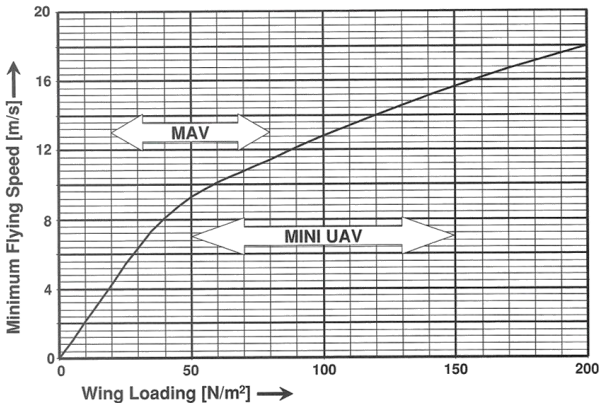

Figure 43: Variation of V_{min} with wing loading (Mueller, 2007)

In an effort to target a MAV group and outline wind-tunnel velocity boundaries, the plot illustrated in Figure 44 was created. This plot shows various relationships for a range of birds, insects, and fixed-wing aerial vehicles. The insects' velocities taken from Walker (1994); Johnson (1969), are mean flight speeds, while the birds' velocities represent cruise speeds taken from Tennekes (2009). A velocity range is depicted as a line for each fixed-wing MAV. The plots show that flapping insects are more relevant to flapping-wing Nano Air Vehicles (NAVs), while soaring and gliding birds are more relevant to fixed-wing MAVs. It is clear from these plots that although various characteristics of MAVs might somehow coincide with those of birds, they seem to be biased towards higher velocities owing to their propulsion system.

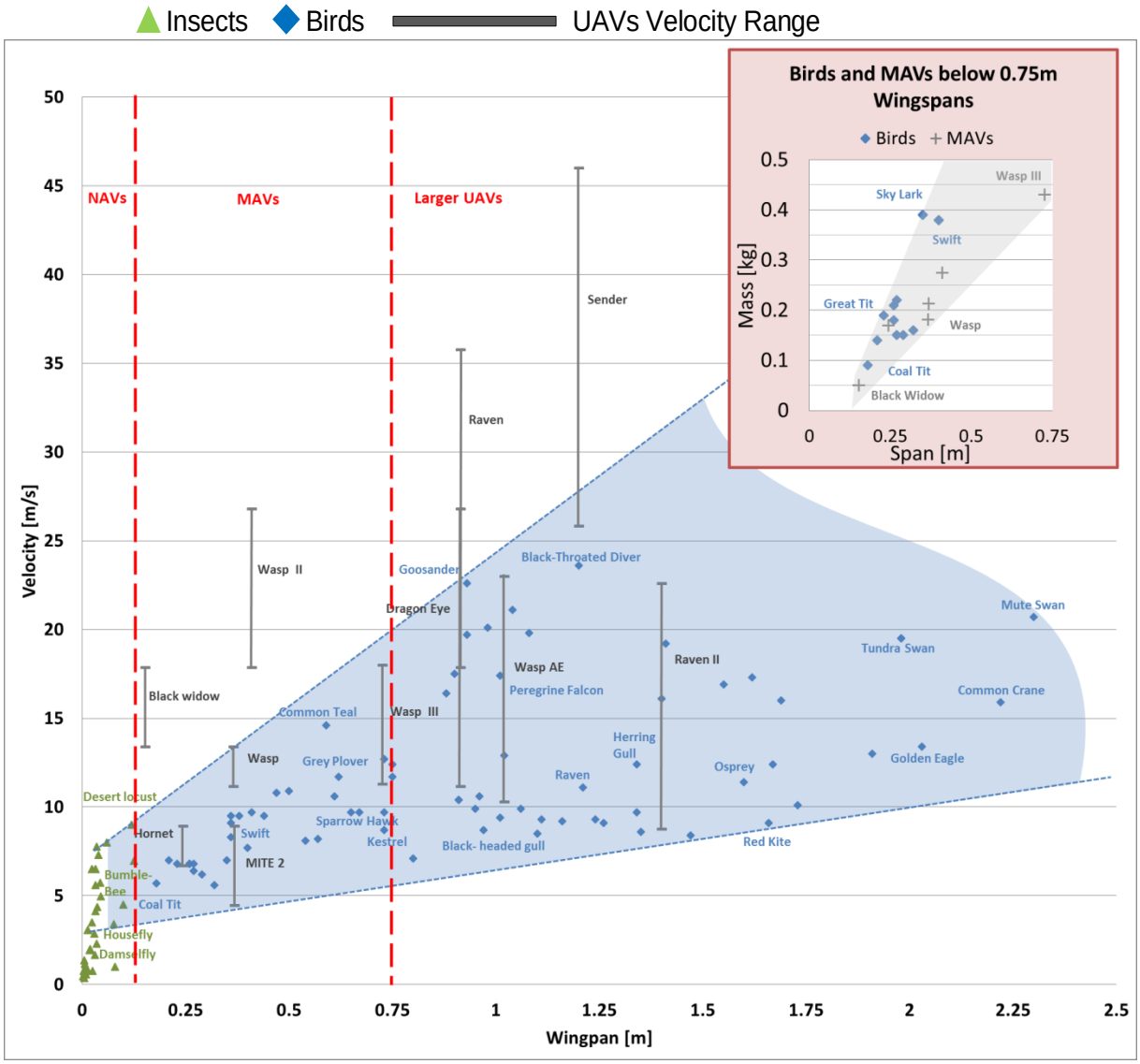

Figure 44: Velocity vs span for a multitude of flying animals and robots

3.2.1 MAV Specifications

In alignment with the discussion detailed in the previous section, a MAV with the following requirements was desired:

- **Wingspan < 500mm:** Represents the nominal size of current MAVs
- **Large control surfaces:** For increased control authority
- **Large internal fuselage spacing**: For equipment inclusion
- **Conventional configuration**: Delta wings would complicate the control architecture (due to elevons)

The requirements resulted in the selection of a commercially available micro-sized aerobatic model aircraft (see specifications in Table 5). The aircraft was electrically powered and based on the Slick 360 aerobatic aircraft (see Figure 45). The entire model was fabricated using a relatively rigid high-

density foam, which was particularly useful for sensor embedment. The all-foam wings of the aircraft were easily replaceable allowing different wing setups to be incorporated. Multiple standalone wings were purchased and modified according to the respective experiment. The wings were a tapered extrusion of a NACA0012 airfoil with no twist or dihedral. The large ailerons (>30% x/c) extended over the entire semi-span. Overall, the all-foam spar-less wing was sufficiently rigid. These features contributed to a neutral lateral stability (no passive stability inherent in its design such as dihedral, sweep, or twist). To check the vehicle's flight stability characteristics, the flight tests outlined below were conducted. These flight tests proved the suitability of the model for the represented research.

1. **Banking aircraft in roll**: This stick-free manoeuvre only requires a differential aileron deflection. No coupling was observed and the vehicle maintained the set bank angle. This manoeuvre only requires the input of rudder deflection. No obvious aileron/rudder coupling was evident.
2. **Yawing the aircraft:** This stick-free manoeuvre only requires a rudder deflection. No coupling with roll was observed due to the relatively large rudder surface below the aircraft's CG and thrust line. No obvious rudder/aileron coupling was evident.
3. **Pitching the aircraft**: This stick-free manoeuvre only requires an elevator deflection. The aircraft maintained a constant pitch angle.

Table 5: MAV specifications.

DESCRIPTION	DETAILS
Airfoil	NACA0012
Wing-span	0.490m
Fuselage length	0.421m
Average chord	0.0885m
Weight	130g
Cruise speed	10m/s
Aspect ratio	5.5

Figure 45: Representative MAV vehicle used in experimentation.

The ailerons of the selected MAV can be actuated separately through two independent servos. This feature is important to allow the ailerons to be controlled and deflected separately (i.e. uncoupled) if needed. As discussed in later chapters, two different control strategies were examined to investigate different aileron control modes in minimising the effects of turbulence. The ailerons have been actuated in a coupled (equal and opposite deflection) and uncoupled mode (ailerons can move independent from each other). The uncoupled deflection mode allowed the ailerons to act as flaps (i.e. flaperons), which counteract large upward or downward moving volumes of air (i.e. L larger than the wingspan).

Due to the large aileron size relative to the chord length, aileron deflections induced a phenomenon known as adverse yaw. The adverse yaw effect refers to the coupling evident between the roll and yaw axes. Adverse yaw is a secondary effect and occurs when the aileron deflections increase the profile and lift-induced drag of one wing relative to the other. In this work, adverse yaw has been observed during coupled and uncoupled aileron deflections. During a right rolling motion, the downward moving aileron on the port wing increases the airfoil's camber increasing profile drag. The lift component of the downward deflected port wing tilts the direction of the lift component towards the rear (aft), further increasing adverse yaw. As expected, the phenomenon is more apparent during large coupled aileron deflections (equal and opposite) as discussed in Section 6.3.1 (see Figure 46). However, the phenomenon is also expected to occur in mixed mode operation. As is discussed in Chapter 6, the adverse yaw effect was evident in the flight test results. Uncoupled ailerons can be used as flaperons, which involves the symmetric deflection of both ailerons in the same direction to replicate the function of flaps. This is particularly useful in countering large gusts which impart on both wings inducing heaving motion (see Figure 13a). Since turbulence is highly

three-dimensional, and random, the gusts which impart on the each wing are rarely identical in magnitude. Uncoupled ailerons are therefore useful to reduce overshooting whereby each aileron only needs to deflect enough to counteract the encountered gust.

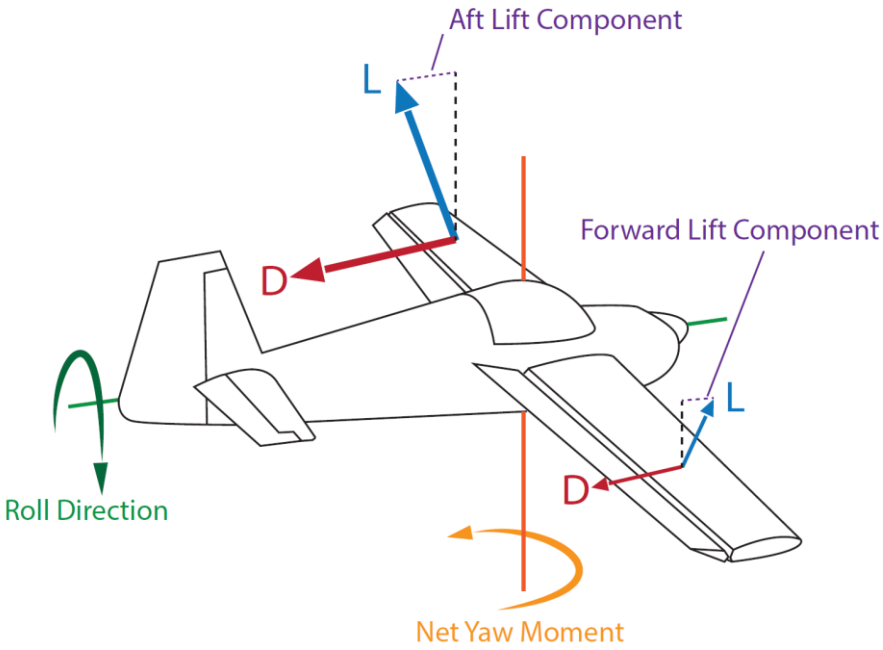

Figure 46: Adverse yaw coupling

3.2.2 Servo Actuators

For the presented research a large range of commercially available servos were surveyed (see Section 1.6). Fastest commercially available micro digital servos were used (see Figure 47). These servos can traverse 60° in 0.05s (for full specifications see Table 6). A frequency sweep function was created to cycle the servo arm between ±60° at a frequency band of 0.01-20Hz. The command input signal and servo's potentiometer output were sampled at 100Hz during the frequency sweep. The frequency response of the servos was estimated using Matlab and illustrated in Figure 48. Data analysis revealed that significant attenuation was evident at frequencies >10Hz. A coherence plot between command signal and servo output reveals that correlation degrades at frequencies >15Hz. The performance of the servos was repeatable as evident from testing a number of servos to the frequency sweep function detailed in Appendix A.

Figure 47: Micro digital servos.

Table 6: Servo specifications

SPECIFICATIONS @ 4.2V	DETAILS
Weight	1.9g
Max speed	0.05s / 60°
Max frequency	20Hz
Max torque	0.12kg
Dead band	<4µs

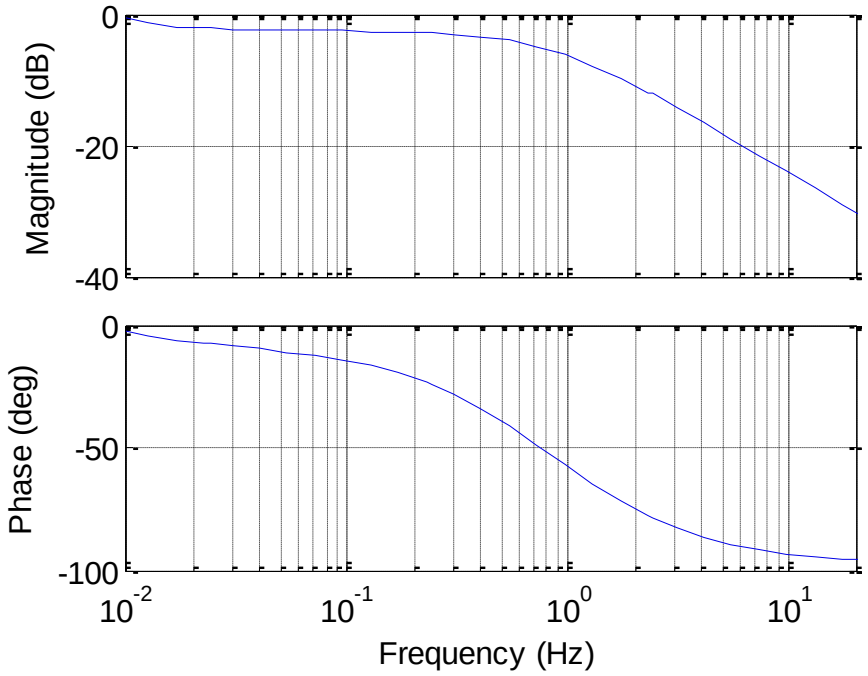

Figure 48: Frequency response of servo

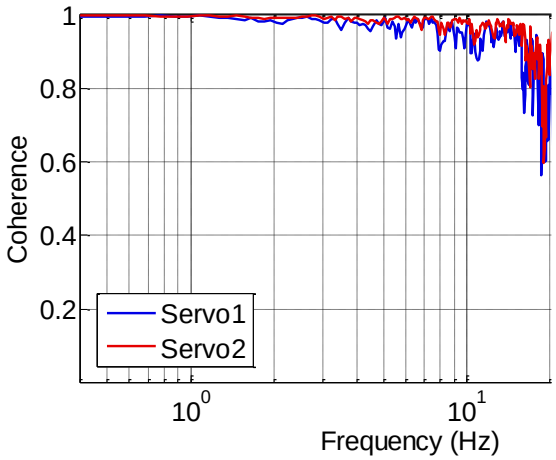

Figure 49: Servo coherence between servo command and servo movement for two parallel servos

3.3 Flow Measurement Instrumentation

3.3.1 Dynamic Pressure Measurement System (DPMS)

A multi-channel Dynamic Pressure Measurement System (DPMS) pressure transducer module (Figure 50), manufactured and calibrated by Turbulent Flow Instrumentation (TFI), was used to measure the pressure fluctuations over the airfoil surface for the correlation studies (Chapter 4 and Chapter 5). The module contained eight pressure transducers, which shared a common reference port. The transducers were located in the MAV's fuselage where the ports were connected to the wing surface through acrylic tubes. To measure wing surface-pressure variation, the tubes were cut flush with the surface (see Figure 51). To embed the tubes inside the all-foam wings, a cavity was created as shown in Figure 52. The wing was later structurally reinforced to cater for the cavity created. As tubes were of the same length, each tube maintains a similar dynamic response across the frequency range.

The DPMS was run by TFI proprietary software that contained the module's scaling factors. The software also allowed amplitude and phase response correction for the tubing system by utilising the Bergh and Tijdeman (1965) tube correction method. The correction method accounted for the dynamic response of the tubing system. A correction was generated by the software using user inputs for each test setup. The software applies the tubing response correction to the data-block size. This was done by transforming the analog data to the frequency domain using the Inverse Fourier Transform (IFT) method, in order to multiply it with the software generated amplitude and phase response, which was also in the frequency domain. The inverse Fourier transform of the result gave the amplitude and phase corrected pressures. Similar experiments using the DPMS experimentally validated the aforementioned correction method (Marino, 2013; Ravi, 2011; Vino, 2005).

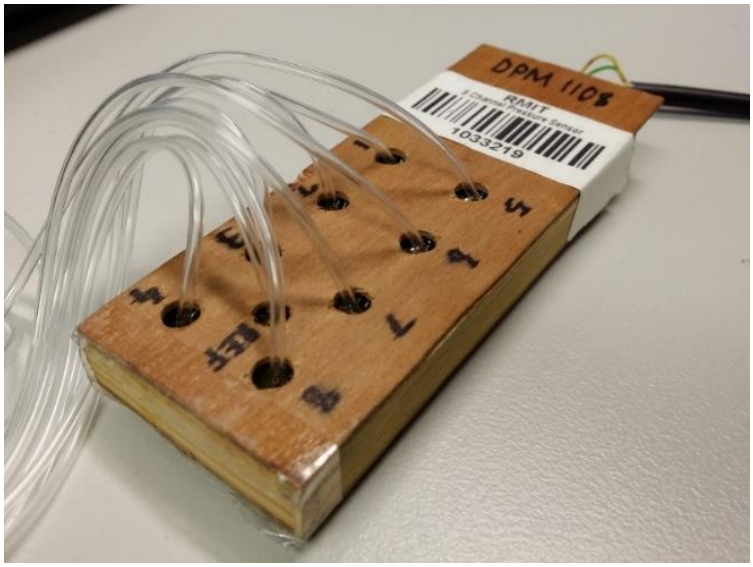

Figure 50: DPMS module with tubes connected. Light weight timber used for covering the sensitive electronics

Figure 51: Pressure taps embedment on the suction side wing surface

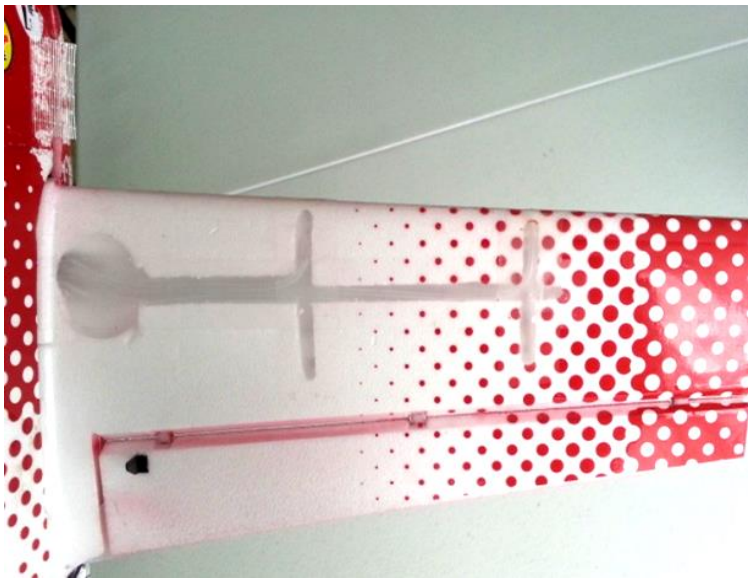

Figure 52: Acrylic tube embedment inside wing

3.3.2 Onboard MEMS Pressure Sensors

During airborne testing the MAV was equipped with four MEMS differential pressure sensors (Honeywell HSCDRRN010MDAA3) placed near the MAV's CG within the fuselage. These sensors provided a compact and portable substitute to the DPMS. The dynamic calibration device described by Fisher et al. (2012) was used to determining the frequency response of the system (see Figure 53). From Figure 53 the frequency response remains relatively flat beyond the frequencies of interest (100Hz). More specific setup details will be described for the corresponding experiments in the relevant chapter.

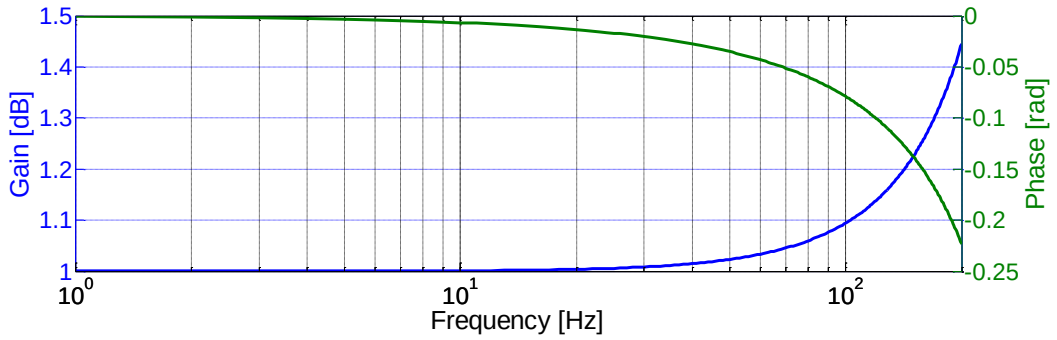

Figure 53: Frequency response of pressure sensor system

3.3.3 Cobra probes

Cobra probes, manufactured by TFI, are devices that are capable of measuring static pressure and velocities in three orthogonal directions. These were used for all of the time-varying velocity measurements made upstream of the wing's leading edge (See Chapter 4). All probes were calibrated at TFI and had a relatively flat dynamic response up to 2.5 kHz (Ravi, 2011). The time-resolved velocity measurements in three orthogonal directions were derived from the pressure variation across the four faces of a single Cobra probe (Figure 54a). Due to the varied orientation angle of the faces, each probe has a ±45^{o} cone of acceptance limit, outside of which the data was not recorded. Instances occurred when the flow direction was outside the cone of acceptance of the Cobra probes. Instances of such measures were removed from the experimental data sets and the number of data removals were limited to <0.05% of the entire sample length. Cobra probes were used because they are a more efficient measurement solution due to its enhanced robustness and simplicity compared with other turbulence measurement systems such as hot-wire or Laser-Doppler anemometry. These probes have been tested and validated in a variety of flow conditions e.g. (Chen et al., 2000; Hooper and Musgrove, 1997; Mousley et al., 1998). Hence, no further dynamic calibration or validation was conducted on the probes.

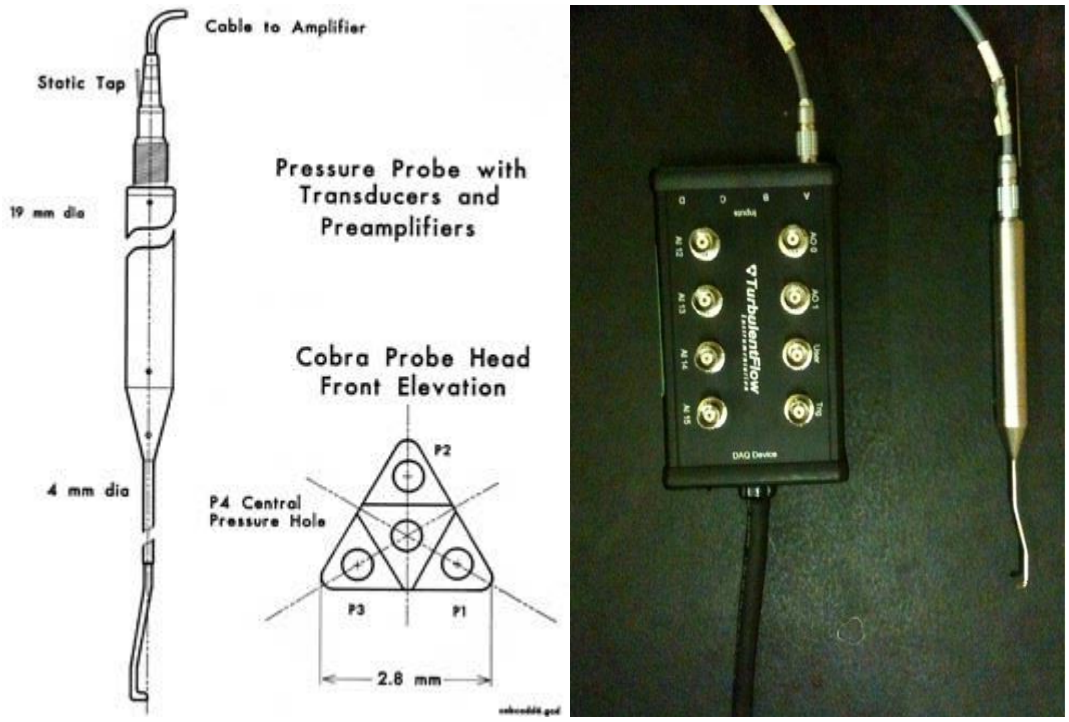

(a) (b)

Figure 54: (a) Cobra probe Schematic (b) Cobra probe connected to breakout box.

The Cobra probe was connected to a breakout box, which was connected to an A/D converter within a computer (Figure 54b). The probes can be operated simultaneously using the same A/D card. The Cobra probes used the same software as the DPMS, allowing simultaneous signals to be acquired from multiple Cobra probes and the DPMS. Measurements were collected at a rate of 2 KHz over a period of 300s. The experimental time of 300s was deemed sufficiently large to capture all the significant flow behaviour (Watkins, 1990; Thompson, 2013). It is also important to note that the measured flow advection rates were relatively slow with respect to the inter-channel-delay and associated phase-lag of the analog to digital converter in the DPMS. Note that Pagliarella (2009a) examines this in detail to find that the inter-channel-delay has insignificant impact on the acquired data.

3.1 Wind-Tunnel Properties and Setup

Wind-tunnels were used to provide a controlled and repeatable testing environment, namely RMIT's Industrial Wind Tunnel and Monash University Wind Tunnel. Utilising the methods detailed by Watkins (2012) and Watkins et al. (2013), the wind-tunnels were modified to generate different Ti and L_{xx}; providing a comprehensive range of experimental conditions for testing. The turbulence setup in the respective tunnels were previously characterised and detailed by Ravi (2011) and are summarised in Table 7.

Table 7: Wind-tunnel characteristics

SPECIFICATION	RMIT WIND TUNNEL	MONASH WIND TUNNEL
Test Section Type	Closed	Closed
Test Section Dimensions (w,h,l)	3m, 2m, 9m	12m, 4m, 30m
Turbulence Intensity, Ti	12.6%	7.8%
Longitudinal Length Scale, L_{xx}	0.31m	1.5m

As previously described in Section 1.4.2, flying through turbulence is different to hovering (no groundspeed) in turbulence. Relative Ti (experienced by a moving vehicle) is less than the statically measured Ti. In a city environment at 100m height the Ti is ~20% (see Figure 5). From the plots derived by Watkins et al. (2006) in Figure 7, it can be seen that the relative Ti at 10ms^{-1} (cruise velocity of the selected MAV) is ~7%. Marino et al. (2012) suggested that a 7% relative Ti represents the nominal turbulence experienced during flight in complex terrain such as urban environments.

Due to the finite length of the wind-tunnel test section, flying at a groundspeed >0ms^{-1} is not feasible. A practical approach was to match the MAV's airspeed with the airspeed inside the test section to maintain a groundspeed of 0ms^{-1} (hovering state relative to oncoming airflow). Turbulence generating grids where installed in the wind-tunnel test sections. The grids in the Monash Wind-Tunnel were selected to generate a Ti of 7.8% with a L_{xx} of 1.5m, which matched the relative turbulence expected in urban environments. The RMIT Wind Tunnel was used for further testing at higher Ti (12.6%) and length scales equivalent to the MAV's wingspan (0.31m). The following sub-sections detail the attributes of the wind-tunnels along with the properties of the turbulence generated.

3.1.1 RMIT Industrial Wind Tunnel

The RMIT Industrial Wind Tunnel was used for the constrained and unconstrained flight testing (see Chapter 6). The wind-tunnel has a closed jet configuration powered by a 225KW thyristor-controlled DC motor which is attached to a six blade impeller along with seven flow straightening vanes upstream the impeller (Ravi, 2011). The DC motor can generate a top speed of 50ms^{-1} in the test section, which is measured using a Pitot-static tube connected to a differential pressure measuring system. The tunnel's test section is 3m wide, 2m high, and 9m long, with a 2:1 contraction upstream. Very low acoustic noise is present in the test section due to the anechoic turning vanes installed (Vino, 2005; Pagliarella, 2009b). A schematic of the wind-tunnel is illustrated in Figure 55.

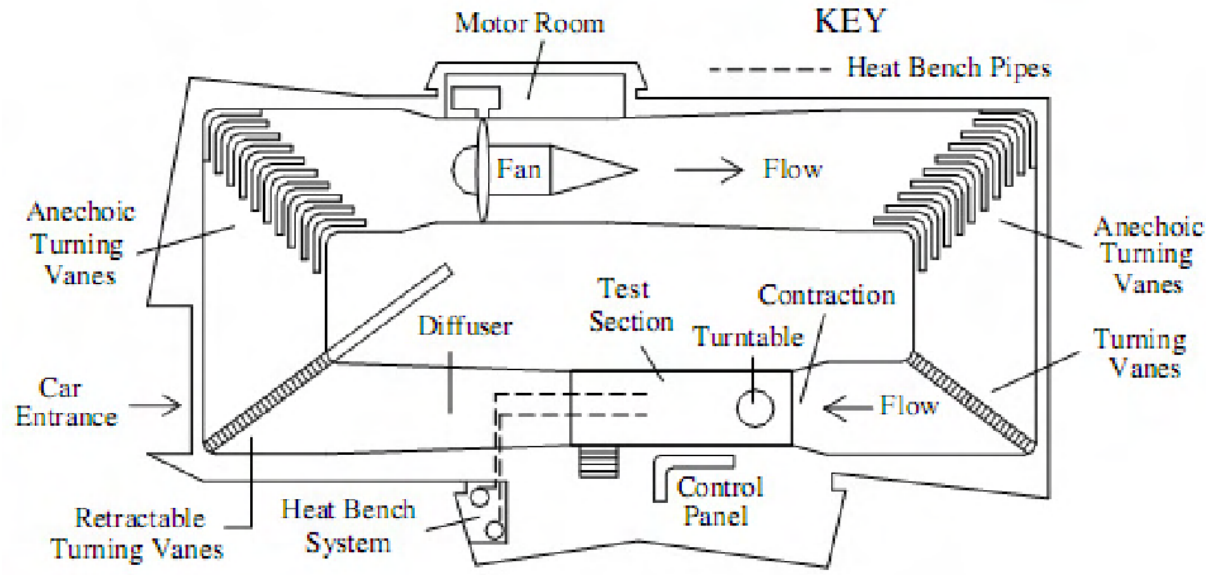

Figure 55: Schematic of RMIT's Wind Tunnel

Turbulence generation within the wind-tunnel relevant for road vehicles and MAVs was studied by several researchers (Watkins, 1990; Milbank et al., 2005; Cruz et al., 2007; Cruz et al., 2008; Ravi, 2011; Marino et al., 2012). Milbank's efforts represent one of the first attempts to generate turbulence levels relevant to MAVs. Grusovin (2006) and Cruz et al. (2008); (2007) successfully attempted similar methods to Milbank's efforts inside RMIT's Wind Tunnel. They used mesh grids of different widths at various locations to induce turbulence. By varying the spacing and size of the mesh grid, the turbulent properties (length scale and intensity) can be controlled.

The RMIT Wind Tunnel's clean configuration generates a Ti of 1.5% along the test section's centreline (Grusovin, 2006; Cruz et al., 2007; 2008). This intensity represents velocity fluctuations in all three orthogonal directions at various locations along the test section. Installation of planar grids at the test section inlet can increase this intensity to 12.6% at 7.75m downstream the grids. At this downstream distance, Grusovin (2006) found a relatively flat velocity profile and consistent turbulence profile, representing well mixed flow (see Figure 57). The disadvantage of grid-generated turbulence is the requirement for a sufficiently long downstream distance from the grid, allowing its induced wake to decay into well-mixed turbulence. Turbulence decay along the length of the test section is plotted in Figure 56. The maximum longitudinal length scale generated using this setup is 0.31m at 7.75m downstream, using the grids.

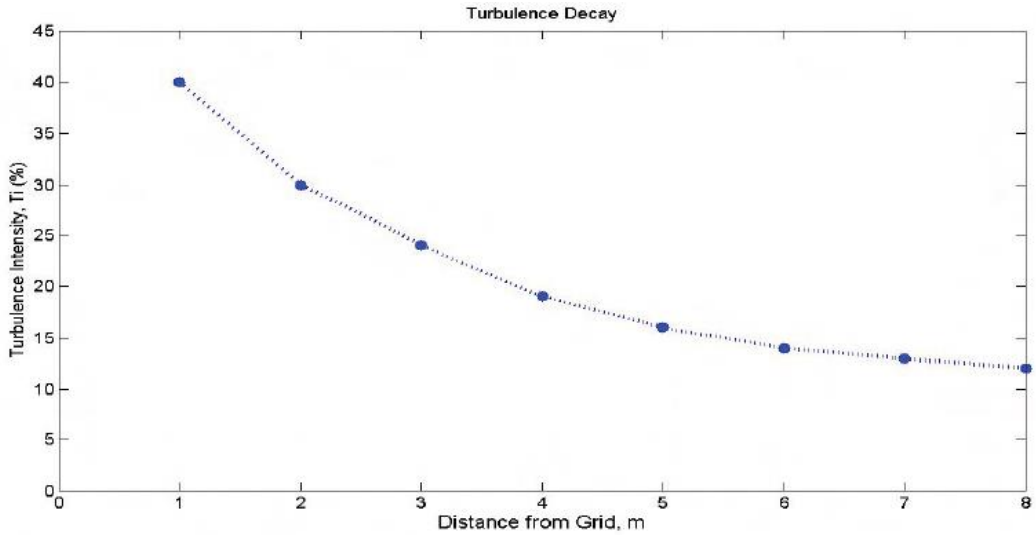

Figure 56: Ti measured at various points downstream of grids within test section (Ravi, 2011)

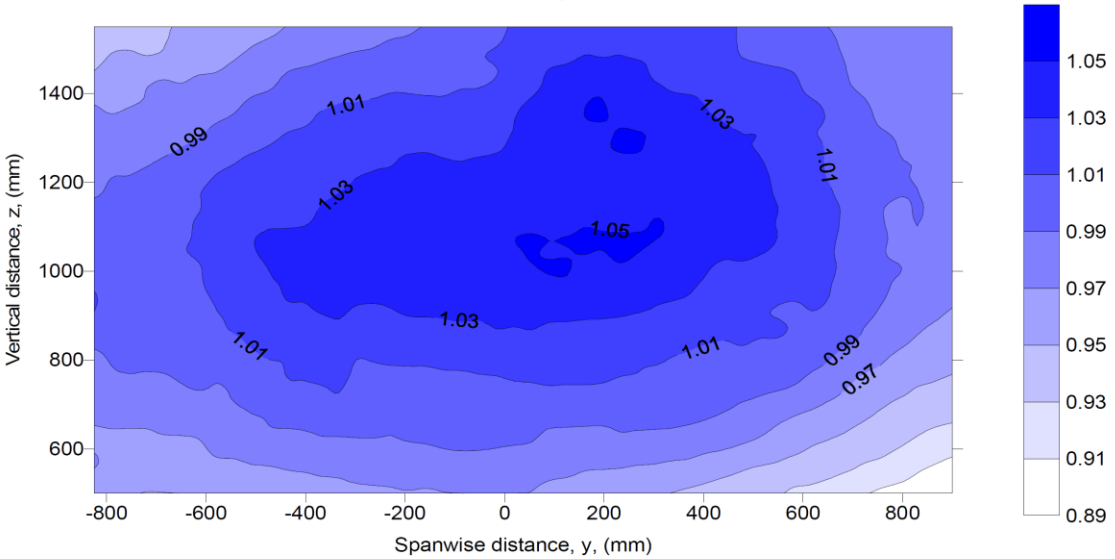

Figure 57: Normalised Freestream velocity distribution contour at 7.75m downstream from grids, (Grusovin, 2006)

Figure 58 shows the associated turbulence spectrum within the wind tunnel measured at a tunnel speed of 10 ms^{-1}. The turbulence spectrum follows the widely accepted -5/3 decay law, depicted as the dashed black line. To demonstrate how the spectrum within the wind tunnel compares with atmospheric turbulence, the atmospheric spectrum measured by Milbank et al. (2005) is presented as a dashed green line. The latter was also measured by Cobra probes installed on a moving vehicle with an Indicated Airspeed (IAS) of 10m/s (representative of MAV flight). The measurement was conducted in a densely populated area in the presence of moderate breeze winds (Beaufort wind force scale of 4). The atmospheric spectrum is included as an indication to a representative turbulence condition likely to be encountered by MAVs operating at low altitudes. It is important to note that higher wind speeds will result in an increase of energy across all frequencies (i.e. shift along y-axis as indicated by the green arrow in Figure 58). As can be seen from Figure 58, the wind-

tunnel cannot replicate the same turbulence energy at low frequency (≤2Hz). This was not considered to be detrimental as for MAVs the lower frequencies can be considered quasi-steady (Watkins et al., 2006).

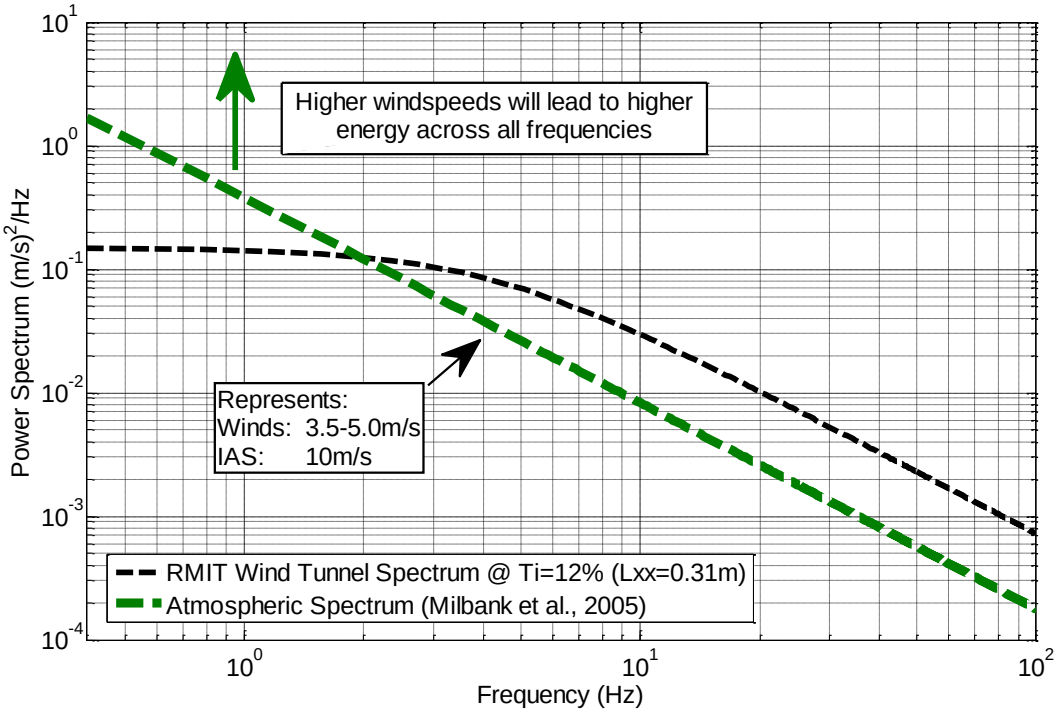

Figure 58: RMIT flow spectra showing exaggeration of high frequencies

3.1.2 Monash Wind Tunnel

The Monash Wind Tunnel (powered by two 1.5MW DC motors) consists of a wind engineering test section at the top level , an open jet test section, and a high Reynolds number closed jet test section on the lower level (see Figure 59). The wind engineering test section was used for unconstrained flight testing due to its large size (12m wide, 4m high and 30m long) and ability to generate large L_{xx}. The wind-engineering test section was configured to generate large scale turbulence by changing the screens and grids at the entrance of the section, combined with changes to the lower part of the tunnel. The test section was configured to generate a Ti of 7.8% in the wind engineering test section, with longitudinal length scales of up to 1.5m.

To allow for proper mixing of the generated turbulence, flight testing was conducted 21m from the test section inlet. A nominally flat velocity profile and Ti were measured near the centreline of the test section at 21m downstream (see Figure 60). The turbulence spectrum was measured at the test location and is illustrated in Figure 61.

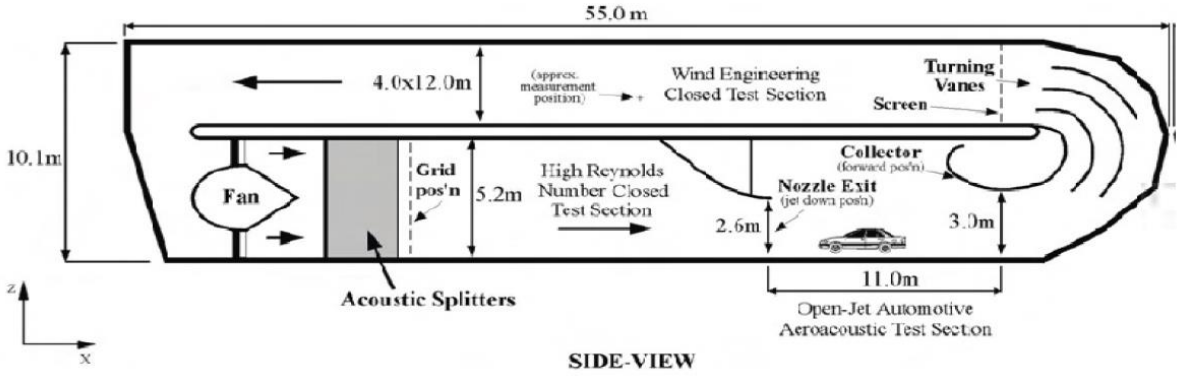

Figure 59: Monash wind tunnel side view

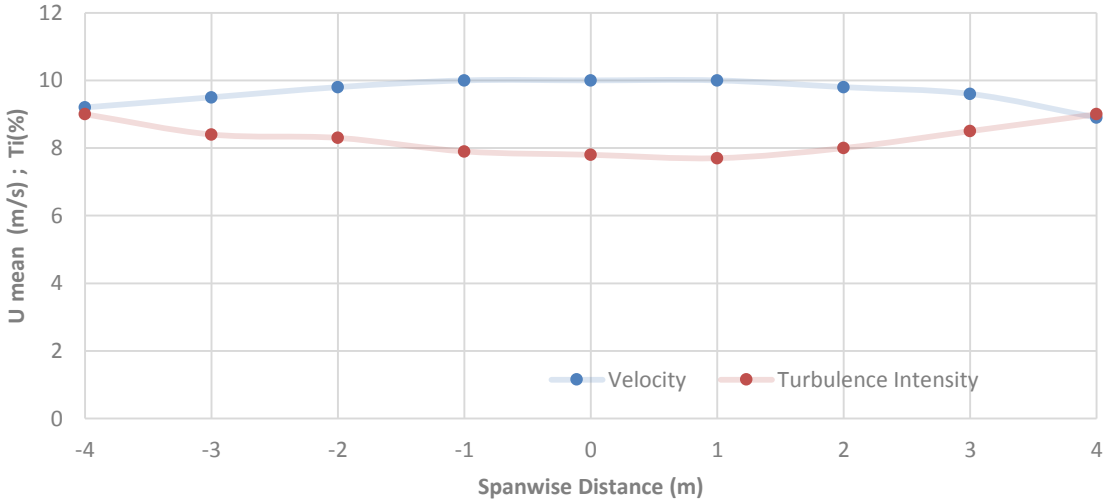

Figure 60: Velocity and Ti variation across the span of the Monash University Wind Tunnel test section.

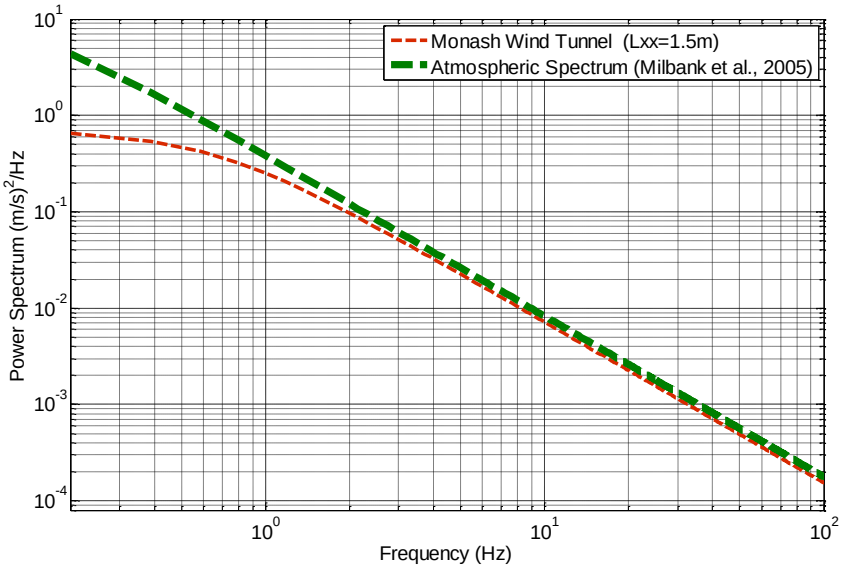

Figure 61: Monash Wind Tunnel flow spectrum compared with atmospheric spectrum.

3.2 Data Analysis

Experimental data were analysed using statistical techniques, which assume linear relationships. This analysis approach is a good starting point in the absence of other knowledge. The following subsections investigate mean and standard deviation of surface pressures to understand the flow behaviour over the wings. Correlation and coherence analysis are then described. The generally high correlation and coherence coefficients demonstrated throughout the results in Chapters 4 and 5, suggests that the statistics presented are sufficient for extracting useful information. The following subsections describe the techniques.

3.2.1 Mean and Standard Deviation of Surface Pressures

Wing surface-pressure distribution is most commonly presented as a Pressure coefficient (C_p) as shown in Equation 10 (Ravi, 2011; Marino, 2013; Marino et al., 2012). The *mean* freestream static (P_∞) and dynamic ($\bar{q}$) pressure were used to calculate *Cp*. This was done so that pressure fluctuations on the wing, which were of primary interest, were not obscured by fluctuations in the freestream velocity and static pressure. Mean and standard deviation were calculated according to standard formulas.

$$C_p = \frac{P - \overline{P_\infty}}{\bar{q}} \tag{10}$$

3.2.2 Correlation Analysis

To determine the degree of similarity between two varying time signals (*a, b*), a normalized cross-correlation function to quantify linear dependency. The normalized cross-correlation function, ρ(τ), was used to study the correlation of two signals as a function of time-lag τ, which corresponds to the phase difference at the point of maximum correlation. The expression illustrated in Equation 11 was used to compute cross-correlation. It is important to note that ρ(τ) was chosen, since similar studies have revealed linearity between upstream and downstream pressure coefficients on small wings under similar experimental conditions (Ravi, 2011; Marino, 2013).

$$\rho(\tau) = \frac{\overline{(a(t)-\bar{a})(b(t-\tau)-\bar{b})}}{\sigma(a)\sigma(b)} \tag{11}$$

3.2.3 Coherence

The degree of similarity of two signals (*a, b*) in the frequency domain was studied using Welch's averaged modified periodogram method to determine the magnitude squared coherence, *C*. Equation 12 was used to compute *C* as a function of frequency, *f,* where G_{ab} is the cross-spectral

density between *a* and *b* while G_{aa} and G_{bb} the auto spectral density of *a* and *b* respectively. Welch's method for coherence has been previously used in a similar context (Ravi, 2011).

$$C_{ab}(f) = \frac{|G_{ab}(f)|^2}{G_{aa}(f)G_{bb}(f)} \tag{12}$$

Chapter 4
Correlation Mapping of MAV Wing

Summary

This chapter answers RQ 1.1 through quantifying the correlation evident between the surface pressure fluctuations over the MAV's wing and oncoming turbulence. As hypothesised in the literature (Thompson et al., 2011a), oncoming flow pitch angle variation was found to be the most correlated feature of turbulence with surface pressure fluctuations. Through pressure tapping the wing, regions of strong correlation were identified to be the vicinity of the leading edge. The knowledge gained in this experiment is then used to provide qualitative insight for the experiment outlined in the subsequent chapters.

4.1 Introduction

The utility of flow sensors for MAV attitude control requires identification of the most significant inputs from turbulence to attitude perturbations. Furthermore, ideal sensor placement seems desirable for minimising the number of sensors required for effective attitude control. Areas over a MAV wing most responsive to oncoming turbulence have been identified through a series of experiments outlined in this chapter. This involved quantifying the correlation between surface pressure fluctuations measured over the wing's top surface and the oncoming velocity vector upstream the MAV's wings. Sensing the disturbances upstream assumed Taylor's Hypothesis (Taylor, 1938). The assumption is that the change in the turbulence structure is insignificant during advection since first detected upstream until it reaches the wing. The validity of Taylor's Hypothesis for atmospheric turbulence has been demonstrated for a range of length scales (Lappe and Davidson, 1963). Additionally, the high levels of correlation presented in this chapter imply validity over the (relatively) short distances between the upstream measurements and the MAV. The experiment outlined in this chapter is designed to answer RQ 1.1

4.2 Experimental Setup

Areas on the wing's upper surface, surmised to have the highest correlation with upstream turbulence, were pressure tapped. The instrumented MAV was then placed in the wind-tunnel, and supported at its CG by a variable AoA sting. Cobra probes were then placed in front of the wing to measure the oncoming velocity vector. Turbulence was generated through the use of planar grids installed at the tunnel's test section inlet. Chord-wise and span-wise correlation studies were conducted to identify regions of the wing with highest correlation to the oncoming turbulence. Figure 62 shows the experimental setup inside the test section of the wind-tunnel.

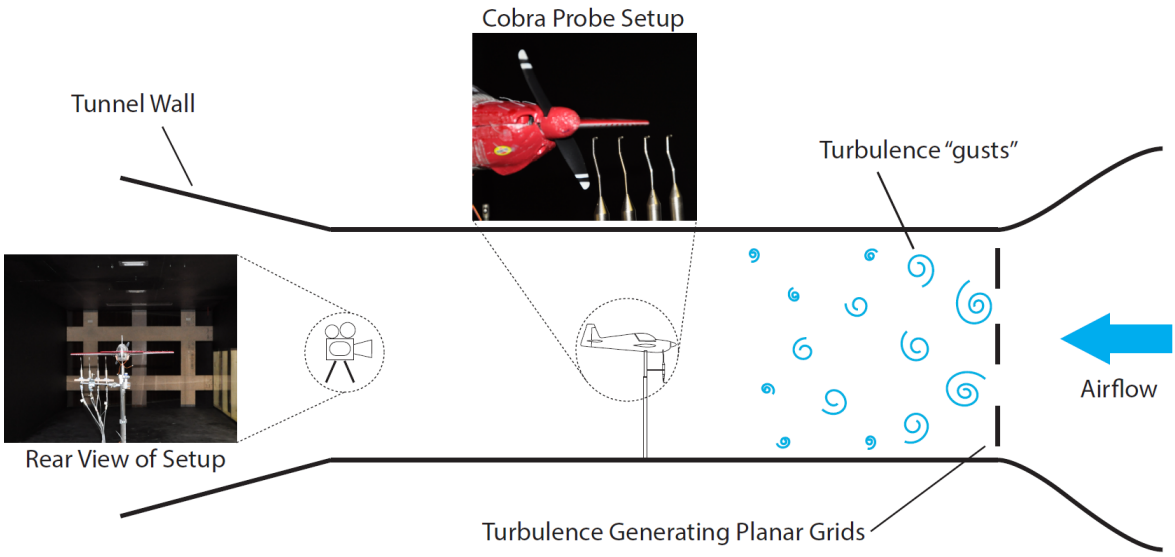

Figure 62: Wind-tunnel setup schematic.

4.2.1 Pressure Tap Placement

Two separate wings were used for internal embedment of the tubes; one for a chord-wise study and another for a span-wise study. For the chord-wise study, a total of seven pressure taps were arranged along the chord at two separate span-wise locations. The second wing (used for the span wise study) was instrumented with three rows of seven pressure taps distributed along the span at three different chord positions (Figure 63 shows the locations). The second wing was created since the two span-wise locations in the chord-wise study were insufficient to indicate the best-correlated tap along the span. Thus, a more detailed span-wise study was required. It is important to note that the pressure tap placement for the span-wise study was influenced by the results of the chord-wise study that indicated that the leading edge (i.e. taps 2 - 4 of Figure 63a) demonstrated high correlation, as will be discussed in the following sub-sections. The tap arrangements used in the chord-wise and span-wise studies are presented in Figure 63 and summarised in Table 8.

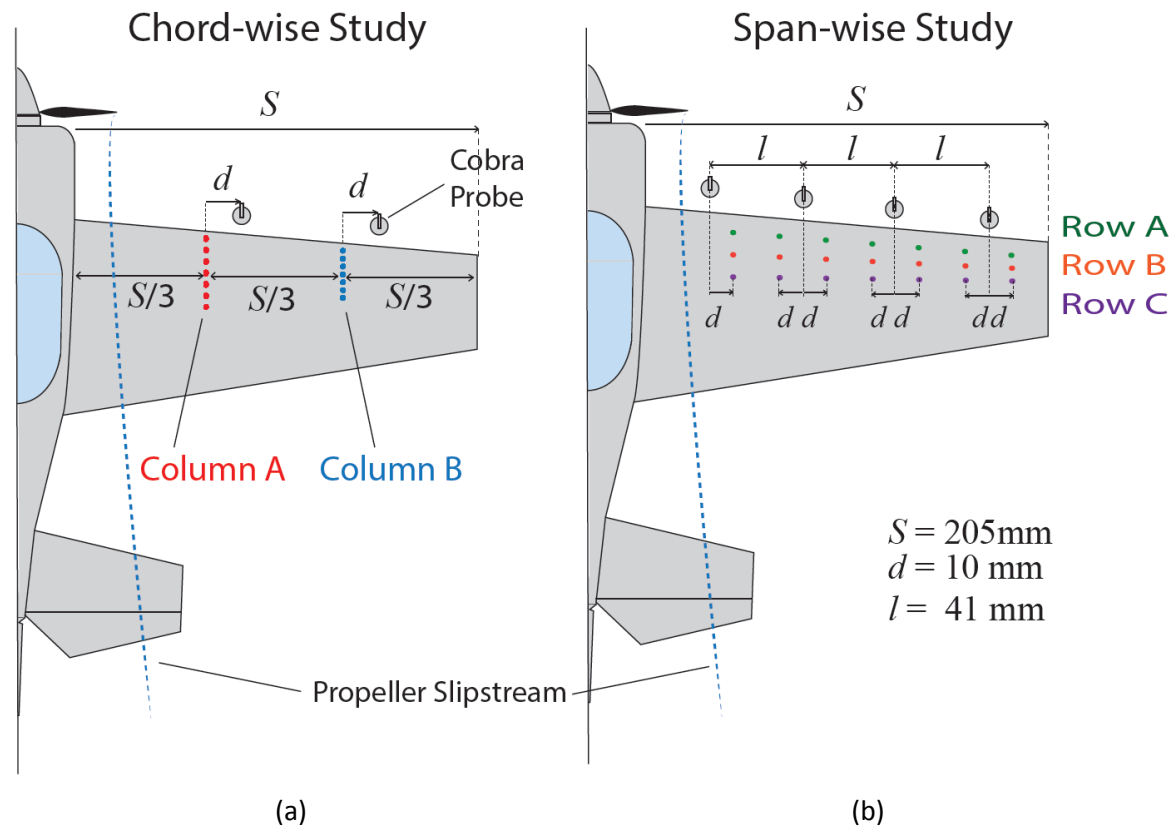

(a) (b)

Figure 63: Experimental setup illustrating the positioning of taps and Cobra probes (a) chord-wise study (b) span-wise study

Table 8: Pressure tap location for the chord-wise and span-wise studies

Pressure taps	Chord-wise Study (x/c)		Span-wise study (y/s)		
	Column A @ y/s= 33.3%	Column B @ y/s= 66.6%	Row A @ (x/c= 5.4%)	Row B @ (x/c=9.8%)	Row C @ (x/c=15.2%)
1	1.6%	1.6%	24.9%	24.9%	24.9%
2	5.4%	5.4%	35.1%	35.1%	35.1%
3	9.8%	9.8%	44.9%	44.9%	44.9%
4	15.2%	15.2%	55.1%	55.1%	55.1%
5	21.8%	21.8%	64.9%	64.9%	64.9%
6	29.4%	29.4%	75.1%	75.1%	75.1%
7	39.2%	39.2%	84.8%	84.8%	84.8%

4.2.2 Cobra Probe Positioning

To avoid flow interference from the probes' measuring heads impinging on the flow in the location of the taps, the Cobra probes were positioned 50mm upstream of the leading edge and 10mm lateral and vertical offset from the taps as shown in Figure 63 and Figure 64. To further minimise flow interference in the span-wise study due to the placement of the Cobra probes, two span-wise taps were correlated to the same Cobra Probe, which was positioned midway between the two taps, see Figure 63b. This technique reduced the number of probes used as shown in Figure 65. The spacing selected was deemed sufficiently large to prevent significant flow blockage. All experiments were conducted with a rotating propeller to account for the influence of the propellers wake. By experimenting with motor on and motor off configurations, it was concluded that the wake from the propeller and the vibrations of the system did not significantly influence any of the results.

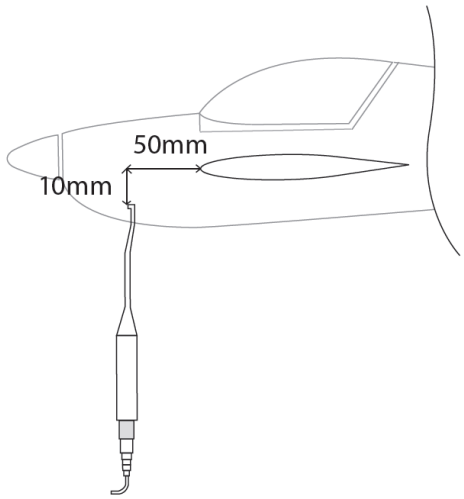

Figure 64: Positioning of Cobra probes relative to wing

Figure 65: Position and alignment of the four cobra probes in the span-wise correlation study wind-tunnel setup

4.2.3 Contour Plot Generation for Span-wise Study

The tap matrix of the span-wise study enabled the generation of contour plots (see Section 4.3) for enhanced visualisation of pressure statistics rather than simple curves. Due to the limited number of Cobra probes and pressure taps used, inferring that continuity exists between pressure tapped locations is inaccurate. The contours are only utilised as an alternative to presenting multiple curve plots, which may be confusing. Furthermore, the contours are skewed due to the taper of the wings as illustrated in Figure 66, however, for ease of representation, the results (see Figure 69 and Figure 70) have been corrected for this skew effect. The contour plots generated have been smoothed using the algorithm described in Appendix B.

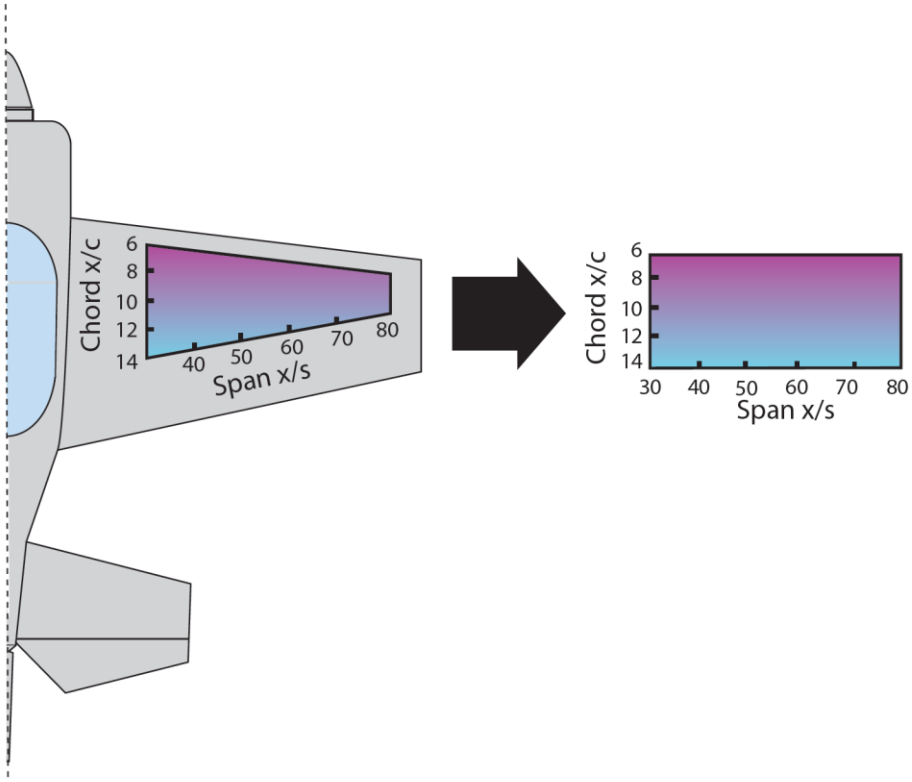

Figure 66: Spatial positioning of contours over the wing. The skewness of the contours caused by tapering of wing is removed for ease of representation.

4.2.4 DPMS Configuration

The DPMS module was installed near the aircraft's CG to minimise coupling between MAV vibration and the pressure transducers. Seven channels from the DPMS were assigned to measure the pressure from the respective taps relative to a reference port, which extended outside the wind-tunnel test section. Measurements were collected at a rate of 2 KHz over a period of 300s. The experimental time of 300s was deemed sufficiently large to capture all the significant flow behaviour (Watkins, 1990; Thompson, 2013).

4.3 Correlation Results and Discussion

Turbulence imposes significant variation in the Pressure Coefficient (*Cp*), as measured by the chord-wise pressure taps. Figure 67 shows this variation for a specific span-wise section. The top surface of the wings induced the greatest pressure variation as the flow was exposed to an unfavourable pressure gradient. Although the pressure surface of the wing did display some pressure variation, it was insignificant at incident angles greater than 0^o, relative to the suction surface due to the compressed nature of the flow in that region. Due to the random nature of oncoming turbulence, it cannot be assumed that the relative incidence angle (per unit span) of oncoming flow impinges the wing at the same incidence across the span. By this logic, it can be assumed that the flow angle relative to the wing is random in nature across the span and in turn will induce roll perturbations. As discussed in Chapter 1, previous research has theoretically identified flow pitch angle variation, in typical atmospheric turbulence, as the most detrimental for MAV attitude stability compared to the velocity magnitude variation (Thompson et al., 2011b). The experimental results presented agree qualitatively with the findings of Thompson et al. (2011b), whereby wing surface pressure fluctuations were found to correlate best with the pitch angle of the upstream flow, rather than with yaw flow angle or the overall velocity magnitude. The statistical results acquired from the chord-wise and span-wise studies are presented in Figure 68 to Figure 70.

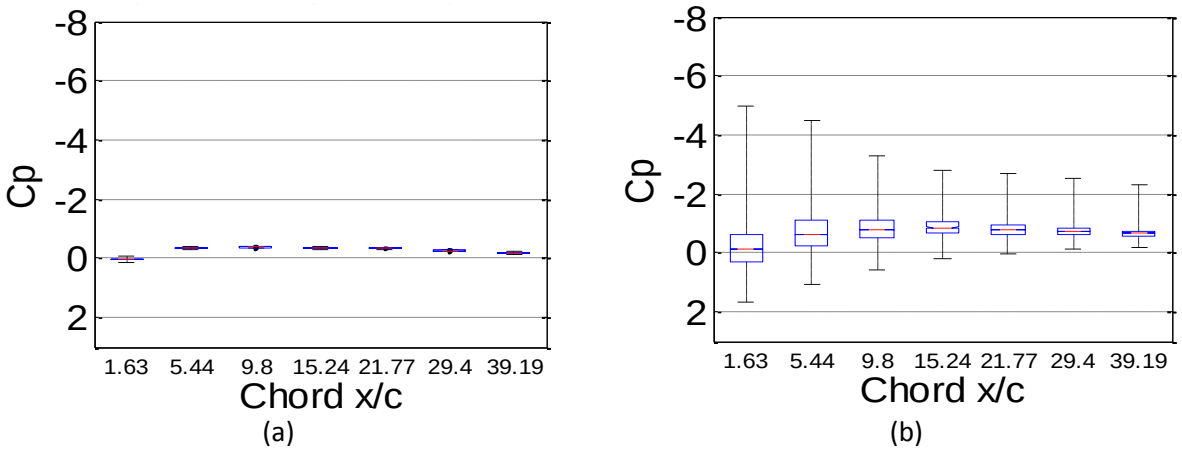

Figure 67: Cp variation measured over top surface of MAV wing (AoA = 0^o, x/s = 66.6%): (a) Ti =1.5% (b) Ti =12.6%

Inboard Taps *(x/s= 33.3%)*	Outboard Taps *(x/s= 66.6%)*

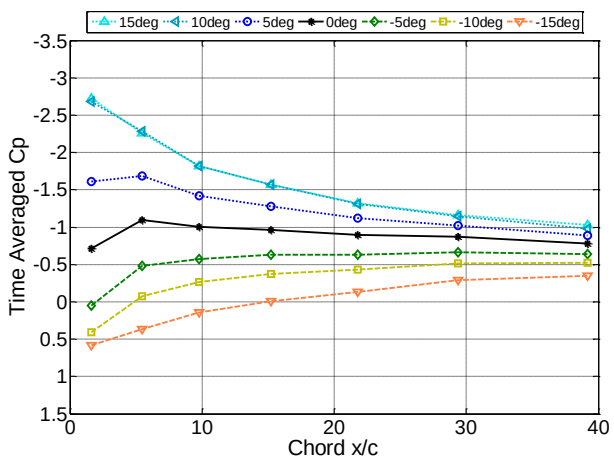

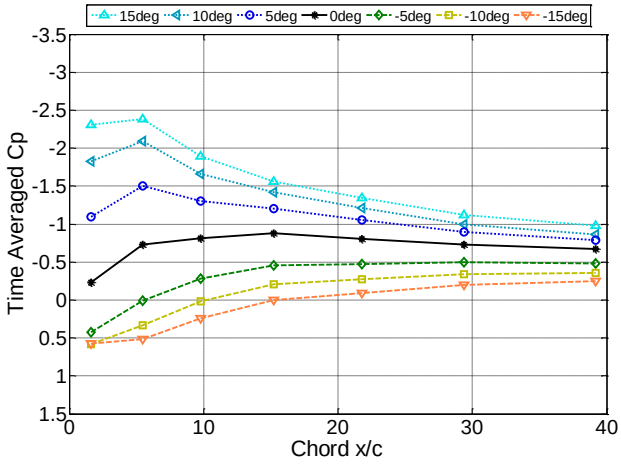

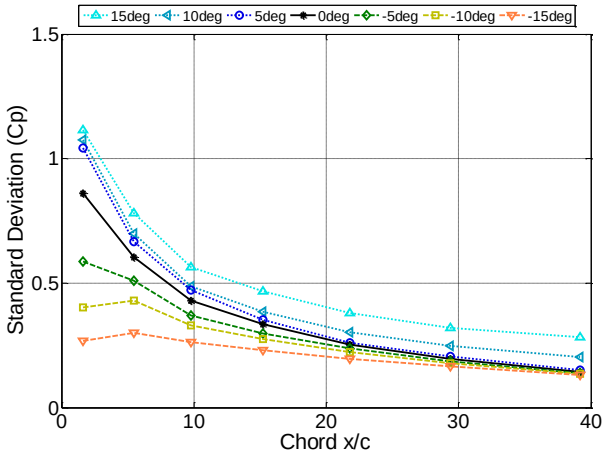

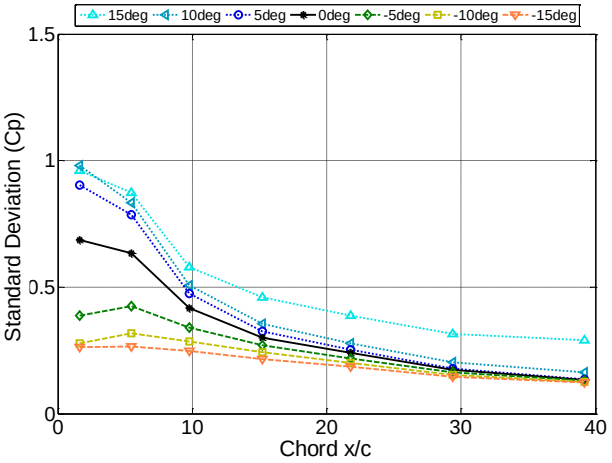

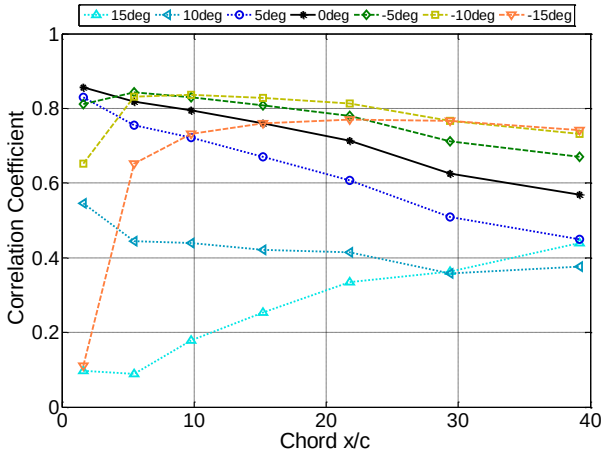

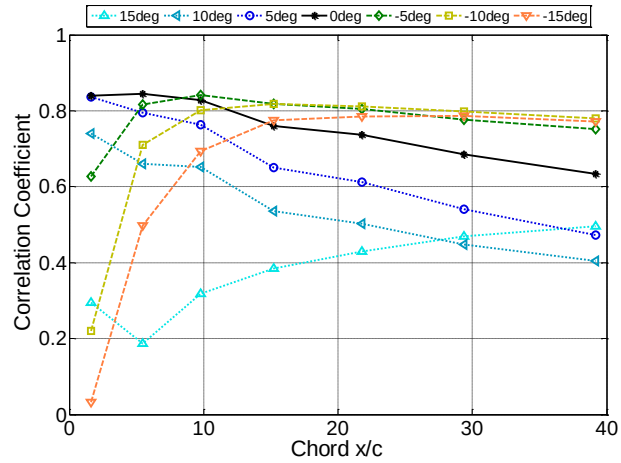

Figure 68: Chord-wise results

Time Averaged Cp Distribution	Standard Deviation (Cp)
AoA=15 º	AoA= 15 º
AoA=10 º	AoA= 10 º
AoA=5º	AoA= 5 º
AoA=0 º	AoA=0 º
AoA= -5 º	AoA= -5 º
AoA= -10 º	AoA=-10 º
AoA=-15 º	AoA=-15 º

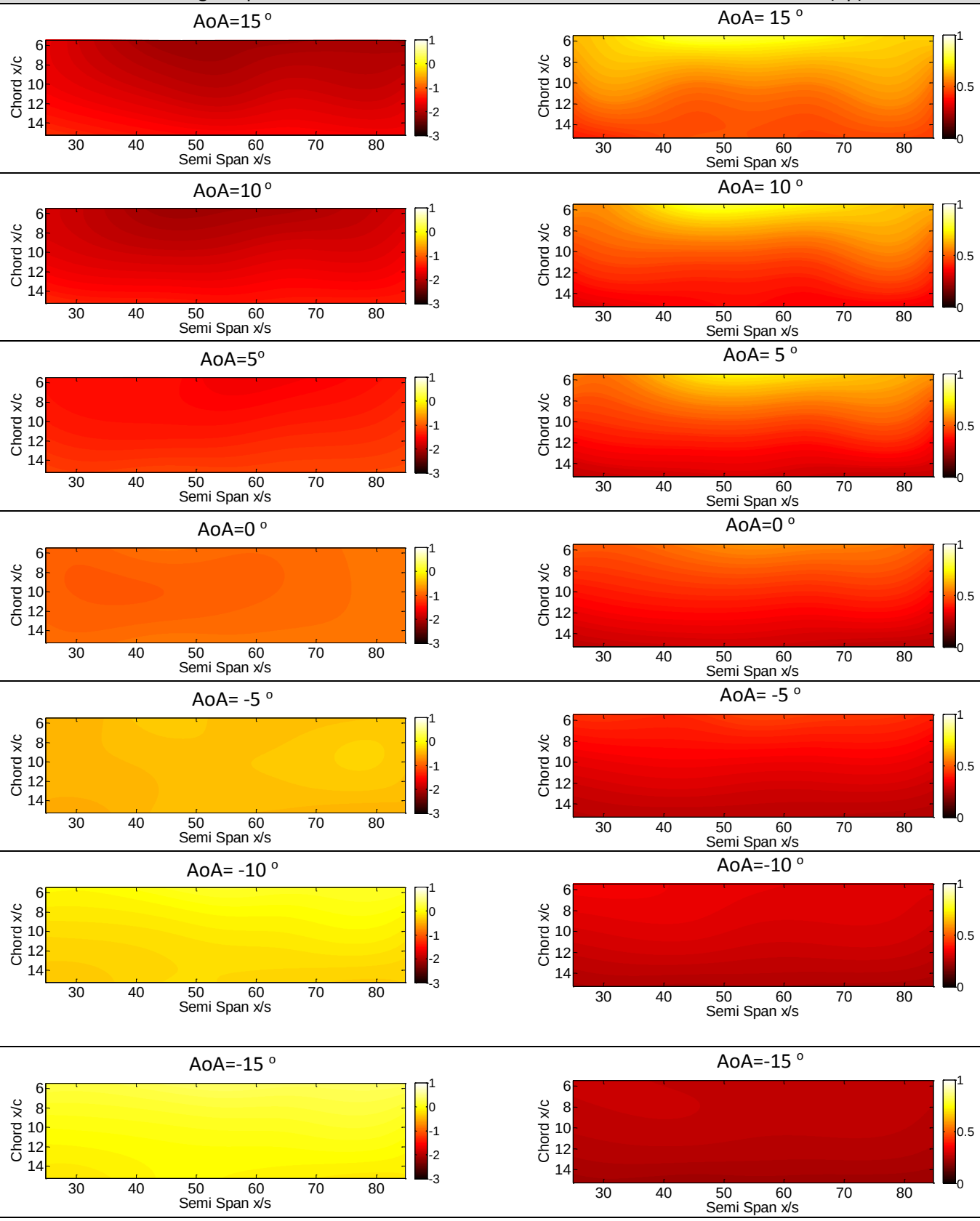

Figure 69: Time averaged pressure contours and standard deviation contours

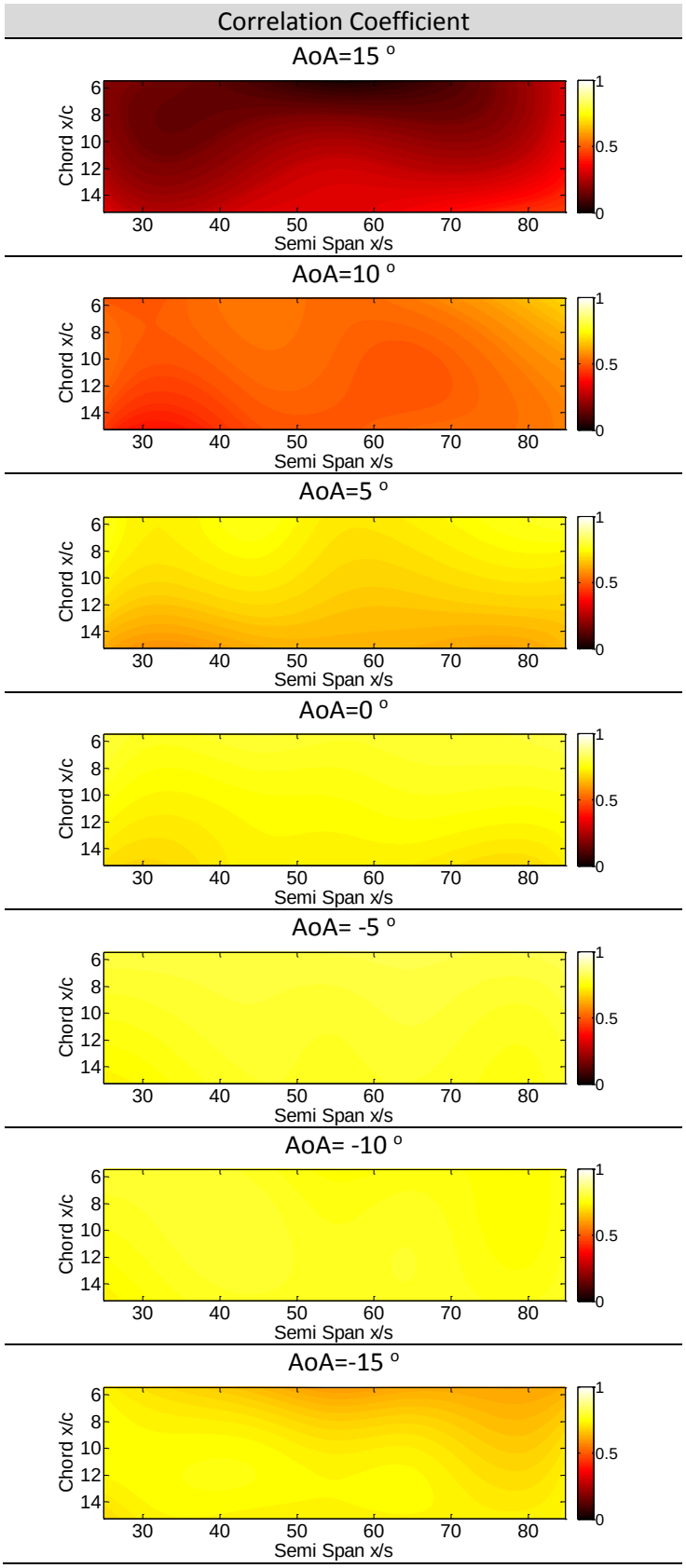

Figure 70: Correlation contours relating upstream flow pitch angle and wing surface pressure

4.3.1 Chord-wise Results

The mean and standard deviation of C_P were included in the results (Figure 68) mainly as an indicator of the correct flow behaviour over the airfoil, which were found to compare well with the time averaged data from Marino et al. (2012). As expected the pressure taps of column A measured lower C_P than those of column B, which is consistent with a quasi-elliptical span-wise lift distribution. The flight speed range for the selected MAV ranges from 5-10 ms^{-1}. As such, identical wind-tunnel tests were performed at 5ms^{-1} and 10ms^{-1}. All results displayed an insignificant variation with test velocity and implied a low sensitivity to Reynolds Number. Hence, only the results at 10ms^{-1} (Re ~ 60,000) are presented (see Figure 68 to Figure 70), which represent the approximate cruise velocity of the MAV.

Correlation reduces along the chord for moderately positive AoAs ($0^{o} < AoA < 10^{o}$) (see Figure 68). The correlation was at a maximum near the leading edge where the pressure fluctuations are highest, with a gradual correlation reduction as x/c increases. Increasing AoA also increases the rate at which the correlation reduces (Figure 68). The maximum AoA of 15^{o} represent a case where the flow was significantly detached from the wings suction surface. This can be clearly seen in the pressure coefficient profile in Figure 68 where the difference in suction pressure between 10^{o} and 15^{o} AoA was negligible and indicates the wing has stopped increasing lift production with increasing AoA. A gradual roll-off in lift at these Reynolds Numbers is normal and has been demonstrated in similar experiments using a flat plate airfoil (Loxton et al., 2009). The significant reduction in correlation, compared to lower AoAs, suggests that the flow mixing induced by flow separation dominates, with little correlation with the oncoming turbulent flow. Other studies have suggested that formation of vortical cores, which can form randomly across the span, contribute significantly to the reduction in correlation (Marino, 2013).

Unlike the suction surface, the pressure surface (negative AoAs) displays a significant correlation reduction at the leading edge of the wing, and an increasing correlation aft of the leading edge. This is primarily due to the influence of the fluctuating nature of the stagnation line in highly turbulent flow, with very rapid gradients in this area (i.e. the stagnation line). This can be seen clearly at AoA = -15^{o}. The correlation between oncoming flow and pressure taps has reduced significantly suggesting that the stagnation point was in close proximity to the pressure tap closest to the leading edge. Ideally, to achieve high correlation at the stagnation point, more pressure taps are required to sense the relatively smaller variation in pressure. As the AoA increases, the stagnation point moves away from the leading edge tap, subsequently the leading edge taps correlation increases

The airflow over the wing begins to separate at $AoA > 10^{o}$ with stall conditions evident with $AoA > 15^{o}$. Simple tuft visualisation confirms this finding and shows the progression of the stall along the

wing (Figure 71). At stall AoAs (10 ^{o} to 15 ^{o}), vortical core structure form at the leading edge. Vortical core structures can often form close to the leading edge and burst further downstream with the flow (Ravi, 2011). This phenomenon does not correlate with the upstream flow pitch angle explaining the drop in correlation near the leading edge (Figure 71). However, reattachment of the flow beyond the vortical core structure allows correlation to increase gradually. The presence of this phenomenon generally reduces the correlation along the entire chord preventing correlation unity, as it was a local and dominant flow formation aft of the leading edge and in turn was isolated from the Cobra Probes. This is illustrated in Figure 72, showing small vortical cores aft of the leading edge. The formation and bursting of vortical cores has been previously shown to be unsteady in nature and occurs at random time intervals as it is reliant on the vertical oncoming flow vector (Marino, 2013; Ravi, 2011).

In general, for moderately positive and negative AoAs (-10°< AoA <10°), the correlation near the leading edge (taps 2 – 4) was reasonable (>0.6). However, at stall AoAs the flow in the vicinity of the leading edge was dominated by non-linear flow phenomena whereby the associated taps had reduced correlation. Applications requiring aggressive manoeuvres (such as the transition to hover perching presented by (Yeo et al., 2012)) may benefit from taps placed away from the leading edge to avoid non-linear phenomenon.

Figure 71: Flow visualisation at 5^{o} AoA showing stall progression.

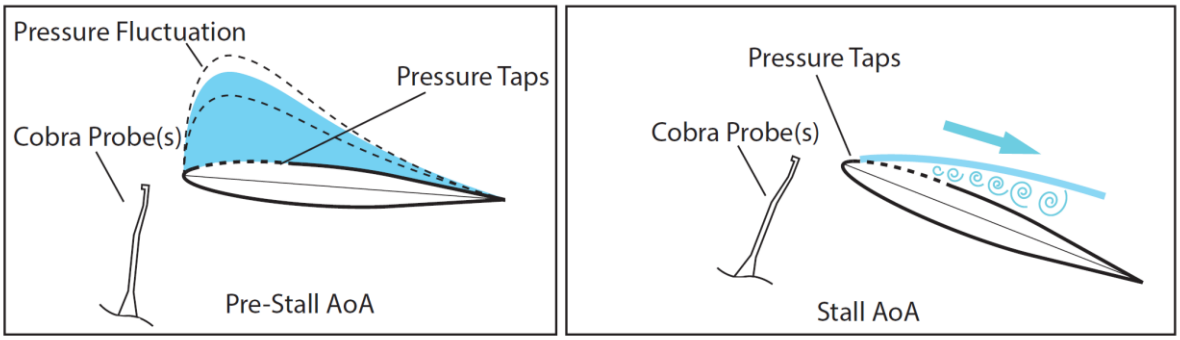

Figure 72: Correlation reduction due to non-linear flow phenomenon post-stall.

4.3.2 Span-wise Result Discussion

The chord-wise study only considered two span-wise locations, which are insufficient for identifying the best span-wise location for tap placement. The results from the span-wise study therefore aid this decision. The results from the three span-wise rows were therefore presented in Figure 69 and Figure 70.

Correlation seems to follow the trend of the stall progression behaviour, whereby most of the tested AoAs (-10°< AoA <5°) experience high correlation along the entire measured surface. Tuft visualisation revealed that the wings started to stall near the trailing edge with a bias towards the fuselage and the stall progressed outboard at higher AoA (see Figure 71). Note that beyond 10^{o}, almost the entire measured surface experiences significant reduction in correlation. Due to the significant separation dominating in this region, at -15^{o}, correlation degrades towards the wingtips. This reduction is thought to be due to the wingtip vortices, which induce a net movement of the flow outboard towards the wingtips (see Figure 73). Due to the misalignment of the flow coming from the Cobra probes towards the taps, the leading edge does not correlate well with the nearest Cobra probe. Taps further away from leading edge experience higher correlation due to the relatively better alignment of the taps with the Cobra probes.

It is concluded that the wing's surface pressure correlation to upstream turbulence strongly matches the flow conditions as being either attached or separated over the wing surface. Correlation along the span and chord was thus dependent on the flow condition. It was therefore sensible to avoid placing taps in areas where the flow was expected to separate.

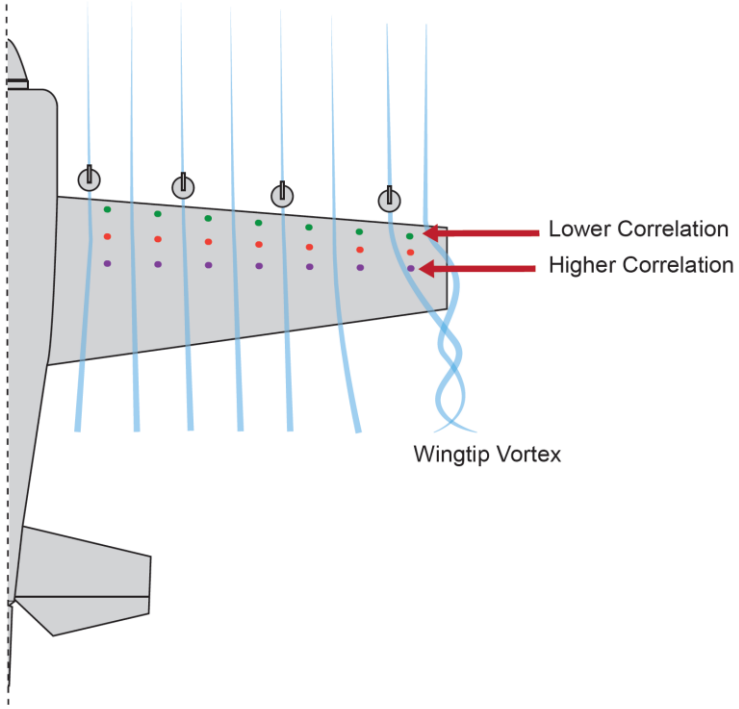

Figure 73: Influence of wingtip vortex on correlation of outboard taps.

4.4 Error Consideration

The correlation results are influenced by the wake of the Cobra probes' heads, which improves correlation over some taps and degrades correlation over others, as illustrated by the minor variation in correlation over the tapped area (Figure 70). The variations visible in the contours are due to the small step size of the colour map used. However, the correlation coefficient variation was relatively small (±0.1). The head size of the Cobra probes was 3mm and the distance to the wing leading edge was 50mm (16.7 characteristic head dimensions). Thus, there would be some very small scale and low intensity turbulence generated from coherent vortex shedding from the small, but relatively bluff Cobra probe head and arm. This was considered negligible, as the grid-generated turbulence would dominate the flow (see Figure 67). To further validate this, C_P and its variation were measured with and without the presence of the Cobra probes upstream. The Cobra probes' upstream distance was also varied ahead of the wing where it was found that its presence did not significantly influence the surface pressures (see Figure 74). All the generated contours, with and without the Cobra probes upstream, also gave closely similar results. The same experiment was conducted in smooth flow, however, due to the insignificant presence of flow pitch angle variations in smooth flow, the contour plots (as expected) showed negligible correlation, thus were not included. Aside from optical methods (e.g. PIV), measuring the flow pitch angle ahead of the wing will involve instrumentation of finite volume and mass which will always introduce interference. However, minimising such interference through the described experimental setup allows key conclusions to be drawn.

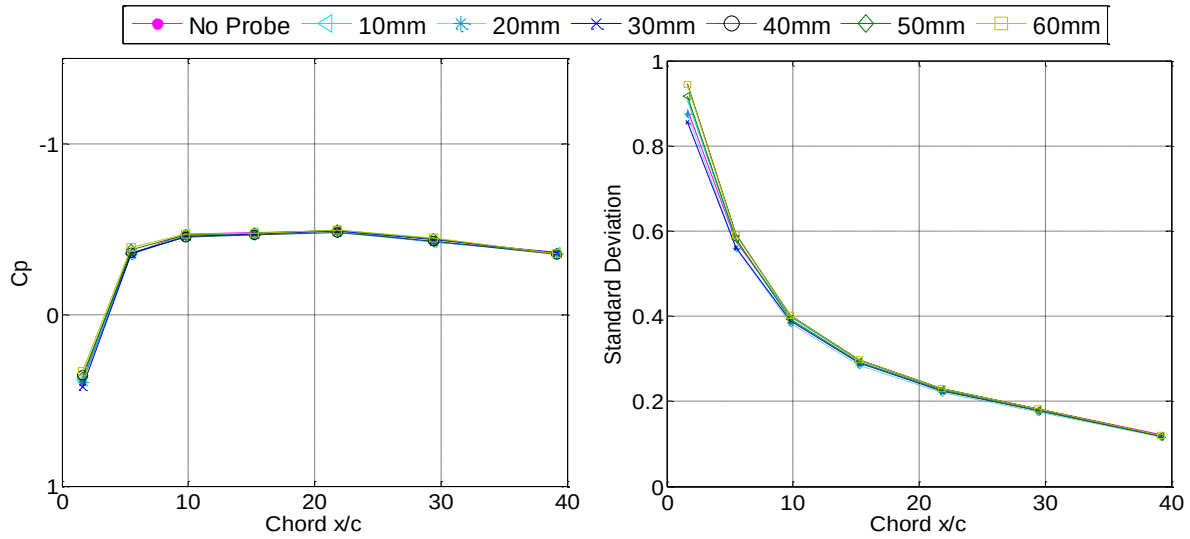

Figure 74: Sensitivity of *Cp* to different Cobra probe positions upstream of the wing (AoA = 0°, V = 10ms^{-1}, Ti = 12.6%, L_{xx} = 0.31m)

To improve the confidence in the presented results, errors in the reported pressure results were estimated by repeating selected wind-tunnel runs. These repeats were done over a long time span so that fluctuating environmental conditions were taken into account. In between repeats, the rig was un-installed/re-installed in the wind-tunnel, the tunnel speed reset, and AoA re-measured and reset. Thus, the influence of all of these factors would show up as precision errors rather than bias errors. Bias errors are likely to occur from temperature variation, which is accounted for in the calibration of the sensors, which were routinely conducted for each test. Appendix A shows the repeatability error bars for a selected column of pressure taps in smooth and turbulent flow, and were found to be acceptable.

4.5 Conclusion and Recommendations

The objective of the study presented in this chapter was to experimentally identify the most significant feature of turbulence, which correlated with surface pressure fluctuations (addressing RQ 1.1). The dynamic flow pitch angles of the oncoming velocity were found to attain the highest correlation to the wing surface-pressure fluctuations, rather than with yaw flow angle or the overall velocity magnitude. It was found that the pressure distribution in the vicinity of the leading edge attained the highest correlation to the oncoming flow pitch angle variation. Flow separation at steep AoAs, was found to degrade correlation significantly since non-linear phenomena dominated the flow. The aforementioned findings from this chapter have only considered a MAV constrained relative to the tunnel floor. The next chapter considers freeing the most sensitive axis to turbulence (roll) to study the correlation evident between turbulence and perturbations in roll.

Chapter 5

Turbulence and its Effects on Roll Perturbations

Summary

This chapter is divided into three main sections. The first section addresses RQ 1.2 through quantifying the degree of correlation and coherence evident between the wing load imbalance (i.e. surface pressure difference between port and starboard wings) and the perturbation in roll. Strong regions of correlation were evident in certain regions of the wing. However, the time-forward advantage between the correlated parameters was found to be insufficiently small. To account for the limited time-forward advantage of surface pressure sensing, the second section of this chapter explores the use of multi-hole pressure-based probes, which extend from the wing into the flow. These specially developed probes allowing sufficient time-forward pressure data to be acquired, catering for the time-lags inherent in a control system. The third and final section addresses RQ 1.3 through using the output of the probe as a dynamic control input by a micro-controller to test the attitude disturbance rejection performance relative to conventional inertial based attitude control systems. Experiments in this chapter were conducted through the aid of a specially designed roll-axis rig, which constrained the motion of the MAV to the roll axis. Error considerations have been outlined for the individual experiments and are further detailed in Appendix A.

5.1 The Correlation of Wing Loading Imbalance with Perturbations

The correlation study discussed in the previous chapter (i.e. using the fixed sting) has shown that surface pressure fluctuations correlated reasonably well to the upstream flow pitch angle variation for pre-stall AoAs. A higher fidelity study is discussed in this chapter exploring the correlation between the surface pressure imbalance (i.e. between port and starboard wings) and the roll acceleration. This study involved dynamic testing through utilisation of a roll-axis rig.

5.1.1 Roll-Axis Rig

A variable AoA roll rig was developed to constrain the perturbation (response) of a representative MAV to purely that of roll. The MAV was fixed to the rig along its thrust line, while the rig itself was guyed to the wind-tunnel floor in order to reduce aerodynamic-induced vibrations (Figure 75a). The rig was equipped with a low-torque rotational potentiometer enabling a direct measurement of the MAV's roll angle (see for Table 9 for specifications). The potentiometer signal was double derived to compute the roll rate and acceleration (see Figure 76).

Table 9: Potentiometer specifications

PARAMETER	DETAIL
Starting Torque	0.0017Nm
Operating Torque	0.001Nm
Rotation	360° (continuous)
Electrical Angle	340° ±4%
Resistance	1KΩ to 100 KΩ, Linear
Linearity	±2%

The MAV's ailerons were not deflected for the duration of the experiments (i.e. stick fixed). This enabled turbulence to be the sole contributor to the perturbations. The rig contained a mechanical stop to prevent the MAV from entering the wake region caused by the rig (Figure 75b). The following subsections further describe the other equipment used in this study.

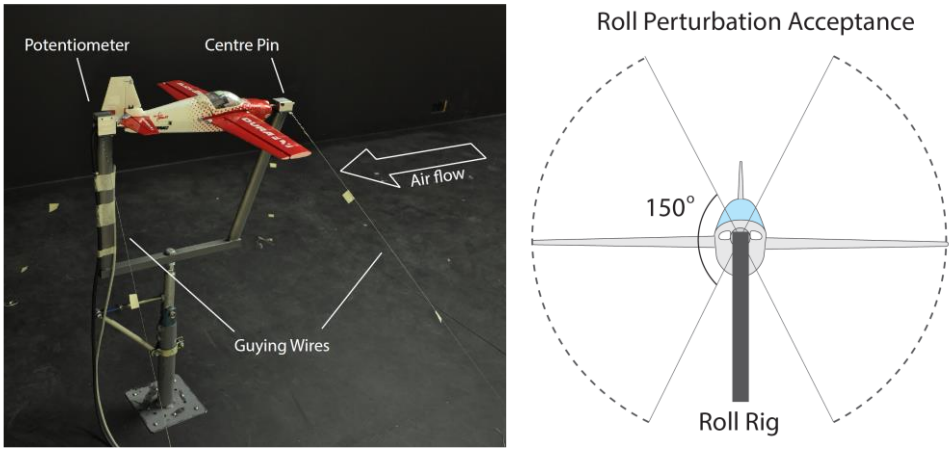

Figure 75: (a) Experimental Setup of roll rig (b) perturbation limits before sample is discarded.

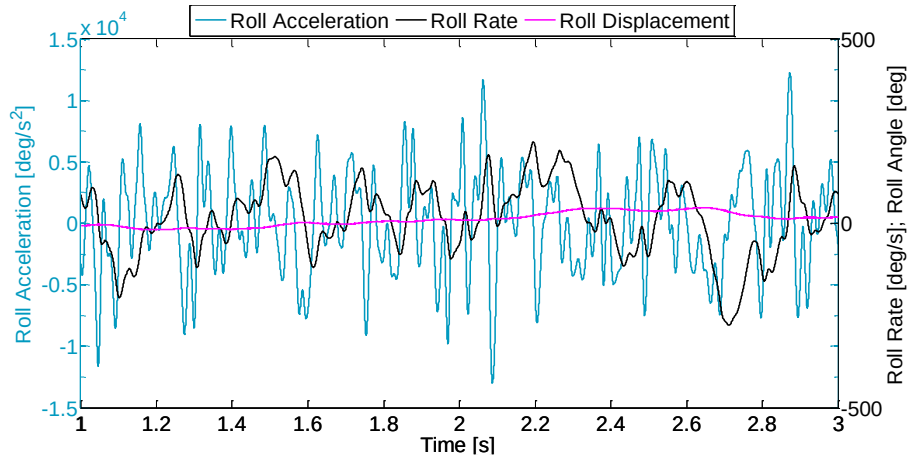

Figure 76: Derivation of the potentiometer's raw signal from displacement to compute rate and acceleration. Data sampled during wind-tunnel speed of 10ms^{-1} and vehicle AoA of 0^{o}.

5.2 Experimental Setup

The same pressure tapped wings introduced in the previous chapter were used for this experiment. However not all taps were used to acquire results. The knowledge gained from the results presented in the previous chapter allowed strategic selection of pressure taps known to attain good correlation with upstream flow disturbances, see Figure 77 and Table 10. Row A from the span-wise study showed relatively higher correlation at a span position of (x/s) = 66.6% compared to the other span-wise locations. This span-wise location happens to coincide with taps in column B of the chord-wise study (see Table 8 and Table 10). Subsequently only row A and column B were considered in this section.

The pressure difference between the symmetric pressure taps (distributed over both wings) was computed in an effort to calculate the wing load imbalance. This approach was chosen as both wings contribute to the roll acceleration. Measurements were collected at a rate of 10 kHz over a period of 300s.

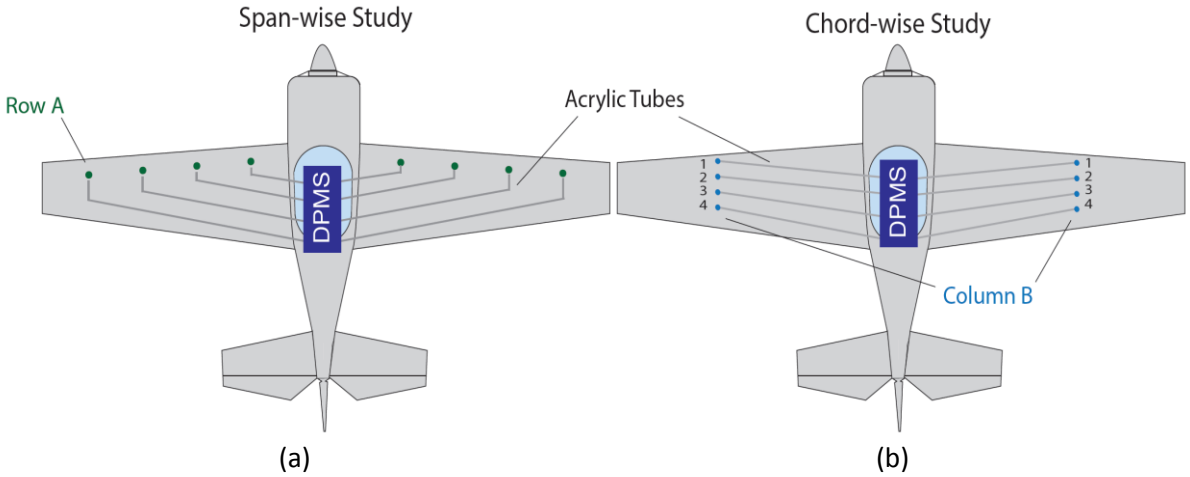

Figure 77: Pressure tap location (a) Span-wise study (b) Chord-wise study

Table 10: Pressure tap location for the chord-wise and span-wise studies

Pressure Taps	Chord-wise Study (x/c) Column B @ x/s= 66.6%	Span-wise study (x/s) @ Row A (x/c= 5.44%)
1	1.63%	24.9%
2	5.44%	44.9%
3	9.80%	64.9%
4	15.24%	84.8%

5.3 Pressure Tap to Roll Acceleration Correlation Results

The correlation results acquired from the span-wise and chord-wise studies are presented in Figure 78. The correlation curves illustrated represent the maximum values for each tap. It was evident from the results that correlation varies with the location of the taps, both chord-wise and span-wise. In the span-wise study, correlation increases gradually along the span to peak at (x/s = 66.6%) then reduces at (x/s = 84.8%). This reduction in correlation towards the wingtips was likely due to the influence of wingtip vortices. The correlation at (x/s = 66.6%) remains above 0.7 for (-15^{o}< AoA < 10^{o}), reaching a maximum of 0.9 at 0^{o} AoA. Generally, surface pressure fluctuations correlated well with the roll acceleration at pre-stall AoAs. The chord-wise wing study shows that correlation near the stagnation point at the leading edge varies significantly with AoA. This was reflected in the results recorded by the tap at (x/c = 1.63%), which experiences a significant reduction in correlation at negative AoAs. Taps located further downstream experience lower variation.

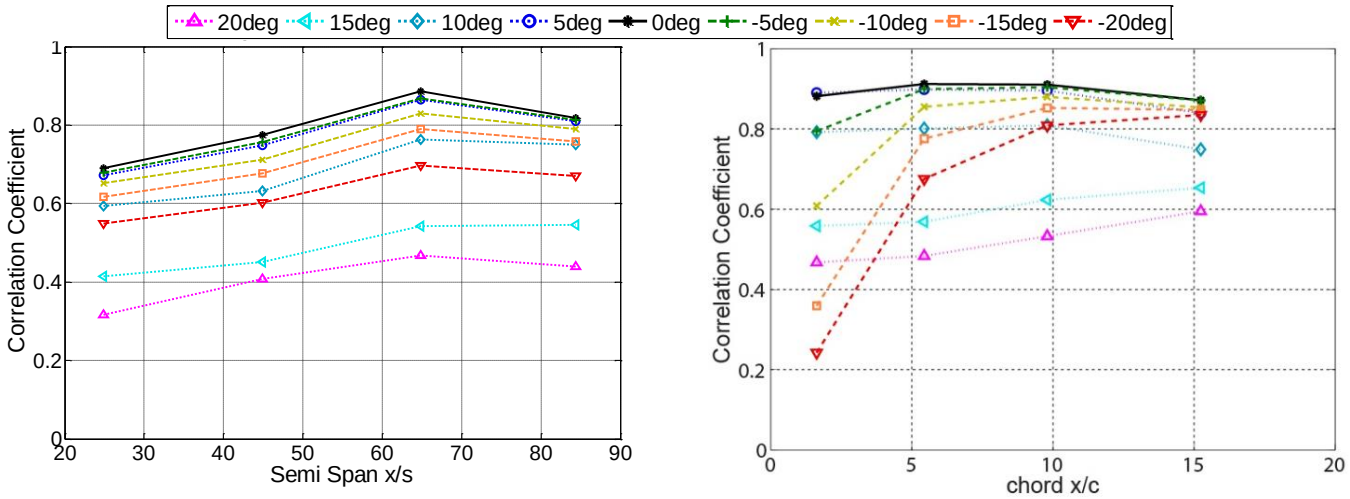

(a) (b)

Figure 78: Correlation Results (a) Spanwise wing study ,Row A (b) Chord-wise wing study results ,Column B

Surfaces such as the horizontal stabiliser and fuselage were not pressure tapped, and will contribute to a reduction in correlation between measured pressure and perturbations in roll. This was particularly evident when the MAV was exposed to the roll rig's local wake at high AoAs creating additional pressure fluctuations not recorded by the pressure taps. In contrast, negative AoAs do not

degrade correlation as much, suggesting that the pressure side of the airfoil provides better positioning of the pressure taps. However, highly negative AoAs were observed to result in reduced correlation due to the stall of the underside of the wing. A reduction in correlation was observed for the taps closest to the leading edge (Figure 78). This was caused by the strong influence of the stagnation region. The taps very close to the leading edge were influenced by the variation in total pressure, which does not appear to correlate well with the roll acceleration.

The time signal from the tap at x/s = 66.6% and x/c = 9.80% was overlaid with roll acceleration in Figure 79 to visually demonstrate the degree of similarity for a three second time interval. The signal segments illustrated represent two AoA conditions representing a correlation coefficient of 0.9 (0^o) and 0.54 (15^o). Figure 79a presents the highest correlated signal whereby the signals are almost identical. The signals presented in Figure 79b, have lower correlation. It is important to note that both signals (*Cp*, roll acceleration) are of different units, and have been therefore scaled to visually match each other.

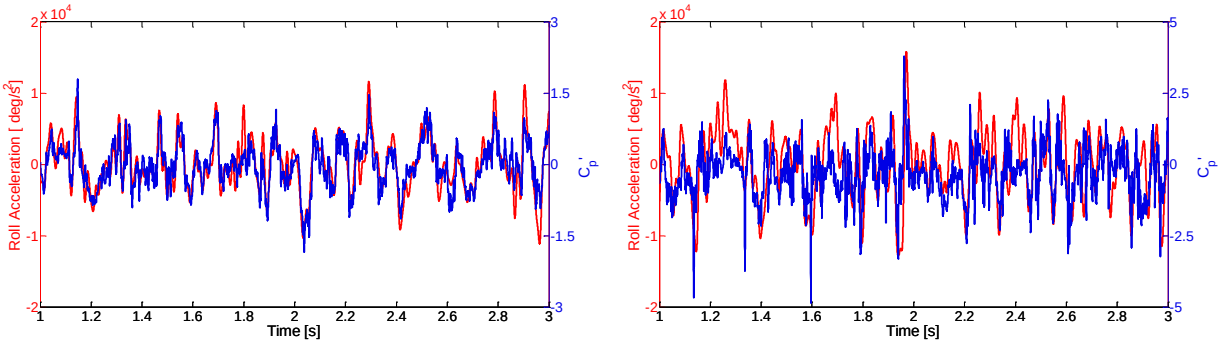

Figure 79: Visual comparison of the measured pressure and the MAV's roll acceleration (a) 0 ^{o} AoA (b) 15^o AoA

5.3.1.1 The Frequency of Perturbations

The coherence results presented in Figure 80 provide a deeper understanding of the correlation in the frequency domain. For readability, only three AoAs are presented, since similar coherence behaviour was observed for the other tested AoAs. Pressure taps per semi-span were summed to generate a total pressure signal. The total pressure from starboard wing was then subtracted from the port wing to compute the load imbalance. This signal was then correlated to the roll acceleration and presented as a black solid line in Figure 80. The latter contrasts the coherence of the individual pressure taps to their sum, giving an indication as to which tap correlates most to the total load imbalance.

The magnitude of coherence was highest at 0^o AoA and was still high for anticipated cruise AoAs as expected. A minor reduction in coherence was observed at negative AoAs, and a significant reduction in coherence was evident at stall AoAs for the reasons explored in the previous section.

Coherence was generally high (>0.8) in the frequency range of 3-20Hz for AoA range of -15° to 5°. This coherence peak shifts to higher frequencies (10-20Hz) at higher AoAs (>15°) while the coherence magnitude falls below 0.8. Significant perturbations in roll were evident up to ~35Hz at a coherence of ~0.6 for level flight. No significant energy was present above 60Hz. This was expected due the moment of inertia of the airframe, which was unable to react fast enough to the higher pressure frequencies due to its polar Moment of Inertia (MOI) thus resulting in negligible coherence. In other words, the vehicle's perturbation acceptance frequency range was limited to ~60Hz. It can also be observed that at the lower end of the frequency spectrum at 15°, coherence seems to peak, which seems to be a by-product of the non-linear flow phenomenon. However, this low frequency component was of little relevance from a control perspective.

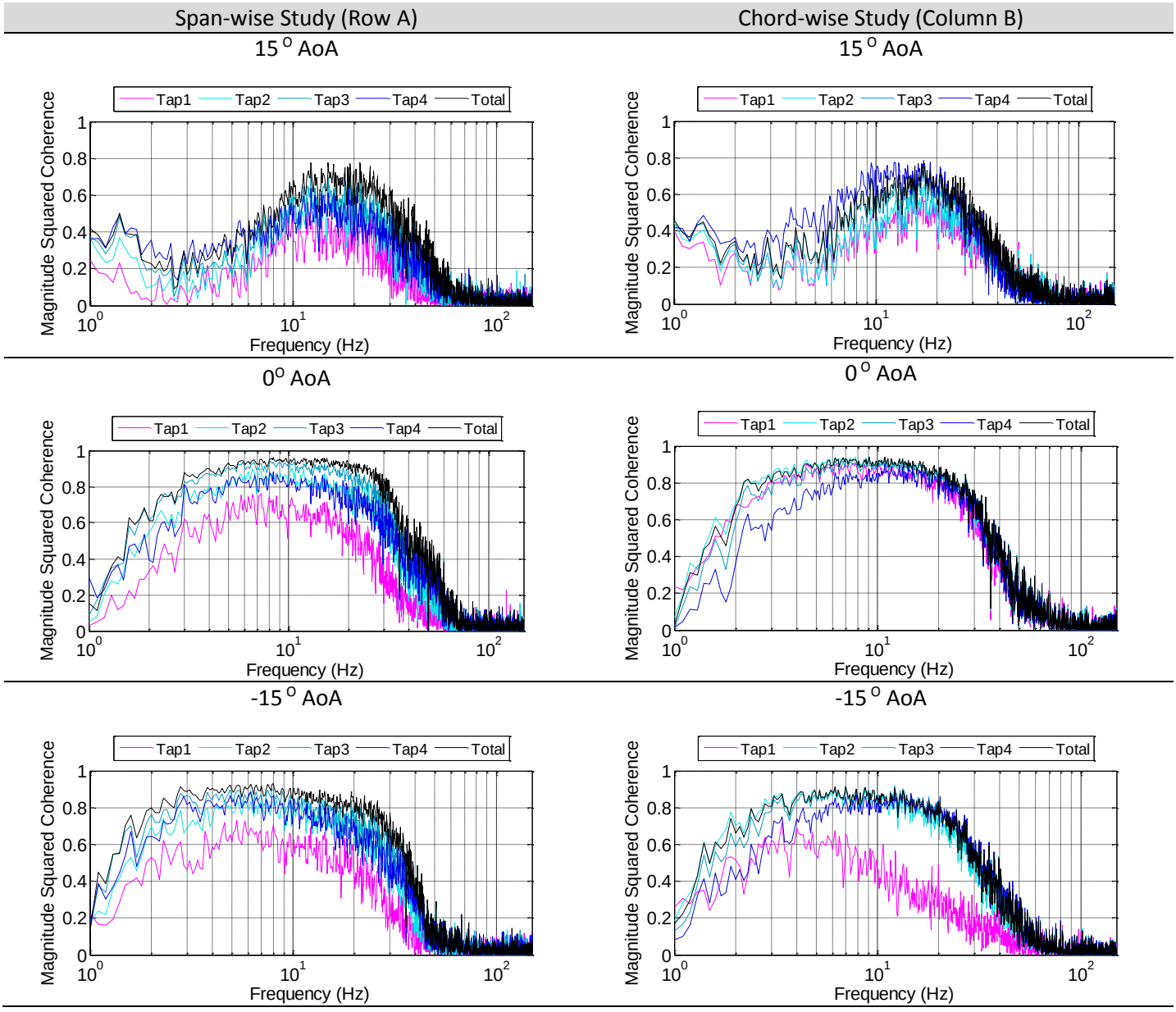

Figure 80: Coherence for a range of AoAs between C_P, measured from different taps, and roll acceleration

5.3.1.2 Time-Lag

In any real control system there is always a time delay between sensing and actuation (~0.52s as discussed in Section 2.1). Thus, it is useful to compute the time-lags evident between wing load imbalance and the induced roll acceleration (see Equation 7). The time-lags presented in Figure 81 corresponds to the phase lag at maximum correlation. Therefore, the confidence in this value increases with increased correlation and vice-versa. Capturing the change of time-lag along the wing span is not the aim of this study. However, of more importance is the fact that instances occur when the time-lag changes signs (i.e. negative values). This quantitatively confirms that sensing wing load imbalance can be phase-advanced relative to the induced roll perturbation. These instances (i.e. negative time-lag) were limited to the certain AoAs thus limiting the exploitation of the concept. Furthermore, the time-forward advantage is not sufficiently large to cater for the time-lags inherent in the control system. Therefore the latter presents the motivation for extending sensing of the flow disturbances upstream of the wing. The following section will explore the use of custom-made multi-hole pressure probes embedded within the wings of the MAV.

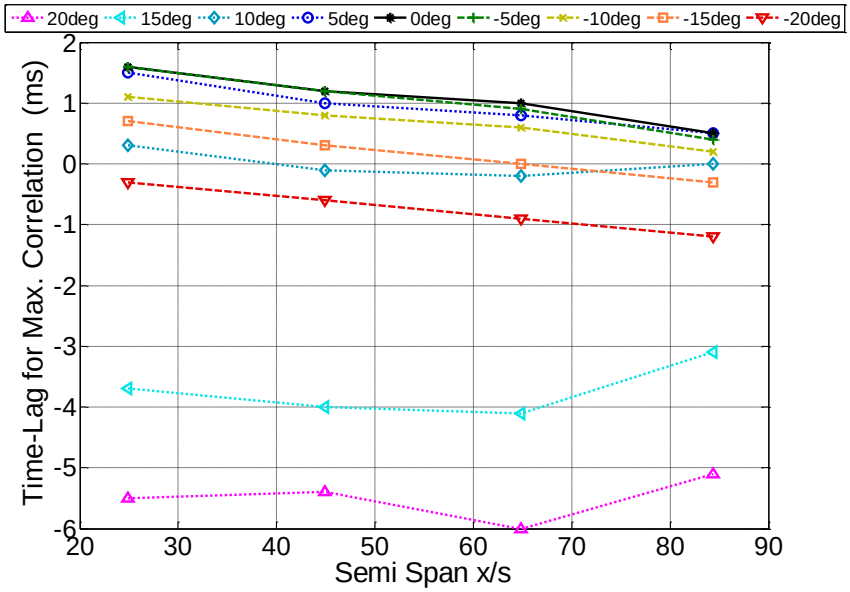

Figure 81: Span-wise wing study results (Row A)

5.4 Phase-Advanced Sensing

Previous section established the possibility of sensing the disturbances upstream before they impart on the wing. Extending the sensing of the flow upstream into the oncoming flow is explored to improve the time-forward advantage. Avian sensing of turbulence provides the inspiration for the work presented in this paper. Strong evidence suggests that birds use their feathers for sensing of the flow over the wing (Brown and Fedde, 1993). In nature, feathers act as the deformable membrane, which vibrate or deflect during flight due to the airflow (Necker, 1985b). This biological sensory system enables a bird to "feel" a number of phenomenon such as the progression of flow separation over its wings during aggressive manoeuvres and the frequency of vibration of its primary and secondary feathers to detect airspeed (Mohamed et al., 2014; Necker, 1985b; a; Hörster, 1990b; a). Further research hypothesised the role of the leading edge feathers in detecting gusts as sensory feedback to the motor control of birds (Carruthers et al., 2007). Based on the findings of Carruthers et al. (2007), it is suggested that birds are capable of feeling the oncoming gusts by detecting and correlating the oscillation of the stagnation line along the leading edge of their wing, (see Figure 82). This suggested avian capability allows *phase-advanced* (i.e. early) detection of the disturbance before the bird experiences an inertial response to the disturbing phenomena. Such sensing architecture allows sufficient time for the bird to counteract the gust by either twisting or morphing its wing accordingly.

In an effort to replicate this biological sensory system, it was decided to extend a 4-hole pressure probes in front of the wing's leading edge (i.e. upstream) designed to sense the oncoming vertical velocity vector (directional tubes) in addition to the longitudinal velocity magnitude, (see Figure 83). The ability to detect gusts (i.e. turbulence) ahead of the wing provides the MAV control system with additional time to command a control surface response and counteract the potential impact of the gust. Ideally, the entire flow field ahead of the wings needs to be mapped. However, given the practical constraints in implementation, the minimum number of sensors needs to comply with the MAV's SWaP requirements.

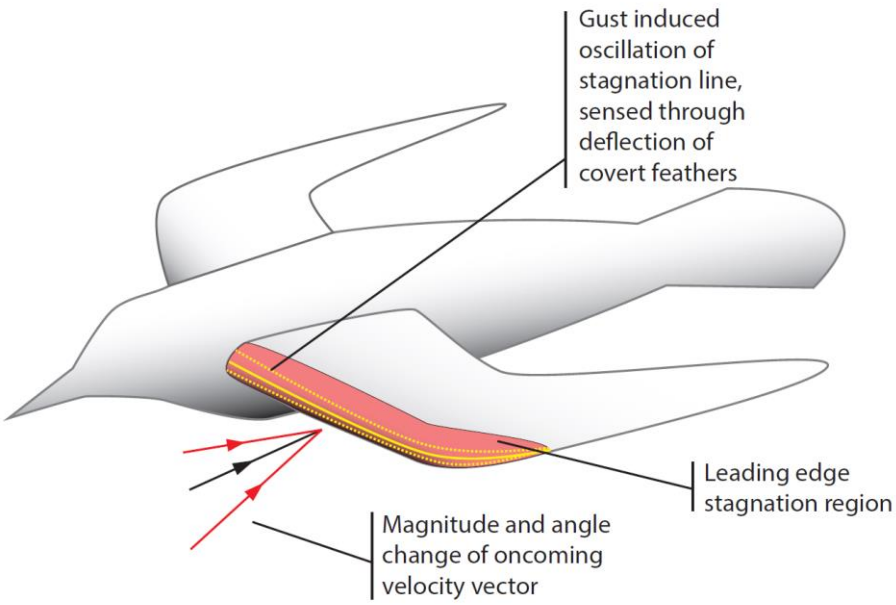

Figure 82: Birds can detect oncoming gusts by feeling the movement of the stagnation line on the leading edge of their wings

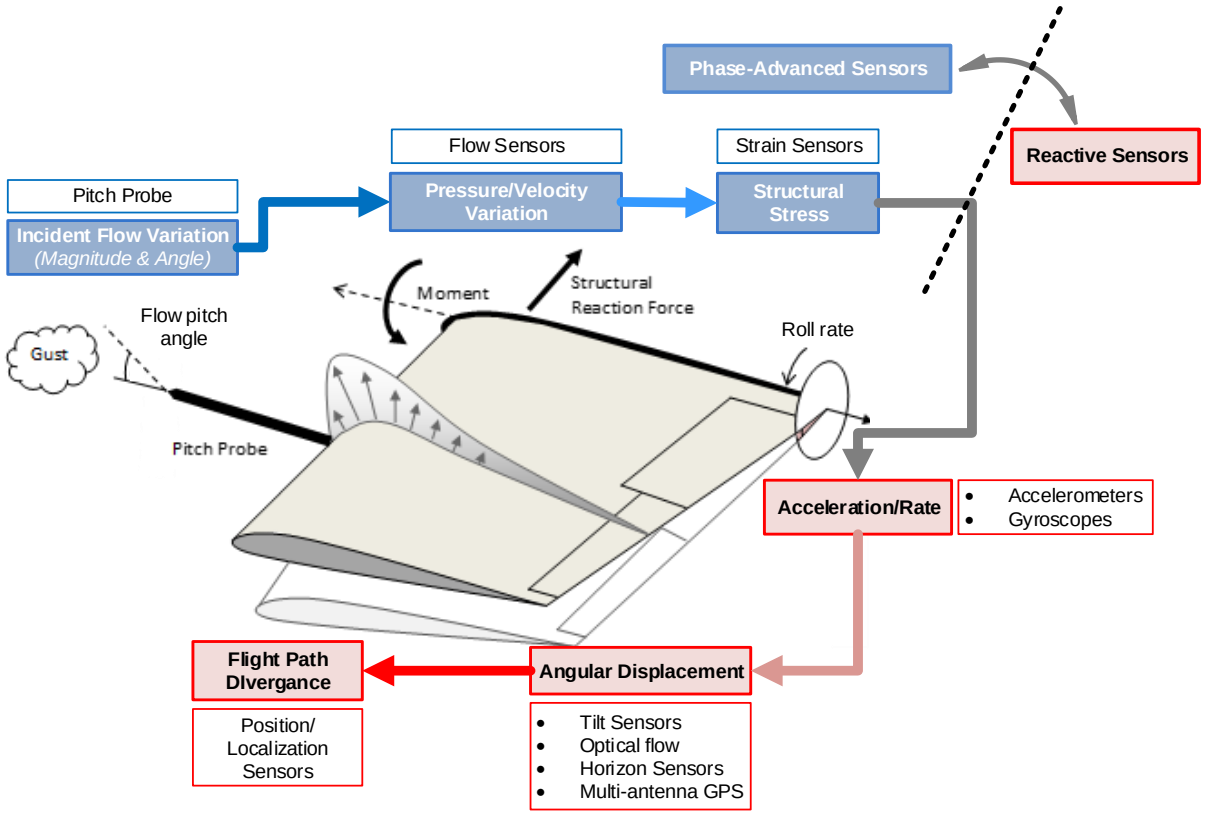

Figure 83: Sequencing of the pitch probes in the gust perturbation process.

5.4.1 Pitch Probe Design

Pressure-based multi-hole probes are commonly used to measure transient flow angles and velocity (Chen et al., 2000; Hooper and Musgrove, 1997; Mousley et al., 1998). With proper calibration, such

instruments can accurately detect flow direction and dynamic pressure of the oncoming flow as per the commercially developed Cobra probe detailed in Section 3.3.3. These probes are relatively heavy thus preventing their use on the (relatively light) MAV.

In order to account for the stringent MAV SWaP requirements, a lightweight carbon fibre probe was designed and embedded in the MAV's wings (Figure 84). The pitch probe consists of three internal lightweight carbon fibre tubes with chamfered leading edges. Their bases are embedded in the MAV's wings. These probes have three vertically aligned holes in addition to static ports surrounding the circumference of the outer diameter of the tube, as shown in Figure 85. The central tube outputs the total pressure, which when subtracted from the static port, allow the dynamic pressure along the tube's longitudinal axis to be computed. The pitch-directional tubes (top and bottom) were used to compute the vertical velocity vector. The probe's directional tubes were chamfered at 45^{o} allowing an angle measurement range of ~90^{o}.

Figure 84: MAV with probes installed

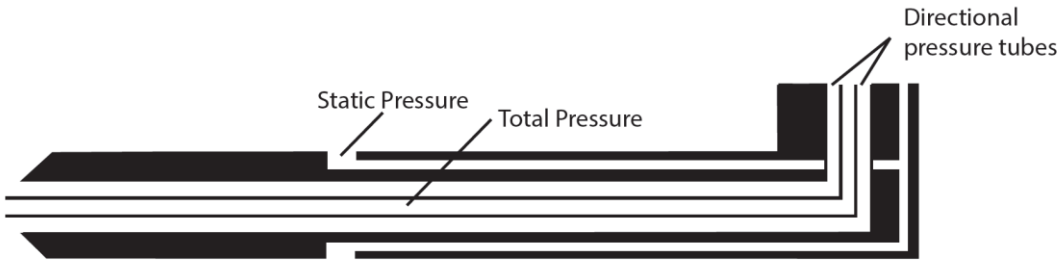

Figure 85: Schematic of specially fabricated airborne pitch probes

The internal tubes of the pitch probe were connected to MEMS differential pressure sensors (see Section 3.3.2) through 150mm long acrylic tubes (1mm dia.). The dynamic calibration device

described by Fisher et al. (2012) was used to determining the frequency response of the sensory system (see Figure 86). The frequency response remains relatively flat up to the sampling frequency (200Hz).

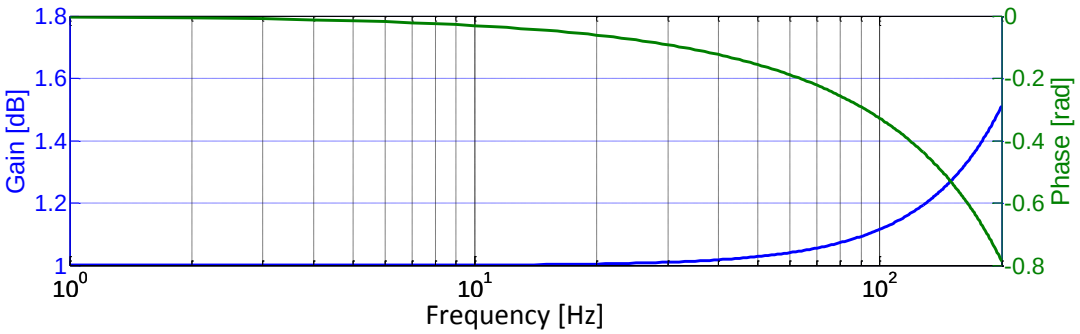

Figure 86: Frequency response of pressure sensor system

As discussed previously in Section 2.1, the typical time-lag of a MAV is 0.52s. For the cruise velocity of 10ms^{-1}, a probe length of 5.2m is required. However, there are practical constraints associated with using relatively long probes as outlined below:

- Increased mass
- More susceptible to vibration and bending
- Dynamic response of tubes (increased phase lag within tubes)
- Degraded correlation due to misalignment of sensing location and aircraft (Figure 87)

A probe length of 150mm was selected to provide as much time-forward advantage as possible within practical constraints. The selected length gives a time-advantage of 0.015s when flying at 10ms^{-1} (MAV's cruise speed). To minimise the number of probes carried on-board only a single probe per wing was utilised. The probes where positioned at x/s=64.9%, which corresponds to the location of highest correlation (see Figure 78).

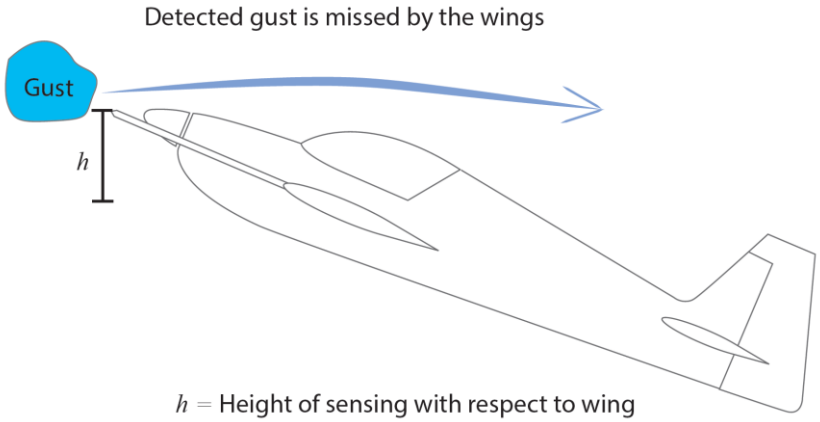

Figure 87: The high position of the probes at high AoAs lowers the detectability of the smaller gusts, resulting in degraded estimation of perturbation

5.4.1.1 Pitch Probe Calibration

The pitch probes were statically calibrated using the approach outlined by Chue (1975). The calibration was conducted in nominally smooth flow to identify the variation of pressure with Angle of Attack (AoA), Figure 88. The MAV and its wing (with pitch probes) were installed on a variable AoA sting. An IMU was installed inside the fuselage to measure AoA in freestream flow, while the sting's AoA was varied during the operation of the wind-tunnel. Testing for various wind-tunnel speeds determined that the probe measurements were insensitive to Reynolds Number effects.

From Figure 88, it can be observed that the pressure measured by the directional tubes follows a reasonably linear relationship with increasing AoA. Deviations from this linear relationship were observed at AoAs of less than -20°. This deviation was due to the proximity of the measuring tip to the boundary layer of the wind-tunnel's floor. The gradient of the linear fit was used as a gain value to measure AoA. The blue line depicted in Figure 88 represents the dynamic pressure variation (sensed with the probe) with AoA, which followed nominally a cosine law. However, measuring the flow pitch angle is the main signal of interest, while the dynamic pressure was only used to measure airspeed.

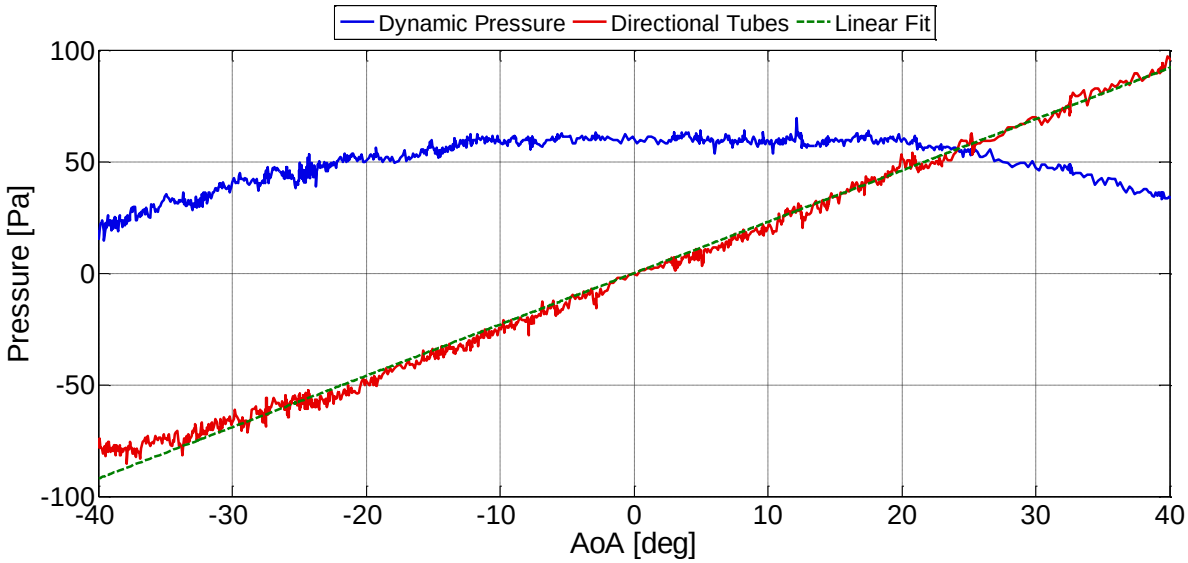

Figure 88: Pitch Probe calibration with upstream AoA

5.4.2 Pitch Probe Coherence Results and Discussion

Figure 89 demonstrates the coherence results acquired at different AoAs using the pitch probes. It is important to note that the presented curves represent a combined signal of both probes (i.e. averaged flow pitch angle). It was sensible to compare the sum of the probes' output since both probes contribute to the angular acceleration (i.e. induced by both wings). The coherence evident at very high and low AoAs (±15°) was lower compared to other AoAs. Ideally, the probe's measuring tip needs to be in alignment with the wings for accurate sensing, however during certain manoeuvres

such as climbing, the probe's sensing-tip position relative to the position of the wing will change, see Figure 87. This change in position will result in reduced correlation. Large enough gusts (which occur at low frequencies) can be detected at high AoAs, however, the relatively smaller gusts (at higher frequencies) can be missed by the wings. When a gust is missed, it will not cause a perturbation sensed by a probe thus reducing correlation. This problem can be overcome by reducing the length of the probes. However, the time-forward advantage will be compromised. The non-linear flow phenomena that occur at low Reynolds Numbers (i.e. vortex core formation and bursting laminar separation bubbles) contribute to reduced correlation. These phenomena only occur over the wing, thus inducing a perturbation not detected by the probes.

Coherence was highest (>0.6) between 2-30Hz for moderate AoAs (-5° to 5°). At these small AoAs coherence was highest due to the location of the probes with respect to the wings. Deviations from this alignment due to increasing AoA will result in reduced correlation. It was previously shown that this particular MAV airframe was irresponsive "inertially" to perturbations above 60Hz. The coherence results here complement previous results where no coherence was evident beyond 60Hz. This was due to the vehicle's inability to react fast enough to the higher turbulence frequencies due to its MOI. Furthermore, the available turbulent energy at these frequencies was insufficient to induce perturbations. The vibrations of the probes themselves as a consequence of advecting flow will adversely influence the correlation. This also limits extension of the probes beyond a certain length.

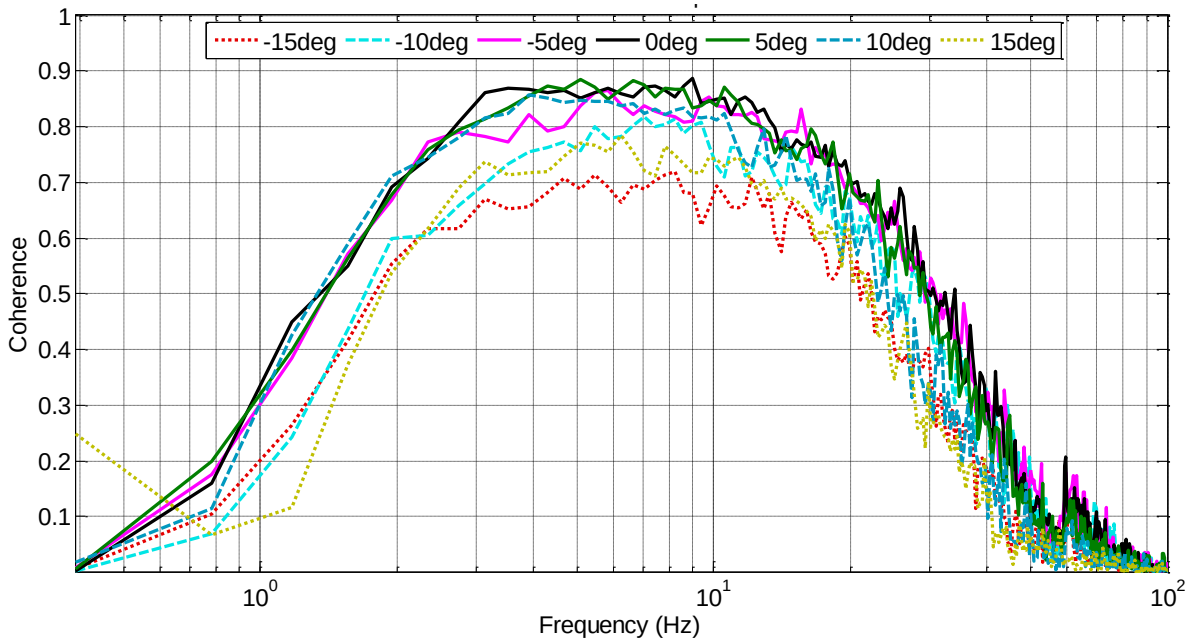

Figure 89: Coherence coefficient between roll acceleration and the probe measured AoA

Figure 90 shows the level of correlation evident between the vertical velocity vector and the roll acceleration. The phase shift evident between these parameters is the time-forward advantage. This

phase difference was converted to a time-lag and quantified for the frequencies which attained high correlation, see Figure 91. It was evident that the nominal time-forward advantage was ~0.015s, which intuitively corresponds to the probe's length and the flow speed.

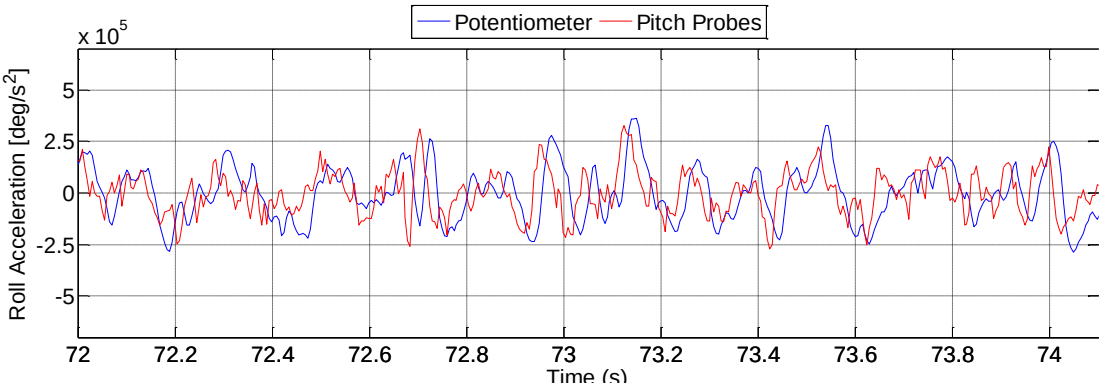

Figure 90: Raw data comparing roll acceleration and pitch probe output

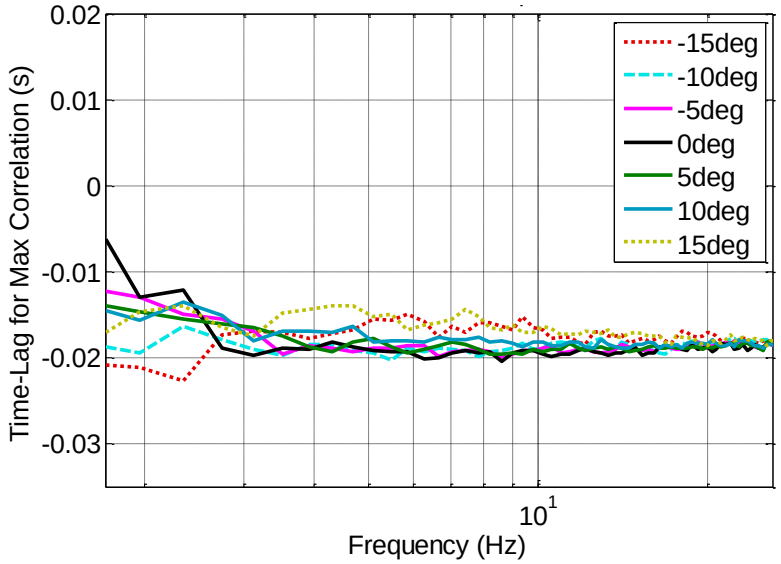

Figure 91: Time-lags per frequency.

5.4.3 Error Considerations

The main sources of error are by-products of the experimental setup, which has various practical constraints. The main undesirable by-products of the experimental setup are outlined below:

- **Influence of the potentiometer:** The motion of the vehicle during perturbations is influenced by the potentiometer. This is assumed negligible due to the low torque characteristics of the potentiometer (see Table 9).
- **Variation in shape of the pitch probe's measuring tip**: Variation in the angle of the chamfered leading edge of the pitch probes influences its output. To minimise this, a shaping template was used during fabrication of the pitch probes to ensure identical tip shapes. Furthermore, the calibration curves for each pitch probe were tested and found to be identical to that shown in Figure 88.

5.5 Phase-Advanced Attitude Control

The high correlation observed in the results of the previous section indicates the feasibility of using the signal from the pitch probes as a dynamic input to control the roll attitude of the MAV. Thus, a commercially available Flight Control System (FCS) manufactured by Shifted Dynamics was utilised in order to see the potential advantage from phase-advanced sensing of flow pitch angle as a method of minimising roll perturbations (see Figure 92). Since the FCS measured angular motion, the potentiometer embedded in the roll-axis rig was only used as a low friction bearing. From this point onwards in this thesis, all data acquisition was through the FCS. The FCS's sampling frequency was set to 200Hz. The following sub-sections describe the FCS and the control architectures implemented.

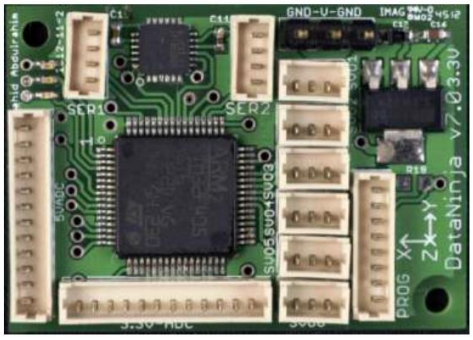

Figure 92: Flight Control System

5.5.1 Flight Control System

The FCS used (specifications outlined in Table 11) was a programmable closed loop control system intended for MAV experimental research. The FCS was not intended as an autopilot (i.e. no GPS), but rather as a data logger and controller for providing stability augmentation in a variety of atmospheric conditions and using a variety of control strategies. The FCS can control up to six servos, which were commanded based on the chosen control architecture, pilot commands, and sensor measurements, both on-board and external. The FCS's on-board 6DOF IMU (MPU-6000 manufactured by Invensense) provides basic inertial feedback, and inputs from additional analogue sensors for feedback/feed-forward.

Table 11: Flight Control System Specifications

FEATURE	DESCRIPTION
Microcontroller	STM32F405RGT6
IMU	Invensense MPU-6000
Input channels	12 digital, 12 analog
Output channels	6
Dimensions	37 x 27 mm
Weight	5.8g
Sampling frequency	Up to 300Hz

The FCS's software allows the user to remotely select between different types of control architectures. Three different Control Levels (CL) were explored: 1) Manual, 2) Control Level One (CL1), and Control Level Two (CL2). Manual control corresponds to the situation where there was no active stability augmentation, with servo commands being determined directly from the remote pilot's input (via a radio transmitter). CL1 was representative of a simple inertial-based sensing controller. CL2 is the same as CL1 with the addition of a feed-forward component utilising the flow pitch angle from the pitch probes. Both CL1 and CL2 take guidance commands from a pilot via a Radio Control (RC) receiver and are further described in the following sub-sections. Switching between the three control architectures during flight was achieved via a switch on the RC transmitter. Switching between the desired controllers in the same flight preserved test conditions (particularly important for outdoor flights) improving confidence in comparison.

5.5.1.1 Inertial-Based Control (CL1)

Due to the ease of tuning the control parameters, a Proportional-Integral-Derivative (PID) controller was used for this study. Many commercial autopilot stability augmentation systems utilise PID controllers (Mystkowski, 2013). The attitude-tracking controller had a PID outer-loop and used the angular-rate tracking inner loops on each of the roll and pitch axes. The directional controller was set to yaw angular rate tracking mode. Block diagrams in Figure 93 illustrate the controllers defined in CL1. The gains of CL1 were initially tuned through a series of flight tests in turbulence. Individual gains were assigned to variable knobs on the RC transmitter for real-time tuning in turbulence. Once the ideal gains were identified (giving the lowest perturbations) they remained unchanged for the duration of the experiments.

The inertial-based controller used an attitude tracking architecture, with an IMU as the only sensor for feedback. This architecture provided an augmented mode in which the remote pilot provided low-frequency guidance commands (see Section 6.1.1) thus was freed from higher frequency attitude stabilisation task. In this mode, the RC transmitter stick inputs were converted into roll pitch and yaw angle commands with the scale factor (percentage stick-to-angle command) adjustable using gains. The attitude-tracking controller had a Proportional-Integral-Derivative (PID) outer-loop and used angular-rate tracking inner loops on each of the roll and pitch axes. The directional controller was a yaw angular rate-tracking mode. Block diagrams in Figure 93 illustrate the controllers defined in CL1. The control architecture of CL1 does not support a "Flap" input (deflections of both ailerons in the same direction) to change pitch or heave motion. Ailerons where only deflected asymmetrically with no differential (i.e. equal and opposite deflection magnitudes). The gains of CL1 were initially tuned through a series of flight tests in turbulence. Individual gains were assigned to variable knobs on the RC transmitter for real-time tuning in turbulence. Once the

ideal gains were identified (giving the lowest perturbations) they remained unchanged for the duration of the experiments.

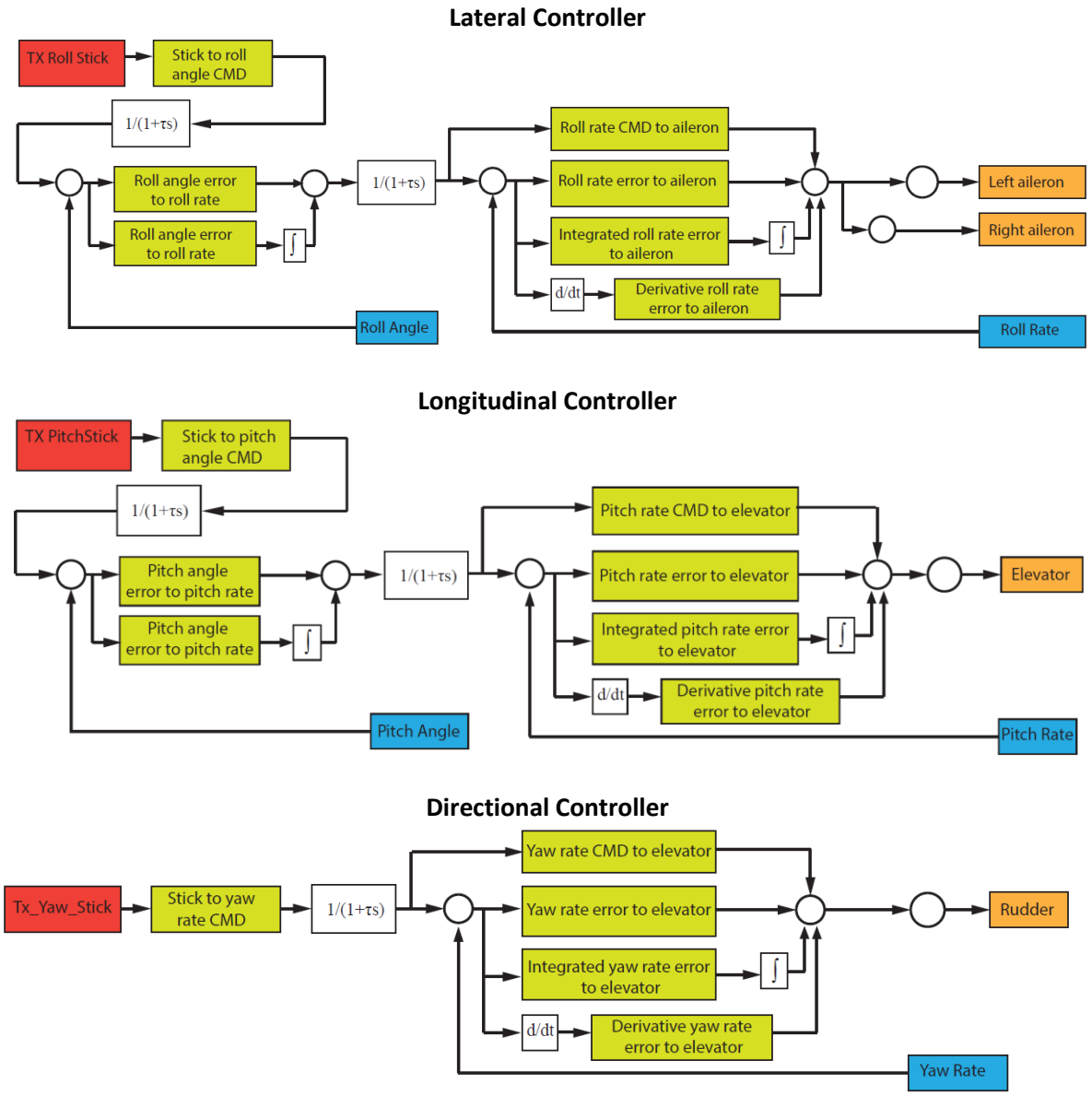

Figure 93: Control architectures programmed in CL1

5.5.1.2 Phase-Advanced Attitude Control (CL2)

CL2 employed the same architecture as CL1 with the exception of the lateral controller, which included an additional feed-forward path (input from pitch probes) to the actuation effort of the individual servos of the respective wings (see Figure 94). The gains defined in CL2 are the same gains defined in CL1 with the exception of the feed-forward component (highlighted in purple in Figure 94). An obvious advantage of CL2 was that each wing servo would actuate independent of each other (i.e. uncoupled deflection). The deflection was based on the sensed oncoming flow disturbance over the respective wing. Coupled asymmetric deflection was an inherent feature of CL1. Overshooting occurs when a disturbance (gust) acts on one wing and not the other, whereby

coupled asymmetric deflection can cause the undisturbed wing to generate unwanted roll moment. The uncoupled deflections of CL2 can compensate for the heave motion induced by large L.

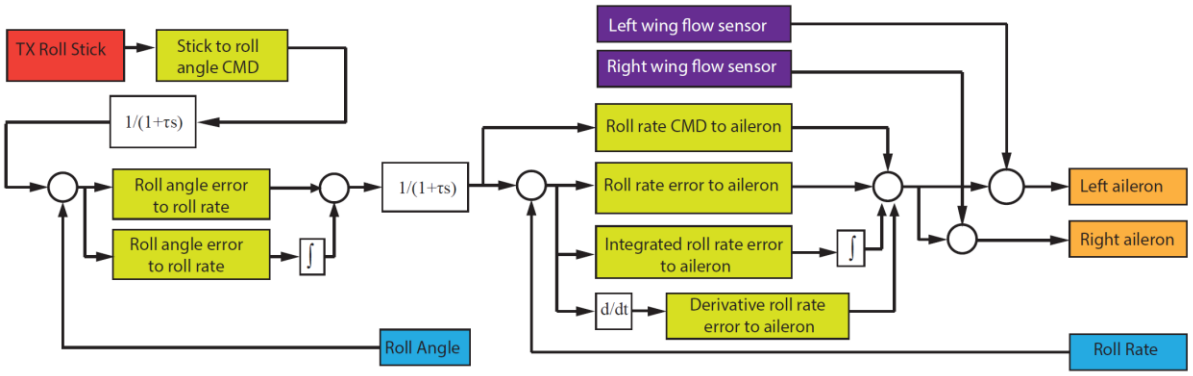

Figure 94: Lateral Control architectures programmed in CL2

5.5.2 Assessment of the Roll Perturbation Disturbance Rejection Performance

The FCS was setup and installed inside the MAV along with the pitch probe system. The MAV was installed on the roll-axis rig (AoA = 0°) and the performance of CL2 was compared to CL1. Each controller was tested for a time segment of 300s. For this test, only the servos associated with controlling the ailerons were connected to the FCS. A number of test runs were conducted within the RMIT Wind Tunnel at a Ti of 12%. Each run produced fairly repeatable data (see Appendix A), subsequently the relevant data from three flights was combined and presented. This is the equivalent of flying the MAV for a period of 15 minutes. Combining the data is based on the assumption that the test conditions remain unchanged. The assumption is considered valid for the wind-tunnel since the average Ti over each sample is the same. However, this generally will not hold for flights in outdoor turbulence.

The random nature of turbulence and severe induced perturbations can challenge parametric modelling. Additionally, characterisation of the system's response through parametric modelling is not the aim of this thesis, but instead to validate the benefits of phase-advanced sensing. Therefore, the presented results focused only on statistically identifying the improvement in disturbance rejection performance of CL1 versus CL2. Statistical hypothesis testing through Confirmatory Data Analysis (CDA) revealed that the perturbation results did not follow known distributions. Subsequently fitting statistical models to the presented data can be misleading. Exploratory Data Analysis (EDA) techniques are therefore utilised to permit a more direct analysis approach, allowing data itself to reveal its underlying structure and model without presuming any statistical models. EDA is therefore an ideal analysis technique often used for initial statistical analysis when the distribution of the data is unknown (Tukey, 1977). Presuming statistical models for the attitude data may be misleading or inaccurate.

Boxplots and histograms where used as EDA techniques displaying the variation in the attitude data (Emerson and Strenio, 2000). Histograms provide density estimation of the attitude data's distribution (measured as the Probability Density Function (PDF)); while the boxplots illustrate the spread and skewness of the standard deviations (see Figure 95). Less attitude perturbations will result in the PDF (histogram) approaching unity at AoA = 0°, in addition to a reduction in the width of the boxplots and vice versa. For the purpose of this work, boxplots and histograms fulfilled the purpose for which the data was gathered.

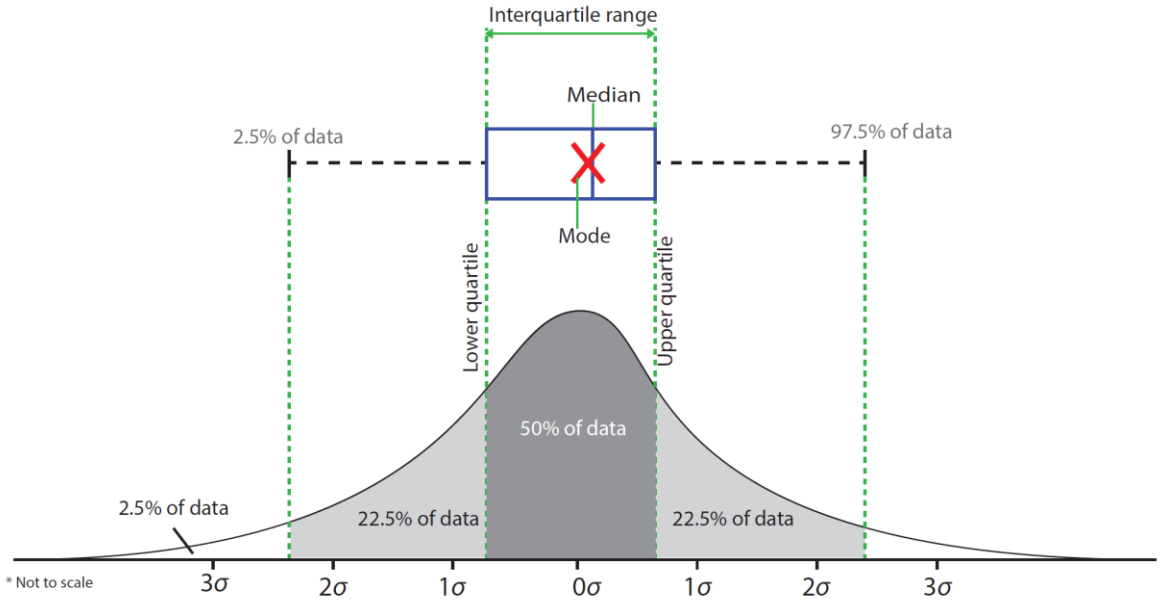

Figure 95: Convention used for plotting the probability density function with boxplots overlaid

Significant improvement of CL2 over CL1 can be observed from the results presented in Figure 96. A video demonstrating the disturbance rejection performance can be found here:

http://youtu.be/UnKvRyqzZq4

The PDF of roll angle and rate at an AoA of 0° is higher for CL2. The dispersion in standard deviation (i.e. perturbations) are noticeably reduced, as observed from the width of the boxplots and histograms. During the test runs, the servos were operating at a noticeably higher frequency at CL2. It is evident that CL2 is mitigating more of the higher frequency perturbations using the output of the pitch probes. This is evident from the spectra of the servo command (CMD), which shows a significant increase in actuation >11Hz (Figure 97a). The servo command spectral peak correlates with the spectral peak of the perturbations (Figure 97b). CL1 is limited by the coupled deflections of

the ailerons thus resulting in a distinct spectral peak at 8Hz. It is evident from the spectrum that CL2 attenuates this peak, implying improved disturbance rejection performance.

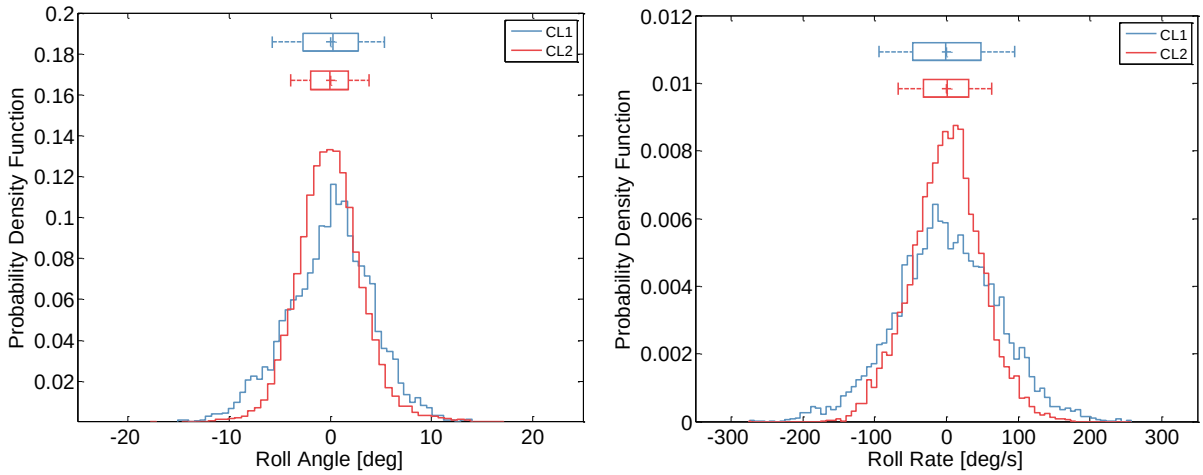

Figure 96: Roll perturbations of CL1 and CL2

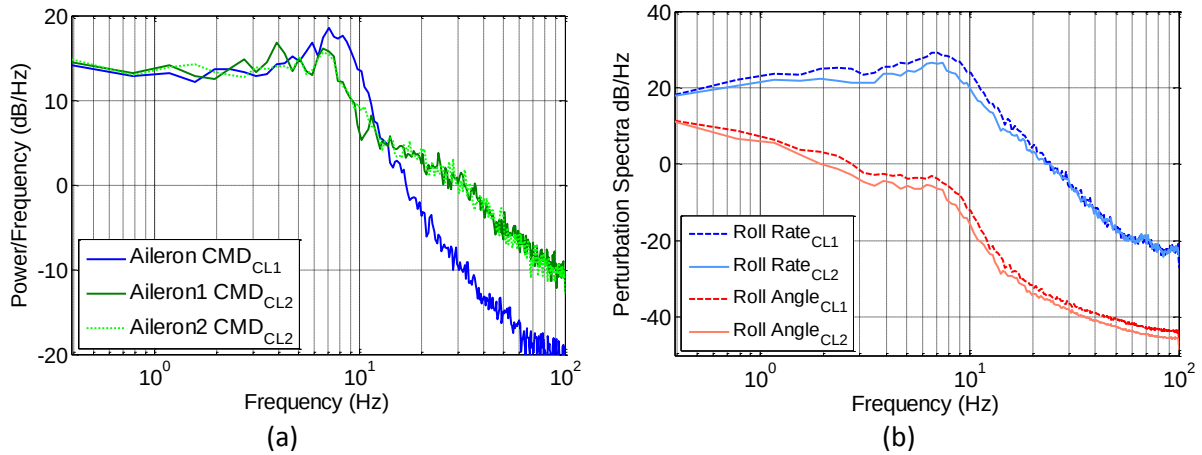

Figure 97: Spectral plots (a) Servo command (b) Roll perturbations

5.5.3 Discussion

In order to further limit perturbations the vertical velocity vector variation across the entire span of the wing's leading edge should be measured and used in the control architecture. Two probes demonstrated the feasibility of the phase-advanced sensing concept. The limited servo bandwidth is another main factor preventing complete elimination of perturbations. Although the servos employed are relatively fast (20Hz) they still fall short of the MAV's maximum perturbation frequency (~60Hz). Its only when both of these parameters meet, perturbations can be completely eliminated. Longer probes will increase the time-forward advantage accounting for the lags of the control system, thus further improving the disturbance rejection performance. However, long probes have their own challenges as discussed previously. Furthermore, the validity of Taylor's hypothesis becomes questionable when the upstream distance is increased.

5.5.4 Error Considerations

The disturbance rejection performance may be influenced by a few factors as outlined below.

- **Accuracy of IMU estimation of attitude:** The selected IMU was calibrated against inclinometers. Additionally the attitude estimate results from the IMU were identical compared to the roll-rig's potentiometer output. This enhances confidence in the accuracy of the perturbation measurements recorded.
- **Sample time:** If the sampling time is not long enough, it may not encapsulate the full spectral range of turbulence. The sample time of 300s was deemed sufficient for the presented experiments since at the largest L_{xx} (0.31m) the flow passes >9600 times over the characteristic chord length of the wing. Furthermore, the repeatability results presented in Figure 98 show that for three different time segments of 300s (measured on different days) the maximum deviation in the measured attitude is < 2%.
- **Actuation:** The deflection range of the servo motors can significantly influence results. Variation in the length of the control linkages connecting the servo's control arm and the aileron will also influence the results. To minimise these errors, the range of the servo motors where all calibrated and checked before each test run along with measuring and ensuring that the length of all the control linkages used are identical. The repeatability results of Figure 98 provide further confidence in results.
- **Servo Degradation:** To account for the degradation in servo performance, servos are replaced after each flight. Additionally repeatability testing proved that variation in the servo performance is <2% (see Appendix A)

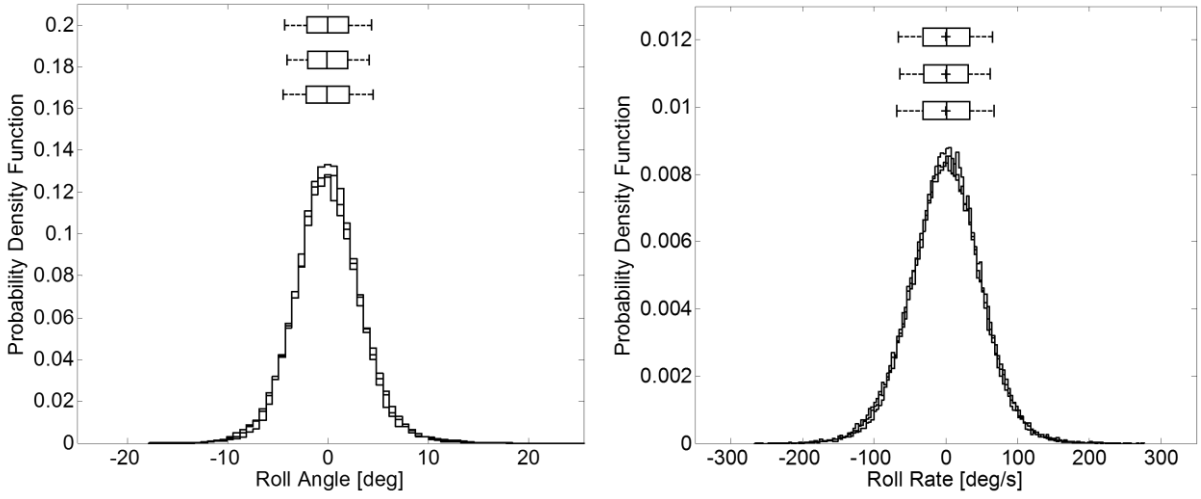

Figure 98: Repeatability results for attitude estimation of MAV while installed on the roll rig (CL2)

5.6 Conclusion and Recommendations

This chapter has demonstrated the feasibility of phase-advanced sensing to enhance the attitude control of MAVs through a restrained setup (roll axis rig) whereby only roll perturbations of the MAV are allowed. High correlation was demonstrated between oncoming flow pitch angle variation and the perturbations in roll. Through the developed probe sensor, a time-forward advantage of 0.015s could be achieved. Significant improvement in disturbance rejection performance was observed of the phase-advanced sensing controller (CL2) compared to conventional inertial sensing (CL1). The following chapter builds on the results from this chapter and investigates the disturbance rejection performance in unrestrained flights. This will enhance the understanding of the effect of the phase-advanced attitude sensing system on other axes during unrestrained flight.

Chapter 6
Unrestrained Flight Trials

Summary

The previous chapter proved the feasibility of phase-advanced sensing through the use of pitch probes extended ahead of the MAV wings. The results were limited to motion about a single axis, that of roll. This chapter continues addressing RQ1.3 through unrestrained flight testing of the phase-advanced sensory system in a number of turbulence conditions. The disturbance rejection performance of the phase-advanced sensory system is quantified for all the vehicle's degrees of freedom. Flight testing was conducted within the test sections of different wind-tunnels with artificially generated turbulence. Testing in outdoor environments in the presence of significant winds were also conducted. It was found that improved performance was not only evident in the roll axis but in pitch and yaw as well. The aircraft's attitude perturbations were successfully attenuated, proving the effectiveness of phase-advanced attitude control. Error considerations have been outlined and are further detailed in Appendix A

6.1 Wind-Tunnel Flight Test Procedure

The two control architectures, described in the previous Chapter, were tested under a wide range of turbulence conditions. Controlled and repeatable test conditions were provided through the use of the Monash and RMIT Industrial Wind Tunnels[3] (Figure 99). Wind-tunnel flight tests were conducted for nominally smooth flow conditions (i.e. $Ti < 1.5\%$). No significant difference in the performance (in terms of attitude stability) between the two controllers was observed for these tests. This was to be expected, as the measured disturbance (turbulence) was small and hence there was little difference between the outputs of the two controllers.

(a) (b)

Figure 99: Flight of MAV within wind-tunnel test sections (a) Monash Wind Tunnel (b) RMIT Wind Tunnel

The MAV was initially flown manually (with no attitude control system) in each wind tunnel. Manual flight (by experienced RC pilots) proved to be excessively difficult with most flights being of short duration; insufficient for data collection, and resulting in crashes. Thus, the data analysis was limited to results from the two controllers (CL1 and CL2) and it was evident that the human control was insufficient in such high turbulence levels. A video of the experiments can be found here:

http://youtu.be/0OQf4jo7XpM

Data were collected for three repeated flights within each of the tunnels, for each of the two control architectures (i.e. CL1 and CL2). Data were recorded for each flight of approximate duration of 300s,

[3] Flights conducted within the RMIT Industrial Wind Tunnel and the Monash Wind Tunnel will be referred to as “RMIT flights” and “Monash flights”, respectively.

via a control switch. A sample representation of the raw flight data acquired for a flight is shown in Figure 100. As previously mentioned the flight time of 300s was deemed sufficient to capture the full spectral range of turbulence. The averaged Ti for each 300s time segment was measured and found to be similar. Furthermore, each flight was repeated three times, and this process was repeated for each wind-tunnel. Figure 101 shows the repeatability results for the roll angle during flight in the RMIT Wind Tunnel, which represents the highest turbulence condition. The maximum deviation is limited to <7% (see Appendix A for more detail). Data equivalent to a flying time of ~15 minutes were collected. Equal amounts of data were collected for the two control architectures.

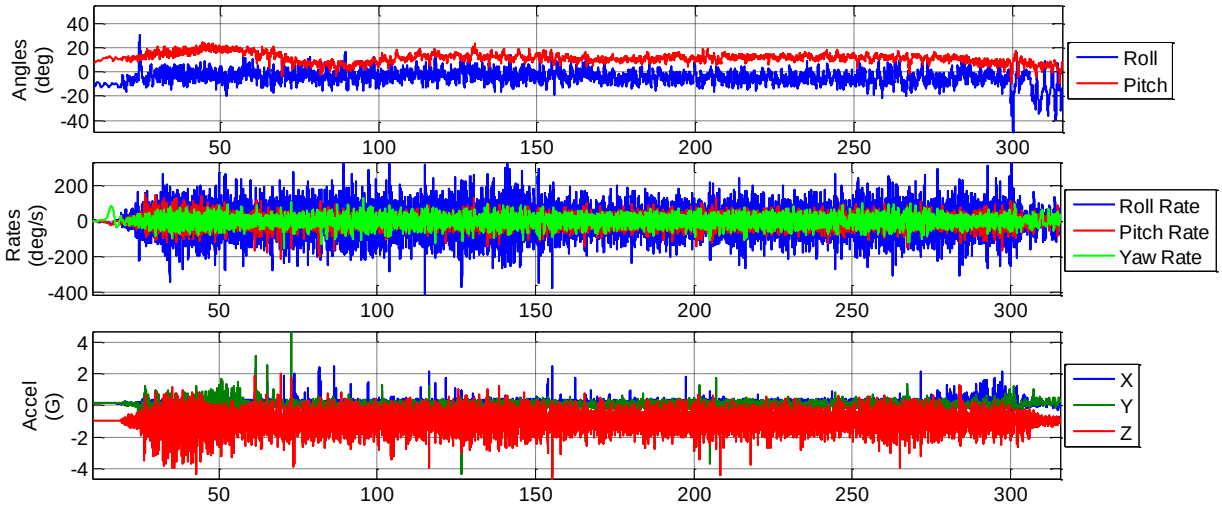

Figure 100: Raw flight data

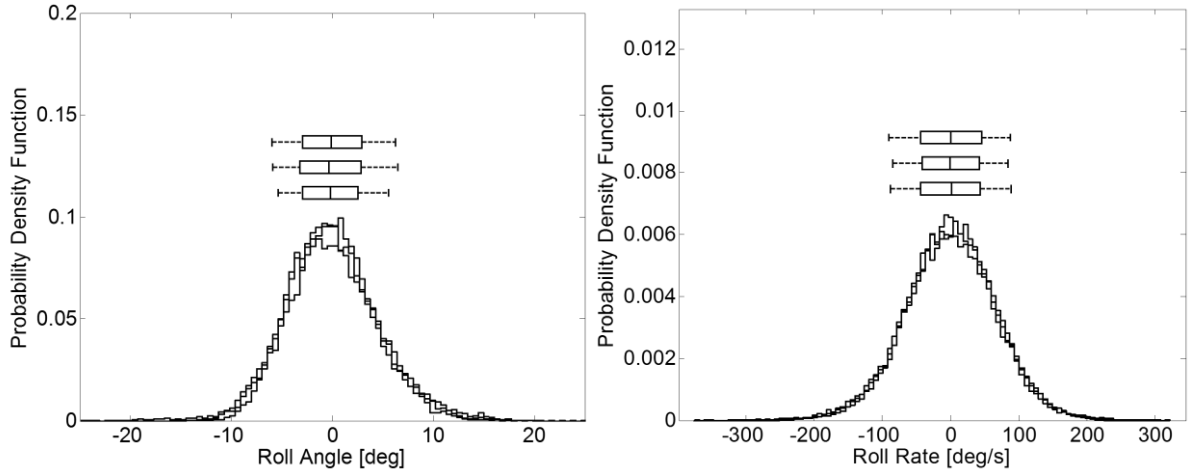

Figure 101: Roll attitude data from three time segments showing little variation

6.1.1 Position Hold Performance (Outer Loop)

It was not possible to accurately measure the aircraft position within the wind-tunnel. A relatively low frequency human control input of less than 3Hz was required to align the vehicle within ±0.5m from the test section's centreline. The pilot input was solely to compensate for flight path deviations (not attitude control), see Section 6.4. Consequently, only low frequency input was being

commanded. Perturbations from turbulent inputs occurred at much higher frequencies (up to 60Hz), which were impossible to correct for by a human pilot since the control bandwidth of a human is limited to a few Hertz (Jenkins et al., 2001; Chen et al., 2014). The pilot refrained from commanding rudder apart from setting an initial bias to account for the torque produced by the motor.

The first set of flight tests were conducted in the Monash Wind Tunnel, which had the lowest Ti and largest L_{xx} (see Table 7). During the testing, it was observed that the pilot was able to maintain position (relative to the walls of the wind-tunnel) much more accurately under CL2 than under CL1. The pilot input required to maintain position was significantly less for CL2 than for CL1 (Figure 102). This would suggest that the use of CL2 contributed to a significant reduction in pilot workload required to operate a MAV in moderate turbulent conditions. It is important to note that roll disturbance rejection was effective to the point where minimal roll axis corrections were required to maintain the same position. A significant increase in the pilot workload was observed for tests conducted in the higher intensity and smaller scale turbulence conditions of the RMIT Wind-Tunnel. The ability of the pilot to maintain position was significantly degraded for both CL1 and CL2 when compared to the tests in the Monash Tunnel. However, the degradation in the position hold performance was less for CL2 than it was for CL1. Further, and similar to the results obtained for flights in in the Monash Tunnel, the pilot input required using CL2 was significantly less than that for CL1.

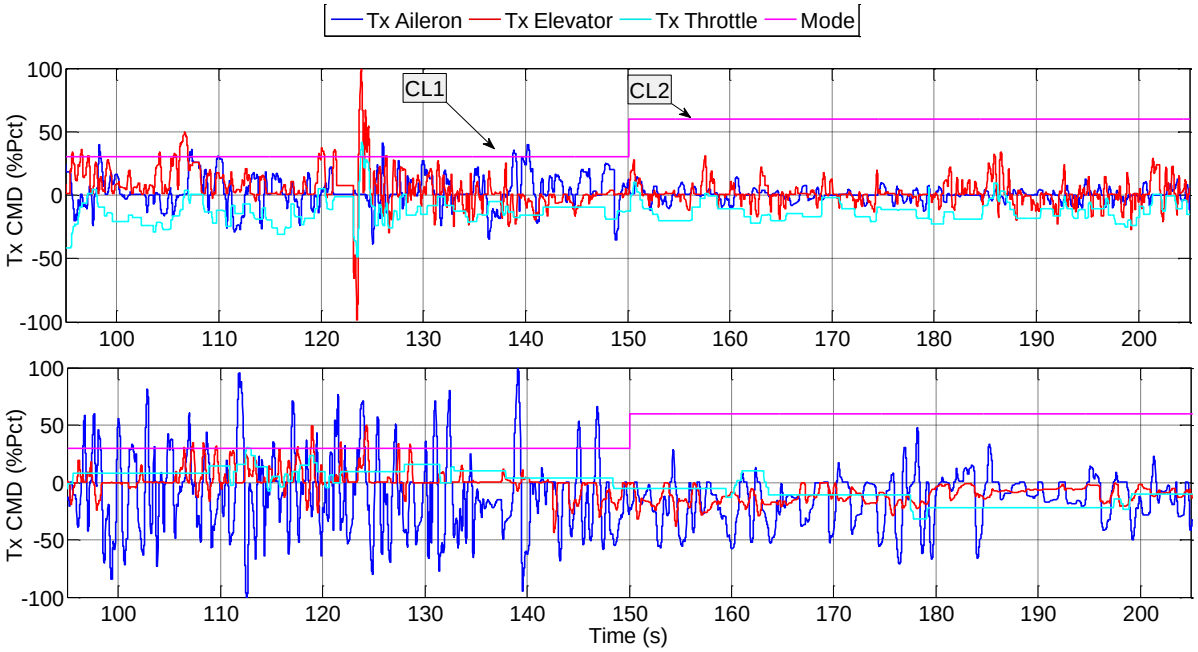

Figure 102: Pilot command input: Monash Flight (Top), RMIT Flight (Bottom)

The aileron servo command spectra (exclusive of the human input) for each controller was compared to the spectra of the pilot's transmitter (Tx) input, see Figure 103. The pilot input was clearly limited to low frequencies, whereas the servos' outputs (which include pilot inputs and the

inputs from FCS) operated at much higher frequencies. The servo command frequency in CL1 was proportional to the perturbations rates (measured inertially by the IMU), which were significantly lower than the flow disturbance rates due to the inertia of the MAV. However, when using CL2 the servo command frequency was proportional to the combination of frequencies of the oncoming flow disturbances (since a direct input was the flow pitch angles). Figure 103 also confirmed that the pilot workload reduced significantly when using CL2 in contrast to CL1 for both Monash and RMIT flights and that in the Monash flights the pilot workload was significantly lower (for CL1 and CL2) than the RMIT flights.

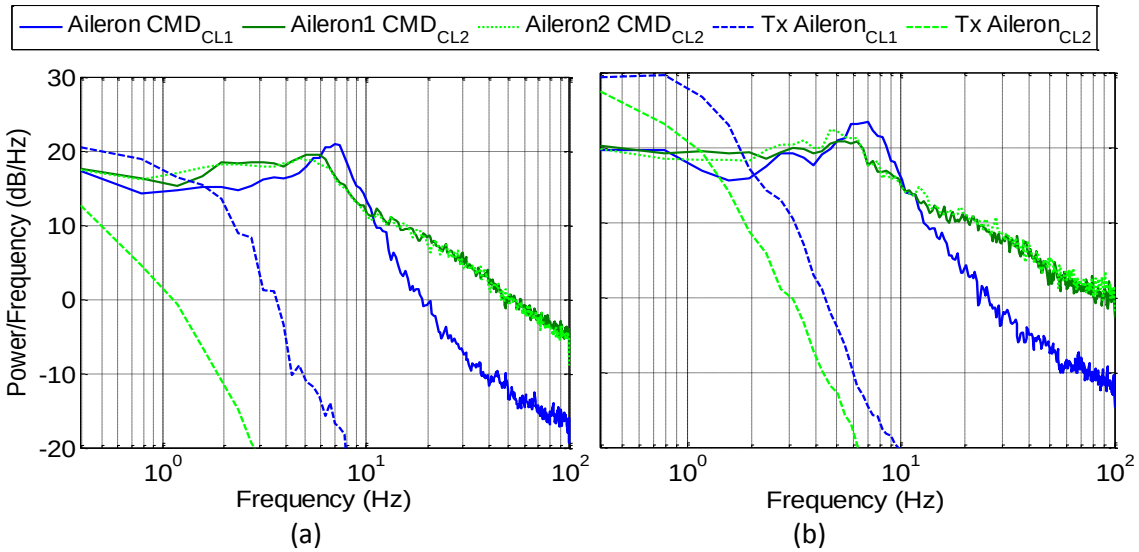

Figure 103: Spectra of aileron CMD and pilot input (Tx) through RC transmitter (a) Monash flight (b) RMIT flight

6.1.2 Measuring Turbulence using the Pitch Probes

It is a difficult task to erect 10m high masts (approximate flight altitude of MAV outdoors) to house the Cobra probes for atmospheric turbulence measurements. Even if this was done, the measurements would not represent the turbulence experienced by the moving MAV. It was therefore realised that the on-board pitch probe sensors could be useful to measure relative turbulence. Although not directly related to the research objectives, airborne measurements of relative turbulence proved useful for outdoor flight testing. To ensure that the turbulence measurements through the pitch probes are accurate, the turbulence spectrum inside the wind-tunnel was measured through stationary measurements (fixed position relative to tunnel walls) and follows the widely accepted -5/3 decay law, as shown through the Von Karman fit (see Figure 104). Turbulence measurements taken during flight (i.e. while airborne) are also shown, which were affected by the vehicle's motion showing spectral attenuation at frequencies >15Hz (see red curve in Figure 104).

As the MAV travels through turbulence the pitch probes move with the gusts due to the finite rigidity of the foam wings (see Figure 105). This movement with the gusts seems to have attenuated the signal output of the probes, thus leading to the reduction in spectra. Ideally, the MAV motion can be subtracted from the probe signal to enhance the accuracy of the measurements, however this was not within the scope of this research. The accuracy of the airborne turbulence measurements were deemed sufficiently accurate to estimate the longitudinal turbulence during flight. Additionally, the more stable the MAV becomes the better the measurement output. Consequently, the turbulence measurements measured during CL2 seemed to experience less spectral attenuation. This is evident in Figure 106, which shows the turbulence spectra measured during test flights conducted within the Monash and RMIT Wind Tunnels. The effect of vehicle motion on the Ti measurement for the different tunnels is presented in Table 12.

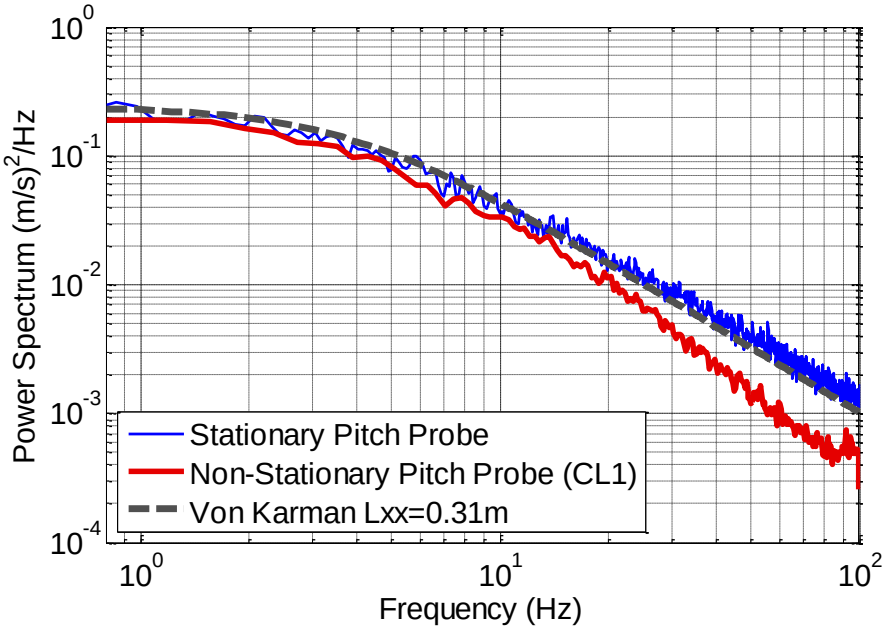

Figure 104: Longitudinal turbulence spectrum measured within RMIT Industrial Wind Tunnel (Ti=12.6%) using pitch probes fixed relative to tunnel floor.

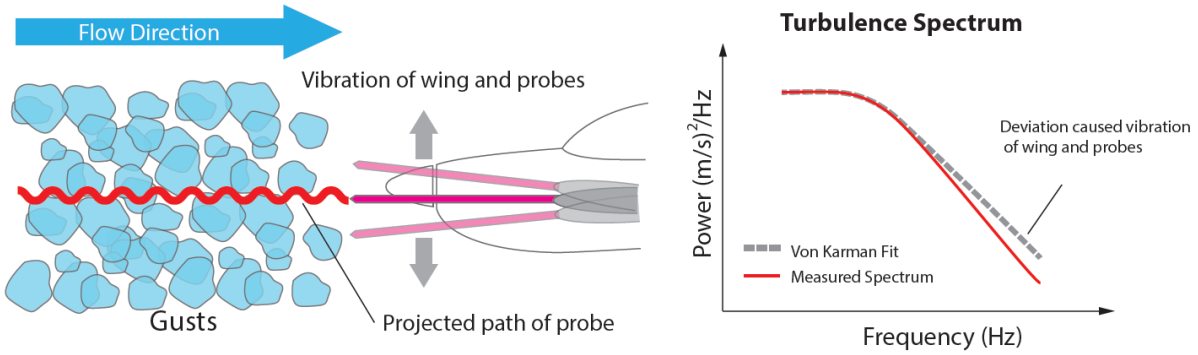

Figure 105: Effect of aircraft motion on turbulence measurement

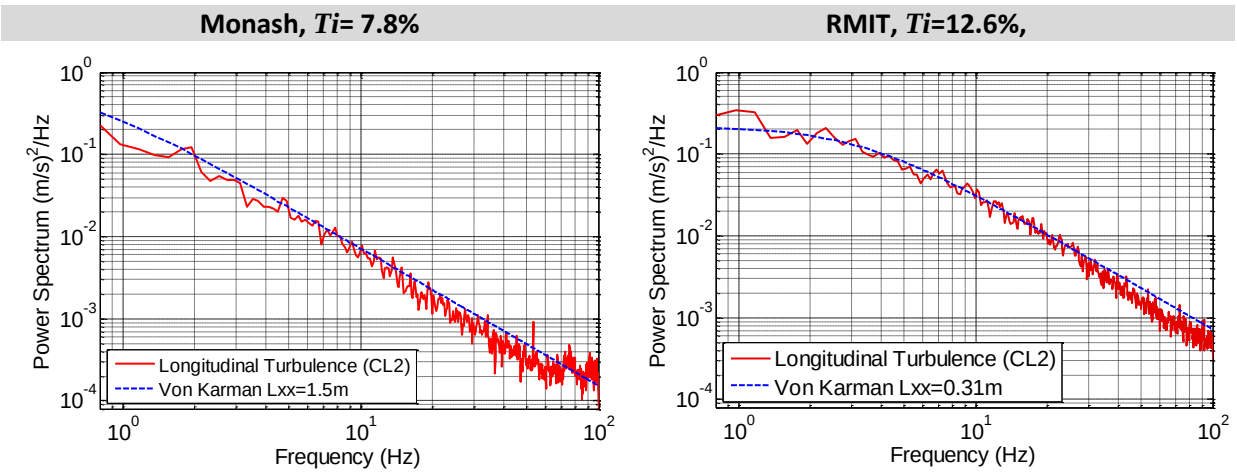

Figure 106: Turbulence spectra measured using the pitch probes during flight

Table 12: Airborne measurements of turbulence (using pitch probes) compared with static measurements

	Ti_{STATIC}, (%)	$Ti_{AIRBORNE}$, (%)
RMIT WIND TUNNEL	12.6	13.2
MONASH WIND TUNNEL	7.8	9

6.2 Outdoor Flight Testing

Turbulence in the atmosphere contains larger length scales (L = 16.4m) compared to that artificially generated in the wind-tunnels. It is expected that larger L, which contain lower frequency components, would be less perturbing and the effects would be considered increasingly quasi-static as frequencies reduce. In order to assess this and to trial the system, a larger range of turbulence length scales are tested through outdoor flight trials (see Figure 107).

Due to safety regulations flight testing in a city environment was not possible. This test site was chosen due to the large number of surrounding trees and low-rise buildings, ensuring a turbulent environment (Ti = 8.3%). The altitude for the flight tests was held relatively constant and below the height of the surrounding tree tops (~10m above ground). This height ensured the MAV was well immersed within the wake turbulence of the surrounding trees and buildings. Flights under a variety of wind speeds were tested. The faster the MAV travels relative to the gusts the lower the perceived turbulence becomes as discussed in Section 1.4.2. To ensure the MAV experienced the highest Ti, wind speeds close to the MAV's cruise speed (10ms^{-1}) were chosen. Such high wind speeds allowed the MAV to maintain a straight flight path for a longer period. Furthermore, the MAV ground speed was very low, allowing a similar test condition as that in the wind-tunnels.

The MAV was flown in the flight pattern shown in Figure 109. This pattern was intentionally chosen to ensure minimum directional input from the pilot, and consistency in the turbulence conditions for each test segment. The straight pass (green path in Figure 109) was conducted at a very low ground

speed of ~0.3ms^{-1} to replicate same test conditions during the wind-tunnel flights. As discussed previously the faster the aircraft flies through the turbulence the lower the relative Ti becomes. The entire turbulence spectrum also slightly shifts upwards. Once the MAV reached the end of the segment, the pilot would reduce throttle, and input minor yaw and pitch commands to bring the vehicle back to the starting position. Only data collected for the straight segments of flight were analysed. Unlike the wind-tunnel flights, where the data from the flights was combined to a total of 15 minutes, outdoor flights were not combined. This was due to the variable conditions of the atmospheric boundary layer. Subsequently, the results presented in Section 6.3.2 are for a single outdoor flight for which the highest encountered Ti was recorded (Ti = 8.3%). The total flight time for a single test was 300s, with 150s of data collected for each of the two controllers.

Figure 107: Outdoor flight of MAV

Figure 108: Selected site for outdoor flights (coordinates: 37°43'20.6"S 145°01'58.6"E)

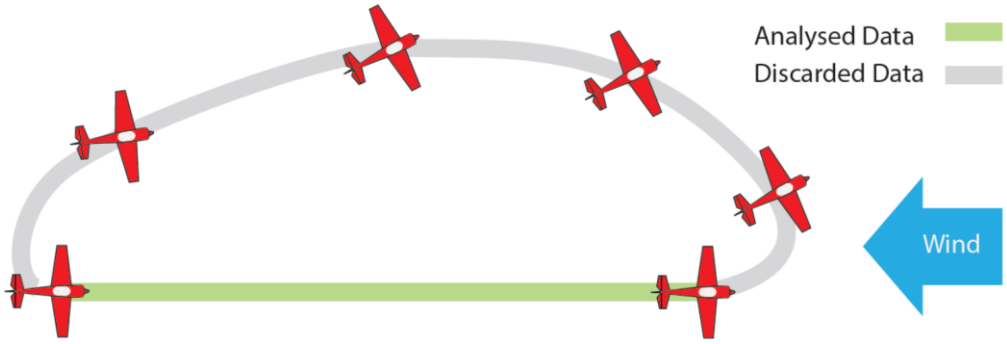

Figure 109: Flight path of MAV during Outdoor flights

A typical measurement of the turbulence spectrum using the pitch probes is illustrated in Figure 110, from a single flight duration of 300s. The corresponding Ti and L_{xx} were 8.3% and 16.4m respectively. The relatively large L_{xx} is comparable to the characteristic lengths of buildings upstream of the test site. For reference, the airborne spectral measurements were compared with the spectra measured within the wind-tunnels (Figure 111). To demonstrate how the measured spectra compare with atmospheric turbulence, the atmospheric spectrum measured by Milbank et al. (2005) is presented as a dashed green line in Figure 111. Milbank et al. (2005) measured the turbulence from a moving vehicle with an Indicated Airspeed (IAS) of 10m/s (representative of MAV flight). The measurement was conducted in a densely populated area in the presence of moderate breeze winds (Beaufort wind force scale = 4). The wind-tunnels exaggerate the higher frequency components of the turbulence spectrum. The scale of the roughness elements (i.e. buildings, trees, mountains, etc.), which induce the turbulence in the atmosphere, are much larger and therefore more power was evident in the low frequency components.

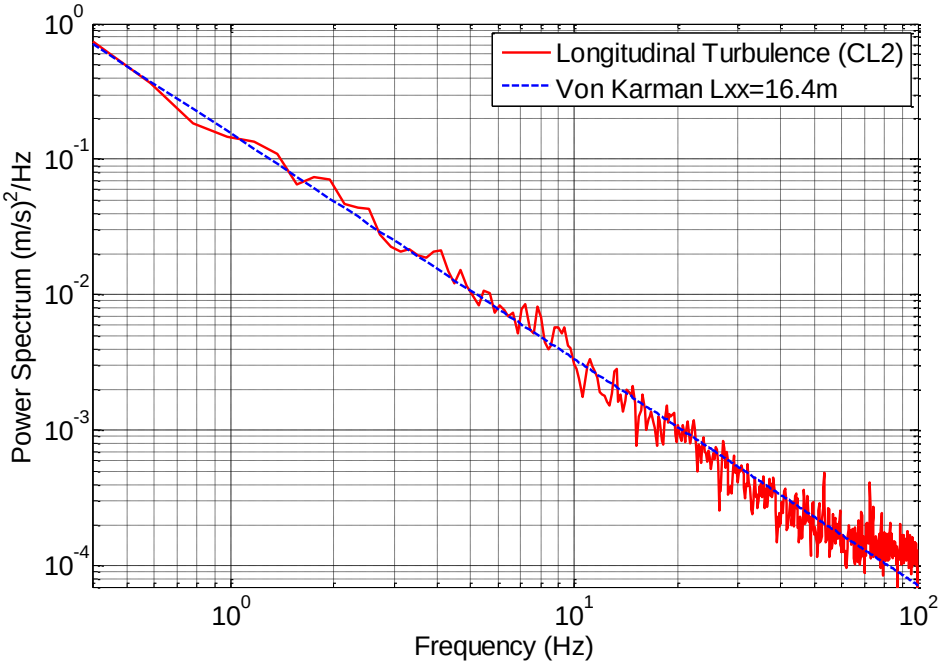

Figure 110: Airborne measurement of turbulence spectra measured by probe during outdoor flight

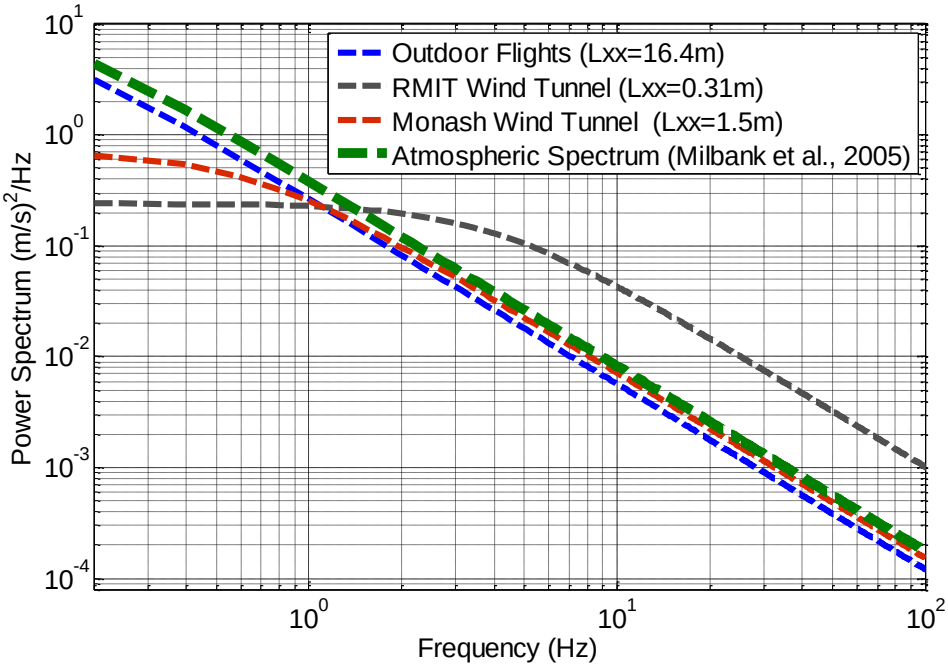

Figure 111: Airborne measured spectra compared with static measurements within the wind-tunnels and atmospheric spectrum extracted from the literature

6.3 Results

6.3.1 Results from Wind-Tunnel Flight Testing

Results from testing at the moderate and high Ti for the two tunnels are presented in Figure 112 through to Figure 114. The figures are histogram plots of the attitude perturbation and angular rate (for roll and pitch), which are representative of the disturbance rejection performance of the controller (commanded angle was level flight). For ease of comparison, the scale of the y-axis was kept constant for the contrasted histograms.

For moderate Ti (Monash Tunnel), the boxplot range (i.e. 95% of the data) of roll angle displacements were observed to be 28% less for CL2 than CL1 (see left column of Figure 112). A similar reduction in boxplot range (32%) of roll rate perturbation was evident when using CL2. CL2 also shows lower dispersion of data around 0°. The PDF peak was also significantly higher for CL2 around 0° in contrast to CL1, implying a lower spread in data about the desired angle of 0°. The roll rates (see bottom left corner of Figure 112) verify the roll displacement results showing a significantly lower distribution in data.

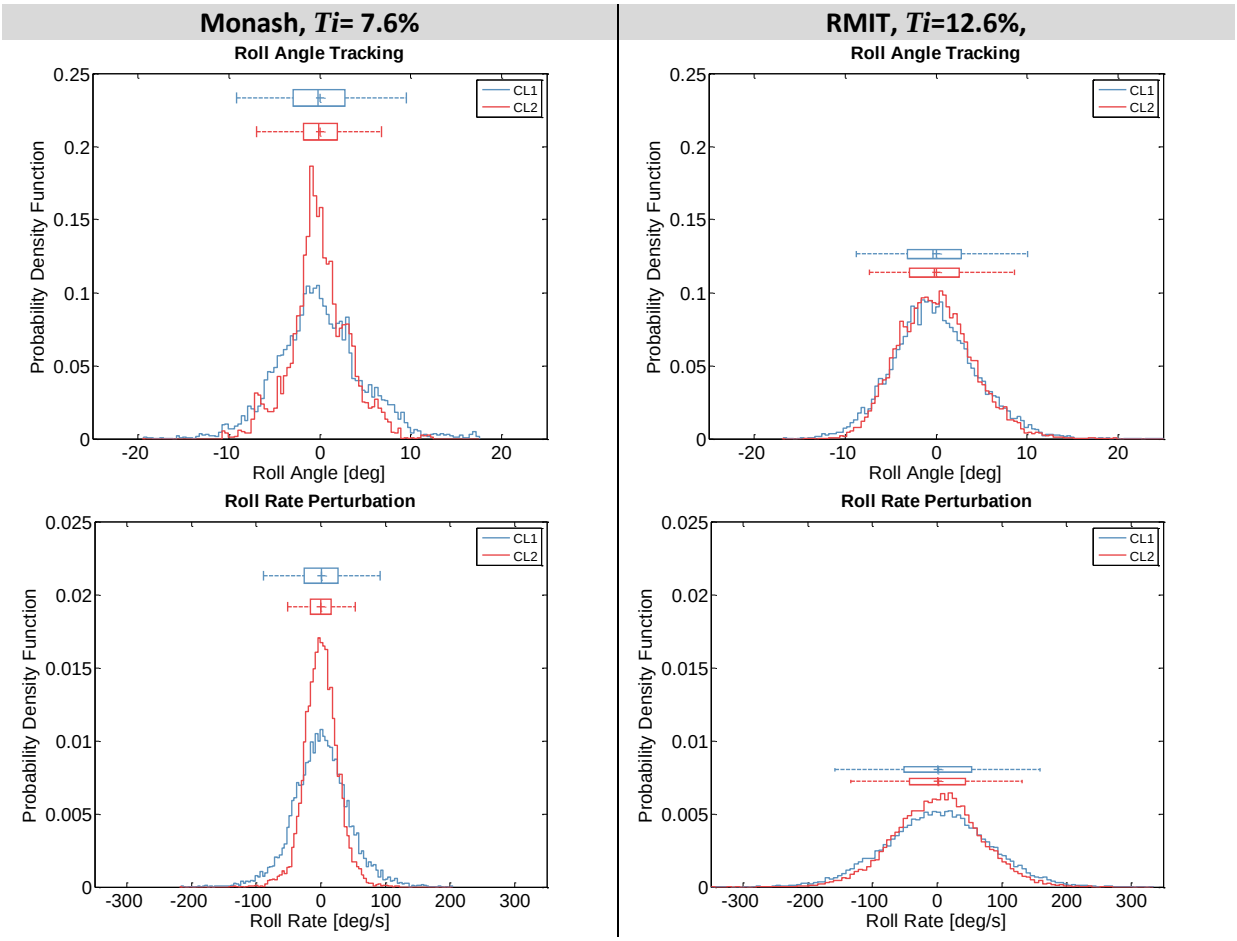

Figure 112: Roll Perturbation comparison for CL1 and CL2

In contrast, the flights within the RMIT Wind Tunnel did not show the same level of improvement (see right column of Figure 112). There was a 15% reduction in the boxplot range of roll angle perturbation data for CL2 compared to CL1, and 16% reduction for roll rate. The reduction in performance was considered due to the increase in Ti and difference in L between tunnels. The roll angle and roll rate histograms for both CL1 and CL2 show more dispersion about the desired angle of 0°. The commanded aileron deflections of CL2 were much closer in amplitude to those commanded in CL1. Whereas, for flights in the Monash Tunnel, commanded deviation in aileron for CL2 were much smaller than CL1. As expected, more aerodynamic control authority is required to cater for higher Ti and smaller L.

The pitch angle perturbation results presented in Figure 113 were biased with a mean of ~10°. This was due to the symmetric airfoil of the MAV, which requires a positive AoA to maintain level flight. Subsequently, a 10° pitch angle trim was programmed in the FCS. Improvements in pitch angle displacement and pitch rate performance were also observed between the two controllers. The boxplot range of the pitch angle displacements of CL2 are 41% and 31% less than CL1 for the Monash and RMIT flights, respectively. However, the pitch rates do not share the same magnitude of improvement of CL2 over CL1, where the improvement was limited to 25% and 9% for the Monash

and RMIT flights respectively. This was an interesting finding, as there was no difference in the pitch control architecture between the two controllers, thus the improvement in pitch perturbations was a secondary effect. The adverse yaw effect discussed in Section 3.2.1 was more evident in CL1 than CL2. This involves the aircraft yawing in the direction opposite to the rolling direction, thus resulting in a pitch angle displacement relative to the flow. The adverse yaw effect (and induced pitch angle variation) was observed during large aileron deflections, which occur frequently for CL1. Subsequently, adverse yaw increases the dispersion of the pitch angle displacement as observed from the results. The FCS detects this pitch angle variation and attempts to correct for it by commanding the elevator. The aileron deflections in CL2 are limited to smaller and faster uncoupled deflections (less overshooting), which reduce the pitch angle variation improving the pitch angle dispersion. The yaw rates presented in Figure 114 confirm this, showing similar improvement of CL2 over CL1 of 12% and 16% for the Monash and RMIT flights respectively. This improvement was due to the attenuated adverse yaw effect. Due to the higher Ti, more dispersion of yaw rates were evident in the RMIT flights.

Adverse yaw could have been minimised in CL1 by utilising aileron differential; whereby the up-going aileron deflects to a greater extent than the opposing down-going aileron thus generating equal drag on both wings and net zero yaw (Perkins and Hage, 1949). However reducing the adverse yaw effect was beyond the scope of this work, and is an unintentional secondary beneficial effect of CL2.

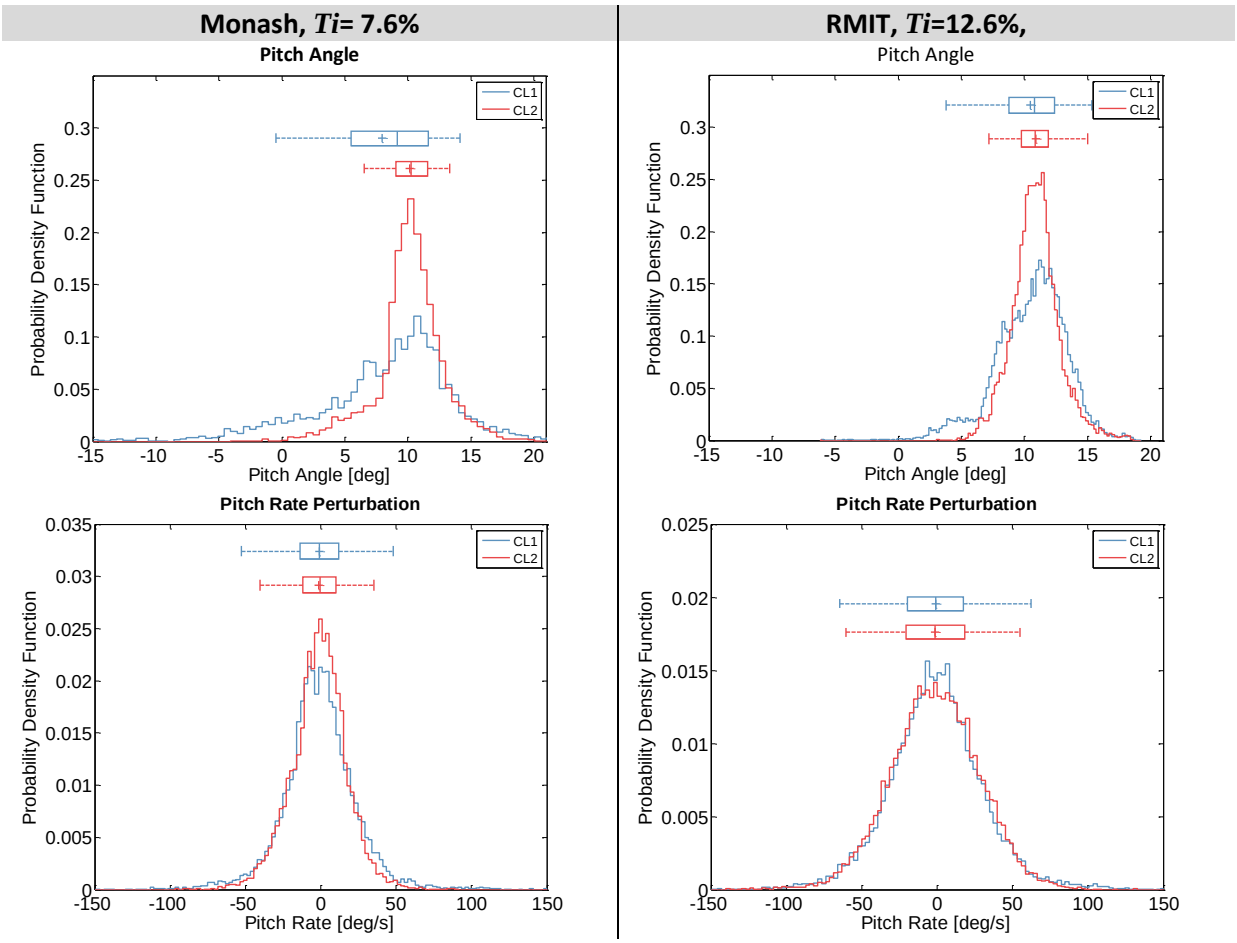

Figure 113: Pitch Perturbation comparison for CL1 and CL2

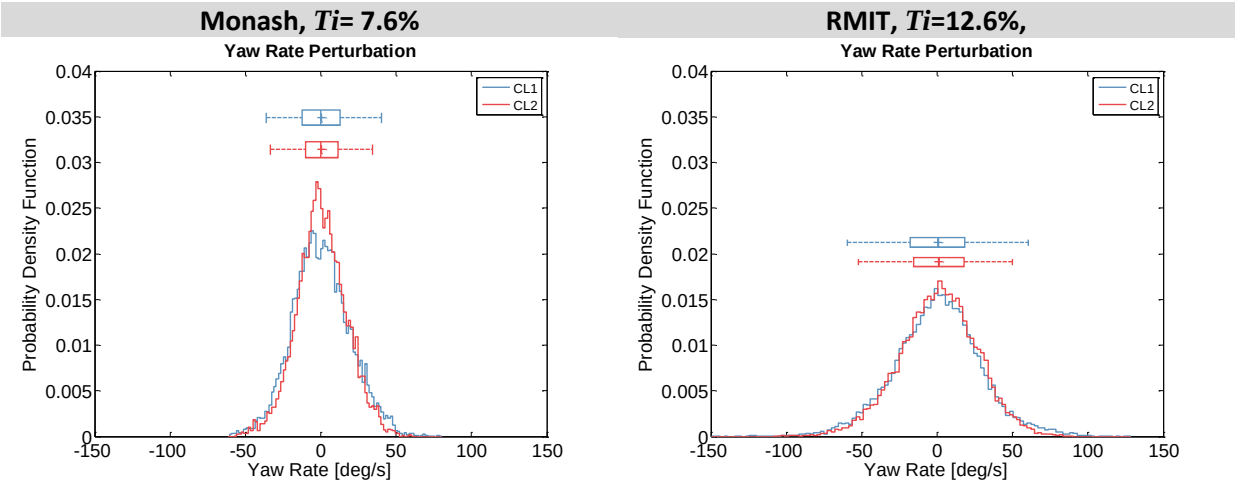

Figure 114: Yaw rate comparison for CL1 and CL2

Although not directly associated with the research objectives, an interesting observation associated with the tested L was the heaving motion of the MAV. The large length scales (L_{xx}=1.5m) in the Monash Wind Tunnel resulted in significant heaving motion compared to the flights in the RMIT Tunnel. In Figure 115 the vertical accelerations (which represent heaving) for CL1 and CL2 are compared. It was evident that heave disturbance rejection (using CL2) was more significant during the Monash flight in contrast to the RMIT flights. Due to the higher turbulent energy in the RMIT

Wind Tunnel, the dispersion in vertical accelerations was greater than those observed in the Monash flight. CL1 attenuated the vertical accelerations (i.e. heaving) solely through the elevator commands. The latter involves changing the MAV's pitch angle, thus increasing the dispersion of the pitch angle displacements. In contrast, CL2 accounts for heaving through the use of both the elevator and ailerons, where the deflections produced while encountering a large gust translates the MAV vertically with less pitch angle variation. This explains why the dispersion in the pitch angle recorded for flights in the RMIT Wind Tunnel was lower.

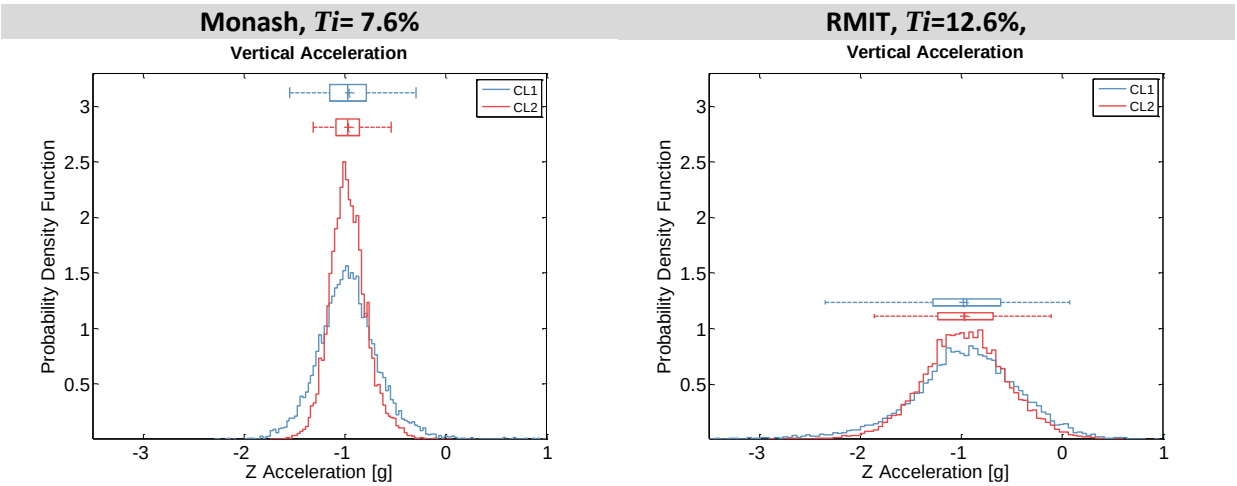

Figure 115: Vertical acceleration comparison for CL1 and CL2

6.3.2 Results from Outdoor Flight Testing

The disturbance rejection performance of the outdoor flights showed similar results to the Monash flights, due to the similar Ti (8.3%). The most noticeable improvement of perturbations was once again evident in the roll axis, (see Figure 116). The range of the boxplot representing roll angle displacements was reduced by 30%. Roll rate boxplots also show a reduction of 35% in the perturbation range of CL2 relative to CL1.

It was evident that the PDF of pitch angle displacements was noticeably higher for both CL1 and CL2 relative to both wind-tunnel results (see Figure 117). This implies better pitch angle tracking of the MAV in turbulence with large L. CL2 reduced the boxplot range of pitch angle displacement by 45% and pitch rate by 9%. The reduction of pitch rate using CL2 was less than the Monash Flights, due to the significantly larger L of the turbulence. A higher peak in the PDF value at 0° for both CL1 and CL2 implies less overall pitch perturbations experienced outdoors. L most detrimental to MAV attitude stability are those equivalent to the wing span (Lissaman, 2009). The large length scales (~16m) measured in the outdoor flights are more easily rejected as a quasi-steady change compared to the smaller more rapid L. The frequency associated with the outdoor length scales (~0.6Hz) was small and easily accounted for by the control system. CL2 was well adept at reducing the pitch perturbations induced by large L through uncoupled deflection of the ailerons (i.e. as flaperons).

The yaw rates boxplot ranges were reduced by 18%, see Figure 118. The reduction in yaw rate dispersion was due to the difference in the amplitude of the aileron deflections of CL2 compared to CL1, where CL2 had smaller faster aileron deflections, subsequently reducing adverse yaw. CL2 has enabled significant reduction in pitch perturbations, which was evident from the noticeably narrower and higher peak of the PDF.

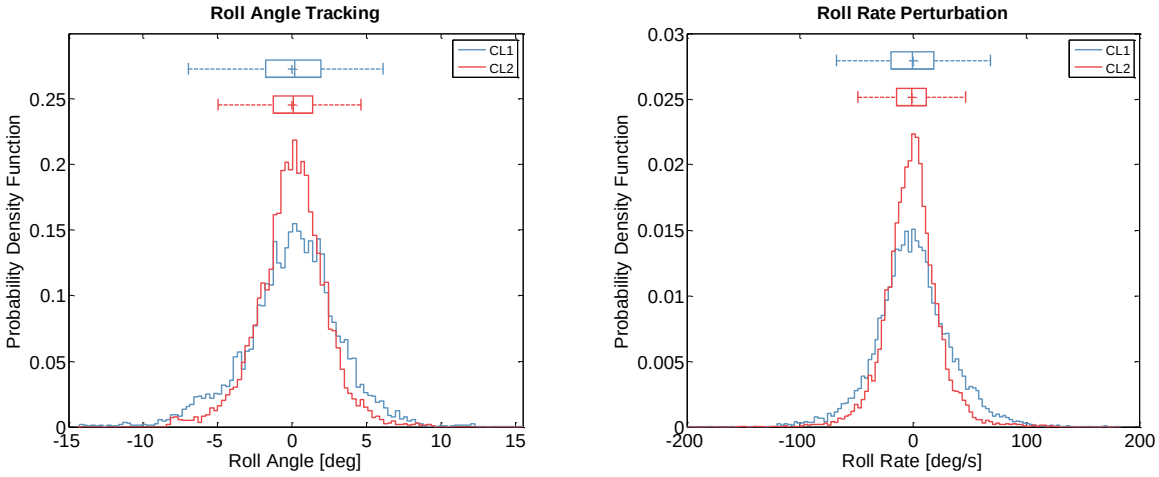

Figure 116: Outdoor roll perturbation comparison for CL1 and CL2

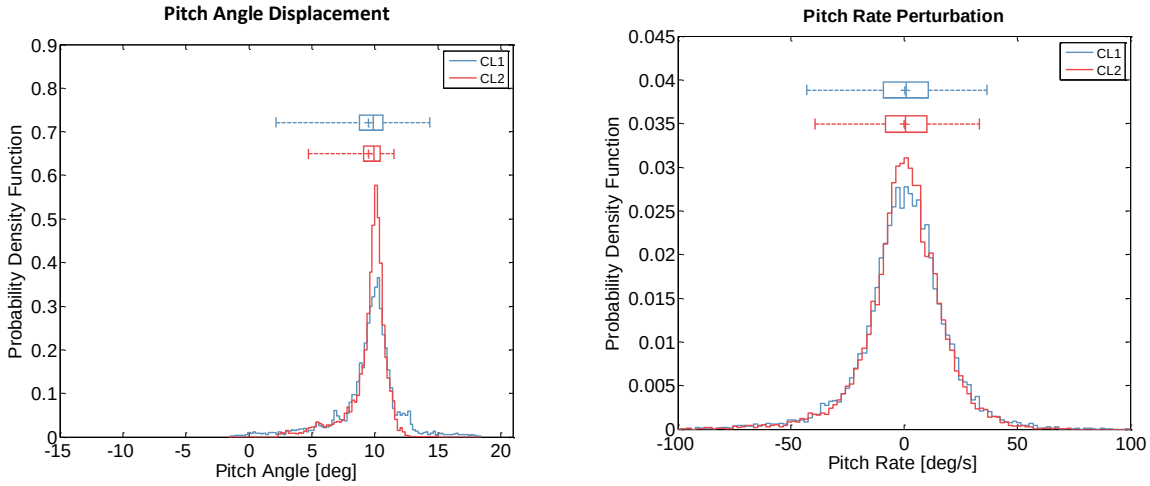

Figure 117: Outdoor pitch perturbation comparison for CL1 and CL2

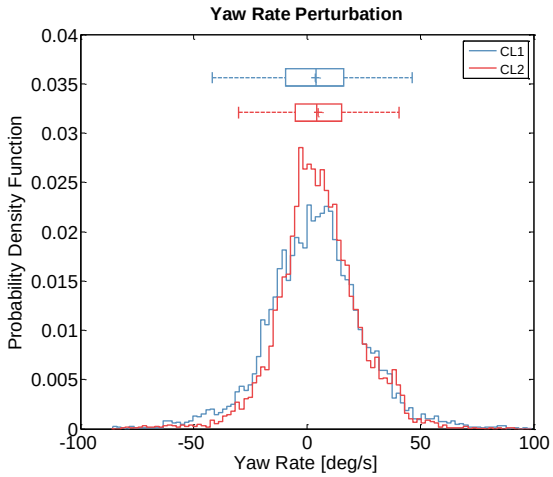

Figure 118: Outdoor yaw perturbation comparison for CL1 and CL2

6.4 Discussion and Consideration of Error

Minor biasing can be observed in the aircraft's roll perturbation results (Figure 116 to Figure 118). This is attributed to the motor and propeller, whereby the vehicle has less opposing torque while turning to one side compared to the other. Furthermore, minor fabrication defects in the shape of the wings may lead to minor asymmetric drag from the wings resulting in a small yaw bias. Other potential sources of error, which may degrade the disturbance rejection performance, include:

1. **Accuracy in prediction of oncoming flow disturbances:** Ideally, the flow angle variation forward of the entire span of the wing's leading edge should be measured and a weighted average of its effects on roll input be used as an input to the controller. However, it was not practical to implement a large number of probes for such a small aircraft and only one probe per wing was used. The probe was effectively positioned along the wingspan in the region that has been shown to attain the highest correlation between upstream flow pitch angle and roll acceleration, see Chapter 4.
2. **Limited actuation speed and control authority:** Although fast commercially available servo motors where utilised (20Hz), the response rate was still slower than the MAV's maximum perturbation acceptance frequency (~60Hz). As actuation rates improve to levels near the perturbation rates through technological advancements, disturbance rejection performance will also improve.

The repeatability of the wind-tunnel flights was demonstrated in Figure 101 showing acceptable variation (<7%) in the most turbulent tested conditions within the RMIT Wind Tunnel. As expected, during outdoor flight testing, it was challenging to get acceptable repeatability as a consequence of the constantly changing weather conditions. During the outdoor flight test campaign (which spanned over several days) the highest recorded turbulence during flight were selected and presented.

6.5 Concluding Remarks

This chapter set out to explore the potential of phase-advanced attitude sensors to mitigate attitude perturbations for MAVs compared with traditional inertial-based sensors. Turbulence characteristics most detrimental to the chosen airframe (with respect to the replicated Ti and L), were conservatively replicated within the controlled environment of wind-tunnels, before proceeding to outdoor flight testing in atmospheric turbulence. By a measured reduction in the variation in perturbations (e.g. roll angle and acceleration), which was significantly greater than the repeatability and errors in the system, it was demonstrated that the phase-advanced system was better at mitigating the effects of the atmospheric turbulence; both replicated in wind-tunnels and outdoors.

The replicated relatively high intensity turbulence within the RMIT Wind Tunnel, combined with the control architecture placed high demands on the servos. As expected, the higher Ti and smaller L (relative to the MAV wingspan) were most detrimental to the disturbance rejection performance. This was evident from the relatively higher perturbation rates of all axes observed during the RMIT flights visually and through the data. This indicates the need for faster actuation and perhaps greater control authority (i.e. larger ailerons and/or movement) for mitigating these high perturbation rates. As MAV scales reduce, it is considered that actuation will be a limiting factor in any turbulence mitigation control strategy. The Monash flights represented less severe turbulence conditions, which were expected to often occur during MAV operations. The control system was shown to cope with the turbulence replicated in the Monash Wind Tunnel with significant improvements of the phase-advanced sensing over traditional inertial-only sensing. Outdoor flight-testing enabled more realistic larger L to be tested, whereby the disturbance rejection performance of the phase-advanced system again demonstrated superior results to a traditional IMU control system. The system also had secondary benefits in terms of reducing heave motion and adverse yaw.

Chapter 7
Conclusions & Recommendations

Summary

This chapter summarises the findings presented in this thesis. Key findings and conclusions from each chapter are summarised and recommendations for future research are outlined. Journal papers published from the research are given.

7.1 Thesis Conclusions

The research presented in this thesis was inspired by birds' ability to gracefully navigate through turbulence. This motivated an exploration of the physics underlying the disturbance (turbulence) along with the avian biological systems associated with sensing the disturbances. The latter exploration aided the introduction of the Gust Perturbation Process, which outlines the sequence of events that lead to attitude perturbations. The Gust Perturbation Process aided the identification of phase-advanced sensors capable of sensing flow disturbances before they result in an inertial response. These sensors were reviewed relative to conventional inertial based attitude sensors where their advantages and possible implementations were explored. An aerodynamic study was conducted to aid the selection and placement of a simple sensory system. Based on pressure probes, the system was capable of sensing the most significant feature of turbulence upstream before a perturbation is initiated providing the control system extra time to counteract it.

The system was tested within the controlled turbulence environments of the wind-tunnels and outdoors. The flights conducted within the RMIT Wind Tunnel possibly represent the most challenging turbulence conditions encountered by MAVs of this scale with respect to the replicated Ti and L. The Monash Wind Tunnel flights represented more likely turbulence conditions, which are expected to often occur during MAV operations. The control system was shown to cope with the turbulence replicated in the Monash flights with significant improvement of the phase-advanced sensory system over a conventional inertial-based sensory system. Outdoor flight testing enabled more realistic (larger) L to be tested. The phase-advanced attitude sensing and control system coped with the larger L of turbulence and significantly mitigating the induced perturbations. Thus, flight testing has proven the feasibility of phase-advanced attitude sensing as an additional useful input to inertial-based attitude control system.

The research has elevated the Technology Readiness Level (TRL) from 1 to 7. The TLR definition used corresponds to that of National Aeronautics and Space Administration (NASA) (Mankins, 2009). The tested system has the potential to significantly reduce the size, cost, weight and power for micro unmanned systems through removing or reducing the need for expensive gimbal-stabilisation systems required to mitigate the impact turbulence has on MAV sensors. This directly translates to improvements in endurance and payload capacity of MAVs. Finally, flight path tracking in extremely turbulent environments can also be improved.

The key findings detailed in the thesis are:

1. Flow pitch angle of the oncoming turbulence attains the highest correlation with surface pressure fluctuation and roll acceleration. Regions in the vicinity of the wing's leading edge attain highest correlation with oncoming turbulence.
2. Perturbations rates induced by turbulence are evident up to 60Hz in the lateral axis (roll) for a 0.49m wing span fixed-wing MAV.
3. The time-forward advantage of surface pressure variation as a phase-advanced signal is typically < 6ms and was found to be too short to cater for the time-lags of the control system.
4. Multi-hole pressure probes can be used as phase-advanced sensors that are capable of supressing attitude perturbations through early sensing of flow disturbances before they induce an inertial response. The use of phase-advanced sensors can reduce attitude perturbations in all vehicular axes. Secondary beneficial effects are:
    a. Accurately measure relative turbulence
    b. Less flight path divergence
    c. Reduced drag
    d. Reduced adverse yaw

7.2 Summary of Original Contributions

This research is the first to publish the following in the public domain:

1. The concept of the Gust Perturbation Process, which outlines the sequence of events underlying a turbulence induced perturbation. The time-lags associated with controlling a perturbation have also been identified.
2. Categorisation of sensors (utilised by the attitude control system) as being either phase-advanced or reactive. This classification aided the identification of potential phase-advanced sensors including the multi-hole probe described in this thesis.
3. Assessing the performance advancements of a phase-advanced sensing technique for attitude control of MAVs through flight testing in high levels of turbulence. This was achieved by comparing disturbance rejection performance of the attitude control system in the controlled turbulence within wind-tunnel test sections in addition to field testing in atmospheric turbulence. Benchmarking the performance of phase advanced sensors with against conventional inertial-based attitude control system

7.3 Research Outputs

The work produced in this thesis has resulted in filing a provisional patent for the phase-advanced sensor system developed. Furthermore, aspects of the work presented in this thesis have been published in a number of peer-reviewed Journals as cited below:

1. **Mohamed A,** Massey K, Watkins S, and Clothier R (2014) "The Attitude Control of Fixed-Wing MAVS in Turbulent Environments", *Progress in Aerospace Sciences*, Vol. 66, April, pp.37-48.
2. **Mohamed A,** Clothier R, Watkins S, and Sabatini R (2014) "Fixed-Wing MAV Attitude Stability in Atmospheric Turbulence PART 1: Suitability of Conventional Sensors" *Progress in Aerospace Sciences*, Vol.70, pp.69-82.
3. **Mohamed A,** Watkins S, Abdulrahim M, Massey K, and Clothier R, (2014) "Fixed-Wing MAV Attitude Stability in Atmospheric Turbulence PART 2: Investigating Bio-inspired Sensors" *Progress in Aerospace Sciences* Vol.71, pp.1-13.
4. **Mohamed A,** Watkins S, Clothier R, and Abdulrahim M, (2014) "Influence of Turbulence on MAV Roll Perturbations" *International Journal of Micro Air Vehicles,* Vol.6 (3), pp.175-191.
5. **Mohamed A,** Watkins S, Fisher A, Marino M, Massey K and Clothier R, (2015) "A Feasibility Study of Bio-Inspired Wing-Surface Pressure Sensing for Attitude Control of Micro Aerial Vehicles", *AIAA Journal of Aircraft* (in press).
6. **Mohamed A,** Abdulrahim M, Watkins S, and Clothier R, (2015) "Development and Flight Testing of a Turbulence Mitigation System for MAVs" *Journal of Field Robotics* (under review)

7.4 Research Questions

Details of the how the research questions were answered are outlined below.

Research Questions	Result	Description
RQ 1.1	Answered	The flow pitch angle of the oncoming turbulence was found to strongly correlate with wing surface pressure fluctuations. Through mapping a large portion of the wing's top surface, the leading edge is found to be most responsive to the flow pitch angle. This experimentally validates the hypothesis suggested by Thompson and Watkins (2010).
RQ 1.2	Answered	Through a correlation study which utilized a roll-axis rig, surface pressure fluctuations near the leading edge of the wing were most correlated with perturbations in roll. The region along the span of the wing which produced the most lift (near mid-span), correlated well with perturbations in roll. A pressure-based probe was placed in this location to sense the flow pitch angle of the oncoming turbulence. High correlation between perturbations in roll and the flow pitch angle has been demonstrated.
RQ 1.3	Answered	Through using the sensed oncoming flow pitch angle as a dynamic control input to the attitude control system of a MAV, the attitude disturbance rejection performance was improved relative to traditional inertial based control systems. Attitude perturbations reductions were observed for all axes.

7.5 Recommendations

Further research stemming from the work presented in this thesis is suggested below:

- **6 DoF Attitude Control:** The embedment of two phase-advanced sensors in the MAV's wings was sufficient for enhancing the disturbance rejection in the roll axis. However, the minimum number of sensors required to enhance the disturbance rejection in the remaining aircraft axes is yet to be explored.
- **Ideal control architecture:** The time-forward measurements sensed by the phase-advanced sensor are used as a feedforward input into a standard PID controller. However, Model Predictive Control may represent an alternative control technique, which may further enhance the disturbance rejection performance.
- **Remote Sensing**: Pressure-based sensing was used to demonstrate the concept of phase-advanced sensors. However sensing the flow disturbances further upstream is inevitable at faster flight speeds. An investigation into the use of remote flow sensors such as LiDAR is necessary, in particular how technological advances will reduce mass of such sensor for employment by MAVs.

Appendix A: Error Considerations

Errors in measurements can be categorised as either precision or bias errors. The latter are those introduce a consistent error into the measurement, which can only be estimated by calibration to an accurate reference value. Precision errors (also known as repeatability errors) on the other hand represent the measurement scatter when repeating the measurements. Such errors are often a by-product of the experimental setup/conditions. Precision errors are measured by remeasuring multiple times in the same conditions to identify the variation. The sources of precision errors for specific experimental setups have been discussed within the corresponding sections. However, this section presents a quantitative measure of the precision errors.

Precision errors are considered to be of more significance, due to the nature of the presented experimental work, which mostly relies on differential pressure measurements (relative measurements). Experimental factors such as tubing length and AoA adjustment, pressure tap placement, and dynamic pressure (for non-dimensional coefficients) are assumed to cause the majority of error in results in relation to those created through bias errors. The following subsections therefore discuss and demonstrate repeatability results for key experiments to improve confidence in the setup and instrumentation used.

Pressure Measurement Error Considerations

The pressure measurements conducted through the wing embedded pressure taps have been repeated multiple times. Errors in the results were measured through error bars as demonstrated in Figure 119. Each repeatability run was conducted with the same conditions however at different times (some tests were conducted on different days after disassembly and assembly of experimental setup). The smooth flow results show that the error bars are relatively small with maximum error of Cp < 5% near leading edge (where non-linear flow phenomena occur) and average error of Cp < 1.5% for other pressure taps. Due to the random and chaotic nature of turbulence, the repeatability bars for the results taken in turbulent flow are larger relative to smooth flow results. It is important to note that the error bars in each graph represent worst-case 95% confidence intervals.

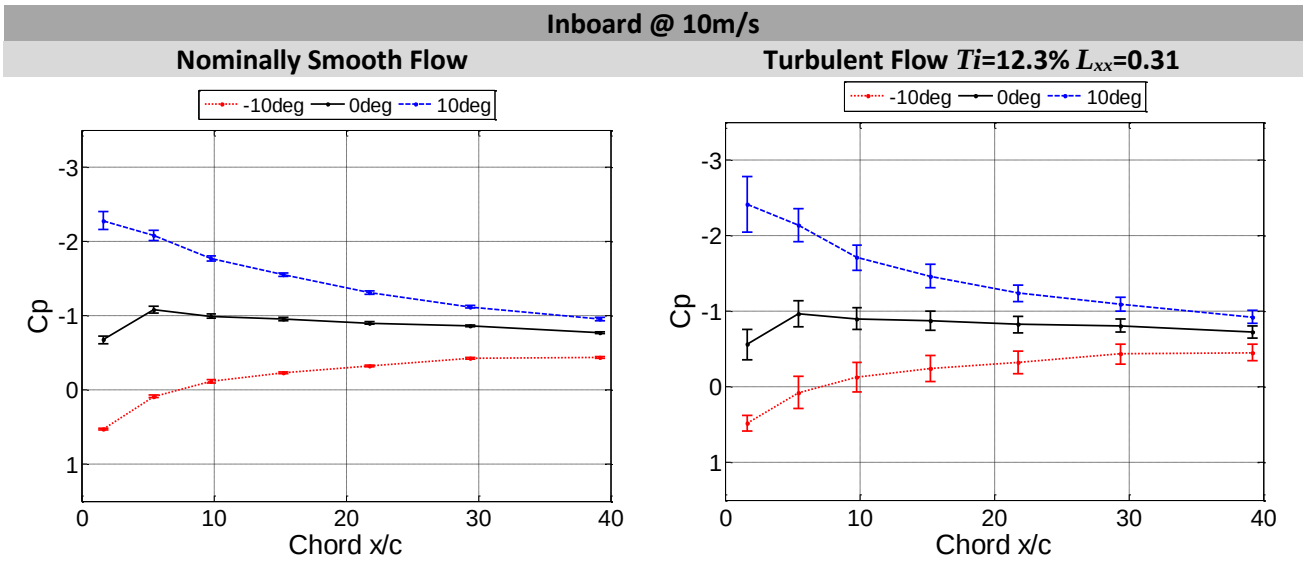

Figure 119: Repeatability of wing surface pressure measurements

Actuators Error Considerations

The servos used on the MAV were discarded after every test flight to ensure that the degradation over time does not influence the results. However, as further assurance, the repeatability was tested and is outlined in this section. The frequency sweep function discussed in Section 3.2.2 was used to test the repeatability the servos. The boxplots presented in Figure 120 show the deflection results for four randomly chosen servos. Each servo was subjected to 12 runs. Variation in deflection was below 2%.

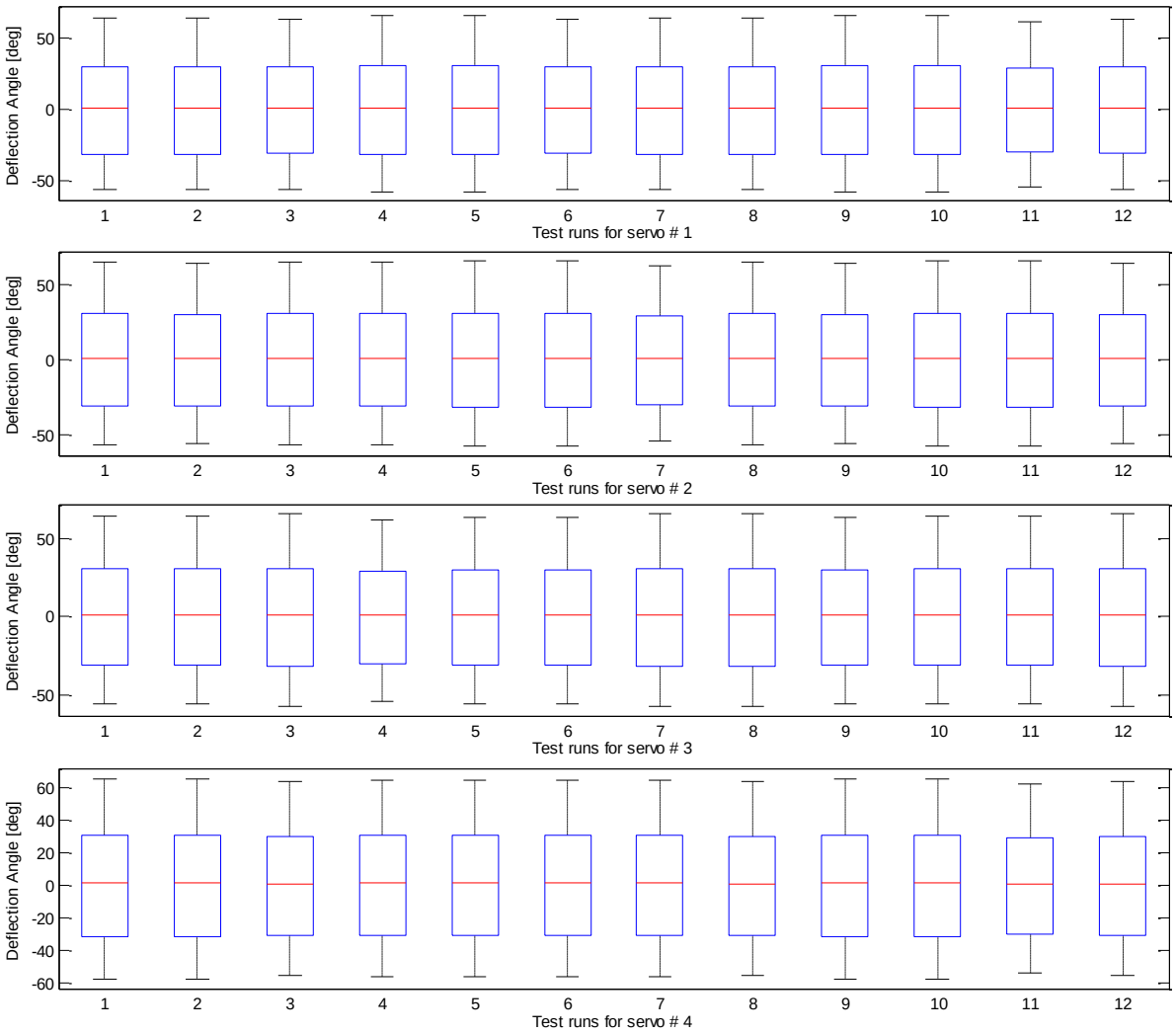

Figure 120: Repeatability of servomotor actuators

Repeatability of the disturbance rejection performance is highly dependent on the random oncoming turbulence, performance of actuators, and the wind-tunnel's ambient conditions. The attitude estimation results measured through FCS have demonstrated high repeatability. The roll rig results of Figure 121 show that the disturbance rejection results are fairly repeatable. This is evident from the boxplots and histograms from a series of three different runs. The maximum deviation in results was < 2%.

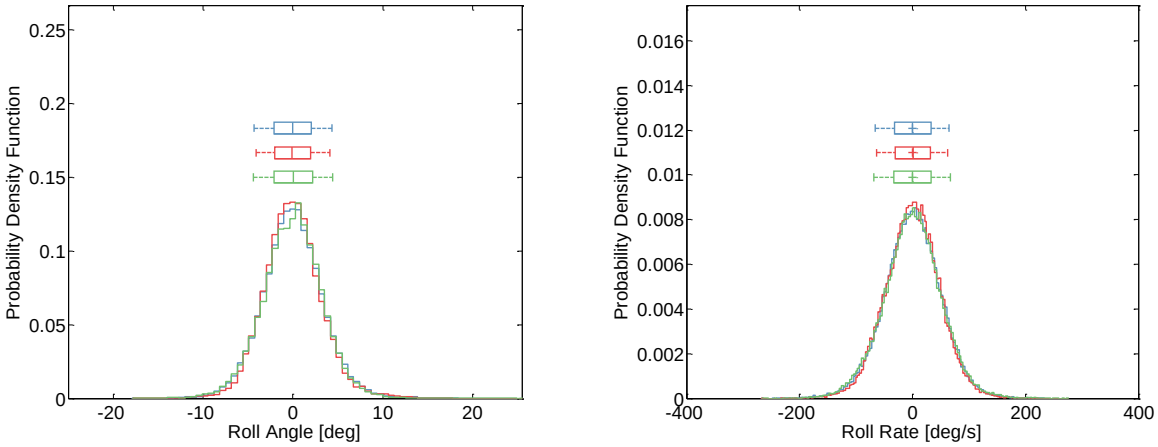

Figure 121: Repeatability results for attitude estimation of MAV while installed on the roll rig

Due to elevated turbulence, unconstrained flight within the RMIT Wind Tunnel has shown more variation in results (see Figure 122). Unlike the roll rig results in Figure 121, the presented histograms associated with unconstrained flight are also less uniform. This is expected since the vehicle is now allowed to perturb in all DoFs. Due to the sensitivity of the vehicle's roll axis to turbulence, the roll angle displacement results showed the highest maximum deviation (<7%). However, other axis showed less maximum deviation (< 5%).

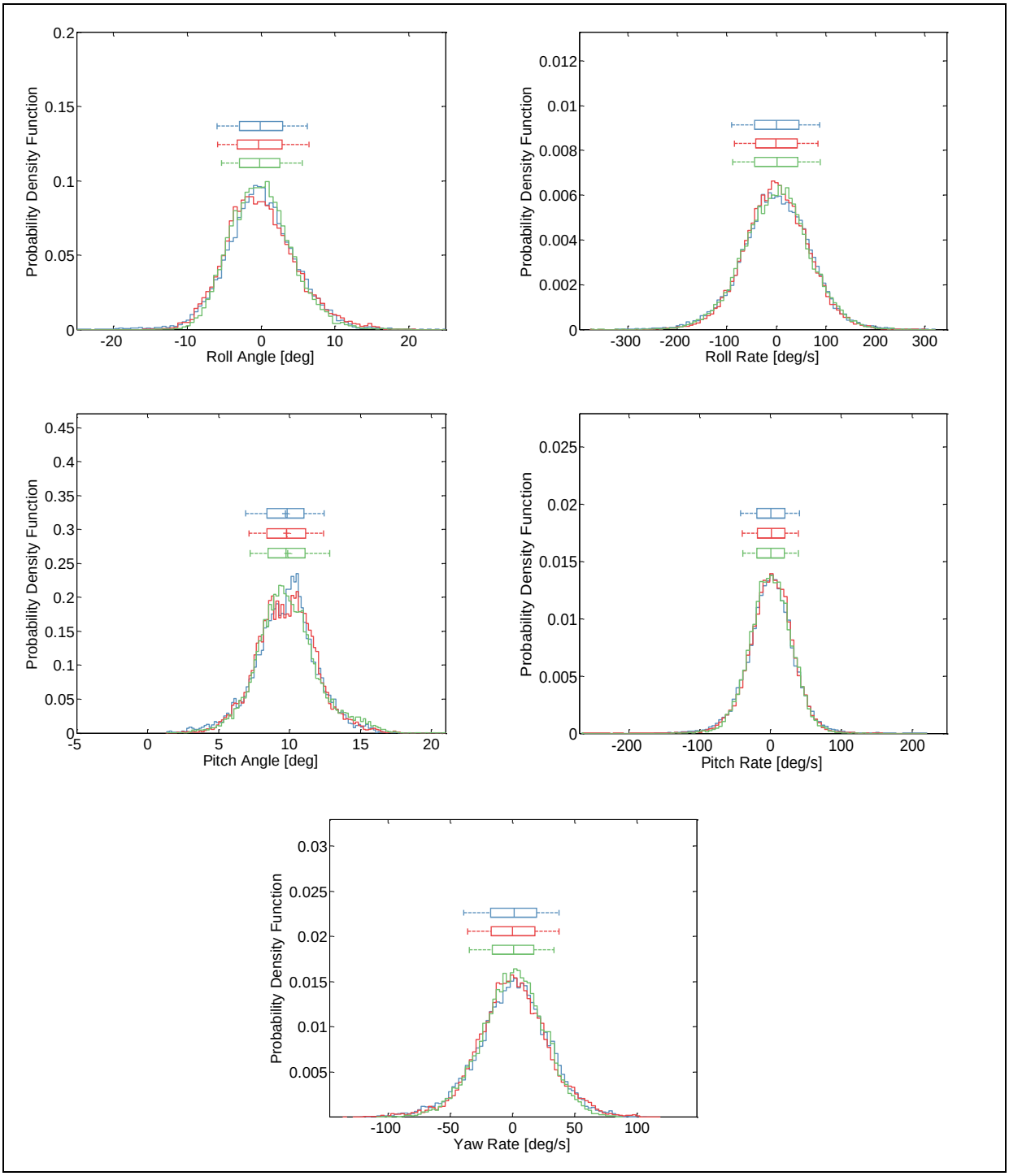

Figure 122: Repeatability results for attitude estimation of MAV flight within the RMIT Wind Tunnel

Appendix B: Smoothing of contour plots

The following Matlab code was used to smoothen the contours while differences in results are shown in Figure 123. Splines where created and then plotted.

```
m=70;
step=1/m;
xi=1:step:size(img,2);
yi=1:step:size(img,1);
[XI YI]=meshgrid(xi,yi);
imgs=interp2(img,XI,YI,'spline');
%-------------------------------------

x = linspace(24.88,84.8,421); % change last value when changinge resolution
M to match
y = linspace(5.44,15.24,141);% change last value when changinge resolution
M to match


figure(j);

 h_xlabel = get(gca,'XLabel');
 h_ylabel = get(gca,'YLabel');
 h_title = get(gca,'Title');

 set(gca,'FontSize',24)
 set(h_xlabel,'FontSize',26);
 set(h_ylabel,'FontSize',26);
 set(h_title,'FontSize',20, 'FontWeight' ,'bold');


 set(gcf, 'Units','pixels', 'Position',[100 100 1100 350])

 [hC hC] = contourf(x,y,imgs, 50);
 set(hC,'LineStyle','none');
 colorbar
 h=colorbar;
set(h,'fontsize',20);

 xlabel('Semi Span x/s');
 ylabel('Chord x/c');
 title('Determination Coefficient [R^2]');

 set(gca,'YDir','reverse');
caxis([0.00 0.81]);
```

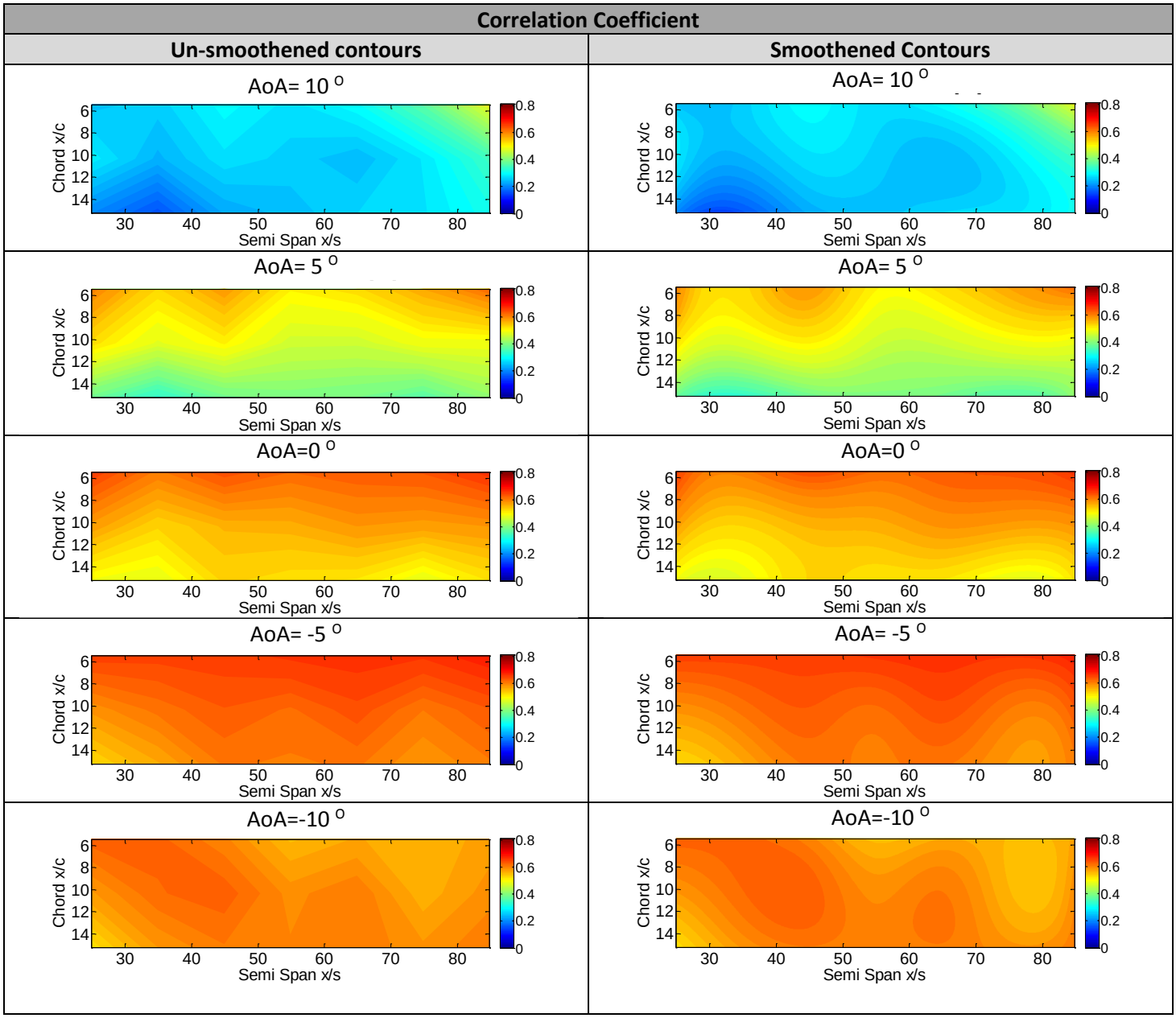

Figure 123: Smoothing function applied to contours

Appendix C: Validity of Taylor's Hypothesis

It is important to understand that the correlation results and the phase-advanced sensing concept presented are largely based on Taylor's hypothesis. The validity of Taylor's Hypothesis for atmospheric turbulence has been demonstrated for a range of L (Lappe and Davidson, 1963). Additionally the high levels of correlation in the results of Sections 4.3, and 5.3 imply validity over the (relatively) short distances between the upstream measurements and the MAV. Flow visualization was conducted to further demonstrate validity qualitatively (see Figure 124 and Figure 125). A film of smoke was released vertically at an upstream location in front of the right wing probe (see Figure 125). The smoke film is free to distort in all axes. This is of particular importance since the film was observed to oscillate laterally along the wingspan, where lateral flow will result in correlation reduction. Note that the flow direction is from right to left. In addition, the flow velocity was limited to $7ms^{-1}$ since at the MAV cruise speed ($10ms^{-1}$) the smoke dispersion is significant, degrading flow visualisation.

From the flow visualisation, it is evident that the validity of Taylor's hypothesis becomes questionable when the upstream distance is increased due to the incremental change in flow structure. However, the change in flow structure over the probe length is not detrimental.

t=10ms

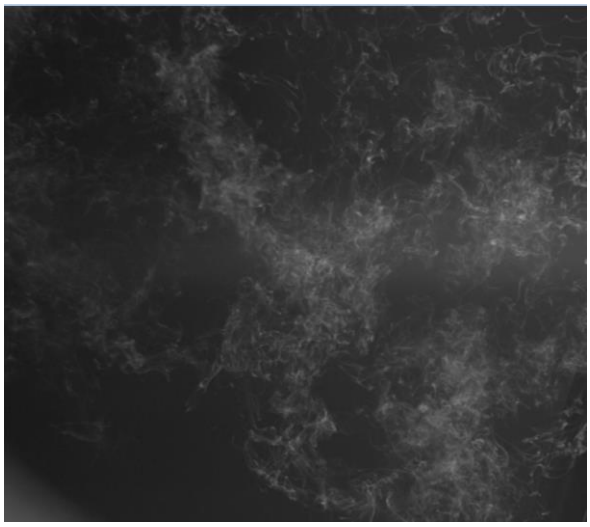

t=40ms

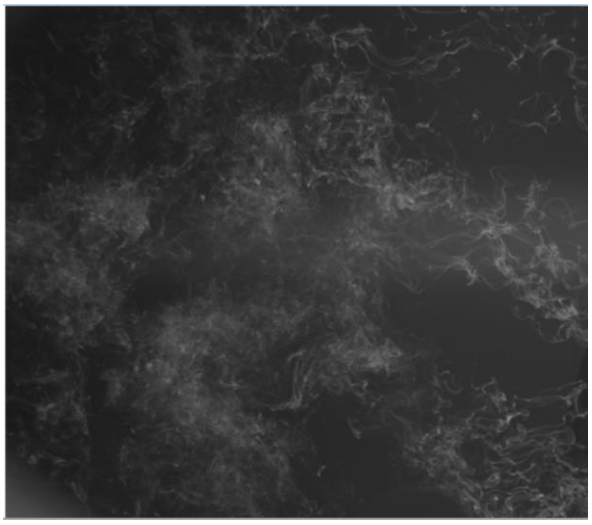

t=20ms

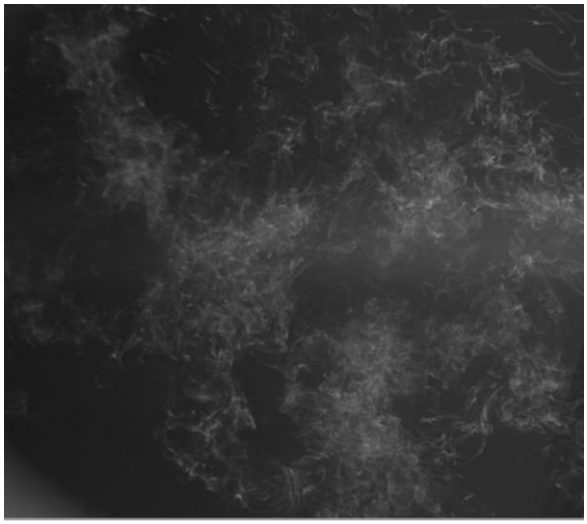

t=50ms

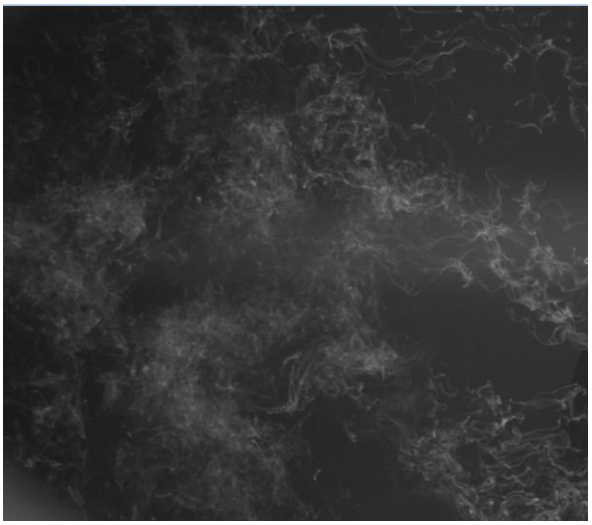

t=30ms

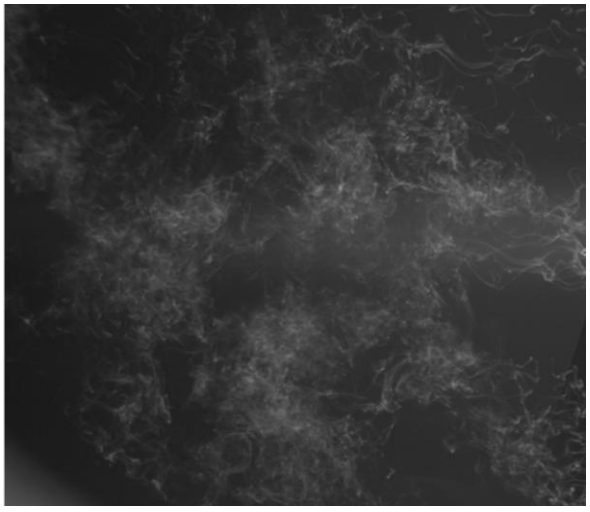

t=60ms

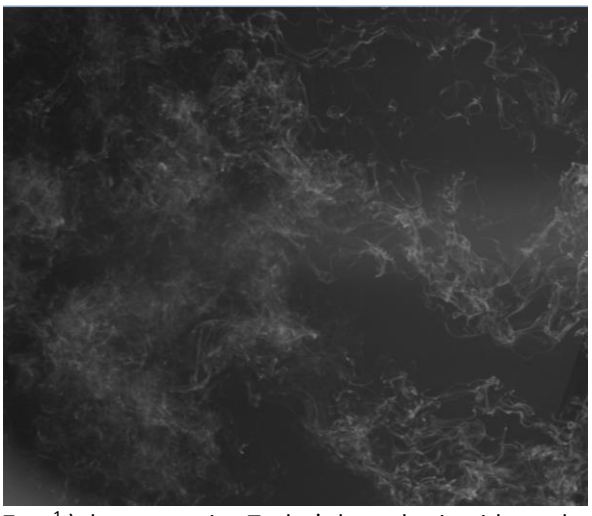

Figure 124: Flow visualization (@ Ti=12.6%, L_{xx}=0.3m, v=7ms^{-1}) demonstrating Taylor's hypothesis without the presence of the MAV.

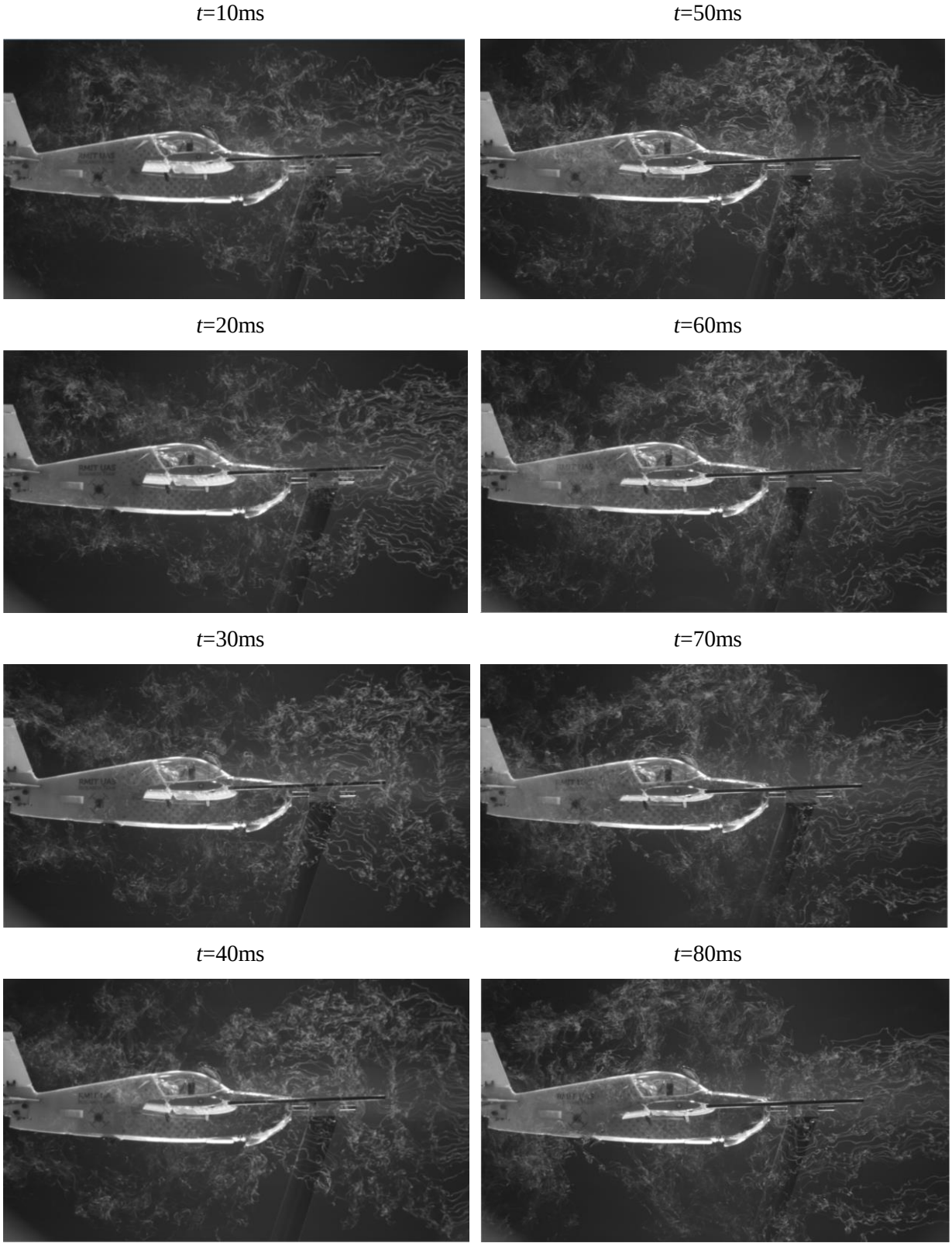

Figure 125: Flow visualization (@ Ti=12.6%, L_{xx}=0.3m, v=7ms^{-1}) demonstrating Taylor's hypothesis

References

A.J.PADGAONKAR, K.W.KRIEGER & A.I.KING 1975. Measurement of angular acceleration of a rigid body using linear accelerometers. *Journal of Applied Mechanics: Transactions on ASME* 42**,** 552-556.

ABATE, G., OL, M. & SHYY, W. 2008. Introduction: Biologically Inspired Aerodynamics. *AIAA Journal,* 46**,** 2113-2114.

ABDULRAHIM, M. 2004. *Dynamic Characteristics of Morphing Micro Air Vehicles.* PhD Thesis, University of Florida.

ABDULRAHIM, M., GARCIA, H., DUPUIS, J. & LIND, R. Flight Characteristics of Wing Shaping for a Micro Air Vehicle with Membrane Wings. International Forum on Aeroelasticity and Structural Dynamics, 2003.

ABDULRAHIM, M., GARCIA, H. & LIND, R. 2005. Flight characteristics of shaping the membrane wing of a micro air vehicle. *Journal of Aircraft,* 42**,** 131-137.

ABDULRAHIM, M., WATKINS, S., SEGAL, R., MARINO, M. & SHERIDAN, J. 2010. Dynamic Sensitivity to Atmospheric Turbulence of Unmanned Air Vehicles with Varying Configuration. *AIAA Journal of Aircraft,* 47**,** 1873-1883.

ABEYSINGHE, D. C., DASGUPTA, S., BOYD, J. T. & JACKSON, H. E. 2001. A novel MEMS pressure sensor fabricated on an optical fiber. *IEEE Photonics Technology Letters,* 13**,** 993-995.

AKAR, O., AKIN, T. & NAJAFI, K. 2001. A wireless batch sealed absolute capacitive pressure sensor. *Sensors and Actuators A: Physical,* A95**,** 29-38.

AKEILA, E., SALCIC, Z. & SWAIN, A. Implementation calibration and testing of GFINS models based on six-accelerometer cube. In: Proceedings of the IEEE Region 10 Conference, 19-21 Nov 2008 Hyderabad, India. 1-6.

ANDERSEN, E. D. & TAYLOR, C. N. Improving MAV pose estimation using visual information. Intelligent Robots and Systems, 2007. IROS 2007. IEEE/RSJ International Conference on, 2007. IEEE, 3745-3750.

ANDREWS, M. K., TURNER, G. C., HARRIS, P. D. & HARRIS, I. M. 1993. A resonant pressure sensor based on a squeezed film of gas. *Sensors and Actuators A: Physical,* A36**,** 219-226.

ANON 1946. Nature's gyroscopes. *Time.*

ANTONE, M. E. & TELLER, S. Automatic recovery of relative camera rotations for urban scenes. In: Proceedings of the IEEE Conference on Computer Vision and Pattern Recognition, , 2000. IEEE, 282-289.

AUBÉPART, F. & FRANCESCHINI, N. 2007. Bio-inspired optic flow sensors based on FPGA: Application to Micro-Air-Vehicles. *Microprocessors and Microsystems,* 31**,** 408-419.

BAKLANOV, A. A., GRISOGONO, B., BORNSTEIN, R., MAHRT, L., ZILITINKEVICH, S. S., TAYLOR, P., LARSEN, S. E., ROTACH, M. W. & FERNANDO, H. J. S. 2011. The Nature, Theory, and Modeling of Atmospheric Planetary Boundary Layers. *Bulletin of the American Meteorological Society,* 92**,** 123-128.

BALDELLI, D. H., OHTA, H. & KYOKO, N. 1993. Gust load alleviation of an aeroelastic wing model. *Japan Society for Aeronautical and Space Sciences, Transactions (0549-3811),* 36**,** 125-142.

BARNWELL, W. 2003. *UAV Flight Control Using Distributed Actuation and Sensing.* Masters Thesis, North Carolina State University

BAZIN, J. C., KWEON, I., DEMONCEAUX, C. & VASSEUR, P. UAV attitude estimation by vanishing points in catadioptric images. IEEE International Conference on Robotics and Automation, 2008. IEEE, 2743-2749.

BEARD, R. W., KINGSTON, D., QUIGLEY, M., SNYDER, D., CHRISTIANSEN, R., JOHNSON, W., MCLAIN, T. & GOODRICH, M. 2005. Autonomous vehicle technologies for small fixed-wing UAVs. *Journal of Aerospace Computing, Information, and Communication,* 2**,** 92-108.

BERGH, H. & TIJDEMAN, H. 1965. *Theoretical and experimental results for the dynamic response of pressure measuring systems*, Nationaal lucht-en ruimtevaartlaboratorium.

BLOWER, C. J., LEE, W. & WICKENHEISER, A. M. 2011. The development of a closed-loop flight controller with panel method integration for gust alleviation using biomimetic feathers on

aircraft wings. *ASME Conference on Smart Materials, Adaptive Structures and Intelligent Systems.* Pheonix, AZ.

BLOWER, C. J., LEE, W. & WICKENHEISERA, A. M. The development of a closed-loop flight controller with panel method integration for gust alleviation using biomimetic feathers on aircraft wings. Proceedings of SPIE, March 11-15 2012 San Diego, CA.

BLOWER, C. J. & WICKENHEISER, A. M. 2010. Biomimetic Feather Structures for Localized Flow Control and Gust Alleviation on Aircraft Wings. *21st International Conference on Adaptive Structures and Technologies.* State College, PA.

BLOWER, C. J. & WICKENHEISER, A. M. Two-dimensional localized flow control using distributed, biomimetic feather structures: a comparative study. Proceedings of SPIE, March 6-10 2011 San Diego, CA. 1-10.

BOGOS, S. & STROE, I. 2012. SIMILARITY CRITERIA FOR "FULL" AND "SCALE" AIRCRAFT ON THE LATERAL STABILTY ANALYSIS. *U.P.B. Sci. Bull., Series D,* 74.

BOWLES, P. O., CORKE, T. C. & MATLIS, E. Stall detection on a leading-edge plasma actuated pitching airfoil utilizing onboard measurement. Proc. 47th Aerospace Sciences Meeting, 2009. 5-8.

BROOKMAN, A. K. 1971. *An Albedo Horizon Sensor Using Hybrid Circuitry,* Farnborough, England, RAE TR 71153.

BROWN, R. E. & FEDDE, M. R. 1993. Airflow sensors in the avian wing. *Journal of Experimental Biology,* 179**,** 13-13.

BRUININK, C., JAGANATHARAJA, R., DE BOER, M., BERENSCHOT, E., KOLSTER, M., LAMMERINK, T., WIEGERINK, R. & KRIJNEN, G. Advancements in technology and design of biomimetic flow-sensor arrays. In: Proceedings of the 22nd IEEE International Conference on MEMS, 25-29 Jan 2009 Sorrento, Italy. 152-155.

BUDER, U., BERNS, A., OBERMEIER, E., PETZ, R. & NITSCHE, W. 2005. AeroMEMS wall hot-wire anemometer on polyimide foil for measurement of high frequency fluctuations. *Sensors, 2005 IEEE.*

BUDER, U., BERNS, A., PETZ, R., NITSCHE, W. & OBERMEIER, E. 2007. AeroMEMS Wall Hot-Wire Anemometer on Polyimide Substrate Featuring Top Side or Bottom Side Bondpads. *Sensors Journal, IEEE,* 7**,** 1095-1101.

BURNS, D. W., ZOOK, J. D., HORNING, R. D., HERB, W. R. & GUCKEL, H. 1995. Sealed-cavity resonant microbeam pressure sensor. *Sensors and Actuators A: Physical,* A48**,** 179-186.

CALLEGARI, S., ZAGNONI, M., GOLFARELLI, A., TARTAGNI, M., TALAMELLI, A., PROLI, P. & ROSSETTI, A. 2006. Experiments on aircraft flight parameter detection by on-skin sensors. *Sensors and Actuators A: Physical,* 130**,** 155-165.

CARRUTHERS, A., THOMAS, A. & TAYLOR, G. 2007. Automatic aeroelastic devices in the wings of a steppe eagle Aquila nipalensis. *The Journal of Experimental Biology,* 210**,** 4136-4149.

CASAS, J., STEINMANN, T. & KRIJNEN, G. 2010. Why do insects have such a high density of flow-sensing hairs? Insights from the hydromechanics of biomimetic MEMS sensors. *Journal of the Royal Society interface,* 7**,** 1487-1495.

CHAE, J., KULAH, H. & NAJAFI, K. 2005. A CMOS-compatible high aspect ratio silicon-on-glass in-plane micro-accelerometer. *Journal of Micromechanics and Microengineering,* 15**,** 336.

CHAHL, J., ROSSER, K. & MIZUTANI, A. Bioinspired optical sensors for unmanned aerial systems. Proceedings of SPIE, 2011. 797503.

CHEN, I. H., LEE, S. C. & DEBRA, D. B. 1994. Gyroscope free strapdown inertial measurement unit by six linear accelerometers. *Journal of Guidance Control and Dynamics,* 17**,** 286-290.

CHEN, J., HAYNES, B. & FLETCHER, D. 2000. Cobra probe measurements of mean velocities, Reynolds stresses and higher-order velocity correlations in pipe flow. *Experimental Thermal and Fluid Science,* 21**,** 206-217.

CHEN, J., ZOU, J. & LIU, C. A surface micromachined, out-of-plane anemometer. In: Proceedings of the 15th IEEE International Conference on MEMS, January 2002 NV, USA. IEEE, 332-335.

CHEN, N., TUCKER, C., ENGEL, J. M., YINGCHEN, Y., PANDYA, S. & CHANG, L. 2007. Design and Characterization of Artificial Haircell Sensor for Flow Sensing With Ultrahigh Velocity and Angular Sensitivity. *Journal of Microelectromechanical Systems,* 16**,** 999-1014.

CHEN, T., CLOTHIER, R., MOHAMED, A. & BADAWY, R. 2014. An Experimental Study of Human Performance in Controlling Micro Aerial Vehicles in Turbulent Environment. *Fourth Australasian Unmanned Systems Conference.* Melbourne Australia.

CHIH-WEI, L., YU-LUNG, L., JIAHN-PIRING, Y. & CHIN-HO, C. 2012. Application of Fiber Bragg Grating Level Sensor and Fabry-Pérot Pressure Sensor to Simultaneous Measurement of Liquid Level and Specific Gravity. *IEEE Sensors Journal,* 12**,** 827-831.

CHINGWEN, Y. & NAJAFI, K. Bulk-silicon tunneling-based pressure sensors. Proceedings of the 1994 Solid-state Sensor and Actuator Workshop, 13-16 June 1994 Hilton Head Island, SC, USA. Transducer Research Foundation, 201-208.

CHO, S. T., NAJAFI, K. & WISE, K. D. 1990. Secondary sensitivities and stability of ultrasensitive silicon pressure sensors. *Tech Digest, Solid-State Sensor and Actuator Workshop.* Hilton Head Island, SC, USA.

CHOPRA, I. Hovering micro air vehicles: challenges and opportunities. Proceedings of American Helicopter Society Specialists' Conference, International Forum on Rotorcraft Multidisciplinary Technology, 2007. 15-17.

CHUE, S. H. 1975. Pressure probes for fluid measurement. *Progress in aerospace sciences,* 16**,** 147-223.

CORNALL, T. D., EGAN, G. K. & PRICE, A. 2006. Aircraft attitude estimation from horizon video. *Electronics Letters,* 42**,** 744-745.

COX, C., GOPALARATHNAM, A. & HALL, C. E. 2010. Flight Test of Stable Automated Cruise Flap for an Adaptive Wing Aircraft. *Journal of Aircraft,* 47**,** 1178-1188.

CROON, G. C. H. E. D., GROEN, M. A., WAGTER, C. D., REMES, B., RUIJSINK, R. & OUDHEUSDEN, B. W. V. 2012. Design, aerodynamics and autonomy of the DelFly. *Bioinspiration & Biomimetics,* 7**,** 025003.

CRUZ, E., WATKINS, S. & LOXTON, B. 2007. A study of the effects of turbulence on airfoils at low reynolds numbers. *Interim Report: USAF Project No: AOARD-06-4037.* Melbourne: RMIT University.

CRUZ, E., WATKINS, S. & LOXTON, B. 2008. A study on the effects on turbulence on airfoils at low Reynolds numbers. *Interm Report : USAF Project No: AOARD-06-4037.* RMIT.

CYBYK, B., MCGRATH, B., FREY, T., DREWRY, D., KEANE, J. & PATNAIK, G. Unsteady urban airflows and their impact on small unmanned air system operations. AIAA guidance, navigation, and control conference, 2009 Chicago, IL. AIAA.

DAGAMSEH, A. 2011. *Bio-Inspired hair flow sensor arrays from nature to MEMS.* PhD thesis, University of Twente.

DAIGLE, M., CORCOS, J. & KE, W. 2007. An analytical solution to circular touch mode capacitor. *IEEE Sensors Journal* 7**,** 502-505.

DAVENPORT, A. G. Applications of statistical concepts to the wind loading of structures. Proccedings Institution of Civil Engineers, 1961. 449-472.

DE GROOT, W., FELNHOFER, D. & GUSEV, E. 2011. Reliability Aspects of Capacitive MEMS Devices. *Procedia Engineering,* 25**,** 180-186.

DE WAGTER, C., KOOPMANS, A., DE CROON, G., REMES, B. & RUIJSINK, R. 2013. Autonomous Wind Tunnel Free-Flight of a Flapping Wing MAV. *Advances in Aerospace Guidance, Navigation and Control.* Springer.

DEMONCEAUX, C., VASSEUR, P. & PÉGARD, C. UAV attitude computation by omnidirectional vision in urban environment. IEEE International Conference on Robotics and Automation, 2007. IEEE, 2017-2022.

DIJKSTRA, M., VAN BAAR, J., WIEGERINK, R., LAMMERINK, T., DE BOER, J. & KRIJNEN, G. 2005. Artificial sensory hairs based on the flow sensitive receptor hairs of crickets. *Journal of Micromechanics and Microengineering,* 15**,** S132.

DINAPOLI, L. D. 1965. *The Measurement of Angular Velocities without the Use of Gyros,* Philadelphia, The Moore School of Electrical Engineering, University of Pennsylvania.

DONG, H., JIA, Y., HAO, Y. & SHEN, S. 2005. A novel out-of-plane MEMS tunneling accelerometer. *Sensors and Actuators A: Physical,* 120**,** 360-364.

DONG, Y., ZWAHLEN, P., NGUYEN, A., FROSIO, R. & RUDOLF, F. Ultra-high precision MEMS accelerometer. Solid-State Sensors, Actuators and Microsystems Conference (TRANSDUCERS), 2011 16th International, 2011. IEEE, 695-698.

DURMAZ, S. & KAYA, M. O. Aeroelastic Response of an Aircraft Wing Modeled as a Thin-Walled Composite Beam. ASME 2013 International Mechanical Engineering Congress and Exposition, 2013. American Society of Mechanical Engineers, V001T01A034-V001T01A034.

DUSHA, D., BOLES, W. & WALKER, R. Attitude estimation for a fixed-wing aircraft using horizon detection and optical flow. 9th Biennial Conference of the Australian Pattern Recognition Society on Digital Image Computing Techniques and Applications, 2007. IEEE, 485-492.

EBEFORS, T., KALVESTEN, E. & STEMME, G. Three dimensional silicon triple-hot-wire anemometer based on polyimide joints. In: Proceedings of the 11th IEEE International Workshop on MEMS, 25-29 January 1998 Heidelberg, Germany. 93-98.

EMERSON, J. D. & STRENIO, J. 2000. Boxplots and Batch Comparison. *In:* HOAGLIN, D. C., MOSTELLER, F. & TUKEY, J. W. (eds.) *Understanding Robust and Exploratory Data Analysis.* New York, USA: John Wiley & Sons.

FAN, Z., CHEN, J., ZOU, J., BULLEN, D., LIU, C. & DELCOMYN, F. 2002. Design and fabrication of artificial lateral line flow sensors. *Journal of Micromechanics and Microengineering,* 12**,** 655-661.

FAROOQUI, M. M. & EVANS, A. G. R. 1987. A polysilicon-diaphragm-based pressure sensor technology. *Journal of Physics E: Scientific Instruments,* 20**,** 1469-1471.

FEI, H., ZHU, R., ZHOU, Z. & WANG, J. 2007. Aircraft flight parameter detection based on a neural network using multiple hot-film flow speed sensors. *Smart materials and structures,* 16**,** 1239.

FISHER, A. 2013. *The Effect of Freestream Turbulence on Fixed and Flapping Micro Air Vehicle Wings.* PhD Thesis, RMIT University.

FISHER, A., WATKINS, S. & WATMUFF, J. 2012. Dynamic calibration of pressure measurement system: an improved method. *18th Australasian Fluid Mechanics Conference.* Launceston, Australia.

FOBELETS, K., VOUNCKX, R. & BORGHS, G. 1994. A GaAs pressure sensor based on resonant tunnelling diodes. *Journal of Micromechanics and Microengineering,* 4**,** 123-128.

FRANCESCHINI, N. 1985. Early processing of colour and motion in a mosaic visual system. *Neuroscience research*.

FUJII, K., MIYAZAWA, Y. & MATSUSHITA, H. 1990. Gust load alleviation control design for the accuracy of an aeroelastic active control model. *Proceedings of the 28th Aircraft Symposium.* JAPAN.

GALIŃSKI, C. & ŻBIKOWSKI, R. 2007. Some problems of micro air vehicles development. *Bulletin of the polish academy of sciences; technical sciences,* 55**,** 91-98.

GALINSKI, C. R. 2006. Gust Resistant Fixed Wing Micro Air Vehicle. *Journal of Aircraft,* 43**,** 1586-1588.

GALLACHER, B., BURDESS, J. & HARISH, K. 2006. A control scheme for a MEMS electrostatic resonant gyroscope excited using combined parametric excitation and harmonic forcing. *Journal of Micromechanics and Microengineering,* 16**,** 320.

GARCIA, H., ABDULRAHIM, M. & LIND, R. Roll control for a micro air vehicle using active wing morphing. AIAA Guidance, Navigation and Control Conference, 2003.

GARRATT, J. R. 1994. *The Atmospheric Boundary Layer*, Cambridge University Press.

GASS, V., VAN DER SCHOOT, B. & DE ROOIJ, N. Nanofluid handling by micro-flow-sensor based on drag force measurements. In: Proceedings of the IEEE MEMS Workshop 93, Feb 1993 FL, USA. 167-172.

GIBSON, J. J. 1950. *The perception of the visual world,* Oxford, England: Houghton Mifflin.

GREEN, W. E., OH, P. Y., SEVCIK, K. & BARROWS, G. Autonomous landing for indoor flying robots using optic flow. In: Proceedings of IMECE, 2003. 1341-1346.

GREENWOOD, J. C. 1984. Etched silicon vibrating sensor. *Journal of Physics E: Scientific Instruments,* 17**,** 650-652.

GRUSOVIN, M. 2006. *Modelling of Atmospheric Boundary Layer in RMIT Industrial Wind Tunnel.* Undergraduate Thesis Project, RMIT.

GUERREIRO, N. M. & HUBBARD JR, J. E. 2008. Pressure Port Placement for Lift Distribution Measurement on a Model Aircraft with Optimized Trailing-Edge Flaps. *26th AIAA Applied Aerodynamics Conference.* Honolulu, Hawaii.

GWOZDECKI, J. A. 2001. *Aircraft Attitude Sensor and Feed- back Control System*. U.S. Patent No. 6,181,989.

HALL, K. C. & HALL, S. R. 2001. A Rational Engineering Analysis of the Efficiency of Flapping Flight. *Fixed and Flapping Wing Aerodynamics for Micro Air Vehicle Applications.* American Institute of Aeronautics and Astronautics.

HALL, S. R. 1998. Micro Air Vehicles: Propulsion and Actuation Issues. *Defense Science Study Group V: Study Reports 1996-1997.* Alexandria, VA: Institute for Defense Analyses.

HANKIN, E. H. 1913. *Animal Flight: A Record of Observation,* London, UK, ILIFFE.

HARTWELL, P., BERTSCH, F., MILLER, S., TURNER, K. & MACDONALD, N. Single mask lateral tunneling accelerometer. In: Proceedings of the 11th IEEE International Workshop on MEMS 1998. 340-344.

HEIMBAUGH, R. 1987. New generation aircraft design problems relative to turbulence stability, aeroelastic loads and gust alleviation. *NASA Langley Research Center Atmospheric Turbulence Relative to Aviation, Missile and Space Programs (SEE N87-22341 15-47).*

HERRMANN, P., BIL, C., WATKINS, S. & TAYLOR, B. 2005. Simulation and flight test of a temperature sensing stabilisation system. *Aeronautical Journal,* 109**,** 167-176.

HIN-LEUNG, C. & WISE, K. D. 1988. An ultraminiature solid-state pressure sensor for a cardiovascular catheter. *IEEE Transactions on Electron Devices,* 35**,** 2355-2362.

HOOPER, J. & MUSGROVE, A. 1997. Reynolds stress, mean velocity, and dynamic static pressure measurement by a four-hole pressure probe. *Experimental thermal and fluid science,* 15**,** 375-383.

HÖRSTER, W. 1990a. Histological and electrophysiological investigations on the vibration-sensitive receptors (Herbst corpuscles) in the wing of the pigeon (Columba livia). *Journal of Comparative Physiology A: Neuroethology, Sensory, Neural, and Behavioral Physiology,* 166**,** 663-673.

HÖRSTER, W. 1990b. Vibrational sensitivity of the wing of the pigeon (Columba livia) — a study using heart rate conditioning. *Journal of Comparative Physiology A: Neuroethology, Sensory, Neural, and Behavioral Physiology,* 167**,** 545-549.

HWANGBO, M. & KANADE, T. Visual-inertial UAV attitude estimation using urban scene regularities. IEEE International Conference on Robotics and Automation, 9-13 May 2011 Shanghai, China. IEEE, 2451-2458.

INTEL. 2014. *ARK: Your Source for Intel Product Information* [Online]. Available: http://ark.intel.com [Accessed 26/09 2014].

JALINK, A., JR, DAVIS, R. E. & DODGEN, J. A. 1972. Conceptual design and analysis of an infrared horizon sensor with compensation for atmospheric variability. *Technical Note TN-D-6616.* NASA

JENKINS, D. A., IFJU, P. G., ABDULRAHIM, M. & S., O. Assessment of Controllability of Micro Air Vehicles. In: Proceedings of the 16th Bristol Unmanned Air Vehicle Systems Conference, April 2001 2001 Bristol, U.K.

JI, X. S. & WANG, S. R. 2005. Analysis of Characteristics on Capacitive Silicon Microaccelerometer System. *Journal of Astronautics,* 26**,** 446-449.

JIAN, W., SARIHAN, V., MYERS, B. & LI, G. 2011. Multidisciplinary Approach for Robust Package Design of MEMS Accelerometers. *IEEE Transactions on Components, Packaging and Manufacturing Technology,* 1**,** 1934-1938.

JOHNSON, C. G. 1969. *Migration and dispersal of insects by flight,* London, UK, Methuen and Co., Ltd.

JOO, J. W. & CHOA, S. H. 2007. Deformation behavior of MEMS gyroscope sensor package subjected to temperature change. *IEEE Transactions on Components, Packaging and Manufacturing Technology,* 30**,** 346-354.

JOSEBA, M., RAFAEL, P. & GRAHAM, J. M. R. 2012. Open-Loop Stability and Closed-Loop Gust Alleviation on Flexible Aircraft Including Wake Modeling. *53rd AIAA/ASME/ASCE/AHS/ASC Structures, Structural Dynamics and Materials Conference.* American Institute of Aeronautics and Astronautics.

KÄLVESTEN, E. 1996. *Pressure and Wall Shear Stress Sensors for Turbulence Measurements.* PhD thesis, Royal Institute of Technology.

KAO, C. F. & CHEN, T. L. 2008. Design and analysis of an orientation estimation system using coplanar gyro-free inertial measurement unit and magnetic sensors. *Sensors and Actuators A: Physical,* 144**,** 251-262.

KARPELSON, M., GU-YEON, W. & WOOD, R. J. A review of actuation and power electronics options for flapping-wing robotic insects. IEEE International Conference on Robotics and Automation, 2008. ICRA 2008. , 19-23 May 2008 Pasadena, CA. 779-786.

KELLER, J. 2013. Epson unveils tiny inertial measurement unit at AUVSI for stabilization subsystems on unmanned vehicles. Available: http://www.avionics-intelligence.com/articles/2013/08/ai-epson-imu.html [Accessed 12/09/13].

KENDOUL, F., FANTONI, I. & NONAMI, K. 2009. Optic flow-based vision system for autonomous 3D localization and control of small aerial vehicles. *Robotics and Autonomous Systems,* 57**,** 591-602.

KIM, D.-K., KANG, S.-G., PARK, J.-Y., SIM, J.-H., SHIN, J.-K., CHOI, P. & LEE, J.-H. 2000. Characteristics of piezoresistive mass flow sensor fabricated by porous silicon micromachining. *Japanese Journal of Applied Physics,* 39**,** 7134-7137.

KIM, J. & BRAMBLEY, G. Dual optic-flow integrated navigation for small-scale flying robots. In: Proceedings of the Australasian Conference on Robotics and Automation, 2007.

KIM, S., KIM, Y. & PARK, S. 2003. A circular-type thermal flow direction sensor free from temperature compensation. *Sensors and Actuators A: Physical,* A108**,** 64-68.

KIM, S., NAM, T. & PARK, S. 2004. Measurement of flow direction and velocity using a micromachined flow sensor. *Sensors and Actuators A: Physical,* 114**,** 312-318.

KINGSTON, D. B. & BEARD, R. W. Real-time attitude and position estimation for small UAVs using low-cost sensors. AIAA 3rd unmanned unlimited technical conference, Workshop and exhibit, 2004. sn, 2004-6488.

KORNBLUH, R. D., PELRINE, R., PEI, Q., HEYDT, R., STANFORD, S., OH, S. & ECKERLE, J. Electroelastomers: applications of dielectric elastomer transducers for actuation, generation, and smart structures. 2002. 254-270.

KRAFT, M. 2000. Micromachined inertial sensors: state-of-the-art and a look into the future. *Measurement+Control,* 33**,** 164-8.

KRAUSE, J. S. 2011. *Micromachined microphone array on a chip for turbulent boundary layer measurements.* PhD thesis, Tufts University.

KRIJNEN, G., LAMMERINK, T., WIEGERINK, R. & CASAS, J. Cricket inspired flow-sensor arrays. In: Proceedings of the 6th IEEE Conference on Sensors, 28-31 Oct 2007 ATL, USA. 539-546.

KRULEVITCH, P., LEE, A. P., RAMSEY, P. B., TREVINO, J. C., HAMILTON, J. & NORTHRUP, M. A. 1996. Thin film shape memory alloy microactuators. *Journal of Microelectromechanical Systems,* 5**,** 270-282.

KULAH, H., CHAE, J. & YAZDI, N. 2006. Noise Analysis and Characterization of a Sigma-delta Capacitive Microaccelerometer. *IEEE Journal of Solid-State Circuits,* 41**,** 352-361.

KUNG, J. T. & LEE, H. S. 1992. An integrated air-gap-capacitor pressure sensor and digital readout with sub-100 attofarad resolution. *Journal of Microelectromechanical Systems,* 1**,** 121-129.

KURODA, T., SUZUKI, K., MITA, S., FUJITA, T., YAMANE, F., SANO, F., CHIBA, A., WATANABE, Y., MATSUDA, K. & MAEDA, T. 1998. Variable supply-voltage scheme for low-power high-speed CMOS digital design. *Solid-State Circuits, IEEE Journal of,* 33**,** 454-462.

LANGELAAN, J. W. & ROY, N. 2009. Enabling new missions for robotic aircraft. *Science,* 326**,** 1642-1644.

LAPPE, U. O. & DAVIDSON, B. 1963. On the Range of Validity of Taylor's Hypothesis and the Kolmogoroff Spectral Law. *Journal of the Atmospheric Sciences,* 20**,** 569-576.

LATT, W. T., TAN, U.-X., RIVIERE, C. N. & ANG, W. T. 2011. Placement of accelerometers for high sensing resolution in micromanipulation. *Sensors and Actuators A: Physical,* 167**,** 304-316.

LEWIS, C. P., KRAFT, M. & HESKETCH, T. G. 1996. Mathematical Model for a Micromachined Accelerometer. *Transactions of the Institute of Measurement and Control,* 18**,** 92-98.

LI, G., MCNEIL, A., KOURY, D., CHAPMAN, M. & MONK, D. Design of Transducer and Package at the Same Time. Proceedings of the International Electronic Packaging Technical Conference and Exhibition, 2005 CA, USA.

LIA, X.-J., QIU, C.-J., DENG, Y.-L., QU, W. & HE, J.-N. 2010. An MEMS Optical Fiber Pressure Sensor Based on a Square Silicon Diaphragm: Numerical Simulation and Experimental Verification. *International Journal of Nonlinear Sciences and Numerical Simulation,* 11**,** 225–229.

LION, S. 2007. *Control Authorities of a distributed Actuation and Sensing Array on a Blended-Wing-Body Uninhabited Aerial Vehicle.* Masters Thesis, North Carolina State University.

LISSAMAN, P. 2009. Effects of Turbulence on Bank Upsets of Small Flight Vehicles. *47th AIAA Aerospace Sciences Meeting including The New Horizons Forum and Aerospace Exposition.* American Institute of Aeronautics and Astronautics.

LIU, C. H., BARZILAI, A. M., REYNOLDS, J. K., PARTRIDGE, A., KENNY, T. W., GRADE, J. D. & ROCKSTAD, H. K. 1998a. Characterization of a high-sensitivity micromachined tunneling accelerometer with micro-g resolution. *Journal of Microelectromechanical Systems,* 7**,** 235-244.

LIU, C. H. & KENNY, T. W. 2001. A high-precision, wide-bandwidth micromachined tunneling accelerometer. *Journal of Microelectromechanical Systems,* 10**,** 425-433.

LIU, H., HONG, T. H., HERMAN, M., CAMUS, T. & CHELLAPPA, R. 1998b. Accuracy vs efficiency trade-offs in optical flow algorithms. *Computer Vision and Image Understanding,* 72**,** 271-286.

LIU, M., CHI, B., LIU, Y. & DONG, J. 2013. A closed-loop MEMS accelerometer with capacitive sensing interface ASIC. *International Journal of Electronics,* 100**,** 21-35.

LOFDAHL, L., STEMME, G. & JOHANSSON, B. 1989. Sensor based on silicon technology for turbulence measurements. *Journal of Physics E. Scientific Instruments,* 22**,** 391-393.

LOXTON, B., WATKINS, S., WATMUFF, J., TRIVALIO, P., CRUZ, E. & RAVI, S. 2009. The Influence of Atmospheric Turbulence on the Aerodynamics of a Flat Plate Micro Air Vehicle Wing. *3rd Australasian Unmanned Air Vehicles Conference.* Melbourne, Australia.

LUCAS, A. M., VALASEK, J. & STRGANAC, T. W. 2009. Gust Load Alleviation of an Aeroelastic System using Nonlinear Control. *AIAA-2009-2536*.

MACKENZIE, D. 2012. A Flapping of Wings. *Science*

MADNI, A. M., COSTLOW, L. E. & KNOWLES, S. J. 2003. Common Design Techniques for BEI GyroChip Quartz Rate Sensors for Both Automotive and Aerospace/Defense Markets. *IEEE Sensors Journal,* 3**,** 569-578.

MANKINS, J. C. 2009. Technology readiness assessments: A retrospective. *Acta Astronautica,* 65**,** 1216-1223.

MARINO, M. 2013. *UNSTEADY PRESSURE SENSING ON A MAV WING FOR CONTROL INPUTS IN TURBULENCE.* PhD Thesis, RMIT University.

MARINO, M., RAVI, S. & WATKINS, S. 2012. Optimum location of pressure measurments around a wing as a dynamic control input in smooth and turbulent conditions. *28th International Congress of the Aeronautical Sciences.*

MCCARLEY, J. S. & WICKENS, C. D. 2004. Human factors concerns in UAV flight. *University of Illinois at Urbana-Champaign Institute of Aviation, Aviation Human Factors Division*.

MCMICHAEL, J. M. & FRANCIS, C. M. S. 1997. Micro Air Vehicles - Toward a New Dimension in Flight. *Unmanned Systems,* 15**,** 10-17.

MCNAMARA, S. & GIANCHANDANI, Y. B. 2011. 5.12 - MEMS-Based Sensors. *In:* PALLAB, B., ROBERTO, F. & HIROSHI, K. (eds.) *Comprehensive Semiconductor Science and Technology.* Amsterdam: Elsevier.

MELVAS, P., KALVESTEN, E. & STEMME, G. A surface micromachined resonant beam pressure sensor. In: Proceedings 14th IEEE International Conference on MEMS, 2001 Interlaken, Switzerland.

MIAO, M., HU, Q., HAO, Y., DONG, H., WANG, L., SHI, Y. & SHEN, S. A Bulk Micromachined Si-on-glass Tunneling Accelerometer with Out-of-plane Sensing Capability. In: Proceedings of the 2nd IEEE International Conference on NEMS, 16-19 Jan 2007. IEEE, 235-240.

MICHELSON, R. C. 2010. Overview of Micro Air Vehicle System Design and Integration Issues. *Encyclopedia of Aerospace Engineering.* john Wiley & Sons, Ltd.

MILBANK, J., LOXTON, B., WATKINS, S. & W.H., M. 2005. Replication of Atmospheric Conditions for the Purpose of Testing MAVs MAV Flight Environment Project: Final Report. *AFOSR Final Report (USAF Project No: AOARD 05-4075).* RMIT.

MING-SHUANG, J., CHIA-CHU, C. & LIN, C. C. K. 2007. An implantable capacitive pressure sensor for biomedical applications. *Sensors and Actuators A: Physical,* 134**,** 382-388.

MITAL, N. K. & KING, A. I. 1979. Computation of rigid-body rotation in three-dimensional space from body-fixed linear acceleration measurements. *Journal of Applied Mechanics: Transactions on ASME,* 46**,** 925-930.

MOHAMED, A., WATKINS, S., CLOTHIER, R., ABDULRAHIM, M., MASSEY, K. & SABATINI, R. 2014. Fixed-Wing MAV Attitude Stability in Atmospheric Turbulence PART 2: Investigating Biologically-Inspired Sensors *Progress in Aerospace Sciences (in press)*.

MOUSLEY, P. D., WATKINS, S. & HOOPER, J. D. Use of a hot-wire anemometer to examine the pressure signal of a high-frequency pressure probe. 13th Australasian Fluid Mechanics Conference. Monash University, Melbourne, Australia, 1998.

MUELLER, T. J. 2007. *Introduction to the Design of Fixed-Wing Micro Air Vehicles: Including Three Case Studies*, American Institute of Aeronautics and Astronautics.

MURPHY, R. 2000. *Introduction to AI robotics*, MIT press.

MURPHY, R. R., PRATT, K. S. & BURKE, J. L. Crew roles and operational protocols for rotary-wing micro-uavs in close urban environments. Human-Robot Interaction (HRI), 2008 3rd ACM/IEEE International Conference on, 2008. IEEE, 73-80.

MUTAMBA, K., FLATH, M., SIGURDARDOTTIR, A., VOGT, A. & HARTNAGEL, H. L. 1999. A GaAs pressure sensor with frequency output based on resonant tunneling diodes. *IEEE Transactions on Instrumentation and Measurement* 48**,** 1333-1337.

MYSTKOWSKI, A. 2013. Robust control of the micro UAV dynamics with an autopilot. *Journal of Theoretical and Applied Mechanics,* 51**,** 751-761.

NAKATA, T., LIU, H., TANAKA, Y., NISHIHASHI, N., WANG, X. & SATO, A. 2011. Aerodynamics of a bio-inspired flexible flapping-wing micro air vehicle. *Bioinspiration & Biomimetics,* 6**,** 045002.

NECKER, R. 1985a. Observations on the function of a slowly adapting mechanoreceptor associated with filoplumes in the feathered skin of pigeons. *Journal of Comparative Physiology,* 156**,** 391-394.

NECKER, R. 1985b. Receptors in the skin of the wing of the pigeon and their possible role in bird flight. *Biona Report 3, Bird Flight - Vogelflug (ed. W. Nachtigall).* Stuttgart: Gustav Fischer.

OBOE, R., ANTONELLO, R., LASALANDRA, E., DURANTE, G. S. & PRANDI, L. 2005. Control of a z-axis MEMS vibrational gyroscope. *Mechatronics, IEEE/ASME Transactions on,* 10**,** 364-370.

OHNSTEIN, T. R., JOHNSON, R. G., HIGASHI, R. E., BURNS, D. W., HOLMEN, J. O., SATREN, E. A., JOHNSON, G. M., BICKING, R. E. & JOHNSON, S. D. Environmentally rugged, wide dynamic range microstructure airflow sensor. 4th Technical Digest, IEEE Solid-State Sensor and Actuator Workshop, 4-7 Jun 1990. 158-160.

OL, M., PARKER, G., ABATE, G. & EVERS, J. 2008. Flight control and performance challenges for MAVs in complex environments. *AIAA Guidance Navigation and Control Conference and Exhibit.*

OLLERO, A. & MERINO, L. 2004. Control and perception techniques for aerial robotics. *Annual Reviews in Control,* 28**,** 167-178.

OSGAR, O., CHRISTOPHER, H., BRANDON, S., ETAN, K., KEVIN, K., TROY, P., PAUL, G. & AARON, B. 2012. Piezoelectric Morphing versus Servo-Actuated MAV Control Surfaces. *53rd AIAA/ASME/ASCE/AHS/ASC Structures, Structural Dynamics and Materials Conference.* Honolulu, HI: American Institute of Aeronautics and Astronautics.

PAGLIARELLA, R. 2009a. *On the Aerodynamic Performance of Automotive Vehicle Platoons Featuring Pre and Post-Critical Leading Forms.* PhD Thesis, RMIT University.

PAGLIARELLA, R. M. 2009b. *On the aerodynamic performance of automotive vehicle platoons featuring pre and post-critical leading forms.* PhD thesis, RMIT University.

PALMER, J. L. 2009. Aerodynamic and Performance Characteristics of Small Unmanned Aerial Vehicles Compared with Those of Manned Aircraft. *3rd Australasian Unmanned Air Vehicles Conference.*

PARK, J.-S. & GIANCHANDANI, Y. B. 2003. A servo-controlled capacitive pressure sensor using a capped-cylinder structure microfabricated by a three-mask process. *Journal of Microelectromechanical Systems,* 12**,** 209-220.

PARK, J. S. & GIANCHANDANI, Y. B. 2000. A capacitive absolute-pressure sensor with external pick-off electrodes. *Journal of Micromechanics and Microengineering,* 10**,** 528-533.

PARK, S. & HOROWITZ, R. 2003. Adaptive control for the conventional mode of operation of MEMS gyroscopes. *Microelectromechanical Systems, Journal of,* 12**,** 101-108.

PARK, S., KIM, S., KIM, S. & KIM, Y. 2003. A flow direction sensor fabricated using MEMS technology and its simple interface circuit. *Sensors and Actuators B: Chemical,* 91**,** 347-352.

PATEL, M. P., SOWLE, Z. H., CORKE, T. C. & HE, C. 2007. Autonomous sensing and control of wing stall using a smart plasma slat. *Journal of aircraft,* 44**,** 516-527.

PERKINS, C. & HAGE, R. 1949. *Airplane performance, stability and control*, John Wiley and Sons.

PERLMUTTER, M. & ROBIN, L. High-performance, low cost inertial MEMS: A market in motion! Position Location and Navigation Symposium (PLANS), 2012 IEEE/ION, 2012. IEEE, 225-229.

PETERSEN, K., POURAHMADI, F., BROWN, J., PARSONS, P., SKINNER, M. & TUDOR, J. Resonant beam pressure sensor fabricated with silicon fusion bonding. In: Proceedings of the 5th International Conference on Solid-State Sensors and Actuators (TRANSDUCERS '91), 24-27 Jun 1991 CA, USA. 664-667.

PRASANNA, S. & SPEARING, S. M. 2007. Materials selection and design of microelectrothermal bimaterial actuators. *Journal of Microelectromechanical Systems,* 16**,** 248-259.

RADHAKRISHNAN, S. & LAL, A. In-channel micromechanical drag flow sensor with electronic readout. In: Proceedings of the 16th Annual International Conference on MEMS, 19-23 Jan 2003. IEEE, 307-310.

RADHAKRISHNAN, S. & LAL, A. 2005. Scalable microbeam flowsensors with electronic readout. *Journal of Microelectromechanical Systems,* 14**,** 1013-1022.

RATTI, J., JUNG-HO, M. & VACHTSEVANOS, G. Towards low-power, low-profile avionics architecture and Control for Micro Aerial Vehicles. Aerospace Conference, 2011 IEEE, 5-12 March 2011 2011. 1-8.

RATTI, J. & VACHTSEVANOS, G. 2010. A Biologically-Inspired Micro Aerial Vehicle. Sensing, Modeling and Control Strategies. *Journal of Intelligent and Robotic Systems,* 60**,** 153-178.

RATTI, J. & VACHTSEVANOS, G. 2012. Inventing a Biologically Inspired, Energy Efficient Micro Aerial Vehicle. *Journal of Intelligent & Robotic Systems,* 65**,** 437-455.

RAVI, S. 2011. *The Influence of Turbulence on a Flat Plate Airfoil at Reynolds Numbers Relevant to MAVs.* PhD thesis, RMIT University.

RECK, K., THOMSEN, E. V. & HANSEN, O. 2011. MEMS Bragg grating force sensor. *Optics Express,* 19**,** 19190--19198.

ROGERS, T., AITKEN, N., STRIBLEY, K. & BOYD, J. 2005. Improvements in MEMS gyroscope production as a result of using in situ, aligned, current-limited anodic bonding. *Sensors and Actuators A: Physical,* 123**,** 106-110.

ROMAN, K., GEORGE, P., BILL, S. & SERGEY, S. 2006. Aerodynamics and Controls Design for Autonomous Micro Air Vehicles. *AIAA Atmospheric Flight Mechanics Conference and Exhibit.* American Institute of Aeronautics and Astronautics.

ROYLANCE, L. M. & ANGELL, J. B. 1979. A batch-fabricated silicon accelerometer. *Electron Devices, IEEE Transactions on,* 26**,** 1911-1917.

RUFFIER, F. & FRANCESCHINI, N. 2005. Optic flow regulation: the key to aircraft automatic guidance. *Robotics and Autonomous Systems,* 50**,** 177-194.

SABATINI, R., BARTEL, C., KAHARKAR, A. & SHAID, T. Design and integration of vision based sensors for unmanned aerial vehicles navigation and guidance. SPIE Photonics Europe, 2012a. International Society for Optics and Photonics, 84390O-84390O-38.

SABATINI, R., RODRIGUEZ, L., KAHARKAR, A., BARTEL, C. & SHAID, T. 2012b. Carrier-phase GNSS attitude determination and control system for unmanned aerial vehicle applications. *ARPN Journal of Systems and Software,* 2**,** 297-322.

SARIHAN, V., JIAN, W., LI, G., KOSCHMIEDER, T., HOOPER, R., SHUMWAY, R. & MACDONALD, J. Designing small footprint, low-cost, high-reliability packages for performance sensitive MEMS sensors. Electronic Components and Technology Conference, 2008. ECTC 2008. 58th, 27-30 May 2008 2008. 817-818.

SARSON-LAWRENCE, J., SABATINI, R., CLOTHIER, R. & GARDI, A. Experimental Determination of Low-Cost Servomotor Reliability for Small Unmanned Aircraft Applications. Applied Mechanics and Materials, 2014. Trans Tech Publ, 202-207.

SAUKOSKI, M., AALTONEN, L. & HALONEN, K. A. I. 2007. Zero-rate output and quadrature compensation in vibratory MEMS gyroscopes. *IEEE Sensors Journal,* 7**,** 1639-1652.

SCHULER, A. R. 1967. Measuring rotational motion with linear accelerometers. *IEEE Transactions on AES* 3 465-472.

SHEN, H. & XU, Y. 2013. Pressure and Shear Information based Three-Axis Attitude Control for a Micro Air Vehicle. *AIAA Atmospheric Flight Mechanics (AFM) Conference.* American Institute of Aeronautics and Astronautics.

SHYY, W., AONO, H., CHIMAKURTHI, S. K., TRIZILA, P., KANG, C.-K., CESNIK, C. E. & LIU, H. 2010. Recent progress in flapping wing aerodynamics and aeroelasticity. *Progress in Aerospace Sciences,* 46**,** 284-327.

SINGH, V., WARREN, L., PUTNAM, N., WALTHER, B., BECKER, P., DANIELSON, A., KORAISHY, B., WOOD, W., JENSEN, D. & SZMEREKOVSKY, A. 2006. A Novel Exploration Into Gust Resistant Operation of MAVs/UAVs Through Transformation. *Second US-Euro MAV Conference.* Destin, FL.

SPENGEN, V., MERLIJN, W., PUERS, R. & DE WOLF, I. 2003. On the physics of stiction and its impact on the reliability of microstructures. *Journal of adhesion science and technology,* 17**,** 563-582.

SRINI, V. P. 2006. A vision for supporting autonomous navigation in urban environments. *Computer,* 39**,** 68-77.

SRINIVASAN, M. V., CHAHL, J. S., WEBER, K., VENKATESH, S., NAGLE, M. G. & ZHANG, S. W. 1999. Robot navigation inspired by principles of insect vision. *Robotics and Autonomous Systems,* 26**,** 203-216.

STEMME, G. N. 1986. A monolithic gas flow sensor with polyimide as thermal insulator. *Electron Devices, IEEE Transactions on,* 33**,** 1470-1474.

STERBING-D'ANGELO, S., CHADHA, M., CHIU, C., FALK, B., XIAN, W., BARCELO, J., ZOOK, J. M. & MOSS, C. F. 2011. Bat wing sensors support flight control. *Proceedings of the National Academy of Sciences,* 108**,** 11291-11296.

STRAUSFELD, N. J. 1976. Atlas of an Insect Brain. Berlin: Springer.

SUMINTO, J. T. A simple, high performance piezoresistive accelerometer. In: Proceedings of the 5th International Conference on Solid-State Sensors and Actuators (TANSDUCERS '91), 1991. 104-107.

SUNG, W. T., SUNG, S., LEE, J. G. & KANG, T. 2007. Design and performance test of a MEMS vibratory gyroscope with a novel AGC force rebalance control. *Journal of Micromechanics and Microengineering,* 17**,** 1939.

SUNG, W. T., SUNG, S., LEE, J. Y., KANG, T., LEE, Y. J. & LEE, J. G. 2008. Development of a lateral velocity-controlled MEMS vibratory gyroscope and its performance test. *Journal of Micromechanics and Microengineering,* 18**,** 055028.

SVEDIN, N., KALVESTEN, E., STEMME, E. & STEMME, G. 1998a. A new silicon gas-flow sensor based on lift force. *Journal of Microelectromechanical Systems,* 7**,** 303-308.

SVEDIN, N., KÄLVESTEN, E., STEMME, E. & STEMME, G. 1998b. A lift-force flow sensor designed for acceleration insensitivity. *Sensors and Actuators A: Physical,* 68**,** 263-268.

SVEDIN, N., KALVESTEN, E. & STEMME, G. 2003a. A new edge-detected lift force flow sensor. *Journal of Microelectromechanical Systems,* 12**,** 344-354.

SVEDIN, N., KÄLVESTEN, E. & STEMME, G. 2003b. A lift force sensor with integrated hot-chips for wide range flow measurements. *Sensors and Actuators A: Physical,* 109**,** 120-130.

TAN, C. W. & PARK, S. 2005. Design of accelerometer-based inertial navigation systems. *IEEE Transactions on Instrumentation and Measurement,* 54.

TAN, Z., SHIKIDA, M., HIROTA, M., XING, Y., SATO, K., IWASAKI, T. & IRIYE, Y. 2007. Characteristics of on-wall in-tube flexible thermal flow sensor under radially asymmetric flow condition. *Sensors and Actuators, A: Physical,* 138**,** 87-96.

TANG, W. C., NGUYEN, T. C. H. & HOWE, R. T. Laterally driven polysilicon resonant microstructures. In Proceedings of Micro Electro Mechanical Systems, 1989. 53-59.

TAYLOR, B., BIL, C., WATKINS, S. & EGAN, G. 2003. Horizon Sensing Attitude Stabilisation: A VMC Autopilot. *18th International UAV Systems Conference.* Bristol, UK.

TAYLOR, G. I. 1938. The spectrum of turbulence. *Proceedings of the Royal Society of London. Series A-Mathematical and Physical Sciences,* 164**,** 476-490.

TAYLOR, G. K. & KRAPP, H. G. 2007. Sensory systems and flight stability: what do insects measure and why? *Advances in insect physiology,* 34**,** 231-316.

TENNEKES, H. (ed.) 2009. *The Simple Science of Flight : from insects to jumbo jets,* London, England: The MIT Press.

THOMPSON, M. 2013. *The Small Scales of Turbulence in Atmospheric Winds at Heights Relevant to Mavs.* PhD Thesis, RMIT University.

THOMPSON, M. & WATKINS, S. 2010. Gust Inputs Relevant to Bees, Birds and MAVs. *25th Bristol International Unmanned Aerial Vehicle Systems Conference.* Bristol, UK.

THOMPSON, M., WATKINS, S., HOMES, J. & WHITE, C. 2011a. Gust Inputs for Birds, Insects and MAVs of Increasingly Small Wingspans. *Journal of The Royal Aeronautical Society,* 115.

THOMPSON, M., WATKINS, S., WHITE, C. & HOLMES, J. 2011b. Span-wise wind fluctuations in open terrain as applicable to small flying craft. *The Aeronautical Journal,* 115**,** 693-701.

THOMPSON, R. A., EVERS, J. H. & STEWART, K. C. Attitude control augmentation using wing load sensing-A biologically motivated strategy. AIAA Atmospheric Flight Mechanics Conference, 2010.

TODOROVIC, S., NECHYBA, M. C. & IFJU, P. G. Sky/ground modeling for autonomous MAV flight. In: Proceedings IEEE International Conference on Robotics and Automation (ACRA'03), 2003 Taiwan.

TRUSOV, A. A., SCHOFIELD, A. R. & SHKEL, A. M. 2009. Performance characterization of a new temperature-robust gain-bandwidth improved MEMS gyroscope operated in air. *Sensors and Actuators A: Physical,* 155**,** 16-22.

TUKEY, J. W. 1977. *Understanding Robust and Exploratory Data Analysis,* Reading, Massachusetts, USA, Addison-Wesley.

VAN DER HOVEN, I. 1957. Power spectrum of horizontal wind speed in the frequency range from 0.0007 to 900 cycles per hour. *Journal of Atmospheric Sciences,* 14**,** 160-164.

VERMEIR, J., RUNACRES, M., DE TROYER, T. & BRUSSEL, E. 2012. CFD modelling and measurements of the atmospheric boundary layer for micrositing of small wind turbines.

VIDELER, J. & GROENEWOLD, A. 1991. Field measurements of hanging flight aerodynamics in the kestrel Falco tinnunculus. *Journal of experimental biology,* 155**,** 519-530.

VINO, G. 2005. *An experimental investigation into the time-averaged and unsteady aerodynamics of the simplified passenger vehicle in isolation and in convoys.* PhD thesis, RMIT University.

VÖRSMANN, P., KASCHWICH, C., KRÜGER, T., SCHNETTER, P. & WILKENS, C. S. 2012. MEMS based integrated navigation systems for adaptive flight control of unmanned aircraft — State of the art and future developments. *Gyroscopy and Navigation,* 3**,** 235-244.

WALKER, T. J. 1994. Book of Insect Records. *In:* DEAN, T. J. (ed.). University of Florida.

WALSHE, D. E. J. 1972. Wind-Excited Oscillation of Structures. *Her Majesty's Stationery Office*.

WANG, Q., DING, M. & ZHAO, P. A new scheme of non-gyro inertial measurement unit for estimating angular velocity. In: Proceedings of the 29th Annual Conference of the IEEE Industrial Electronics Society, 2-6 Nov 2003. 1564-1567.

WANG, Q. M. & CROSS, L. E. 1998. Performance analysis of piezoelectric cantilever bending actuators. *Ferroelectrics,* 215**,** 187-213.

WANG, S., LI, Y. & HE, W. 2011. Flight attitude estimation for MAV based on M-estimation. *2011 International Conference on Consumer Electronics, Communications and Networks (CECNet),* .

WATKINS, S. 1990. *Wind Tunnel Modelling of Vehicle Aerodynamcis: With Emphasis on Turbulent Wind Effects of Commercial Vehcle Drag.* PhD Thesis, RMIT University.

WATKINS, S. 2012. Turbulence Characteristics of The Atmospheric Boundary Layer and Possibilities of Replication for Aircraft. *Joint Symposium of DFG and DLR-Airbus "Third-Symposium-Simulation of Wing and Nacelle Stall".* Technical University of Braunschweig, Germany.

WATKINS, S., FISHER, A., MOHAMED, A., MARINO, M., THOMPSON, M., CLOTHIER, R. & RAVI, S. 2013. The Turbulent Flight Environment Close to the Ground and Its Effects on Fixed and Flapping Wings at Low Reynolds Number. *5th European Conference for Aeronautics and Space Sciences.*

WATKINS, S. & MELBOURNE, W. 2003. Atmospheric Winds: Implications for MAVs. *Unmanned Air Vehicle Systems, 18th International Conference.* University of Bristol, Bristol, UK.

WATKINS, S., MILBANK, J., LOXTON, B. & MELBOURNE, W. 2006. Atmospheric winds and their effects on micro air vehicles. *AIAA Journal,* 44**,** 2591-2600.

WATKINS, S., THOMPSON, M., LOXTON, B. & ABDULRAHIM, M. 2010a. On Low Altitude Flight through The Atmospheric Boundary Layer. *International Journal of Micro Aerial Vehicles,* 2 (2)**,** 55-67.

WATKINS, S., THOMPSON, M., SHORTIS, M., SEGAL, R., ABDULRAHIM, M. & SHERIDAN, J. 2010b. An Overview of Experiments on the Dynamic Sensitivity of MAVs to Turbulence. *Aeronautical Journal,* 114**,** 485-492.

WEIBEL, R. E. 2005. *Safety considerations for operation of different classes of unmanned aerial vehicles in the national airspace system.* M.Sc thesis, Massachusetts Institute of Technology.

WEINBERG, M. & KOUREPENIS, A. 2006. Error sources in in-plane silicon tuning-fork MEMS gyroscopes. *Journal of Microelectromechanical Systems,* 15 479- 491.

WELHAM, C. J., GREENWOOD, J. C. & BERTIOLI, M. M. 1999. A high accuracy resonant pressure sensor by fusion bonding and trench etching. *Sensors and Actuators A: Physical,* A76**,** 298-304.

WHITE, C., LIM, E. W., WATKINS, S., MOHAMED, A. & THOMPSON, M. 2012. A Feasibility Study of Micro Air Vehicles Soaring Tall Buildings. *Journal of Wind Engineering and Industrial Aerodynamics,* 103**,** 41-49.

WHITE, L. 1961. Eilmer of Malmesbury, an Eleventh Century Aviator: A Case Study of Technological Innovation, Its Context and Tradition. *Technology and Culture 2,* 2**,** 97-111.

WILLIAMS, W. & HARRIS, M. The Challenges of Flight-Testing Unmanned Air Vehicles. In: Proceedings of the Systems Engineering, Test and Evaluation Conference, October 2002. 1-10.

WOOTTON, R. 2000. Aerodynamics: From insects to microvehicles. *Nature,* 403**,** 144-145.

XIAO, F., CHE, L., XIONG, B., WANG, Y., ZHOU, X., LI, Y. & LIN, Y. 2008. A novel capacitive accelerometer with an eight-beam-mass structure by self-stop anisotropic etching of (1 0 0) silicon. *Journal of Micromechanics and Microengineering,* 18**,** 075005.

XU, Y., JIANG, F., NEWBERN, S., HUANG, A., HO, C.-M. & TAI, Y.-C. 2003. Flexible shear-stress sensor skin and its application to unmanned aerial vehicles. *Sensors and Actuators A: Physical,* 105**,** 321-329.

YAMAMOTO, S., NAKAO, O. & NISHIMURA, H. Touch mode capacitive pressure sensor for passive tire monitoring system. Proceedings of the IEEE Sensors Conference, 2002 FL, USA. IEEE.

YAZDI, N., AYAZI, F. & NAJAFI, K. Micromachined inertial sensors. Proceedings of the IEEE, 1998. 1640-1659.

YEO, D., ATKINS, E. M., BERNAL, L. P. & SHYY, W. 2012. Aerodynamic Sensing for a Fixed Wing UAS Operating at High Angles of Attack. *AIAA Atmospheric Flight Mechanics Conference.* Minneapolis, Minnesota.

YOUNG, L. A., AIKEN, E. W., JOHNSON, J. L., DEMBLEWSKI, R., ANDREWS, J. & KLEM, J. 2002. *New concepts and perspectives on micro-rotorcraft and small autonomous rotary-wing vehicles*, Defense Technical Information Center.

ZAPPA, B., LEGNANI, G., BOGERT, A. J. & ADAMINI, R. 2001. On the number and placement of accelerometers for angular velocity and acceleration determination. *Journal of Dynamic Systems, Measurement, and Control* 123**,** 552-553.

ZHANG, P., GU, J., MILIOS, E. E. & HUYNH, P. Navigation with IMU/GPS/digital compass with unscented Kalman filter. Mechatronics and Automation, 2005 IEEE International Conference, 2005. IEEE, 1497-1502.

ZUFFEREY, J. C. & FLOREANO, D. 2006. Fly-inspired visual steering of an ultralight indoor aircraft. *Robotics, IEEE Transactions on,* 22**,** 137-146.